

**ECO FRIENDLY SYNTHESIS AND CHARACTERIZATION OF MESOPOROUS SILICA
NANOPARTICLES USING AGRICULTURAL WASTE**

A project submitted to

ST MARY'S COLLEGE (Autonomous). Thoothukudi

Affiliated to

Manonmaniam Sundaranar University,

Tirunelveli

In partial fulfilment of the award of the degree of

MASTER OF SCIENCE IN CHEMISTRY

Submitted by

E.SNOWBIYA

Reg. No: 19SPCH04

Under the Supervision and Guidance of

Mrs.D.Carolin Jeniba Rachel M.Sc. M.Phil., SET.,



PG DEPARTMENT OF CHEMISTRY (SSC)

St. Mary's College (Autonomous),

Thoothukudi

April – 2021

**ECO FRIENDLY SYNTHESIS AND CHARACTERIZATION OF MESOPOROUS SILICA
NANOPARTICLES USING AGRICULTURAL WASTE**

A project submitted to

ST MARY'S COLLEGE (Autonomous). Thoothukudi

Affiliated to

Manonmaniam Sundaranar University,

Tirunelveli

In partial fulfilment of the award of the degree of

MASTER OF SCIENCE IN CHEMISTRY

Submitted by

E.SNOWBIYA

Reg. No: 19SPCH04

Under the Supervision and Guidance of

Mrs.D.Carolin Jeniba Rachel M.Sc. M.Phil., SET.,



PG DEPARTMENT OF CHEMISTRY (SSC)

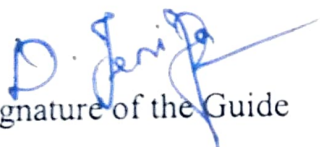
St. Mary's College (Autonomous),


Thoothukudi

April – 2021

CERTIFICATE


This is to certify that this project work entitled " **ECO FRIENDLY SYNTHESIS AND CHARACTERIZATION OF MESOPOROUS SILICA NANOPARTICLES USING AGRICULTURAL WASTE**" is submitted to **St. Mary's College (Autonomous)**, Thoothukudi affiliated to **Manonmaniam Sundaranar University**, Tirunelveli in partial fulfilment for the award of the **Degree of Master of Science in Chemistry** and this work done during the year 2020 - 2021 by **E.SNOWBIYA (Reg. No: 19SPCH04)**


Signature of the Guide



Signature of the Coordinator


Signature of the Director
Director

Self Supporting Courses
St. Mary's College (Autonomous)
Thoothukudi - 628 001.


Signature of Principal

Principal
St. Mary's College (Autonomous)
Thoothukudi - 628 001.


Signature of the Examiner

DECLARATION

I do hereby declare that the project entitled " **ECO FRIENDLY SYNTHESIS AND CHARACTERIZATION OF MESOPOROUS SILICA NANOPARTICLES USING AGRICULTURAL WASTE**" submitted for the degree of Master of Science in Chemistry is my original work carried out under the guidance of **Mrs.D.Carolin Jeniba Rachel M.Sc.,M.Phil.,SET., Assistant Professor, PG Department of Chemistry (SSC), St. Mary's College (Autonomous), Thoothukudi** and that it has not previously formed the basis for award of any Degree.

Station: Thoothukudi

Date:

E.SNOWBIYA

ACKNOWLEDGEMENT

I express my first and humble thanks to **GOD ALMIGHTY** for giving an opportunity to devote this work

I would like to express my sincere thanks to our principal **Dr. Sr. A.S.J. LUCIA ROSE**, Secretary **Sr. FLORA MARY**, Deputy principal **Dr. S. C. SHIBANA** Director of SSC, **Sr. F. MARY JOYCE BABY** and **Dr J.ANTONY RAJAM M.Sc., M. Phil., SET, Ph.D**, (SSC Coordinator), St Mary's College (Autonomous), Thoothukudi for providing the permission to complete the project work.

I find it difficult for me to write something in short to acknowledge my guide **Mrs.D.CAROLIN JENIBA RACHEAL M.Sc., M.Phil., SET.**, she taught me to think and solve the unconventional problems in a conventional way. Her constant inspiration, evaluable guidance tremendous patience and constructive criticism helped a lot to focus my views in the proper perspective I take this opportunity to express my deepest sense of gratitude and reference towards her for guiding me in the right direction throughout the course of this work My deep personal regards are due for her forever.

I heartly express my sincere thanks to my parents and Friends.

CONTENT

S.NO	TITLE	PAGE NO.
1	INTRODUCTION	1
2	REVIEW OF LITERATURE	12
3	SCOPE OF WORK	21
4	MATERIALS AND METHODS	23
5	RESULTS AND DISCUSSION	36
6	CONCLUSION	58
7	REFERENCE	59

LIST OF ABBRIVIATION

MSNs	Mesoporous silica nanoparticles
UV- Vis	Ultra – Violet Visible Spectroscopy
FT- IR	Fourier Transform Infrared Spectroscopy
XRD	X-Ray Diffraction
SEM	Scanning Electron Microscope
EDAX	Energy Dispersive X- Ray Analysis
AFM	Atomic Force Microscope

1.1 Mesoporous Silica Nanoparticles

Mesoporous silica nanoparticles (MSNs) are silica nanoparticles with pores that range in diameter from 2 to 50 nm and have an overall diameter below 1 μm . Their range of pore sizes is consistent with the IUPAC definition of *mesoporous* [1] and make them ideal materials for applications ranging from catalysis and environmental chemical removal to biomedicine. Here at nanoComposix, we bring the synthetic expertise required to tailor the design of MSNs to target an intended application with the utmost control.

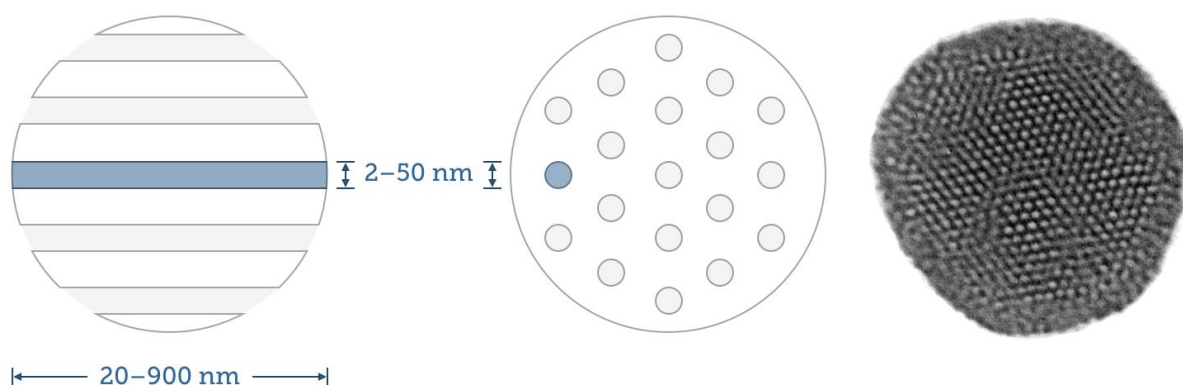


Fig:1.1 Mesoporous silica nanoparticles with pores

1.1.1 Design Characteristics of Mesoporous Silica Nanoparticles

In addition to their biocompatibility, key advantages of MSNs are associated with their high surface area and facile surface tunability. Often described as “nanosponges,” MSNs can adsorb large amounts of molecules dissolved in solution thanks to this high surface area; in fact, 5 grams of mesoporous silica nanoparticles possess the same surface area as an American football field. This highly ordered porosity can be controlled during the synthesis of MSNs.

1.1.1a Tunable Pore Sizes For Size-Selective Adsorption

MSNs can be made to have very narrow pore size distributions, yielding nanoparticles that will selectively adsorb molecules of a specific size.[2] The figure below illustrates that only molecules within a specific size range (small green circles) will enter the MSN cavities, while other larger molecules (large red circles) will be excluded. This feature is useful for molecule separation by size exclusion.

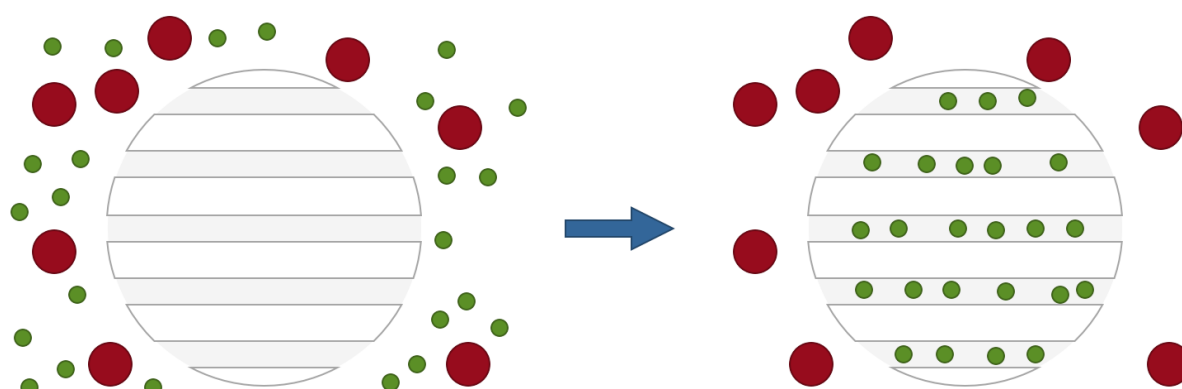


Fig: 1.1.1a molecules within specific range

1.1.1b Tunable Surface Chemistry For Functionally-Selective Adsorption

The versatility of the silica, it's possible to modify the surfaces of MSNs with specific functional groups that will interact selectively with certain categories of molecules. One can imagine coating the pores with a positive surface in order to attract negatively charged molecules, or using a hydrophobic surface to attract more hydrophobic molecules. MSN in which the pores are modified to allow molecules with a specific surface functionality (represented as green circles) to adsorb inside the particles, [3] whereas others (red pentagons) are excluded. This type of selective adsorption has numerous uses in hydrophobic drug encapsulation, environmental chemical removal, and various other applications.

1.1.1c Variable Pore Structures For Controlled Release

The organizational structure of the pores can also be modulated (MCM-41, MCM-48, radial, cubic, wormlike, etc.), as represented in the following figure. The use of one type over the others will depend on the application, as the pore structure controls the release/leakage of molecules loaded inside the pores.

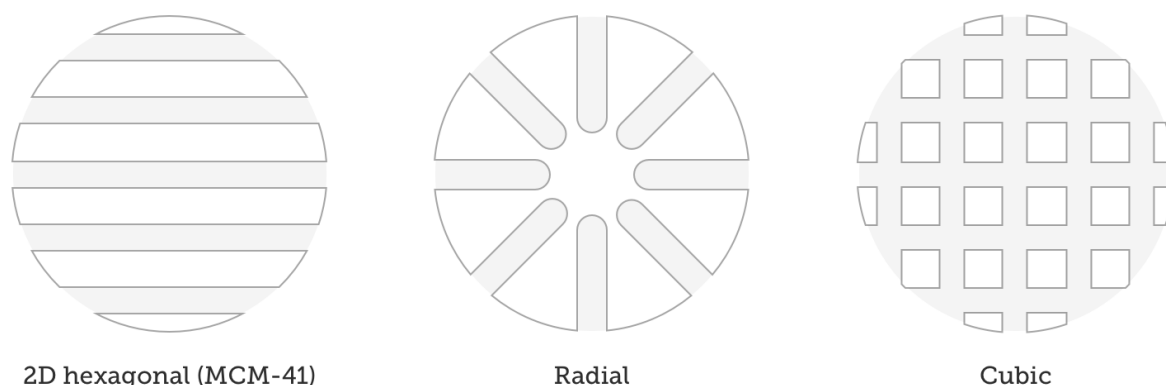


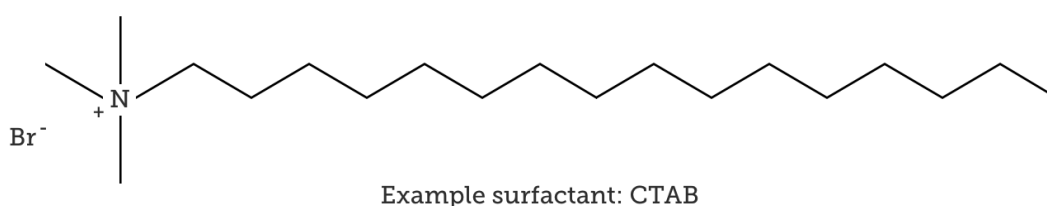
Fig:1.1.1b structure of the pores

For example, MSNs with the hexagonal pore arrangement can release cargo from both ends of a specific channel whereas in the cubic arrangement, molecules can travel freely inside the intricate network and be released from any pore outlet. In the radial pore arrangement, the molecule can only access a single pore and thus must exit through the pore it entered, making this particular system less prone to premature leaking[4] (in the case of drug encapsulation).

1.2 Synthesis & Purification of Mesoporous Silica Nanoparticles

Compared to the synthesis of regular silica nanoparticles that generally follow the Stöber process, MSNs are synthesized in a water-based solution in the presence of a base catalyst and a pore forming agent more widely known as a surfactant. Surfactants are molecules that present the particularity to have a hydrophobic tail (alkyl chain) and a hydrophilic head (charged group, such as a quaternary amine for example). [5]As these surfactants are added to a water-based solution, they will coordinate to form micelles with increasing concentration in order to stabilize the hydrophobic tails.

During the early stage of the hydrolysis and condensation of the silica precursor, oligomeric forms of silica appear. Like the final material, these oligomers possess silanol groups (Si-OH) that are deprotonated under the basic conditions of the reaction, forming negatively charged oligomers that can in turn condense on the surface of the positively charged micelles[6]. As the reaction proceeds, the oligomers grow larger around the micelles ultimately forming a hybrid organic/inorganic silica network templated by surfactant molecules. After the reaction, the removal of the template will create the porosity that defines mesoporous silica nanoparticles.



It is also possible to design and synthesize nanoparticles with various structures by modulating the porosity; such nanoparticles can have a hollow interior and a mesoporous silica shell, or a larger hollow interior and a thin microporous silica shell[7]. At nanoComposix we can also prepare particles with a microporous core and a thick mesoporous shell; the possibilities are almost infinite and limited only by the imagination.

1.3 Mesoporous-Silica Shelled Nanoparticles

The presence of the surfactants (e.g. CTAB) in the synthesis of MSNs conveniently enables the incorporation of a core of different material types at the center of the nanoparticle. Cores made up of other inorganic materials and even other types of silica can be suspended in these aqueous surfactant solutions for subsequent shell deposition and growth.

For these core-shell syntheses, the inorganic nanoparticles are generally stabilized directly by a surfactant on their surface. The presence of the surfactants provides the steric

stability needed for the inorganic nanoparticles to be dispersed in aqueous solutions. The extra layer of CTAB on the surface of the inorganic particles can act as an anchor point for the solubilized silicate species[8] (obtained after hydrolysis of the silica precursor), leading to the growth of silica around the inorganic nanoparticles. This technique has been used to prepare core-shell nanoparticles composed of silver, gold, iron oxide or quantum dot cores surrounded by a mesoporous silica shell.

Such materials combine both the advantages of the mesoporous silica (biocompatibility, drug delivery platform) with the unique properties of the core (plasmonics, imaging, photothermal, magnetic, etc.) and are widely used in the relatively new research field of theranostics. It can also be applied to different particle morphologies to make a wide variety of interesting heterostructures (see image below).

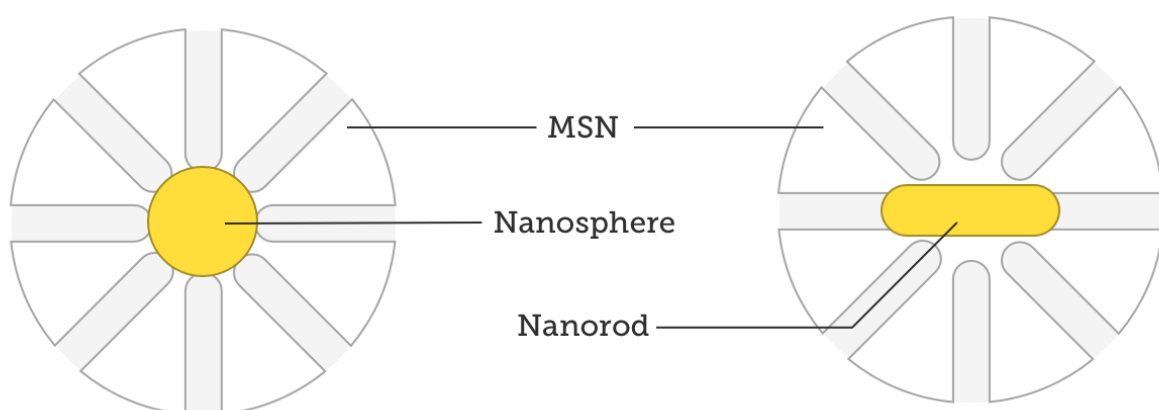


Fig:1.3 heterostructures of pores

1.4 Large-Pore Mesoporous Silica Nanoparticles

Since 2010, there has been increased interest and research done on synthesizing mesoporous silica with large dendritic pores ranging from 5–30 nm in diameter[9]. There are multiple pore expanding agents that are in current use today ranging from ring structures such as cyclohexane and trimethyl benzene, to chain structures such as octadecene.^{10, 11} There have

also been successful syntheses using less harsh agents like sodium salicylate and sodium trifluoroacetate for an anion enhanced expansion.¹²

1.5 Applications of mesoporous silica nanoparticles

1.5.1 Protein adsorption and separation

Owing to the facile preparation, low cost, high specific surface area, and availability of diverse surface functionalization, silica nanoparticles are ideal for specific protein adsorption and separation. For example, Ester-functionalized polypyrrole silica nanoparticles have the ability to bind covalently with human serum albumin (HSA) protein. The resulting HAS functionalized silica nanoparticle can form flocculation when incubating with anti-HAS, and thus diagnostic assays and biosensors can be developed based on the silica nanoparticles[10].

Recent techniques enable the silica nanoparticle to serve as a solid medium for protein immobilization. On the other hand, silica-coated iron oxide nanoparticles have been utilized for protein binding and separation, taking the advantage of their magnetic properties which afford a simple and fast approach for separation[11]. In this case, the iron oxide magnetic core can respond to external magnetic field, and used for fast particle separation, while the silica shell offers biocompatibility, stability, and a platform for protein entrapment. Such well-designed nanostructure system is very useful for enzyme immobilization, bioseparation, biosensors, and immunoassays.

1.5.2. Nucleic acid detection and purification

Silica nanoparticles have also been used for DNA detection, separation and purification. The adsorption of DNA onto the surface of silica nanoparticles is mainly influenced by three effects: weak electrostatic repulsion forces, dehydration, and hydrogen bond formation. Silica nanoparticles are also designed as DNA biosensors by means of their functionalization with oligonucleotides by hybridization with target complementary DNA or RNA probes to obtain variable fluorescent intensity. Just similar to protein separation, silica-coated magnetic nanoparticles are also employed to extract DNA from biological samples.

1.5.3. Drug and gene delivery

Mesoporous nanoparticles and surface functionalized nanoparticles are two different types of silica nanoparticles applied as a carrier for drugs and genes delivery[12]. The pores in the nanoparticles provide sites to keep drug molecules, and addition agents like gold nanoparticles, are required as caps to close the pores. To release the drugs, certain molecules that can break the covalent and open the pores are needed. Functionalized silica nanoparticles require good affinity to conjugate with genes. As DNA molecules are negatively charged, thus the silica nanoparticles have to be prepared with positively charged prosperity. Weak interactions are preferable between the functionalized silica nanoparticles and the genes ensure the release of genes.

1.5.4. Imaging contrast agents construction

Silica nanoparticles play an important auxiliary role in medical imaging, and they are utilized to encapsulate contrast agents particles, such as organic dyes, quantum dots, gold nanoparticles, iron oxide. Silica nanoparticles are capable of offering outstanding biocompatibility, low cytotoxicity, controllable size with a narrow distribution, and considerable options of surface functionalization. In addition, the silica nanoparticles can be developed as multifunctional tools featured with contrast agents, and drug/gene/protein delivery[13].

1.6 Corn husk

Corn husk, a lignocellulosic fibre generally discarded as waste, has the potential of being explored as a textile fibre. Corn or maize is the second-largest agricultural crop in the world. Cultivation of corn generates stover (stalk, leaves and husks) by-products that have been considered for a variety of uses.



Fig: 1.6.1 Corn husk

Corn stover typically consists of about 50 per cent stalks, 23 per cent leaves, 15 per cent cobs and 14 per cent husk. So, for hundreds of years, as we eat the corn, we have been throwing away most of the plant[14]. The leafy outer shell/covering of an ear of maize is referred to as corn husk. Each husk is relatively thin and flat, unlike the adult and juvenile foliar leaves. The sheaths of husks are broader and thinner than the sheaths of the foliar or ordinary leaves. Corn husk fibres have a high content of cellulose about 80-87 per cent and low content of lignin of about 6-8 per cent. The ash content is about 4-5 per cent. Untreated corn husk strands have cellular deposits with thick protective material covering on the surface.

Individual cells inside this layer are kept in place by other binding materials like lignin, hemicelluloses and pectin. A chemical or mechanical pre-treatment is required to break down this protective coating to obtain fibres with required properties. Corn husk fibres are extracted from the husk by alkali and enzymatic treatments. The raw material is treated in alkali solutions at high temperatures (85-90°C) for a particular time to extract fibre from husk[15]. Corn husk requires less chemical and/or physical treatment conditions and produces relatively superior quality of fibre compared to the fibre from stalks.

After treatment, the fibres are washed to remove the dissolved substances and short fibres. An additional enzyme treatment may be required to remove hemicellulose and lignin and to obtain finer fibres. Typical yield of fibres from husks or stalks varies from 10 to 30 per cent depending on the severity of the treatment and quality of fibres desired.

The main environmental benefit of using corn husk fibre is conservation of land and resources since you get fibre and food from the same plant. Corn husk is commonly available, with no geographical limitations, and is of limited commercial value. Therefore, corn husks show greater promise in providing large quantities of natural cellulose fibres with significant economic benefits than any other agricultural by-product[16]. As corn is grown in large quantity all over the world, corn husk is readily available. Corn husk offers an annually renewable, low cost and abundant source of cellulosic fibre.

The structure of the corn husk fibre is similar to that of cotton. Individual cells in corn husk appear to have natural convolutions that improve its fibre to fibre contact and

cohesiveness, aiding in the spinning of fibres. Corn husk fibres appear to be twisted ribbon-like with intermittent reversal in the direction of the twists.

Studies have been done by researchers on production of corn husk yarns by ring or friction spinning by blending it with other sustainable fibres like bamboo and cotton. The fabric produced from corn husk fibre has the distinctive advantage of moderate strength, toughness and high elongation with high durability, pliability and softness. These properties make corn husk a desired fibre for apparel, home furnishings and similar applications[17].

1.7 Wheat husk

Wheat is the most common and important human food grain and ranks second in total production as a cereal crop. Wheat grain is a staple food used to make flour for leavened, flat and steamed breads; cookies, cakes, pasta, noodles and couscous; and for fermentation to make beer [18] alcohol or biofuel. Wheat is planted to a limited extent as a forage crop for livestock and the straw can be used as fodder for livestock or as a construction material for roofing thatch. Wheat husk is a lignocellulosic waste product which is about 15–20% of wheat and some extents of wheat husk uses as cattle food and fuel . Rye (*Secale cereale*) is a cereal grown extensively as a grain and forage crop. It is a member of the wheat tribe (*Triticeae*) and is closely related to wheat. Rye grain is used for flour, rye bread, rye beer, whiskies, vodkas, and animal fodder. Non-food part of rye is agro waste which is about 15–20% of rye. The use of the cereal residues or by-products as a filler or reinforcement in the production of plastic composites alleviate the shortage of wood resources and can have the potential to start a natural fibre industry in countries where there are little wood resources left.

The composite industries are looking into alternative low cost lignocellulosic sources, which can decrease overall manufacturing costs and increase properties of the materials. Cereal husk raw material could be a potential alternative replacing wood for making composites material particularly for automobile, packaging and construction applications. Last couple of years, cereal lignocellulosic raw material (straw, cornstalk, husk, begases) has been used for making composites with polypropylene, polyethylene, polyester, polyvinyl acetate, polyurethane, poly (3-hydroxybutyrate-co-3-hydroxyvalerate) and Novolac resin It can also be pointed out that the development of biodegradable packaging materials from renewable natural resources has received widespread government support in

the EU countries and many national or international organisations have been established to facilitate the development in this area . Apart from composite materials, the particleboards from cereal by-product could be another potential alternative[19].



Fig: 1.7.1 wheat husk

1.8 Rice brand

Rice brands are the waste materials after the rice grains have been removed and are predominantly composed of silica. They can be used as an energy source, but the high ash content, relative to other biomass materials, makes their use problematic during co-firing. Ash contents of 15–20% (on a dry basis) are not uncommon with >60–70% SiO₂ content. Pellets made from a mixture of rice husks and olive residues have also been marketed, but it is unclear as to whether this product has been commercially successful[20].

Rice brand is an organic waste and is produced in large quantities. It is a major by-product of the rice milling and agro-based biomass industry. Rice brand is a cellulose-based fiber and contains approximately 20% silica in amorphous form. In addition, it consists of 60–65% volatile matter, 10–15% fixed carbon, and 17–23% ash. It contains approximately 40% cellulose, 30% lignin group, and 20% silica. Rice brand can absorb water ranging from 5% to 16% of unit weights, and the unit weight of rice[21].



Fig: 1.8.1 rice brand

Brand is $83\text{--}125\text{ kg/m}^3$. The ash of rice brand contains approximately 90% silica, which is a highly porous structure and is lightweight, with high specific surface area. Rice brand has been applied as an additive in many materials and applications, such as refractory brick, [22] manufacturing of insulation, and materials for flame retardants. This is due to its highly porous structure and its good insulating property. The properties of rice brand silica vary according to the firing temperature and time. The rice brand addition increased the porosity of sintered samples. Furthermore, the increase in the sintering temperatures increased the compressive strength of the fired brick[23].

▲ Christian Argyo, Veronika Weiss, Christoph Brauchle, and Thomas Bein studied by Multifunctional Mesoporous Silica Nanoparticles was a Universal Platform for Drug Delivery. Nano sized mesoporous silica particles with high colloidal stability attract growing attention as drug delivery systems for targeted cancer treatment and as bio imaging devices. This perspective described recent breakthroughs in mesoporous silica nanoparticle designed to demonstrate their high potential as multifunctional drug delivery nanocarriers. These types of nanoparticles could feature a well-defined and tunable porosity at the nanometer scale, high loading capacity, and multiple functionality for targeting and entering different types of cells. We focused on the requirements for an efficient stimuli-responsive and thus controllable release of cargo into cancer cells and discuss designed principles for smart and autonomous nanocarrier systems. Mesoporous silica nanoparticles were viewed as a promising and flexible platform for numerous biomedical applications. [24]

▲ Wei Wang,, Hu Chena, Jiaojiao Fang and Min Lai reported by Large-scale preparation of rice husk derived mesoporous SiO₂ and TiO₂ as efficient and promising photocatalysts for organic contaminants degradation. Mesoporous SiO₂ TiO₂ photocatalysts with application prospect for organic contaminants degradation were prepared by utilizing rice husk (RH), an easy-available bioresource, as the bio template. Structures and physicochemical properties of RH-derived SiO₂ and TiO₂ photocatalysts were systematically characterized and discussed. Results indicates the RH-derived mesoporous and thermal stable template, which could postponed the anatase rutile phase transition of TiO₂ at high temperatures, was mainly consisted of tightly compacted amorphous SiO₂ nanoparticles. Optimized calcination temperature of 700 °C was positive for prepared the most active RH derived SiO₂ and TiO₂, which had the anatase phase, mesoporous structure, proper crystalline degree 22.75 m, specific surface area of 41.13m²/g, and high ability in separating the photogenerated electron-hole pairs for removal of Rhodamine B (RhB) in aqueous solutions under both the xenon lamp and visible light irradiation. Moreover, large-scale preparation, stable, and recyclable properties of the photocatalysts were also confirmed, which makes them as promising photocatalysts for practical application[25].

▲ Chutima Vanichvattanadecha, Wadwan Singhapong, Angkhana Jaroenworarluck investigated by Different sources of silicon precursors influencing on surface characteristics and pore morphologies of mesoporous silica nanoparticles. Mesoporous silica nanoparticles

(MSNs) were synthesized via a sol–gel method simplified by using pluronic F127 surfactant as a pore template without following the two steps of butanol co-surfactant mixing and hydrothermal processing. Tetraethyl orthosilicate (TEOS) and rice husk (RH) were used as chemical and natural sources of silicon (Si) precursors, respectively. As received RH was pretreated with naturally enzyme solutions to extract its impurities. A synthesized powders were calcined at 500°C and 600 °C to optimize heating conditions for removing organic matters. Surface characteristics, chemical functionalities and ordered disordered mesopores of the calcined powders were characterized using various techniques. Experimental results revealed that highly ordered (SBA-16) and disordered MSNs were obtained from the synthesized routes using TEOS and pre-treated RH, respectively. Disordered mesopores formed had been explored and discussed in terms of metal oxides, trace elements and surface characteristics analyzed by X-ray fluorescent analysis (XRF), X-ray photoelectron spectroscopy (XPS) and Atomic force microscopy (AFM), respectively. In summary, SBA-16 and the disordered MSNs obtained from the synthesized method had potential as drug deliveries or catalyst supports due to their high purities and typical characteristics of the mesopores with possessing large surface areas and pore sizes.[26]

▲ Jinyoung Chuna, Yang Mo Gwa, Jongkook Hwang, Kyeong Keun Oh and Jin Hyung Lee analysed by Synthesis of ordered mesoporous silica with various pore structures using high-purity silica extracted from rice husk. Rice husk was a promising abundant bio resource for the production of high value-added silica materials because it had the highest SiO₂ content among all plant-based resources. In this study, ordered mesoporous silica with various pore structures were synthesized from rice husk by combining acid leaching, chemical dissolution, and co-assembly with additional surfactants. Depending upon the type of the surfactant used and the co-assembly conditions, various mesoporous silica that had controlled pore structures (mesocellular forms and hexagonal nano channel structures), pore sizes (3–60nm), large surface areas (297–895 m²/g), and pore volumes (0.81–1.77cm³/g) were successfully synthesized from a sodium silicate solution, which was made from high-purity silica (99.8%) extracted from rice husk. The synthesis of high value-added silica from an abundant bio resource could open up new avenues for sustainable and environment-friendly industrial development.[27]

▲ Maryam Azadeh, Cyrus Zamani, Abolghasem Ataie, J.R Morante reported by Three-dimensional rice husk-originated mesoporous silicon and its electrical properties. A

facile and cost-effective process to synthesize nanostructured silicon from rice husk-originated silica was introduced. Rice husk was acid-washed and then calcined at various temperatures in the range of 600–900 °C. Nanostructured silicon was obtained through magnesiothermic reduction process of SiO₂. Products of the magnesiothermic process, elemental silicon together with magnesia and magnesium silicate, were subjected to leaching to remove the latter two phases. Based on XRD and XRF results, nanometric silica powder obtained after 3 h calcination at 700 °C was selected for further processing. After reduction process, the formation of a three dimensional silicon skeleton 70–90 nm in thickness with the specific surface area of 53.02m²/g was confirmed through HRTEM, SEM and BET observations, in agreement with X-ray pattern. The electrical response of the silicon-based electrode was measured to be 0.0023 Ω m, indicates the employed synthesis route as a promising one for electrode fabrication[28].

▲ Mohsen Ghaferi, Maedeh Koochi Moftakhari Esfahani, Aun Raza, Sitah Al Harthi, Hasan Ebrahimi Shahmabadi and Seyed Ebrahim Alavi reported by Mesoporous silica nanoparticles: synthesis methods and their therapeutic use-recent advances. Mesoporous silica nanoparticles (MSNPs) were a particular example of innovative nanomaterials for the development of drug delivery systems. MSNPs have recently received more attention for biological and pharmaceutical applications due to their capability to deliver therapeutic agents. Due to their unique structure, they can function as an effective carrier for the delivery of therapeutic agents to mitigate diseases progress, reduce inflammatory responses, and consequently improve cancer treatment. The potency of MSNPs for the diagnosis and management of various diseases has been studied. This literature review will take an in-depth look into the properties of various types of MSNPs (e.g., shape, particle and pore size, surface area, pore volume, and surface functionalization), and discussed their characteristics, in terms of cellular uptake, drug delivery, and release. MSNPs would then be discussed in terms of their therapeutic applications (passive and active tumor targeting, theranostics, biosensing, and immune stimulative), biocompatibility, and safety issues. Also, emerging trends and expected future advancements of this carrier would be provided.[29]

▲ Mehrez E. El-Naggar ,Nader R. Abdelsala, Moustafa M.G. Fouda, and Essam E. Kandil by Soil Application of Nano Silica on Maize Yield and Its Insecticidal Activity Against Some Stored Insects After the Post-Harvest. Maize was considered one of the most imperative cereal crops worldwide. In this work, high throughput silica nanoparticles (SiO₂-NPs) were prepared via the sol–gel technique. SiO₂-NPs were attained in a powder form followed by full analysis using the advanced tools (UV-vis, HR-TEM,SEM, XRD and zeta potential). To this

end, SiO₂-NPs were applied as both nanofertilizer and pesticide against four common pests that infect the stored maize and cause severe damage to crops. As for nanofertilizers, the response of maize hybrid to mineral NPK, “Nitrogen (N), Phosphorus (P), and Potassium (K)” (0% = untreated, 50% of recommended dose and 100%), with different combinations of SiO₂-NPs; (0, 2.5, 5, 10 g/kg soil) was evaluated. Afterward, post-harvest, grains were stored and fumigated with different concentrations of SiO₂-NPs (0.0031, 0.0063, 0.25, 0.5, 1.0, 2.0, 2.5, 5, 10 g/kg) in order to identify LC₅₀ and mortality % of four common insects, namely *Sitophilus oryzae*, *Rhizopertha dominica*, *Tribolium castaneum*, and *Orizaephilus surinamensis*. The results revealed that, using the recommended dose of 100%, mineral NPK showed the greatest mean values of plant height, chlorophyll content, yield, its components, and protein (%). By feeding the soil with SiO₂-NPs up to 10 g/kg, the best growth and yield enhancement of maize crop is noticed. Mineral NPK interacted with SiO₂-NPs, whereas the application of mineral NPK at the rate of 50% with 10 g/kg SiO₂-NPs, increased the highest mean values of agronomic characters. Therefore, SiO₂-NPs can be applied as a growth promoter, and in the meantime, as strong unconventional pesticides for crops during storage, with a very small and safe dose.[30]

▲ Siva Kumar Natarajan and Stalin Selvaraj reported by Mesoporous silica nanoparticles: importance of surface modifications and its role in drug delivery. Mesoporous nanoparticles are special examples of silica nanoparticles. They were well known for their variety of applications in various fields including biomedicine. This had been attributed to their size, tenability and easily modifiable capabilities because of the presence of functional groups, and their biocompatibility. In this review, we specifically focused on different modes of surface modifications using amino propyl and organic chains which facilitate maximum drug loading and sustained release. This review provides complete information about the importance of surface modifications and their biological consequences that would be helpful to understand the use of MCM-41 and SBA 15 as suitable drug delivery systems.[31]

▲ Reema Narayan, Usha Y. Nayak, Ashok M. Raichur and Sanjay Garg investigated by Mesoporous Silica Nanoparticles: A Comprehensive Review on Synthesis and Recent Advances. Recent advancements in drug delivery technologies utilizing a variety of carriers had resulted in a path-breaking revolution in the approach towards diagnosis and therapy alike in the current times. Need for materials with high thermal, chemical and mechanical properties had led to the development of mesoporous silica nanoparticles (MSNs). These ordered porous

materials had garnered immense attention as drug carriers owing to their distinctive features over the others. They can be synthesized using a relatively simple process, thus making it cost effective. Moreover, by controlling the parameters during the synthesis; the morphology, pore size and volume and particle size could be transformed accordingly. Over the last few years, a rapid increase in research on MSNs as drug carriers for the treatment of various diseases had been observed indicates its potential benefits in drug delivery. Their widespread application for the loading of small molecules as well as macromolecules such as proteins, RNA and so forth, had made it a versatile carrier. In the recent times, researchers had sorted to several modifications in the framework of MSNs to explore its potential in drug resistant chemotherapy, antimicrobial therapy. In this review, we had discussed the synthesis of these multitalented nanoparticles and the factors influencing the size and morphology of this wonder carrier. The second part of emphasizes on the applications and the advances made in the MSNs to broaden the spectrum of its use especially in the field of biomedicine. We had also touched upon the lacunae in the thorough understanding of its interaction with a biological system which poses a major hurdle in the passage of this carrier to the clinical level. In the final part of this review, we had discussed some of the major patents filed in the field of MSNs for therapeutic purpose.[32]

▲ N Ramel, K Jumbri, R A Wahab, A Ramli, F Huyop analysed by Synthesis and characterization of mesoporous silica nanoparticles using ionic liquids as a template. Mesoporous silica nanoparticles (MSN) were successfully synthesized using different types of ionic liquids (ILs) with different length of side alkyl chain as the template. The formed MSN were characterised by FTIR, XRD and BET. In this study, ILs of long alkyl chains of cation was found to decrease the pore size of the MSNs thus, increasing the surface area. FTIR spectroscopy affirmed the formation of SiO₂ while the broad peak in the X-ray diffractogram conveyed that the silica of MSNs was amorphous.[33]

▲ Olivija Plohl, Saso Gyergyek Lidija Fras Zemlji reported by The focus of the article is on the design of environmentally friendly nano carriers for improved controlled pesticide release, which have low environmental toxicity and nitrogen elemental composition as the most important components of fertilisers. In this study, a novel delivery system was developed

for post loading a bio pesticide to mesoporous silica nanoparticles (MeSiNPs) functionalised with N-rich derived polymer. Initially, MeSiNPs were synthesised by the template assisted method, which yielded MeSiNPs in the nm range, together with highly ordered mesoporous channels with a pore size of 2.9nm. Subsequently, the water-soluble branched polyethyleneimine was derived systematically with epoxy orthosilicate, and functionalised on MeSiNPs to create a source of N-nutrients. The carefully designed novel nano carrier was analysed by several physicochemical and structural analyses, which confirmed the successful attachment of the derived MeSiNPs. Further, the novel nano-synthesised system was used as a delivery for the model biopesticide citridiol. The loading efficiency of citridiol in/on MeSiNPs_bPEI was 19%, while the loading capacity of citridiol was proven to be 5 mg biopesticide/1 mg MeSiNPs_bPEI. The MeSiNPs with loaded citridiol was investigated for kinetic release. The system showed a fast initial release behaviour in the first 300 min, which was continued by slow release behaviour and started to reach equilibrium after 10 days. It has been shown that the MeSiNPs showed an excellent potential for use in agrochemical applications, not only as a nanocarrier for controlled and slow pesticide release, but may also act as a soil improver by providing Si and N as key nutrient sources.

▲ Amirala Bakhshian Nik, Hossein Zare, Seyedsahameddin Razavi, Hesameddin Mohammadi, Pooya Torab Ahmadi, Narges Yazdani, Mehrdad Bayandori, Navid Rabiee, Jalal Izadi Mobarakeh analysed by Smart drug delivery: Capping strategies for mesoporous silica nanoparticles. Systematic delivery of therapeutic agents to specific sites, with a stimulusresponsive drug release profile was currently a rapidly growing area. Mesoporous silica nanoparticles (MSNs) were the useful platforms as drug/gene delivery systems due to their unique properties including the ability to control the pore size, high porosity, and morphology, which can directly affect the mechanism and profile of drug release. The appropriate fabrication strategy can tailor the particle shape and size, leading to enhanced delivery and release mechanisms. The MSN surface can be modified by using either organic or inorganic molecules to induce smart and site-specific drug delivery and release. Furthermore, application of molecules that function as pore gatekeepers with the ability to uncap via physiochemical stimuli can enhance the efficiency of drug delivery and release. This report aims to highlight the recent efforts and developments of strategies applied to render MSNs smarter and more effective for drug delivery applications[34].

▲ Naiara I. Vazquez, Zoilo Gonzalez, Begona Ferrari, Yolanda Castro investigated by synthesis of mesoporous silica nanoparticles by sol–gel as nano container for future drug delivery applications. Development of mesoporous silica nanoparticles as carriers for drug delivery systems has increased exponentially during the last decade. The present work is focused on the synthesis of silica carriers by sol–gel from tetraethyl orthosilicate (TEOS) as precursor of silica and cetyltrimethylammonium bromide (CTAB) as pore generating agent. The synthesis conditions were modified varying the molar ratio of water TEOS, NH_3 , TEOS and amount of CTAB. The silica particles were characterized by scan electron microscopy techniques (FESEM) high resolution transmission electron microscopy (HR-TEM), N_2 adsorption desorption isotherms, Zeta-potential and Dynamic Light Scattering (DLS). The results show that the specific surface area and the porosity of silica particles were strongly affected by the addition of CTAB and the amount of H_2O . The dispersion and stability of silica mesoporous particles is achieved in spite of the high surface reactivity. The synthesis formulation affects considerably to the particle morphology, which changes from spheres to rods when the molar ratio of H_2O increases. A maximum specific surface area of $1480 \text{ m}^2/\text{g}$ was obtained with pore sizes ranging 2.5–2.8 nm.[35]

▲ H X Nguyen analysed by Nanosilica synthesis from rice husk and application for soaking seeds. Nanosilica was synthesized from rice husk. At first, the rice husk ash was obtained by annealing at temperatures 700°C for 6 hours, then nanosilica particles were extracted by using 0.5N NaOH solution followed by forming gel with HCl acid solution. The structural features of the products were characterized by techniques including Energy dispersive X-ray, Field Emission Scanning Electron Microscopes, Fourier Transformation Infrared, Fourier Transformation Infrared. The results showed that the SiO_2 nanoparticles have average size about 30-100 nm and >98 % purity. The present experiment was conducted to test the beneficial effects of nanosilica on the seed germination. Seeds (BC rice, Bacthom rice and bean) were analyzed with regard to germination percentage (GP), mean germination time, seed germination index, seed vigour index to investigate the efficiency of nanosilica. Among the treatments, the addition of 40 mg/L nanosilica for BC rice seed, 60 mg/L for Bacthom rice seed showed the most promising results that yielded significant differences from the control in terms. Compare to GP of BC and Bacthom sample after treatment (100%), GP of sample with nanosilica are 93.33% and 53.33%, respectively. Besides, the samples which added nanosilica have higher average length of shoot and root than blank sample[36].

▲ N Rameli & K Jumbri reported by Synthesis and characterization of mesoporous silica nanoparticles using ionic liquids as a template Mesoporous silica nanoparticles (MSN) were successfully synthesized using different types of ionic liquids (ILs) with different length of side alkyl chain as the template. The formed MSN were characterised by FTIR, XRD and BET. In this study, ILs of long alkyl chains of cation was found to decrease the pore size of the MSNs thus, increasing the surface area. FTIR spectroscopy affirmed the formation of SiO₂ while the broad peak in the X-ray diffractogram conveyed that the silica of MSNs is amorphous[37].

▲ Sung Kyoo Park reported by Preparation of silica nanoparticles: determination of the optimal synthesis conditions for small and uniform particles. Silica nanoparticles were prepared from tetraethylorthosilicate (TEOS) dissolved in ethanol by using a semi-batch process in order to control the particle properties. In this work, the statistical experimental method was also used to compare the properties (particle size and SD) of the SiO₂ particles according to the four parameters ($R = [\text{H}_2\text{O}] / [\text{TEOS}]$), concentration of ammonia (NH₃), the feed rate of reactant, reaction temperature. We have obtained monodispersed silica particles having size ranging from 10 to 350nm by our experiment. It was found that the optimal synthesis conditions for the preparation of SiO₂ nanoparticles with narrow size distribution in semi-batch process were as follows; ($R=[\text{H}_2\text{O}]/[\text{TEOS}]$, 30–55; concentration of ammonia (NH₃), 0.2–0.35 mole l⁻¹; feed rate of reactant, 13–17 cm³ min⁻¹; reaction temperature, 55–65°C). The above-mentioned optimal conditions were used to prepare the particles with minimum particle size (30nm) and its SD (5nm), simultaneously. Experimental results measured by using the optimal synthesis conditions were in a good agreement with simulated value and the smallest size (10 nm in diameter) was obtained. Also, we found that the effect of parameters on the particle size and SD in the preparation of SiO₂ nanoparticles was increased in the following order; reaction temperature,($R=[\text{H}_2\text{O}]/[\text{TEOS}]$); concentration of ammonia (NH₃), feed rate of reactant. [38]

▲ Xiao-Dong Wang, Zheng-Xiang Shen, Tian Sang investigated by Preparation of spherical silica particles by Stöber process with high concentration of tetraethylorthosilicate. In this paper, Stöber process with high concentration of tetraethylorthosilicate (TEOS) up to 1.24 M is used to prepare mono disperse and uniform size silica particles. The reactions are carried out at $[\text{TEOS}] = 0.22\text{--}1.24$ M, low concentrations of ammonia ($[\text{NH}_3] = 0.81[\text{TEOS}]$), and $[\text{H}_2\text{O}] = 6.25[\text{TEOS}]$ in isopropanol. The solids content in the resulting suspension achieves a

maximum value of 7.45% at 1.24 M TEOS. Various sized particles in the range of 30–1000 nm are synthesized. The influences of TEOS, NH_3 , and H_2O on the size and size distribution of the particles are discussed. A modified monomer addition model combined with aggregation model is proposed to analyze the formation mechanism of silica particles.[39]

Nanostructural materials have become attractive because of their unique characteristics that can hardly be obtained from conventional bulk materials owing to their quantum size and surface effects. So there has been considerable interest in fabrication of low dimensional nanosized materials such as nanowires, nanorods and nanotubes because they possess distinctive geometries, novel, physical and chemical properties and have potential applications in nanodevices and find diverse application in nanotechnology.

Agricultural waste are choosen to synthesize silica nanoparticles in Eco-friendly manner. The synthesis via this method does not required by several physical methods. The product obtained after the reaction is homogenous.

SiO₂ nanoparticles have applications in the electromagnetic machines due to their high magnetic saturation values and they are used in magnetic resonance imaging and in coatings of plastics, nanowire, nanofibre and textiles and in certain alloy and catalyst application. So in this, we prepare a silica, oxygen compound nanoparticles form the agricultural waste.

3.2 OBJECTIVES:

SiO₂ are prepared by chemical synthesis using agricultural waste

- To synthesis SiO₂ nanoparticle using agricultural waste.
- To study the optical properties by using UV- Visible spectrometer.
- To identify the various stretching frequencies and bonding within the nanocomposites using Fourier Transform-InfraRed spectroscopy.
- To determine the surface morphology and size of the particles using Scanning Electron Microscope and Atomic Force Microscopy
- To find out particle size and shape of the crystals using X-Ray Diffraction studies.
- To confirm the elements present in the synthesied nanoparticles using Energy Dispersive X-ray spectroscopy.

4.1 MATERIALS

- ❖ Rice brand
- ❖ Wheat husk
- ❖ Maize husk
- ❖ Con. HCl – nice bran LR grade
- ❖ Silica crucible

4.2 METHODS

4.2.1 PREPARATION OF RICE BRAND

Rice brand is collected washed well with distilled water and dried at 100°C in hot air oven. The dried sample is allowed to cool and chapped into small pieces. The substance is taken in a silica crucible and kept into muffle furnace for \approx to 8 hrs at \approx 600°C. It is then allowed to cool and purified used in con.HCl. It is washed with distilled water thoroughly to remove excess acid and then dried 120° c for about 2hrs in hot air oven and cooled. Now the particle grained used in mortal testle into finer particle. The prepared silica nanoparticles is named as SO-Rb.

4.2.2 PREPARATION OF WHEAT HUSK

Wheat husk is collected washed well with distilled water and dried at 100°C in hot air oven. The dried sample is allowed to cool and chapped into small pieces. The substance is taken in a silica crucible and kept into muffle furnace for \approx to 8 hrs at \approx 600°C. It is then allowed to cool and purified used in con. HCl. It is washed with distilled water thoroughly to remove excess acid and then dried 120° c for about 2hrs in hot air oven and cooled. Now the

particle grained used in mortal testle into finer particle. The prepared silica nanoparticles is named as SO-W.

4.2.3. PREPARATION OF MAIZE HUSK

Maize husk is collected washed well with distilled water and dried at 100°C in hot air oven. The dried sample is allowed to cool and chapped into small pieces. The substance is taken in a silica crucible and kept into muffle furnace for \approx to 8 hrs at \approx 600°C. It is then allowed to cool and purified used in con. HCl. It is washed with distilled water thoroughly to remove excess acid and then dried 120° c for about 2hrs in hot air oven and cooled. Now the particle grained used in mortal testle into finer particle. The prepared silica nanoparticles is named as SO-M.

4.3 INSTRUMENTATION

4.4 UV-Visible spectrometer

A light beam is passed through an object and wavelength of the light reaching the detector is measured[40]. The measured wavelength provides important information about chemical structure and number of molecules (present in intensity of the measured signal). Thus, both quantitative and qualitative information can be gathered. Information may be obtained as transmittance, absorbance or reflectance of radiation in 160 to 3500 nm wavelength range . The absorption of incident energy promotes electrons to excited states or the anti-bonding orbitals. For this transfer to occur, photon energy must match the energy needed by electron to be promoted to next higher energy state. This process forms the basic operating principle of absorption spectroscopy. Potentially, there may be three types of ground state orbitals involved:

1. σ (bonding) molecular orbital
2. π (bonding) molecular orbital
3. n (non-bonding) atomic orbital

Besides, the anti-bonding orbitals are:

- i. σ^* orbital.
- ii. π^* orbital

A transition involving excitation of an electron from s bonding orbital to σ anti-bonding orbital is called σ to σ^* transition. [41] Likewise, π to π^* represents the excitation of an electron of a lone pair (non-bonding electron pair) to an antibonding π orbital. Electronic transitions occurring due to absorption of UV and visible light are:

- I. σ to σ^* ;
- II. n to σ^* ;
- III. n to π^* ;
- IV. π to π^* .

The transitions s to σ^* and n to σ^* involve higher energies and thus usually occur in far UV region or weakly in 180 to 240nm region. Thus, saturated groups do not show strong absorption in UV region. Molecules with unsaturated centres undergo n to π^* and π to π^* transitions; these transitions involve lesser energies and thus occur at longer wavelengths than transitions to σ^* anti-bonding orbitals.

When light having specific wavelength and energy is focused onto the sample, it absorbs some energy of the incident wave. A photodetector measures energy of transmitted light from sample, and registers absorbance of the sample[42]. The absorption or transmission spectrum of the light absorbed or transmitted by the sample against the wavelength is formed.



Fig:4.4.1 UV-Vis spectrometer

Applications

UV/Vis spectroscopy is routinely used in analytical chemistry for the quantitative determination of different analytes, such as transition metal ions,

highly conjugated organic compounds, and biological macromolecules. Spectroscopic analysis is commonly carried out in solutions but solids and gases may also be studied.

- Solutions of transition metal ions can be colored (i.e., absorb visible light) because d electrons within the metal atoms can be excited from one electronic state to another. The colour of metal ion solutions is strongly affected by the presence of other species, such as certain anions or ligands. For instance, the colour of a dilute solution of copper sulfate is a very light blue; adding ammonia intensifies the colour and changes the wavelength of maximum absorption (λ_{max}).
- Organic compounds, especially those with a high degree of conjugation, also absorb light in the UV or visible regions of the electromagnetic spectrum. The solvents for these determinations are often water for water-soluble compounds, or ethanol for organic-soluble compounds. (Organic solvents may have significant UV absorption; not all solvents are suitable for use in UV spectroscopy. Ethanol absorbs very weakly at most wavelengths.) Solvent polarity and pH can affect the absorption spectrum of an organic compound. Tyrosine, for example, increases in absorption maxima and molar extinction coefficient when pH increases from 6 to 13 or when solvent polarity decreases.
- While charge transfer complexes also give rise to colours, the colours are often too intense to be used for quantitative measurement[43].

The Beer–Lambert law states that the absorbance of a solution is directly proportional to the concentration of the absorbing species in the solution and the path length. Thus, for a fixed path length, UV/Vis spectroscopy can be used to determine the concentration of the absorber in a solution. It is necessary to know how quickly the absorbance changes with concentration. This can be taken from references (tables of molar extinction coefficients), or more accurately, determined from a calibration curve.

4.5 FT-IR Spectroscopy

Fourier-transform infrared spectroscopy (FTIR) is a technique used to obtain an infrared spectrum of absorption or emission of a solid, liquid or gas. An FTIR spectrometer simultaneously collects high-resolution spectral data over a wide spectral range. This confers a significant advantage over a dispersive spectrometer, which measures intensity over a narrow range of wavelengths at a time.

The term Fourier-transform infrared spectroscopy originates from the fact that a Fourier transform (a mathematical process) is required to convert the raw data into the actual spectrum. Fourier-transform spectroscopy is a less intuitive way to obtain the same information. Rather than shining a monochromatic beam of light (a beam composed of only a single wavelength) at the sample, this technique shines a beam containing many frequencies of light at once and measures how much of that beam is absorbed by the sample. Next, the beam is modified to contain a different combination of frequencies, giving a second data point. This process is rapidly repeated many times over a short time span. Afterwards, a computer takes all this data and works backward to infer what the absorption is at each wavelength[44].

The beam described above is generated by starting with a broadband light source one containing the full spectrum of wavelengths to be measured. The light shines into a Michelson interferometer a certain configuration of mirrors, one of which is moved by a motor. As this mirror moves, each wavelength of light in the beam is periodically blocked, transmitted, blocked, transmitted, by the interferometer, due to wave interference. Different wavelengths are modulated at different rates, so that at each moment or mirror position the beam coming out of the interferometer has a different spectrum.



Fig: 4.5.1 FT-IR Spectrometer

Applications

FTIR can be used in all applications where a dispersive spectrometer was used in the past. In addition, the improved sensitivity and speed have opened up new areas of

application. Spectra can be measured in situations where very little energy reaches the detector and scan rates can exceed 50 spectra a second. Fourier transform infrared spectroscopy is used in geology, chemistry, materials and biology research fields.

- **Biological material:** FTIR is used to investigate proteins in hydrophobic membrane environments. Studies show the ability of FTIR to directly determine the polarity at a given site along the backbone of a trans membrane protein.
- **Microscopy and imaging:** An infrared microscope allows samples to be observed and spectra measured from regions as small as 5 microns across. Images can be generated by combining a microscope with linear or 2-D array detectors. The spatial resolution can approach 5 microns with tens of thousands of pixels. The images contain a spectrum for each pixel and can be viewed as maps showing the intensity at any wavelength or combination of wavelengths. This allows the distribution of different chemical species within the sample to be seen. Typical studies include analysing tissue sections as an alternative to conventional histopathology and examining the homogeneity of pharmaceutical tablets[40].
- **Nanoscale and spectroscopy below the diffraction limit:** The spatial resolution of FTIR can be further improved below the micrometer scale by integrating it into scanning near-field optical microscopy platform. The corresponding technique is called nano-FTIR and allows for performing broadband spectroscopy on materials in ultra-small quantities (single viruses and protein complexes) and with 10 to 20 nm spatial resolution.
- **FTIR as detector in chromatography:** The speed of FTIR allows spectra to be obtained from compounds as they are separated by a gas chromatograph. However this technique is little used compared to GC-MS (gas chromatography-mass spectrometry) which is more sensitive. The GC-IR method is particularly useful for identifying isomers, which by their nature have identical masses. Liquid chromatography fractions are more difficult because of the solvent present. One notable exception is to measure chain branching as a function of molecular size in polyethylene using gel permeation chromatography, which is possible using chlorinated solvents that have no absorption in the area in question[67].

4.6 X-ray Diffraction (XRD)

X-ray diffraction is now a common technique for the study of crystal structures and atomic spacing. X-ray diffraction is based on constructive interference of monochromatic X-rays and a crystalline sample. These X-rays are generated by a cathode ray tube, filtered to produce monochromatic radiation, collimated to concentrate, and directed toward the sample. The interaction of the incident rays with the sample produces constructive interference (and a diffracted ray) when conditions satisfy Bragg's Law ($n\lambda=2d \sin \theta$). This law relates the wavelength of electromagnetic radiation to the diffraction angle and the lattice spacing in a crystalline sample[66]. These diffracted X-rays are then detected, processed and counted. By scanning the sample through a range of 2θ angles, all possible diffraction directions of the lattice should be attained due to the random orientation of the powdered material. Conversion of the diffraction peaks to d-spacings allows identification of the mineral because each mineral has a set of unique d-spacings. Typically, this is achieved by comparison of d-spacings with standard reference patterns[68].

- All diffraction methods are based on generation of X-rays in an X-ray tube. These X-rays are directed at the sample, and the diffracted rays are collected. A key component of all diffraction is the angle between the incident and diffracted rays. Powder and single crystal diffraction vary in instrumentation beyond this.



Fig : 4.6.1 schematic representation of XRD spectrometer

Applications

X-ray powder diffraction is most widely used for the identification of unknown crystalline materials (e.g. minerals, inorganic compounds). Determination of unknown solids is critical to studies in geology, environmental science, material science, engineering and biology[45].

Other applications include:

- characterization of crystalline materials
- identification of fine-grained minerals such as clays and mixed layer clays that are difficult to determine optically
- determination of unit cell dimensions
- measurement of sample purity

With specialized techniques, XRD can be used to:

- determine crystal structures using Rietveld refinement
- determine of modal amounts of minerals (quantitative analysis)
- characterize thin films samples by:
 - determining lattice mismatch between film and substrate and to inferring stress and strain
 - determining dislocation density and quality of the film by rocking curve measurements
 - measuring superlattices in multilayered epitaxial structures
 - determining the thickness, roughness and density of the film using glancing incidence X-ray reflectivity measurements[69]

4.7 Field Emission Scanning Electron Microscope (FESEM)

Field emission scanning electron microscopy (FESEM) provides topographical and elemental information at magnifications of 10x to 300,000x, with virtually unlimited depth of field. Compared with convention scanning electron microscopy (SEM), field emission SEM (FESEM) produces clearer, less electrostatically distorted images with spatial resolution down to 1 1/2 nanometers –

three to six times better. electron source designed for high-resolution imaging and suitable for various kinds of materials is field emission, which uses field emitter gun (FEG) to emit electrons[65]. The SEM that uses FEG as the emitter type is called field emission scanning electron microscope (FESEM); whereby the emitter type is used as a part of its name to distinguish it from the classic SEM. FEG is made up of tungsten wire that has diameter about 100 nm, preferably a single crystal type, designed in such that the 310 plane is perpendicular to the electron optical axis. The gun tip is placed near an anode which held at +2-6 kV, the sharpness of the point produces fields of $\sim 10^{10}$ V/m near its surface. This will result electrons to tunnel through the barrier into the vacuum at a much focused beam (~ 2 nm). The current emitted is seldom reaching more than 5-10 μA , [46] however it has brightness far higher than thermionic emitter. FESEM is developed based on a technology for high-resolution imaging and different contrasting methods aiming for a comprehensive characterization of specimens. FESEM can be used in wide range of applications including imaging surface sensitive and non-conductive samples without the need for pre-treatment. FESEM also comes with various attachments for elemental analysis. This paper describes the technical specifications



Fig:4.7.1 schematic representation of FESEM spectrometer

Applications Of FESEM

- ▲ Materials science: In modern materials science, investigations into nanotubes and nanofibres, high temperature superconductors, mesoporous architectures and alloy strength, all rely heavily on the use of FESEM for research and investigation. In fact,

just about any material science industry, from aerospace and chemistry to electronics and energy usage, have only been made possible with the help of FESEM.

- ▲ **Nanowires For Gas Sensing:** Researchers are exploring new ways nanowires can be used as gas sensors by improving existing fabrication methods and developing new ones. Electron microscopy is vitally important in helping characterise nanowires and understanding their gas sensing behaviour.
- ▲ **Semiconductor inspection:** Reliable performance of semiconductors requires accurate topographical information. The high resolution three dimensional images produced by SEMs offers a speedy, accurate measurement of the composition of the semiconductor. In fact, in just about all wafer manufacturing processes, SEMs are one of three essential quality control tools used. In the case of repetitive daily quality control tests, larger monitors (19 inches) have been shown to reduce visual fatigue for inspectors[47].
- ▲ **Microchip assembly:** Microchip production is increasingly relying on SEMs to help gain insight into the effectiveness of new production and fabrication methods. With smaller and smaller scales and materials, as well as the potential of complex self assembling polymers, the high resolution, three-dimensional capacity of FESEM is invaluable to microchip design and production. As the Internet of Things (IoT) becomes more prevalent in the day to day lives of consumers and manufacturers, SEMs will continue to play an important role in the design of low cost, low power chipsets for non-traditional computers and networked devices.
- ▲ **Forensic investigations:** Criminal and other forensic investigations utilise FESEM to uncover evidence and gain further forensic insight.
- ▲ **design of new treatments). Soil and rock sampling:** Geological sampling using a scanning electron microscope can determine weathering processes and morphology of the samples. Backscattered electron imaging can be used to identify compositional differences, while composition of elements can be provided by microanalysis.
- ▲ **Medical science :** Broadly speaking, SEMs are used in medical science to compare blood and tissue samples in determining the cause of illness and measuring the effects of treatments on patients.

4.8 Atomic force microscopy (AFM)

The AFM consists of a cantilever with a sharp tip (probe) at its end that is used to scan the specimen surface[48]. The cantilever is typically silicon or silicon nitride with a tip radius of curvature on the order of nanometers. When the tip is brought into proximity of a sample surface, forces between the tip and the sample lead to a deflection of the cantilever according to Hooke's law. Depending on the situation, forces that are measured in AFM include mechanical contact force, van der Waals forces, capillary forces, chemical bonding, electrostatic forces, magnetic forces (see magnetic force microscope, MFM), Casimir forces, solvation forces, etc. Along with force, additional quantities may simultaneously be measured through the use of specialized types of probes[65].

- ▲ Atomic force microscope topographical scan of a glass surface. The micro and nano-scale features of the glass can be observed, portraying the roughness of the material. The image space is $(x,y,z) = (20\ \mu\text{m} \times 20\ \mu\text{m} \times 420\ \text{nm})$.
- ▲ The AFM can be operated in a number of modes, depending on the application. In general, possible imaging modes are divided into static (also called *contact*) modes and a variety of dynamic (non-contact or "tapping") modes where the cantilever is vibrated or oscillated at a given frequency[48].

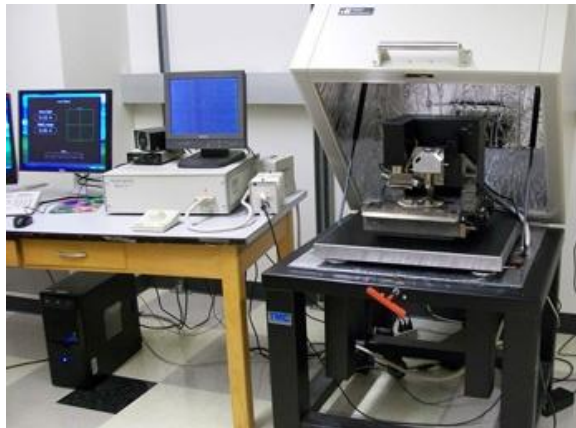


Fig:4.8.1 schematic representation of AFM spectrometer

Applications

- ▲ The AFM has been applied to problems in a wide range of disciplines of the natural sciences, including solid-state physics, semiconductor science and technology, molecular engineering, polymer chemistry and physics, surface chemistry, molecular biology, cell biology, and medicine.
- ▲ Applications in the field of solid state physics include (a) the identification of atoms at a surface, (b) the evaluation of interactions between a specific atom and its neighboring atoms, and (c) the study of changes in physical properties arising from changes in an atomic arrangement through atomic manipulation[49].
- ▲ In molecular biology, AFM can be used to study the structure and mechanical properties of protein complexes and assemblies. For example, AFM has been used to image microtubules and measure their stiffness.
- ▲ In cellular biology, AFM can be used to attempt to distinguish cancer cells and normal cells based on a hardness of cells, and to evaluate interactions between a specific cell and its neighbouring cells in a competitive culture system. AFM can also be used to indent cells, to study how they regulate the stiffness or shape of the cell membrane or wall[64]. In some variations, electric potentials can also be scanned using conducting cantilevers. In more advanced versions, currents can be passed through the tip to probe the electrical conductivity or transport of the underlying surface, but this is a challenging task with few research groups reporting consistent data.

4.9 Energy dispersive X – ray spectroscopy (EDAX)

EDAX is an analytical technique used for the elemental analysis or chemical characterization of a sample. It relies on an interaction of some source of X – ray excitation and a sample. Energy-dispersive X-ray spectroscopy (EDS, EDX, EDXS or XEDS), sometimes called energy dispersive X-ray analysis (EDXA or EDAX) or energy dispersive X-ray microanalysis (EDXMA), is an analytical technique used for the elemental analysis or chemical characterization of a sample. It relies on an interaction of some source of X-ray excitation and a sample [50]. Its characterization capabilities are due in large part to the fundamental principle that each element has a unique atomic structure allowing a unique set of peaks on its electromagnetic emission spectrum (which is

the main principle of spectroscopy). The peak positions are predicted by the Moseley's law with accuracy much better than experimental resolution of a typical EDX instrument.

Four primary components of the EDS setup are

1. The excitation source (electron beam or x-ray beam)
2. The X-ray detector
3. The pulse processor
4. The analyzer

Electron beam excitation is used in electron microscopes, scanning electron microscopes (SEM) and scanning transmission electron microscopes (STEM). X-ray beam excitation is used in X-ray fluorescence (XRF) spectrometers. A detector is used to convert X-ray energy into voltage signals; this information is sent to a pulse processor, which measures the signals and passes them onto an analyzer for data display and analysis[63]. The most common detector used to be Si(Li) detector cooled to cryogenic temperatures with liquid nitrogen. Now, newer systems are often equipped with silicon drift detectors (SDD) with Peltier cooling systems.



4.10 Characterization techniques

Computer controlled JASCO V-650 was used to study UV-Vis spectral behaviour. The FT-IR spectra were recorded using a Nicolet iS5 instrument. The surface morphology of the nanoparticles was done using MIRA3 TESCAN equipment. EDAX measurements were carried out by Quantax 200 with X-Flash Bruker. XRD measurements were made by ECO D8 ADVANCE diffractometer, measurement range: 10 to 90 degree in 2 θ and particle size

was calculated using Scherrer's equation. The AFM was recorded using Nanosuf Easy Scan 2 Controller instrument.

5.1 UV – Vis analysis

The UV visible spectrum of SO-Rb, SO-W, SO-M nanoparticles (figure 5.1a.b.c) shows an absorption band in region of 200 -1000 nm, which originates primarily from the absorption and scattering of UV radiation by magnetic nanoparticles. The absorption band around at 0.3019,0.3437,0.3987 for SO-Rb,SO-W,SO-M respectively. This blue shift is attributed to the smaller size of nanoparticles. This indicates the formation of smaller particle[51]s.

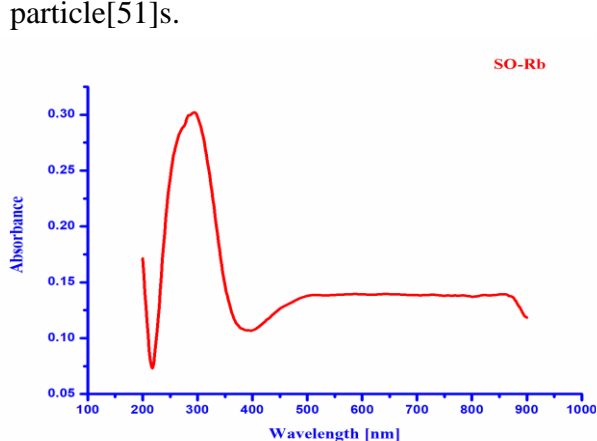


Fig:5.1.1a UV-Vis spectrum of SO-Rb

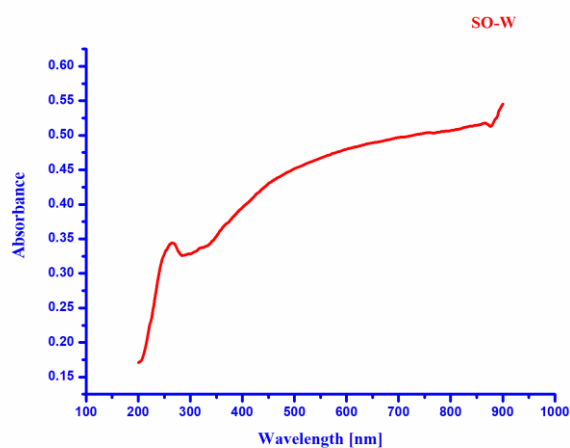


Fig: 5.1.1b UV-Vis spectrum of SO-W

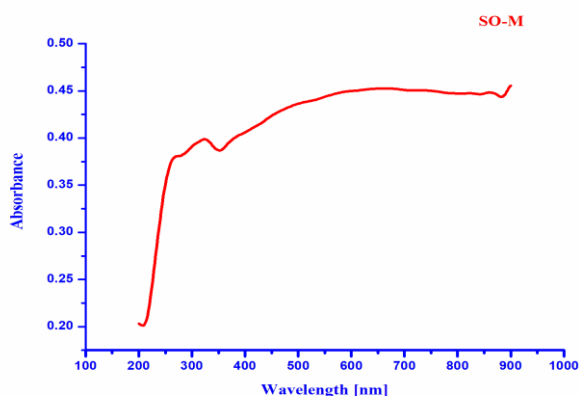


Fig: 5.1.1c UV-Vis spectrum of SO-M

Band gap energy

The band gap energy in a nanomaterial could be obtained from the absorption maxima. According to quantum confinement theory, electrons in the conduction band and holes in the valence band are spatially confined by the potential barrier of the surface. From the absorption peak the energy band gap of SiO₂ nanoparticles has been calculated using the formula.

$$E_{gn} = h\nu_{gn} = hc/\lambda_{gn}$$

Where h = plank's constant

E_{gn} = energy band gap of the semiconducting nanoparticles in the optical spectra.

The band gap energy for SO-Rb nanoparticle is **4.18866 eV**

The band gap energy for SO-W nanoparticle is **4.71423 eV**

The band gap energy for SO-M nanoparticle is **4.67865 & 3.83853 eV**

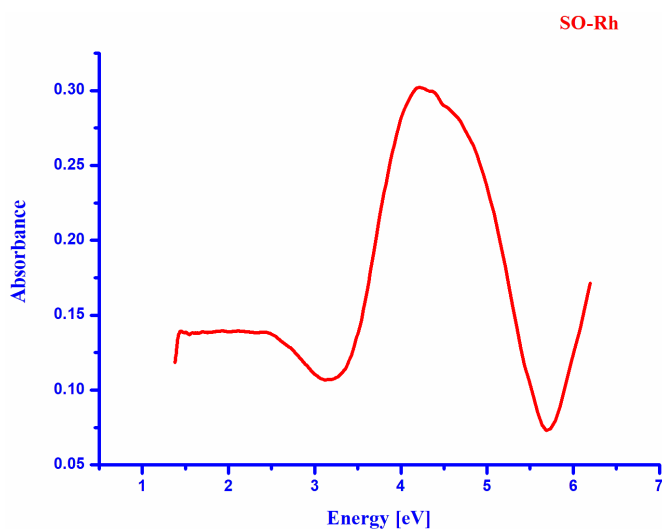


Fig: 5.1.1d energy spectrum of SO-Rb

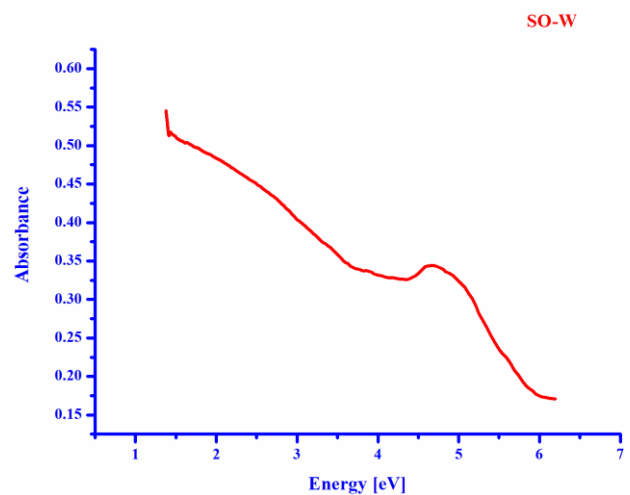


Fig: 5.1.1e energy spectrum of SO-W

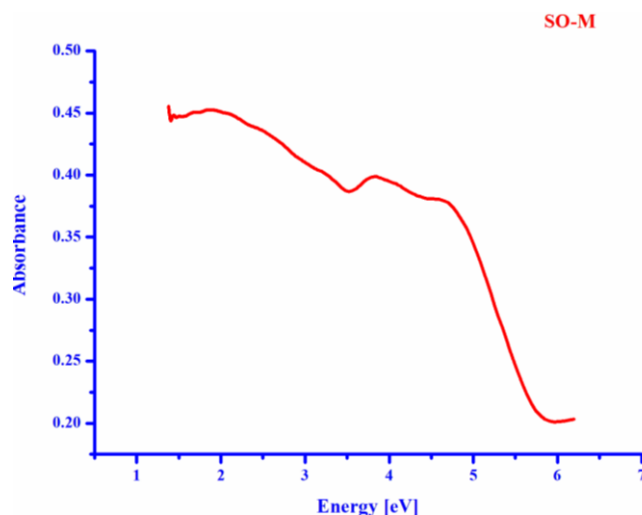


Fig: 5.1.1f energy spectrum of SO-W

5.2 FT-IR analysis:

FT – IR spectra of SO-Rb shows absorption band from 400 – 3000 cm^{-1} . The transmittance at 408.91 cm^{-1} and 1080.14 cm^{-1} determines Si-O-Si stretching. The peak at 601.79 indicates Si-OH stretching. The absorption peak at 1080.14 cm^{-1} is due to Si-H stretching whereas peak at 2360.87 cm^{-1} and 2885.51 cm^{-1} is due to the stretching vibration mode of C-H. The IR spectra at 3726.47 cm^{-1} is due to C-OH stretching[52].

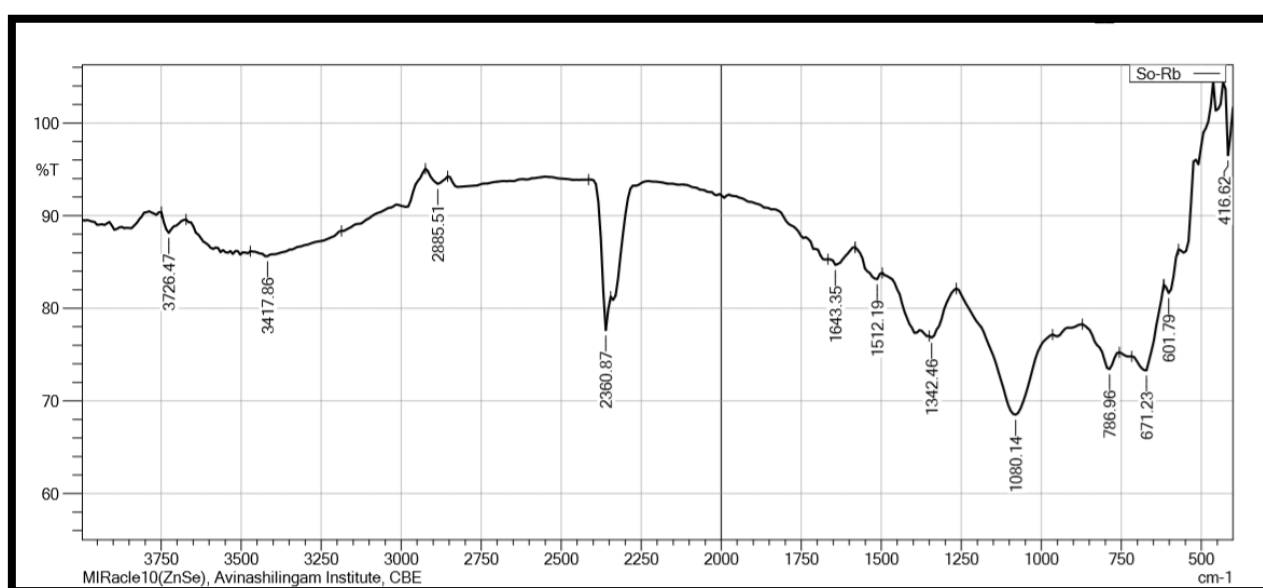


Fig : 5.2.a FT-IR spectra of SO-Rb

Table 5.2.1 shows the FT-IR data of SO-Rb

VIBRATION	WAVENUMBER cm^{-1}
Si – O – Si stretching	408.91 ,1080.14
Si-OH stretching	601.79
Si-H stretching	1080.14
C-H stretching	2360.87 , 2885.51
C-OH stretching	3726.47

5.2a FT-IR Analysis of SO-W

FT – IR spectra of SO-W shows absorption band from $400 - 3000 \text{ cm}^{-1}$. The transmittance at 416.62 cm^{-1} and 1064.71 cm^{-1} determines Si-O-Si stretching. The peak at 671.23 cm^{-1} indicates Si-OH stretching. The absorption peak at 1064.71 cm^{-1} is due to Si-H stretching where as peak at 2360.87 cm^{-1} and 2885.51 cm^{-1} is due to the stretching vibration mode of C-H. The IR spectra at 3726.47 cm^{-1} is due to C-OH stretching[53].

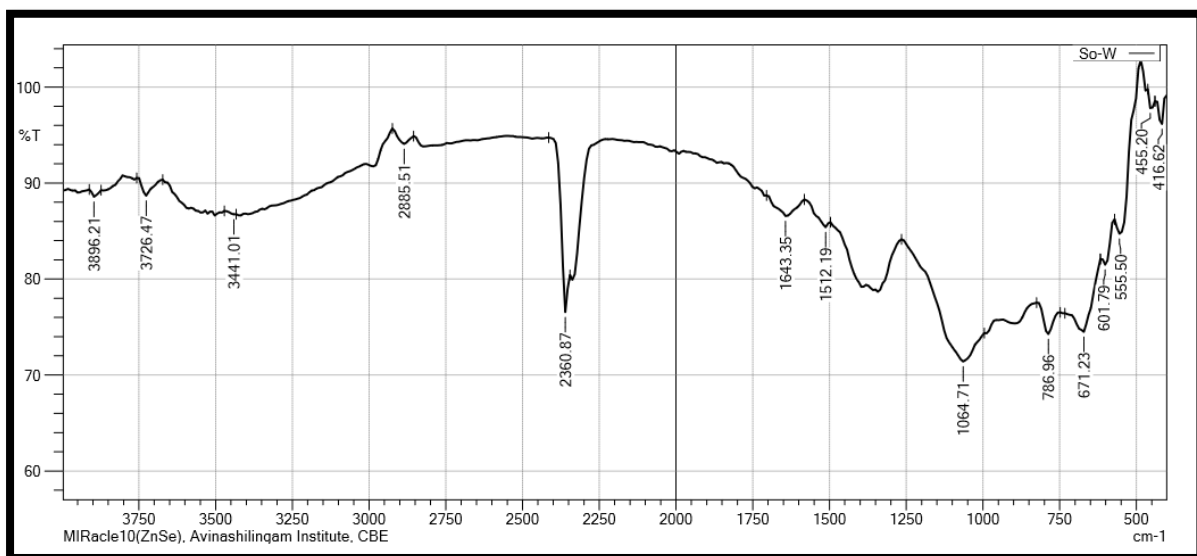


Fig: 5.2.b FT-IR spectra of SO-W

Table 5.2.2 shows the FT-IR data of SO-W

VIBRATION	WAVENUMBER cm^{-1}
Si – O – Si stretching	416.62 , 1064.71
Si-OH stretching	671.23
Si-H stretching	1064.71
C-H streching	2360.87 , 2885.51
C-OH stretching	3726.47

5.2b FT-IR Analysis of SO-M

FT – IR spectra of SO-M shows absorption band from 400 – 3000 cm^{-1} . The transmittance at 408.91 cm^{-1} and 1064.71 cm^{-1} determines Si-O-Si stretching. The peak at 671.23 cm^{-1} indicates Si-OH stretching. The absorption peak at 1064.71 cm^{-1} is due to Si-H stretching where as peak at 786.96 cm^{-1} and 2885.51 cm^{-1} is due to the stretching vibration mode of C-H. The IR spectra at 3726.47 cm^{-1} is due to C-OH stretching.[53].

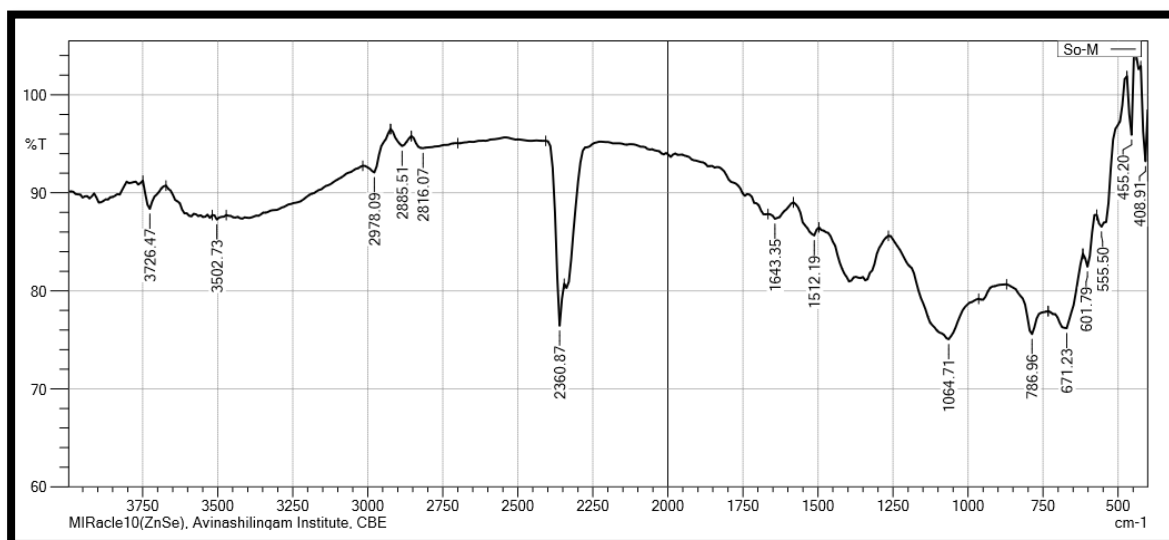


Fig:5.2.c FT-IR spectra of SO-M

Table 5.2.2 shows the FT-IR data of SO-M

VIBRATION	WAVENUMBER cm⁻¹
Si – O – Si stretching	1064.71
Si-OH stretching	671.23
Si-H stretching	786.96
C-H stretching	2360.87 , 2885.51
C-OH stretching	3726.47

5.3 XRD Analysis

5.3.1 XRD Analysis of SO-Rb

The structural properties of SO-Rb nanoparticles were studied using XRD analysis. the average crystalline size of SO- Rb nanoparticle is 3nm which was calculated by Debye – Scherer formula,

$$D = \frac{K\lambda}{\beta \cos \theta}$$

Where D is the average crystalline diameter in nanometer.

K is the dimensionless shape factor,

λ is the X- ray wavelength,

β is the line broadening at half the maximum intensity (FWHM)

$$\beta = \frac{\pi}{180} \times 2\theta$$

θ is the Bragg angle.

5.3.1a Calculation of average crystalline size

2θ	θ	Cosθ	B	D
0.3011	0.1505	1	0.3801	4.0213
0.4015	0.2007	1	0.6274	2.3080

Average = 3.1601nm

5.3.1b Identification of the lowest common quotient be k

2θ	θ	$\sin^2 \theta$	$\frac{\sin^2 \theta}{2}$	$\frac{\sin^2 \theta}{3}$	$\frac{\sin^2 \theta}{4}$	$\frac{\sin^2 \theta}{5}$	$\frac{\sin^2 \theta}{6}$	$\frac{\sin^2 \theta}{7}$	$\frac{\sin^2 \theta}{8}$
21.8456	10.9228	0.0359	0.0179	0.0119	0.0089	0.0071	0.0059	0.0051	0.0044
36.0609	18.0304	0.0958	0.0479	0.0319	0.0239	0.0191	0.0159	0.0136	0.0119

k = 0.0119

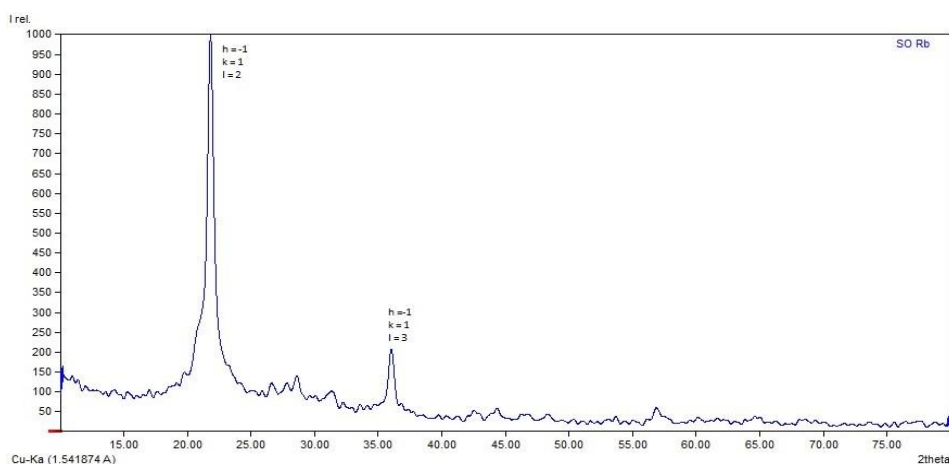


Fig: 5.3.2 XRD Spectrum of SO-Rb with h,k,l value [68]

5.3.1c Calculation of the lattice value

$$a = \frac{K\lambda}{2\sqrt{k}}$$

$$a = \frac{0.94 \times 1.5406}{2\sqrt{0.0119}}$$

$$a = 6.6400\text{Å}$$

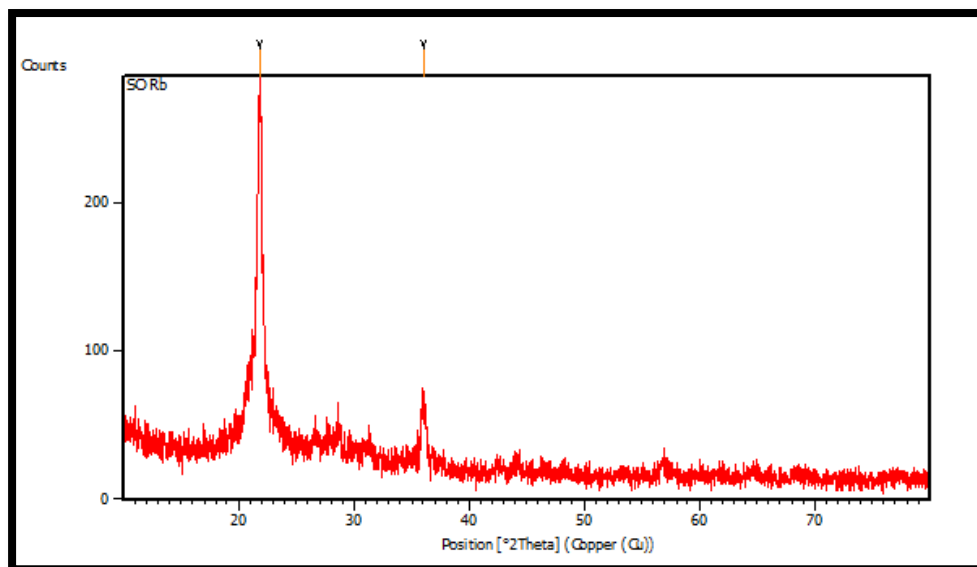


Fig: 5.3.1.1 XRD Spectrum of SO-Rb

5.3.2 XRD Analysis of SO-W

The structural properties of SO-W nanoparticles was studied using XRD analysis. The average crystalline size of SO-W nanoparticle is 2nm.

5.3.2a Calculation of average crystalline size (D)

2θ	θ	Cosθ	B	D
0. 2342	0.1171	1	0.3794	3.8168
0.4015	0.2007	1	0.5447	2.6585
0.5353	0.2676	1	0.6263	2.3121
0.8029	0.4014	1	0.9892	1.4639
Average				2.5628nm

5.3.2b Identification of the lowest common quotient be k

2θ	θ	$\sin^2 \theta$	$\frac{\sin^2 \theta}{2}$	$\frac{\sin^2 \theta}{3}$	$\frac{\sin^2 \theta}{4}$	$\frac{\sin^2 \theta}{5}$	$\frac{\sin^2 \theta}{6}$	$\frac{\sin^2 \theta}{7}$	$\frac{\sin^2 \theta}{8}$
21.8048	10.9024	0.0357	0.0178	0.0119	0.0089	0.0071	0.0059	0.0051	0.0044
31.3085	15.6542	0.0728	0.0364	0.0242	0.0182	0.0145	0.0121	0.0104	0.0091
35.9954	17.9977	0.0954	0.0477	0.0318	0.0238	0.0191	0.0159	0.0136	0.0119
56.8557	28.4278	0.2266	0.1133	0.0755	0.0566	0.0453	0.0377	0.0323	0.0283

k = 0.0119

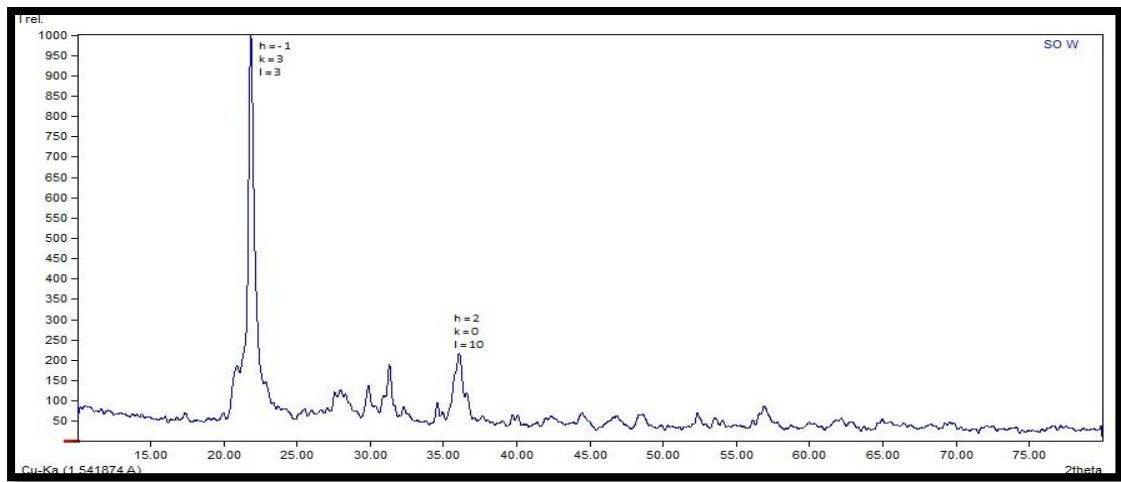


Fig: 5.3.2 XRD Spectrum of SO-W with h,k,l value[69]

5.3.2c Calculation of lattice value

$$a = \frac{K\lambda}{2\sqrt{k}}$$

$$a = \frac{0.94 \times 1.5406}{2\sqrt{0.0119}}$$

$$\mathbf{a = 6.6400 \text{ \AA}}$$

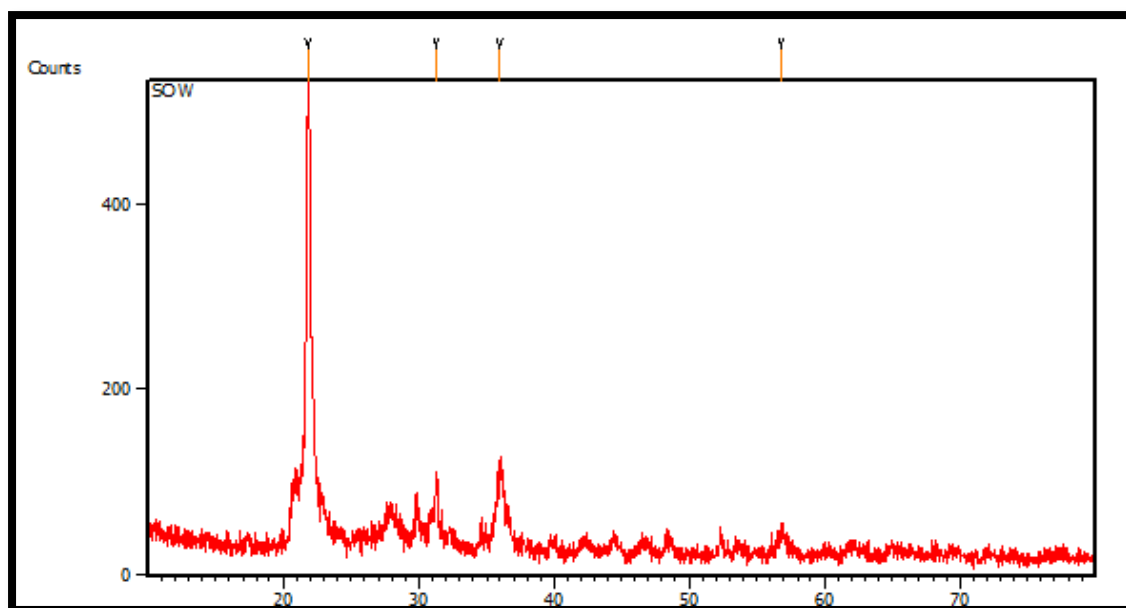


Fig : 5.3.2.1 FT-IR spectra of SO-W

5.3.3 SO-M

The structural properties of SO-M nanoparticles was studied using XRD analysis. The average crystalline size of SO-W nanoparticle is 2nm.

5.3.3a Calculation of average crystalline size (D)

2θ	θ	cosθ	B	D
0.2676	0.1338	1	0.3602	4.0202
0.2676	0.1338	1	0.3799	3.8117
0.4015	0.2007	1	0.5459	2.6526
0.3346	0.1673	1	0.6281	2.3055
0.5353	0.2676	1	0.7748	1.8689
0.8029	0.4014	1	0.8131	1.7809
0.8029	0.4014	1	0.9933	1.4579
Average				2.5568nm

5.3.3b Identification of the lowest common quotient be k

2θ	θ	$\sin^2 \theta$	$\frac{\sin^2 \theta}{2}$	$\frac{\sin^2 \theta}{3}$	$\frac{\sin^2 \theta}{4}$	$\frac{\sin^2 \theta}{5}$	$\frac{\sin^2 \theta}{6}$	$\frac{\sin^2 \theta}{7}$	$\frac{\sin^2 \theta}{8}$
20.7057	10.3529	0.0323	0.0161	0.0107	0.0080	0.0064	0.0053	0.0046	0.0040
21.8351	10.9175	0.0358	0.0179	0.0119	0.0089	0.0071	0.0059	0.0051	0.0044
31.3743	15.6871	0.0731	0.0365	0.0243	0.0182	0.0146	0.0121	0.0104	0.0091
36.1020	18.0510	0.0960	0.0480	0.0320	0.0240	0.0192	0.0160	0.0137	0.0120
44.5310	22.2655	0.1435	0.0717	0.0478	0.0358	0.0287	0.0239	0.0205	0.0179
46.7320	23.3660	0.1572	0.0786	0.0524	0.0393	0.0314	0.0262	0.0224	0.0196
57.0883	28.5441	0.2283	0.1141	0.0761	0.0570	0.0456	0.0380	0.0326	0.0285

K = 0.0179

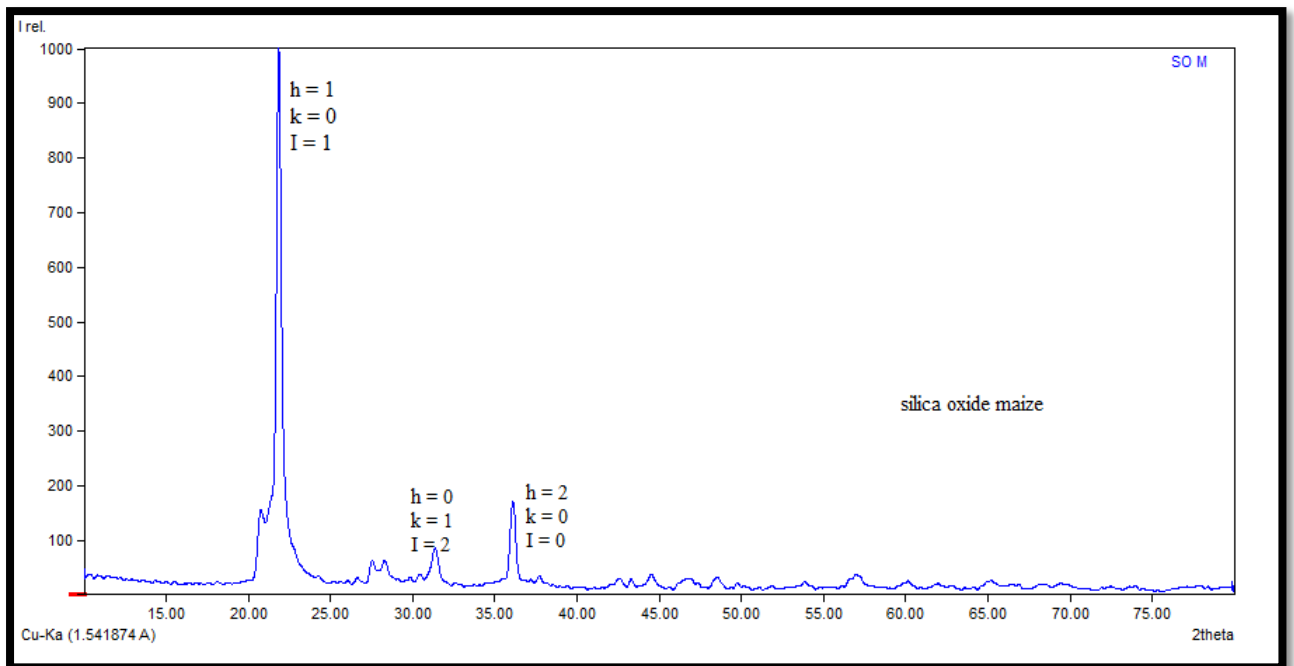


Fig: 5.3.3.1 XRD Spectrum of SO-M with h,k,l value[70]

5.3.3c Calculation of the lattice value

$$a = \frac{K\lambda}{2\sqrt{k}}$$

$$a = 0.94 \times 1.5406 / 2\sqrt{0.0179}$$

$$a = 5.4138 \text{ \AA}$$

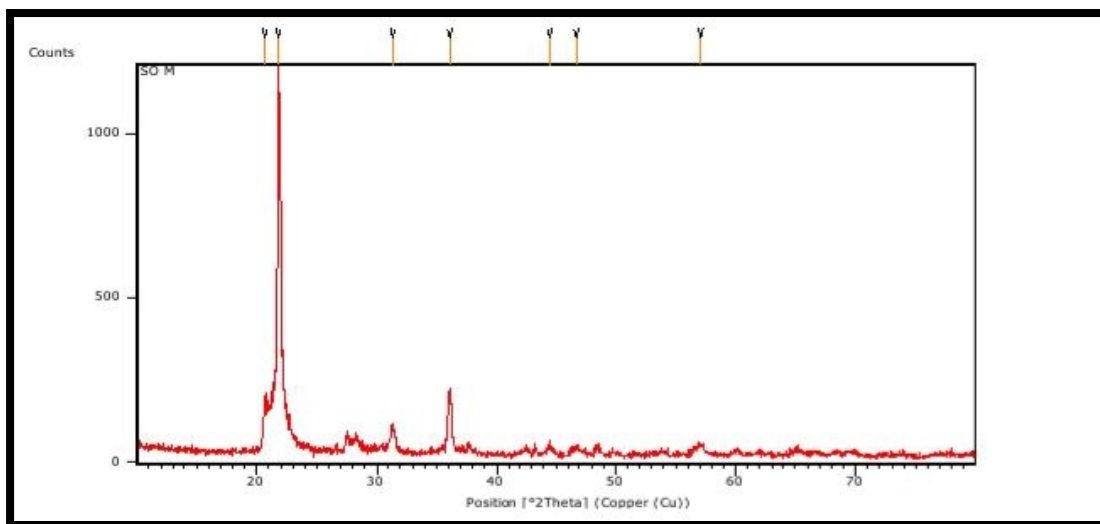


Fig: 5.3.3.2 XRD spectrum of SO-M

5.4 SEM Analysis

5.4.1 SEM Analysis of SO-Rb

SEM characterization reveals the surface morphology of SO-Rb nanoparticles prepared by agricultural waste. SO-Rb nanoparticles are magnified in the ranges from $20\mu\text{m}$ – 500nm nm which was shown in **figure 5.4.1.a – f** respectively. SEM images shows that the particles are heavily aggregated due to surface activity. From SEM results, it is concluded that the surface morphology of SiO_2 nanoparticles are **nano flakes** in lower magnification in higher frequency range[54].

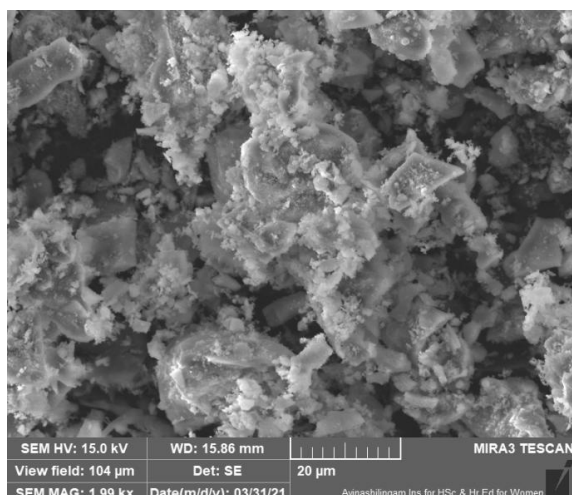


Fig: a

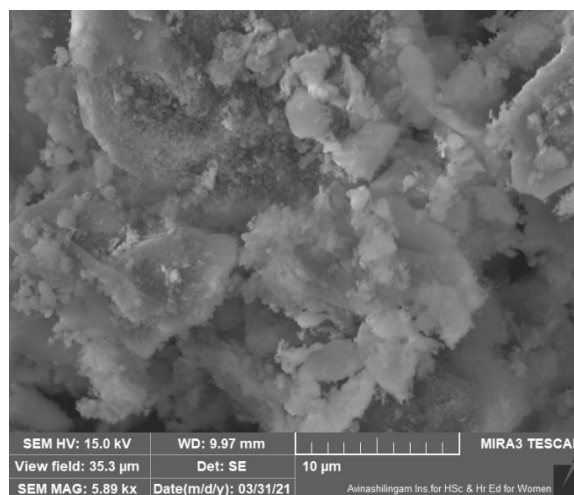


Fig: b

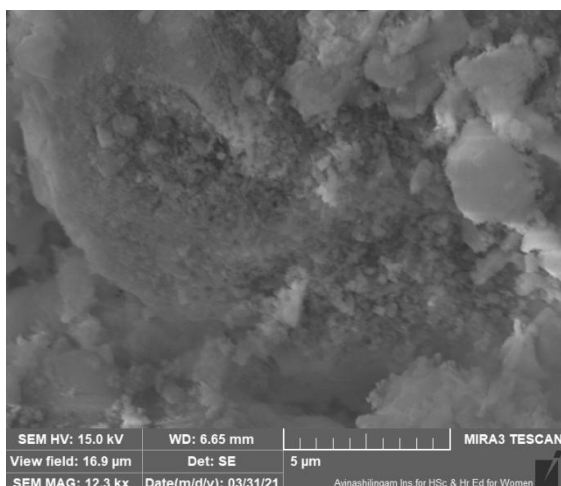


Fig: c

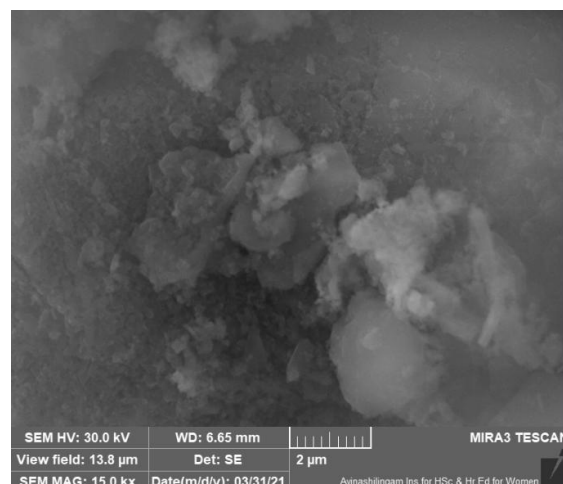


fig: d

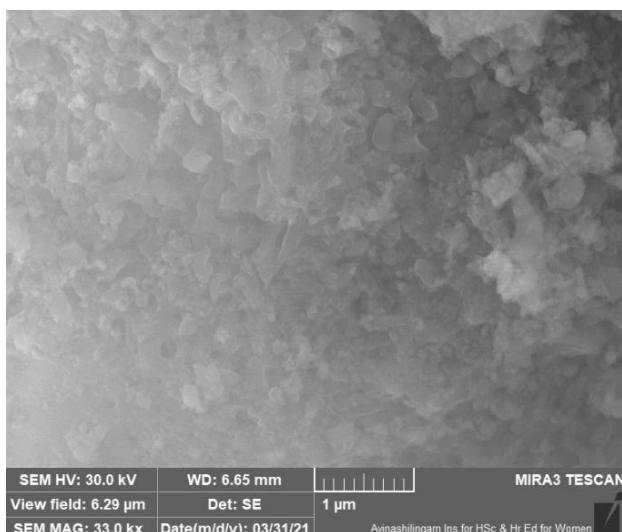


Fig: e

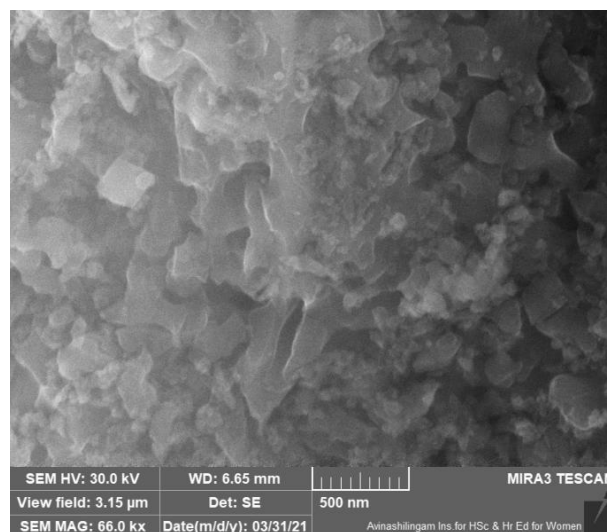


Fig: f

Fig : 5.4.1.a – f SEM images of SO-Rb

5.4.2 SEM Analysis of SO-W

SEM characterization reveals the surface morphology of SO-W nanoparticles prepared by agricultural waste. SO-W nanoparticles are magnified in the ranges from $100\mu\text{m}$ – 500nm which was shown in **figure 5.4.2a-5.4.2f** respectively. SEM images shows that the particles are heavily aggregated due to surface activity. From SEM results, it is concluded that the surface morphology of SiO_2 nanoparticles are **nano rods** in lower magnification in higher frequency range[55].

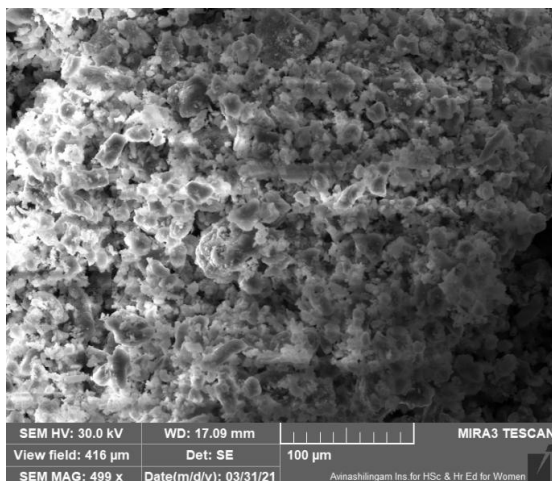


Fig:a

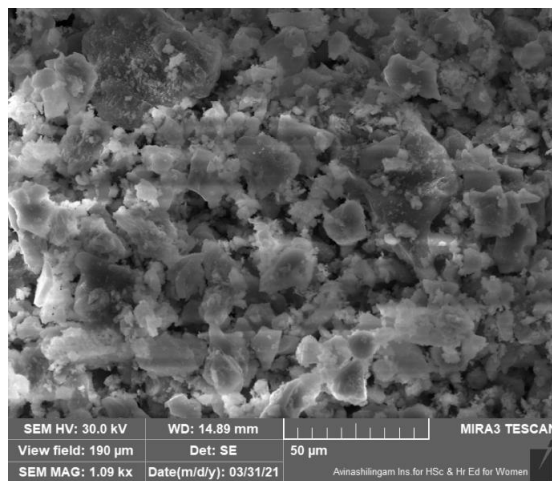


Fig:b

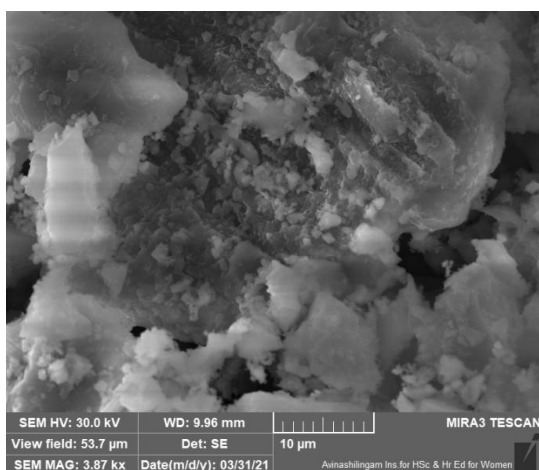


Fig:c

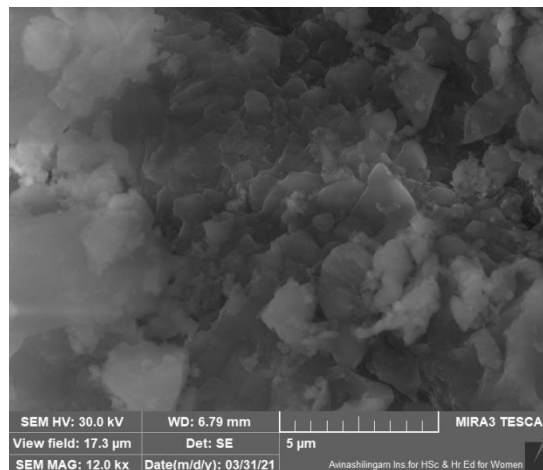


Fig: d

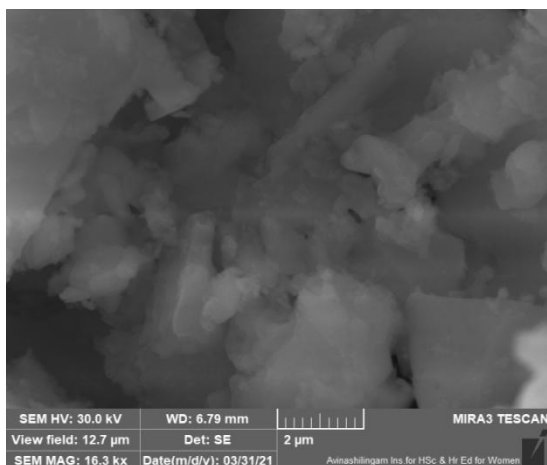


Fig: e

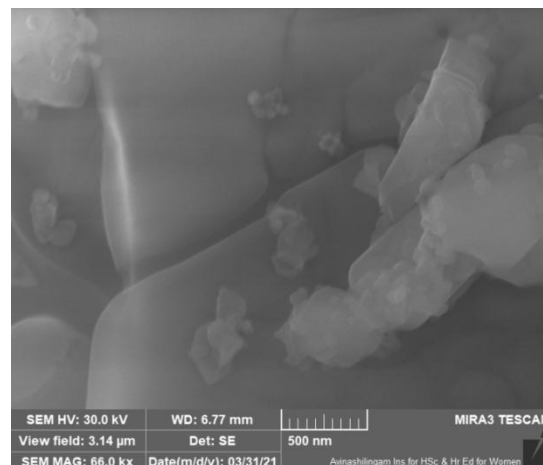


Fig: f

Fig: 5.4.2. a to f SEM images of SO-W

5.4.3. SEM Analysis of SO-M

SEM characterization reveals the surface morphology of SO-M nanoparticles prepared by agricultural waste. SO-M nanoparticles are magnified in the ranges from $100\mu\text{m}$ – 500nm which was shown in **figure 5.4.3a-5.4.3f** respectively. SEM images shows that the particles are heavily aggregated due to surface activity. From SEM results, it is concluded that the surface morphology of SiO_2 nanoparticles are **nano rods** in lower magnification in higher frequency range[56].

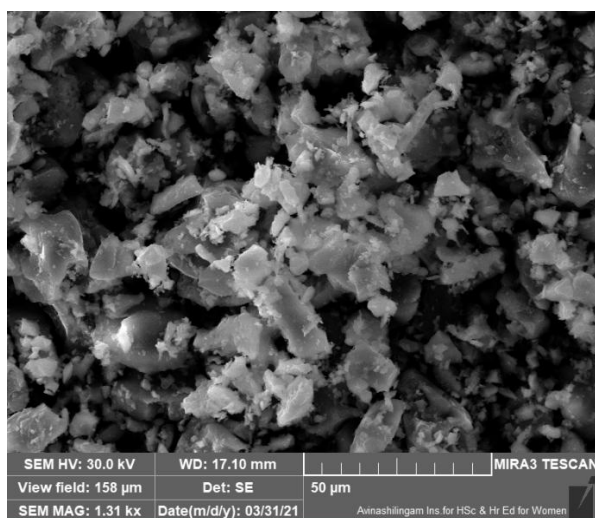


Fig: a

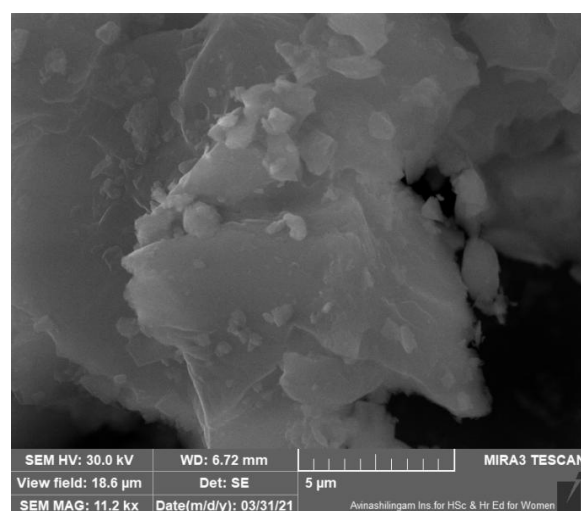


Fig: b

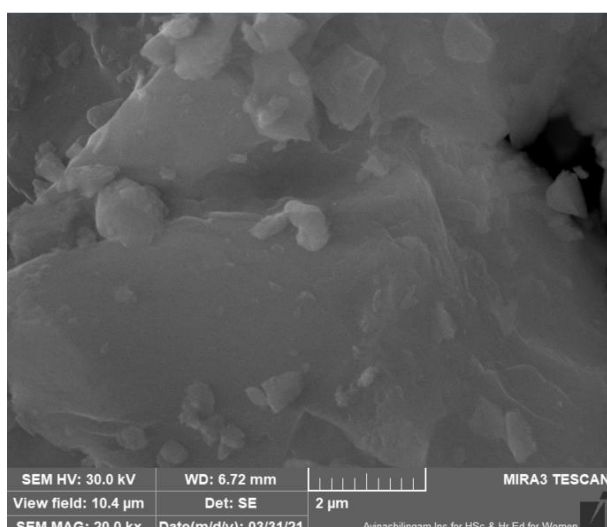


Fig: c

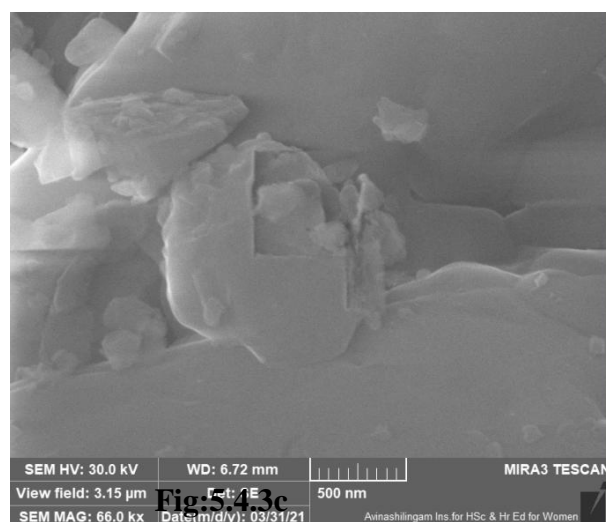


Fig:d

Fig: 5.4.3.a – d SEM images of SO-M

5.5 EDAX analysis

5.5.1 EDAX Analysis of SO-Rb

Energy dispersive x-ray analysis was used to confirm the elemental composition of SO-Rb nanoparticles. The **figure 5.5.1a – 5.5.1c** shown below indicates the presence of **silicon, oxygen** respectively in synthesized SiO_2 nanoparticles[57].

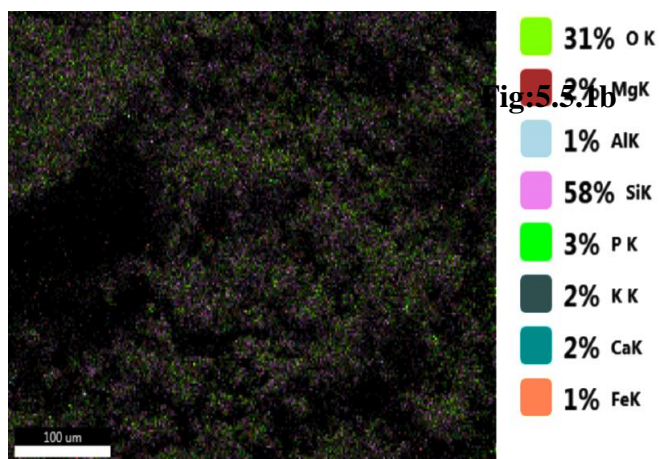


Fig:a Various elements in SO-Rb nanoparticles of EDAX

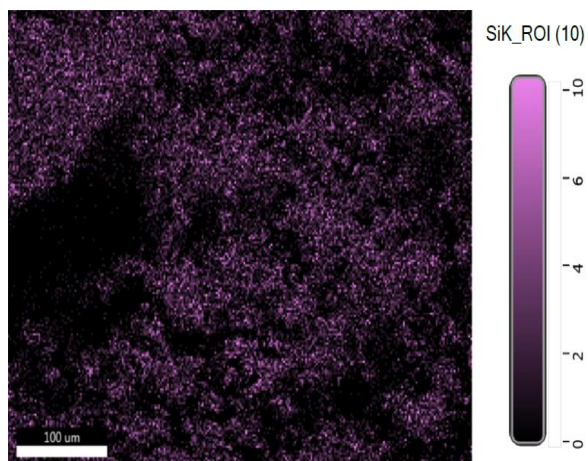


Fig:b

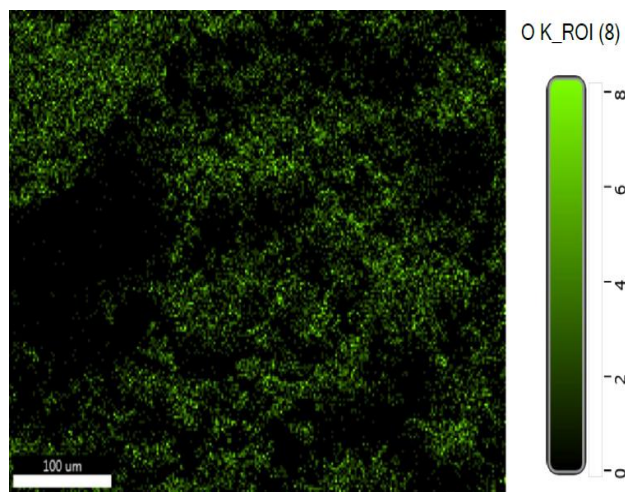


Fig:c

Fig : b&c Distribution of silicon & oxygen in SO-Rb nanoparticles using EDAX

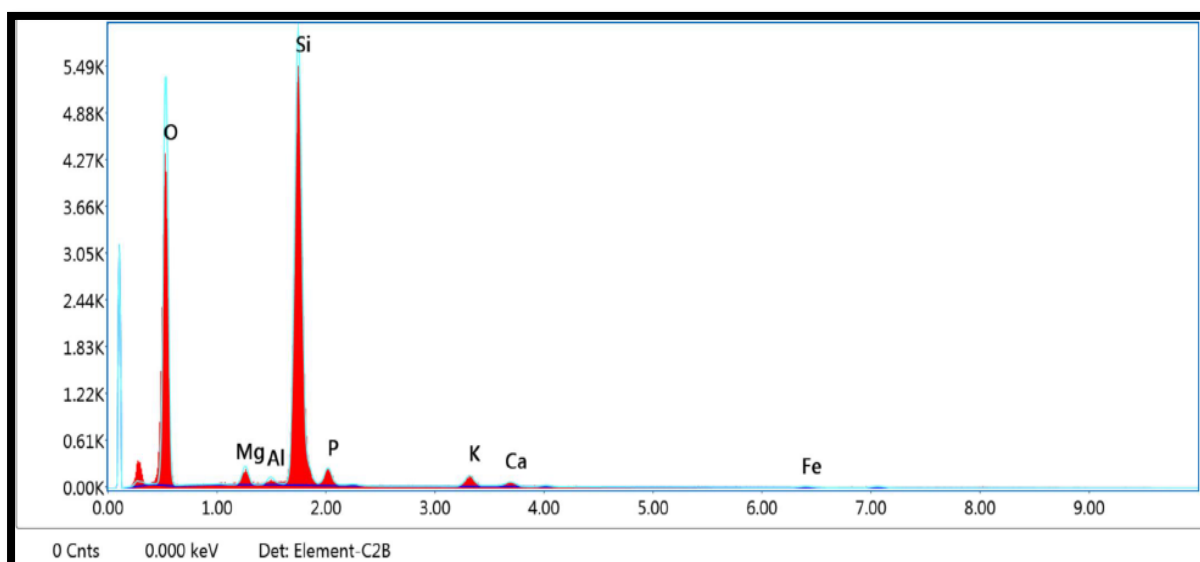


Fig:5.5.1d EDAX spectrum of SO-Rb

5.5.2 EDAX Analysis of SO-W

Energy dispersive x-ray analysis was used to confirm the elemental composition of SO-W nanoparticles. The **figure 5.5.2a – 5.5.2c** shown below indicates the presence of **silicon, oxygen** respectively in synthesized SiO_2 nanoparticles[58].

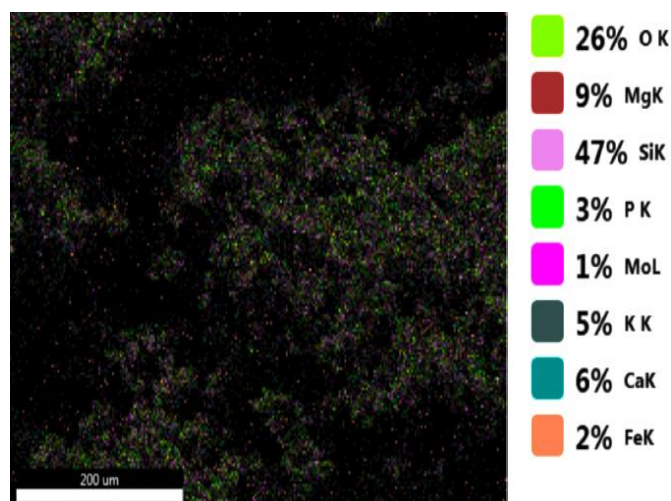


Fig:a Various elements in SO-W nanoparticles of EDAX

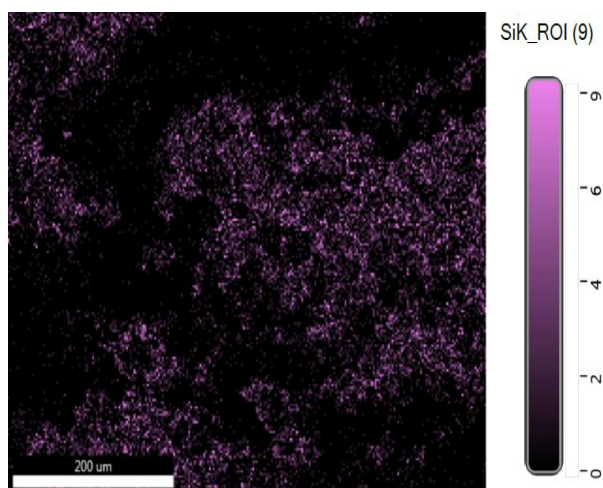


Fig:b

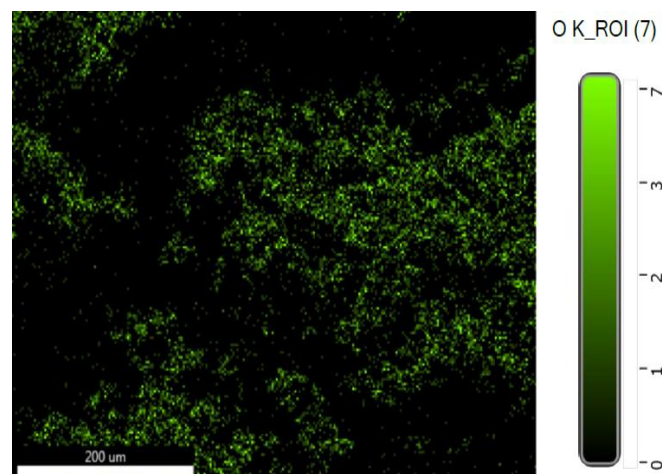


Fig:c

Fig : b&c Distribution of silicon & oxygen in SO-W nanoparticles using EDAX

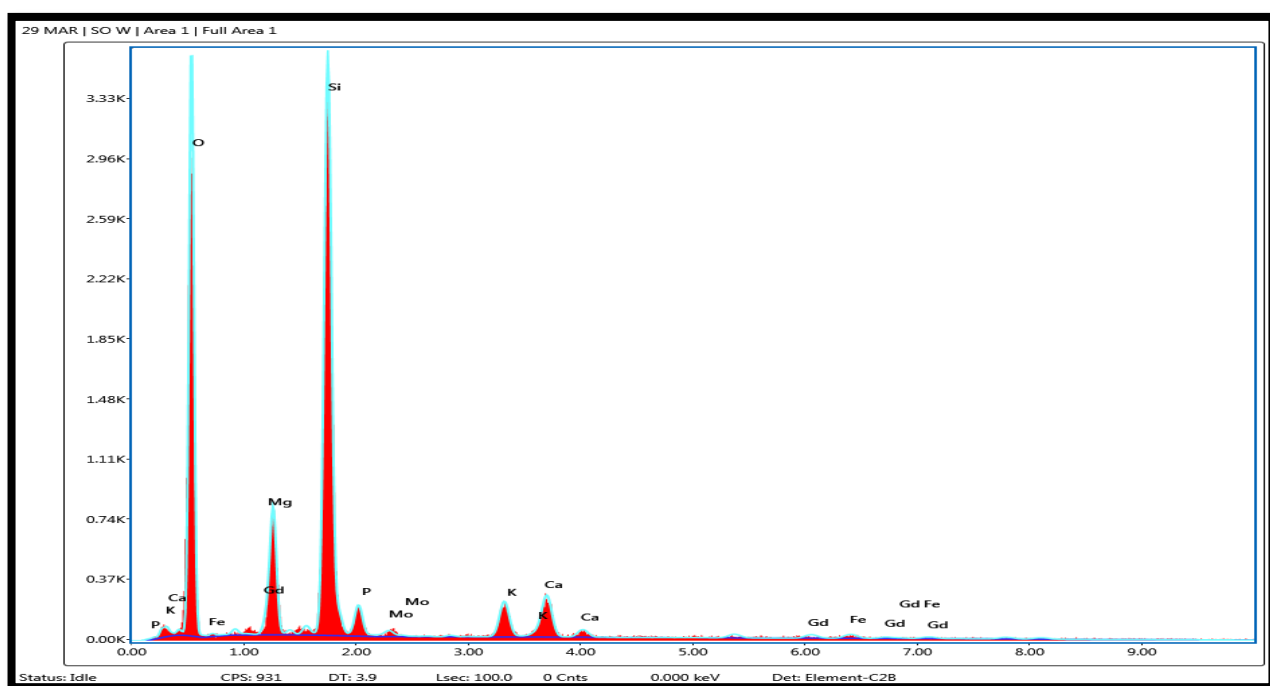


Fig:5.5.2d EDAX spectrum of SO-W

5.5.3 EDAX Analysis of SO-M

Energy dispersive x-ray analysis was used to confirm the elemental composition of SO-M nanoparticles. The **figure 5.5.3a – 5.5.3c** shown below indicates the presence of **silicon, oxygen** respectively in synthesized SiO_2 nanoparticles[59].

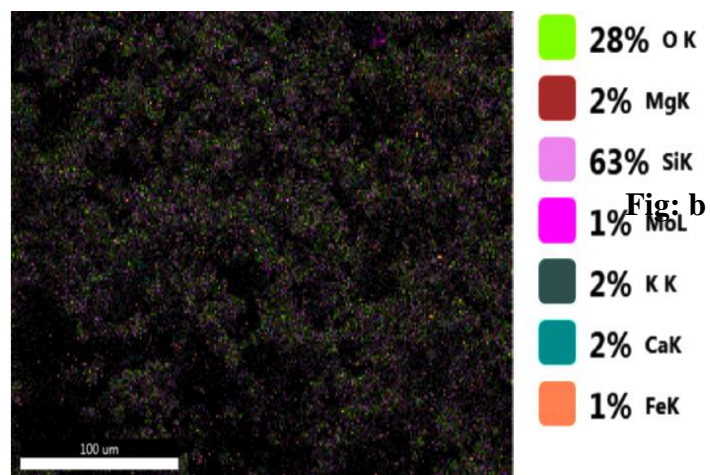


Fig:a Various elements in SO-M nanoparticles of EDAX

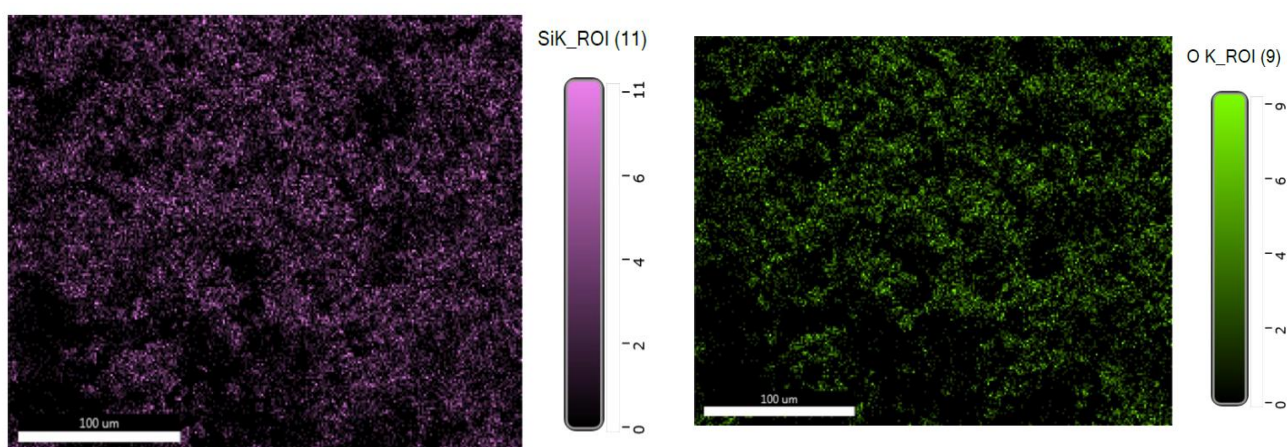


Fig: b

Fig: c

Fig : b&c Distribution of silica & oxygen in SO-M nanoparticles using EDAX

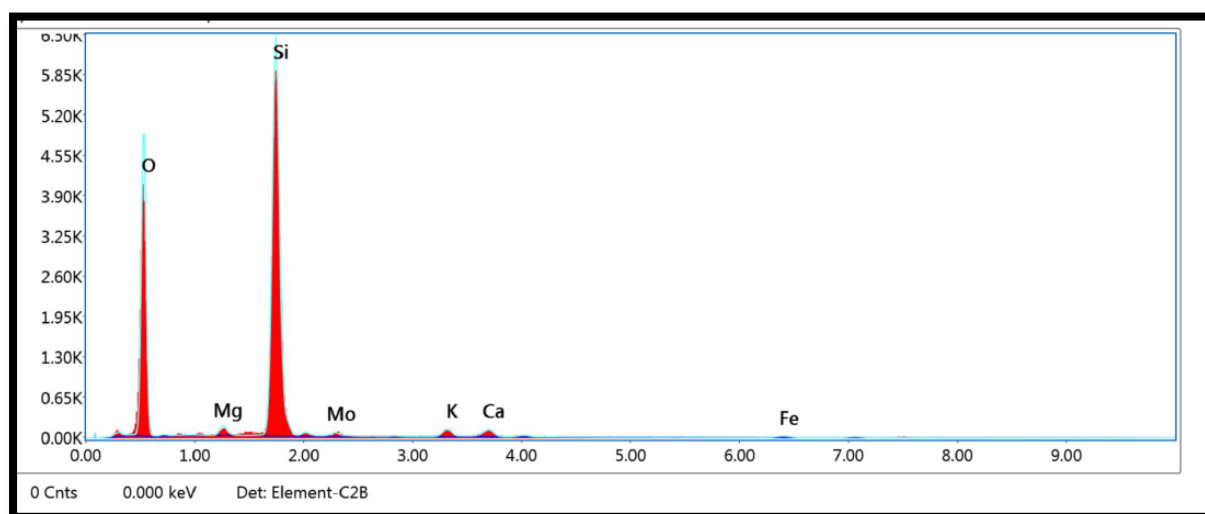


Fig: 5.5.3d EDAX spectrum of SO-M

5.6 AFM analysis

5.6.1 AFM Analysis of SO-Rb

Fig: 5.6.1a shows the AFM spectral image of SO-Rb nanoparticle synthesized using agricultural waste with the scanning area of **9.842 μm^2** between **3.13 μm .6.25 μm** , **1.56 μm** smooth peaks and pits were found to be distributed over an irregular surface. The size of the range of **46.1nm to 343nm**. From the surface roughness analysis it is observed that the surface roughness of SO-Rb is estimated to be about **4.6007mv,3.2272mv,11.25mv** for the root mean square roughness (S_q) and **3.4509 μv ,2171.8 μv , 7.1734 μv for the average surface (S_a)[60].**

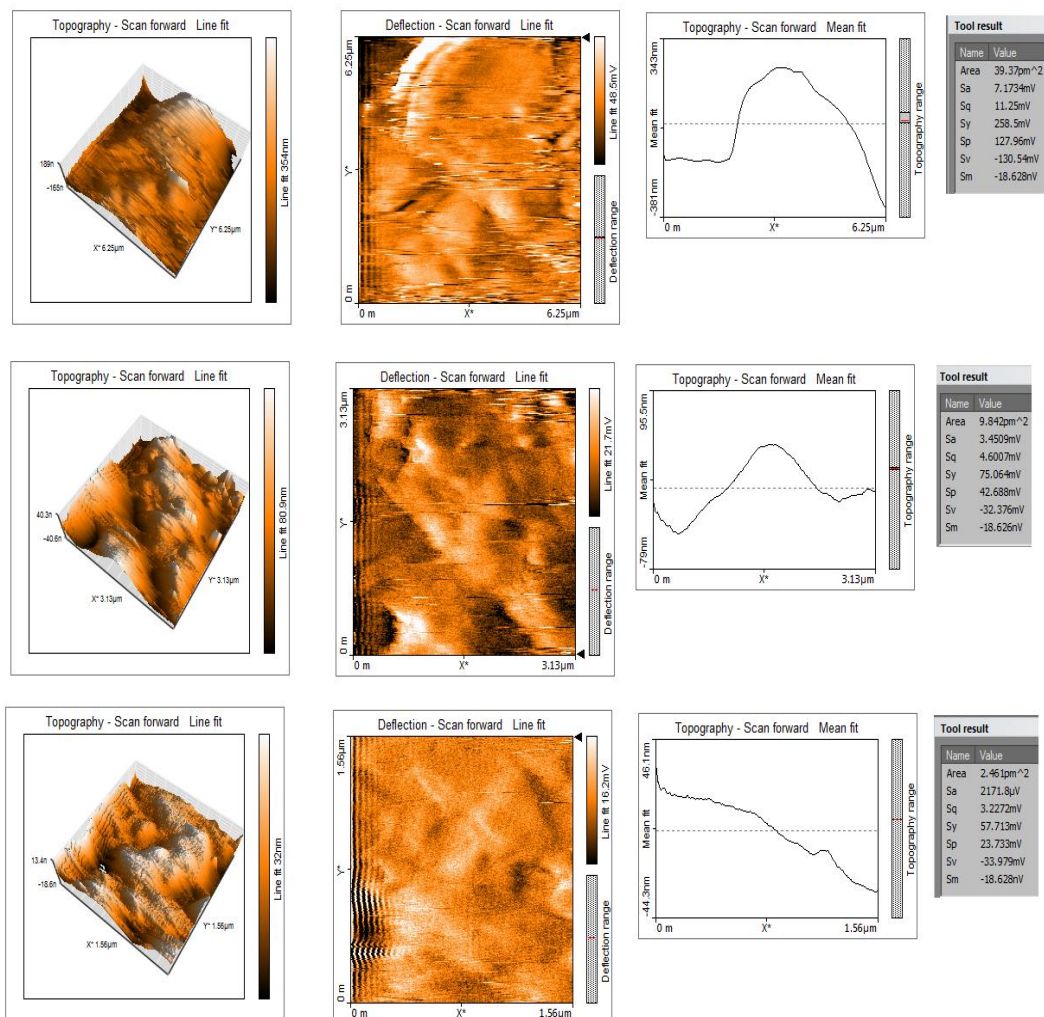


Fig: 5.5.2a Various Magnification of AFM of SO-Rb

5.6.2 AFM Analysis of SO-W

Fig: 5.6.2a shows the AFM spectral image of SO-W nanoparticle synthesized using agricultural waste with the scanning area of $2.461\mu\text{m}^2$ between $1.56\mu\text{m}$ to $3.13\mu\text{m}$. Smooth peaks and pits were found to be distributed over an irregular surface. The size of the range of 25.6 nm to 51nm . From the surface roughness analysis it is observed that the surface roughness of SO-W is estimated to be about $5.9483\mu\text{v}$, $2.388\mu\text{v}$, $2302.6\mu\text{v}$ for the root mean square roughness (S_q) and 4.2342mv , 5.9432mv , 1679.5mv for the average surface (S_a) [61].

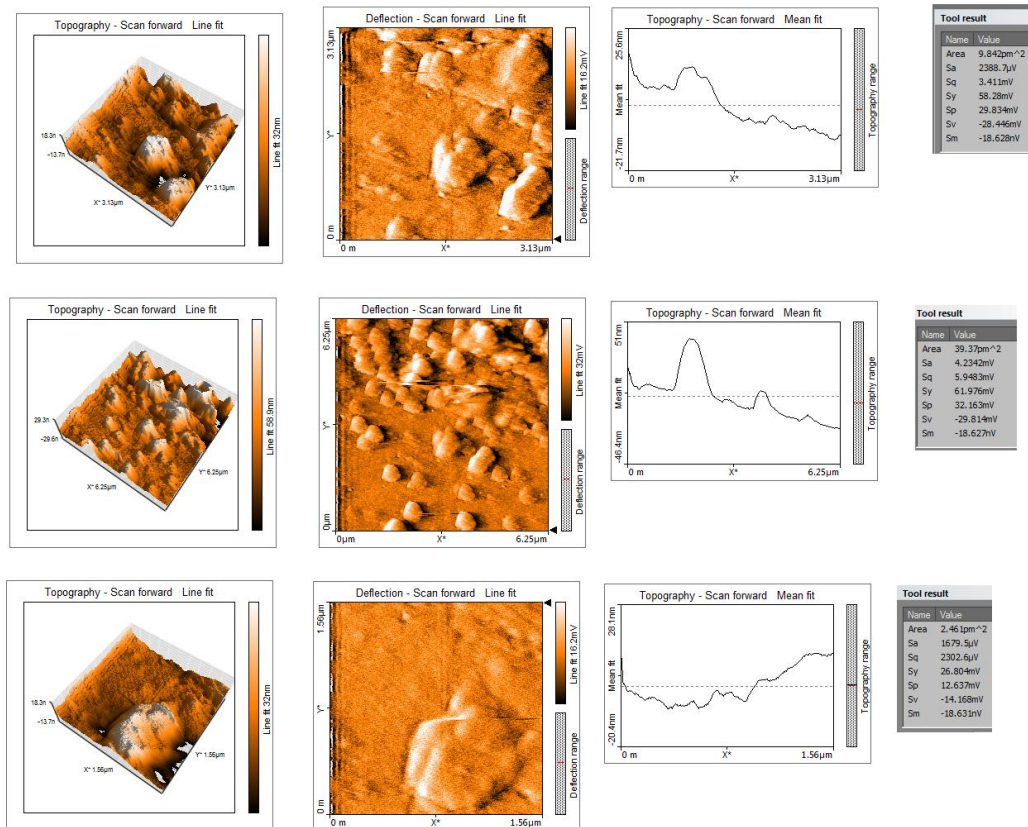


Fig: 5.5.2a Various Magnification of AFM of SO-W

5.6.3 AFM Analysis of SO-M

Fig: 5.6.3a shows the AFM spectral image of SO-W nanoparticle synthesized using agricultural waste with the scanning area of $9.842\mu\text{m}^2$ between $1.56\mu\text{m}$ to $3.13\mu\text{m}$ to $6.25\mu\text{m}$. smooth peaks and pits were found to be distributed over an irregular surface. The size of the range of 263 nm to 324nm . From the surface roughness analysis it is observed that the surface roughness of SO-W is estimated to be about 18.924mv , 20.353mv , 6.9127mv for the root mean square roughness (S_q) and $11.937\mu\text{v}$, $13.387\mu\text{v}$, $5.3053\mu\text{v}$ for the average surface (S_a)[62].

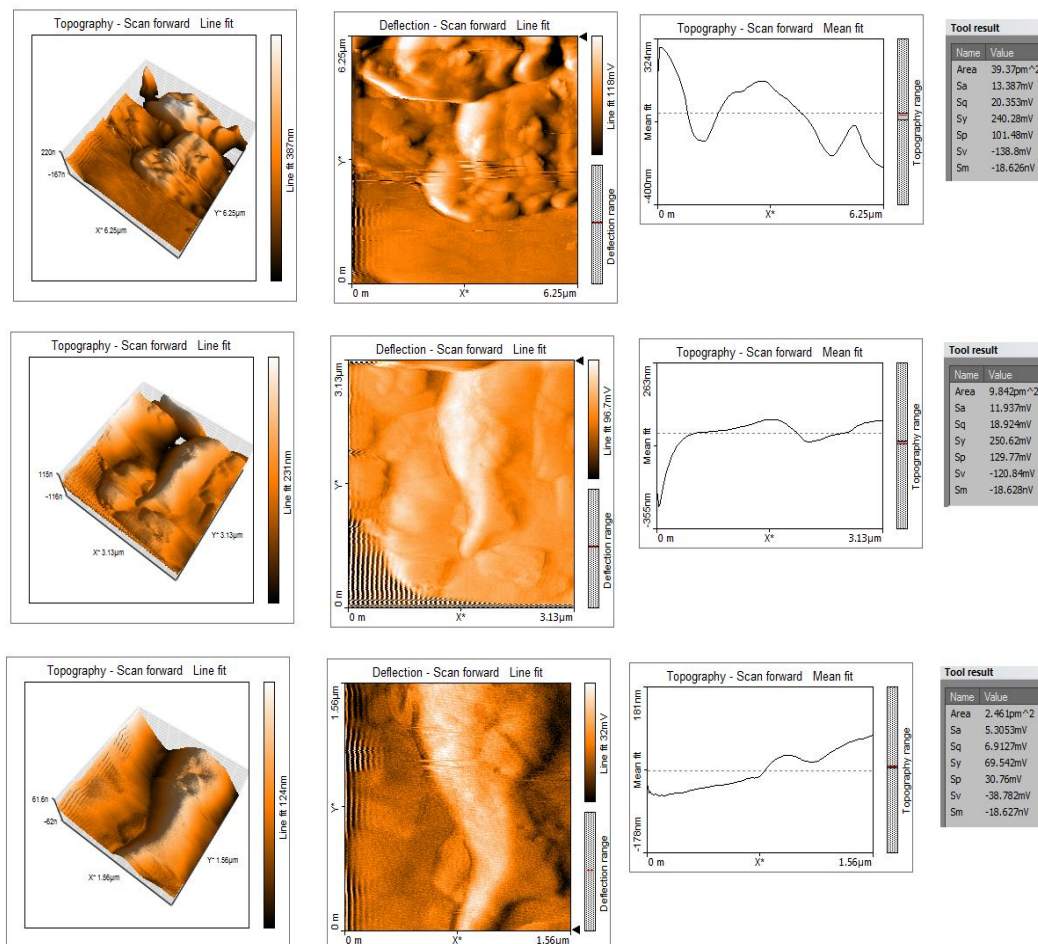


Fig: 5.5.3a Various Magnification of AFM of SO-M

- ▲ The shape and size are more important factors in determining the structural, physical, and chemical properties of nanoparticles. Shape controlled synthesis of nanoparticles has become a focus point as different morphologic nanoparticles would have different electronic, optic and magnetic properties.
- ▲ SO-Rb, SO-W, SO-M nanoparticles are synthesized by organic synthesis using Agricultural Waste.
- ▲ The prepared SiO₂ nanoparticles are characterized using several techniques such as UV-Vis, FT-IR, XRD, SEM, EDAX, AFM.
- ▲ From FT-IR the Metal-Oxygen stretching vibrations are confirmed the Formation of SiO₂, nanoparticles
- ▲ The morphology and size of the prepared nanoparticles are nanorods and nanoflakes which was detected by SEM and AFM analysis
- ▲ The composition of element in SiO₂ nanoparticles are founded by EDAX

CHAPTER - 7

REFERENCE

1. N. Rameli et al K. Jumpri, J. Phys; '*Synthesis and characterization of mesoporous silica nanoparticles using ionic liquids as template*' doi:10.1088/1742 – 6596. **2018**
2. Reema Narayan , Usha Y. Nayak ,Ashok M. Raichur and sanjay garg '*Mesoporous Silica Nanoparticles: A Comprehensive Review on Synthesis and Recent Advances*'**2015**
3. Jongkook Hwang , Jin Hyung Lee , Jinyoung Chun , '*Facile approach for the synthesis of spherical mesoporous silica nanoparticles from sodoium silicate* ' **2020.**
4. Mehrez E. El – Nagger , Nadar R. Abdelsalem '*Soil Application of Nano Silica on Maize Yield and its Insecticidal activity against some stored insects after the post – harvest*' **2020.**
5. Yuning Qu , Yumei Tian , Bozou , Jian Zhang, '*A Novel mesoporous lignin/ silica hybrid from rice husk produced by a sol- gel method*' **2010.**
6. Gemma Turnes Palomino , Juan Jose Cuart Pascual, '*FT – IR studies on the acidity of gallium – substituted mesoporous silica* '. **2004.**
7. D. An, Y. Guo, B. Zou, Y. Zhu, Z. Wang, *A study on the consecutive preparation of silica powders and active carbon from rice husk ash, Biomass Bioenergy* **2011**
8. Vallet-Regí, M., *mesoporous silica nanoparticles for triple-responsive drug delivery*.doi: 18179–18187. **2013.**
9. Mueller, P. P.; Stieve, M.; Lenarz, T.; Behrens, P., *Facile synthesis of chitosan capped mesoporous silica nanoparticles: a pH responsive smart delivery platform* . **2013.**
10. Vitale-Brovarone, C.; Baino, F.; Miola, M.; Mortera,, *J. Mater.. Hybrid mesoporous-microporous nanocarriers for overcoming multidrug resistance* . **2009.**
11. Li, Z.; Barnes, J. C.; Bosoy, A.; Stoddart, J. F.; Zink, J. I., *pH-responsive controlled release of mesoporous silica nanoparticles*. **2012.**
12. Vivero-Escoto, J. L.; Slowing, II; Trewyn, B. G.; Lin, V.*studies on the formation of black particles in rice husk silica ash.* **2010.**
13. Yang, P.; Gai, S.; Lin, J., *Effect of calcination temperature and heating rate on the optical properties and reactivity of rice husk*. **2012.**

14. Wang, Y.; Yu, A.; Caruso, F., *Surface properties of silicas produced by thermal treatment of rice husk ash*. **2005**.
15. S. Sankar, et al., “Biogenerated silica nanoparticles synthesized from sticky, red, and brown rice husk ashes by a chemical method”, *Ceram. Int.*, vol. 42, no. 4, pp. 4875-4885, 2016.
16. C. Yamagata, D. R. Elias, M. R. S. Paiva, A. M. Misso and S. R. H. M. Castanho, *J. Mater. Sci. Eng. B*, 2(8), 429–436 (2012)
17. Abu Bakar BH, Putrajaya R, Abdulaziz H: *Malaysian rice husk ash - improving the durability and corrosion resistance of concrete: pre-review*. *Concr Res Lett* **2010**
18. Real C, Alcala D, Maria C, Jose M: *Preparation of silica from rice husks*. *J Am Ceram Soc* **2012–2016**
19. Wang, Y.; Yan, Y.; Cui, J.; Hosta-Rigau, L.; Heath, J. K.; Nice, E. C.; Caruso, *mesoporous silica nanoparticles end-capped with natural chitosan*, *Chem* **2010**
20. Wu, S. H.; Hung, Y.; Mou, C. Y., *Chem. Commun.* **2011**.
21. P. Zhang, Z. Zhao, B. Dyatkin, C. Liu, J. Qiu, *Green Chem.* **2016**
22. G. Zhang, H. Wang, S. Guo, J. Wang, J. Liu, *Appl. Surf. Sci.* **2016**.
23. L. Yao, J. He, *Prog. Mater. Sci.* **2014**.
24. J. Wang, C. Lu, J. Xiong, *Appl. Surf. Sci.* **2014**.
25. C.C. Dong, J.H. Ji, B. Shen, M.Y. Xing, J.L. Zhang, *Environ. Sci. Technol.* **2018**
26. Y. Zhang, Z. Ding, C.W. Foster, C.E. *Adv. Funct. Mater.* **2017**.
27. J. Zhang, Y. Huang, L. Jin, Vetrone, J.P. Claverie, *ACS Appl. Mater.* **2017**..
28. N. Liu, Y. Chang, Y. Feng, Y. Cheng, X. Sun, H. Jian, Y. *Appl. Mater. Interface* **2017**.
29. Y. Yang, L.C. Yin, Y. Gong, P. Niu, J.Q. Wang, L. Gu, X. H.M. *Adv. Mater.* **2018**.
30. J. Wan, W. Chen, C. Jia, L. Zheng, J. Dong, X. Zheng, Y. Wang, W. Yan, C. Chen, Q. Peng, D. Wang, Y. Li, *Adv. Mater.* **2018**.
31. M.H. Huang, G. Naresh, H.S. Chen *Appl. Mater. Interface* **2018**.

32. E.J. Crossland, N. Noel, V. Sivaram, T. Leijtens, *Nature* **2013**.
33. J. Li, X.A. Dong, Y. Sun, W. Cen, F. Dong, *Appl. Catal. B: Environ.* **2018**
34. G. Zhang, S. Zhang, L. Wang, R. Liu, Y. Zeng, X. Xia, Y. Liu, *Appl. Surf. Sci.* **2017**.
35. R. Zhou, B. Qu, D. Li, X. Sun, X.C. Zeng, *Adv. Funct. Mater.* **2018**.
36. X. Wang, L. Bai, H. Liu, X. Yu, Y. Yin, C. Gao, *Adv. Funct. Mater.* **2018**.
37. B. Li, B. Xi, Z. Feng, Y. Lin, J. Liu, J. Feng, Y. Qian, S. Xiong, *Adv. Mater.* **2018**.
38. K. Lan, Y. Liu, W. Zhang, Y. Liu, A. Elzatahry, R. Wang, Y. Xia, D. Al-Dhayan, N. Zheng, D. Zhao, *J. Am. Chem. Soc.* **2018**.
39. Y. S.W. Han, I.H. Kim, J.H. Kim, H.O. Seo, Y.D. Kim, *Polymer* **2018**.
40. H. Bel Hadjltaief, S. M. Ben Zina, M. Elena Galvez, *Appl. Clay Sci.* **2018**
41. Y. Lvov, W. Wang, L. Zhang, R. Fakhrullin, *Adv. Mater.* **2016**.
42. J. Ma, Q. Liu, L. Zhu, J. Zou, K. Wang, M. Yang, S. Komarneni, *Appl. Catal.* **2016**.
43. A. Ivanova, M.C. Fravventura, D. Fattakhova-Rohlfing, J. Rathouský, L. Movsesyan, P. Ganter, T.J. Savenije, T. Bein, *Chem. Mater.* **2015**.
44. S. Rtimi, J. Kiwi, *Appl. Catal.* **2017**.
45. G. Zan, Q. Wu, *Adv. Mater.* **2016**.
46. W.J. Liu, H. Jiang, H.Q. Yu, *Chem. Rev.* **2015**.
47. Y. Zhang, L. Zuo, L. Zhang, Y. Huang, H. Lu, W. Fan, T. Liu, *ACS Appl. Mater. Interface* **2016**.
48. C. Choi, K.-J. Hwang, Y.J. Kim, G. Kim, J.-Y. Park, S. Jin, *Nano Energy* 2016.
49. Y. Li, J.Y. Lan, J. Liu, J. Yu, Z. Luo, W. Wang, L.. *Chem. Res.* 2015.
50. Z. Wang, J. Yu, X. Zhang, N. Li, B. Liu, Y. Li, Y. Wang, W. Wang, Y. Li, L. Zhang, S. Dissanayake, S.L. Suib, L. Sun, *ACS Appl. Mater. Interface* **8** **2016**.
51. W. Wang, J. Fang, S. Shao, M. Lai, C. Lu, *Appl. Catal.* **2017**.
52. T. Cai, Y. Liu, L. Wang, S. Zhang, Y. Zeng, J. Yuan, J. Ma, W. Dong, C. Liu, S. Luo,

Appl. Catal. **2017**.

53. X. Zheng, Q. Kuang, K. Yan, Y. Qiu, J. Qiu, S. Yang, *ACS Appl. Mater. Interface* **5** 2013.
54. Y. Zheng, P. Jensen, A. Jensen, B. Sander, H. Junker, D. Wang, *Chem* **4** **2018**.
55. D. Zhao, Q. Huo, J. Feng, B.F. Chmelka, G.D. Stucky, *Nonionic triblock and star diblock copolymer and mesoporous silica structures* **2008**
56. J. Aburto, M. Ayala, I. Bustos-Jaimes, C. Montiel, E. Terrés, J.M. Domínguez, E. Torres *mesoporous materials, Micropor. Mesopor.* **2005**.
57. Y. Hu, J. Wang, Z. Zhi, T. Jiang, S. Wang, *Facile synthesis of 3D cubic mesoporous silica microspheres.* **2011**.
58. G.F. Andrade, D.C.F. Soares, R.G. dos Santos, *Mesoporous silica nano* **2012**
59. L.B. de Oliveira Freitas, I.J.G. Bravo, W.A. de Almeida Macedo, E.M.B. de Sousa, *Mesoporous silica materials function* **2016**
60. G. Gonzalez, A. Sagarzazu, A. Cordova, M.E. Gomes, J. Salas, L. Cotreras, K. Noris-Suarez, L. Lascano, *Comparative study of two silica mesoporous materials* **2010**
61. S.M.L. dos Santos, K.A.B. Nogueira, M. de Souza Gama, J.D.F. Lima, I.J. da Silva Júnior, D.C.S. de Azevedo, *Synthesis and characterization of ordered mesoporous silica for adsorption of biomolecules, Micropor. Mesopor* **2007**
62. J. Browne, *Seven Elements That Have Changed The World: Iron, Carbon, Gold, Silver, Uranium, Titanium, Silicon,* **2013**.
- 63.. N. Soltani, A. Bahrami, M. Pech-Canul, L. González, *Review on the physicochemical treatments of rice husk for production of advanced materials,* **2015**.
64. Z.G.L.V. Sari, H. Younesi, H. Kazemian, *Synthesis of nanosized ZSM-5 zeolite using extracted silica from rice husk without adding any alumina source,* **2014**.

65. E.-P. Ng, H. Awala, K.-H. Tan, F. Adam, R. Retoux, S. Mintova, *EMT-type zeolite nanocrystals synthesized from rice husk, Microporous Mesoporous* **2015**
66. S.K. Rajanna, D. Kumar, M. Vinjamur, M. Mukhopadhyay, *Silica aerogel microparticles from rice husk ash for drug delivery*,**2015**
67. J. Alvarez, G. Lopez, M. Amutio, J. Bilbao, M. Olazar, *Upgrading the rice husk char obtained by flash pyrolysis for the production of amorphous silica and high quality activated carbon, Bioresour.***2014**
68. Nieuwenkamp W, "Die Kristallstruktur des Tief-Cristobalits Si O₂", *Zeitschrift fuer Kristallographie, Kristallgeometrie, Kristallphysik, Kristallchemie* (-144,1977) **92**, 82-88 (1935).
69. Han Guopeng, Wang Ying, Littao Yang Zhihua, Pan Shilie, 'A Lithium Difluorophosphate With Aneutal Polyhedral Mioporous Architecture,'*Chemical Communications.*(2019)
70. J. Lou, X. Xu, Y. Gao, D. Zheng, J. Wang, Z. Li, *Preparation of magnetic activated carbon from waste rice husk for the determination of tetracycline antibiotics in water samples*,**2016**.
71. H. Muramatsu, Y.A. Kim, K.S. Yang, R. Cruz-Silva, I. Toda, T. Yamada, M. Terrones, M. Endo, T. Hayashi, H. Saitoh, *Rice husk-derived graphene with nano-sized domains and clean edges*,**2014**.
72. L. Lin, S.-R. Zhai, Z.-Y. Xiao, N. Liu, Y. Song, B. Zhai, Q.-D. An, *Cooperative effect of polyethylene glycol and lignin on SiO₂ microsphere production from rice husks, Bioresour.***2012**.
73. T.-H. Liou, C.-C. Yang, *Synthesis and surface characteristics of nanosilica produced from alkali-extracted rice husk ash*,**2011**.
74. K. Kaviyarasu, E. Manikandan, J. Kennedy, M. Jayachandran, M. Maaza, *Rice husks*

as a sustainable source of high quality nanostructured silica. 2009

75. A. Bazargan, M. Bazargan, G. McKay, *Optimization of rice husk pretreatment for energy production*,²

**A STUDY ON A NOVEL ADSORBENT FOR THE REMOVAL OF COPPER
IONS FROM AQUEOUS SOLUTION**

A project submitted to

St.Mary's College (Autonomous), Thoothukudi

Affiliated to

Manonmaniam Sundaranar University,

Tirunelveli

In partial fulfilment of the award of the degree of

MASTER OF SCIENCE IN CHEMISTRY

Submitted by

J.MAKREENA

Reg. No: 19SPCH02

Under the Supervision and Guidance of

Dr. J. Antony Rajam M.Sc.,M.Phil., SET, Ph.D.



PG DEPARTMENT OF CHEMISTRY (SSC)

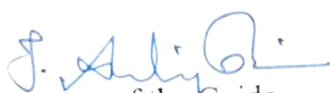
St. Mary's College (Autonomous),

Thoothukudi


April – 2021

CERTIFICATE

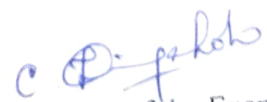
This is to certify that this project work entitled "A STUDY ON A NOVEL ADSORBENT FOR THE REMOVAL OF COPPER IONS FROM AQUEOUS SOLUTION" is submitted to St. Mary's College (Autonomous), Thoothukudi affiliated to Manonmaniam Sundaranar University, Tirunelveli in partial fulfilment for the award of the Degree of Master of Science in Chemistry and this work done during the year 2020 - 2021 by J.MAKREENA (Reg. No: 19SPCH02).


Signature of the Guide


Signature of the Coordinator


Signature of the Director
Director
Self Supporting Courses
St. Mary's College (Autonomous)
Thoothukudi - 628 001.


Signature of Principal
Principal
St. Mary's College (Autonomous)
Thoothukudi - 628 001.


Signature of the Examiner

DECLARATION

I do hereby declare that the project entitled "**A STUDY ON A NOVEL ADSORBENT FOR THE REMOVAL OF COPPER IONS FROM AQUEOUS SOLUTION**" submitted for the degree of Master of Science in Chemistry is my original work carried out under the guidance of **Dr. J. Antony Rajam M.Sc.,M.Phil.,SET.,Ph.D. Assistant Professor, PG Department of Chemistry (SSC), St. Mary's College (Autonomous), Thoothukudi** and that it has not previously formed the basis for award of any Degree.

Station: Thoothukudi

Date:

J.MAKREENA

ACKNOWLEDGEMENT

I express my first and humble thanks to **GOD ALMIGHTY** for giving an opportunity to devote this work

I would like to express my sincere thanks to our principal **Dr. Sr. A.S.J. Lucia Rose**, Secretary **Dr. Sr. Flora Mary**, Deputy principal **Dr. Sr. C. Shibana** Director of SSC **Dr. Sr. F. Mary Joyce Baby** and **Dr. J. ANTONY RAJAM M.Sc., M. Phil., SET, Ph.D.**, (SSC Coordinator), St Mary's College (Autonomous), Thoothukudi for providing the permission to complete the project work.

I find it difficult for me to write something in short to acknowledge my guide **Dr. J. ANTONY RAJAM M.Sc., M. Phil., SET, Ph.D.** she taught me to think and solve the unconventional problems in a conventional way. Her constant inspiration, valuable guidance, tremendous patience and constructive criticism helped a lot to focus my views in the proper perspective. I take this opportunity to express my deepest sense of gratitude and reference towards her for guiding me in the right direction throughout the course of this work.

I heartily express my sincere thanks to my parents and Friends.

CONTENT

CHAPTERS	CONTENTS	PAGE
CHAPTER I	INTRODUCTION	1
CHAPTER II	REVIEW OF LITERATURE	8
CHAPTER III	SCOPE ON THE WORK	18
CHAPTER IV	EXPERIMENT	20
CHAPTER V	RESULT AND DISCUSSION	32
CHAPTER VI	CONCLUSION	48
CHAPTER VII	REFERENCE	50

LIST OF TABLE

TABLE NO	CONTENTS	PAGE
Table No:1	Effect of time variation parameters for the adsorption of heavy metal ions on chitin.	32
Table No:2	Effect of adsorbent variation parameters for the adsorption of heavy metal ions on chitin	34
Table No:3	Effect of concentration variation parameters for the adsorption of heavy metal ions on chitin	37
Table No:4	Effect of temperature variation parameters for the adsorption of heavy metal ions on chitin	40
Table No:5	Adsorption isotherm model for Freundlich	41
Table No:6	Adsorption isotherm model for Langmuir	43
Table No:7	Adsorption isotherm model for Temkin	44
Table No:8	Adsorption kinetics for first order	45
Table No:9	Adsorption kinetics for second order	46

Table No:10	Intraparticle diffusion	47
Table No;11	Thermodynamic	48

LIST OF FIGURES

FIGURE 1	Plot of t/q_t Vs time	32
FIGURE 2	Polt of q_t Vs time	36
FIGURE 3	Polt of $\ln k_d$ Vs $1/T$	41
FIGURE 4	FT-IR spectrum of chitin before adsorption	42
FIGURE 5	FT-IR spectrum of chitin after adsorption	43
FIGURE 6	UV-Visble spectra of chitin before adsorption	

FIGURE 7	UV-Visble spectra of chitin after adsorption	43
FIGURE 8	SEM image of chitin without copper ion	44
FIGURE 9	SEM image of chitin with copper ion	47

CHAPTER - 1

INTRODUCTION

1. INTRODUCTION

1.1 Problem Statement

The purpose of this project is to identify the effect that surface modifications have on the urban heat island phenomenon and related ozone problem in the metropolitan area of Chicago.

The analysis is divided into three main parts the first section of this report introduces the cause of ground level ozone and its effect in urban area. It explains both the chemistry and transport associated with ozone exceedances. The second section is a compilation of the most viable mitigation strategies of urban heat islands increasing vegetative cover and increasing proportions of light to dark surfaces. The effect implementation strategies and specific strengths and weaknesses associated with each approach are described including a comparison of asphalt and concrete pavements using a life cycle analysis approach. The final section provides a case study of the Chicago area. This study entailed an examination of the land use development of an urban fabric analysis in which total vegetative paved and roofed surfaces are investigated and quantified and discussion on the effectiveness of possible mitigation strategies in the Chicago area. In general the associated findings of my research are located within this final section.

1.2 Health Effects of Heavy Metal Toxicity in Human

Heavy metal toxicity can have several health effect in the body. Heavy metal can damage and alter the functioning of organs such as the brain, kidney, lungs, liver and blood. Heavy metal toxicity can either be acute or chronic effects.

Lead:

Toxicity due to lead exposure is called lead poisoning. Lead poisoning is mostly related to the gastrointestinal tract and central nervous system in children and adults. Lead poisoning can be either acute or chronic. Acute exposure of lead cause headache, loss of appetite, sleeplessness, Hypertension, mental retardation, weight loss, hyperactivity, muscular weakness, kidney damage, brain damage, coma and may even cause death.

Mercury:

Mercury is an element that can easily combine with other element to form inorganic mercury. Short-term exposure to metallic mercury vapour at higher levels can lead to vomiting, nausea, skin rashes, lung damage, high blood pressure. Mercury exposure to pregnant women can affect the foetus and offspring may suffer from mental retardation etc.

1.3 Structure of chitin

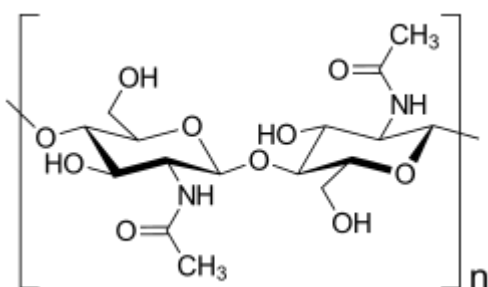
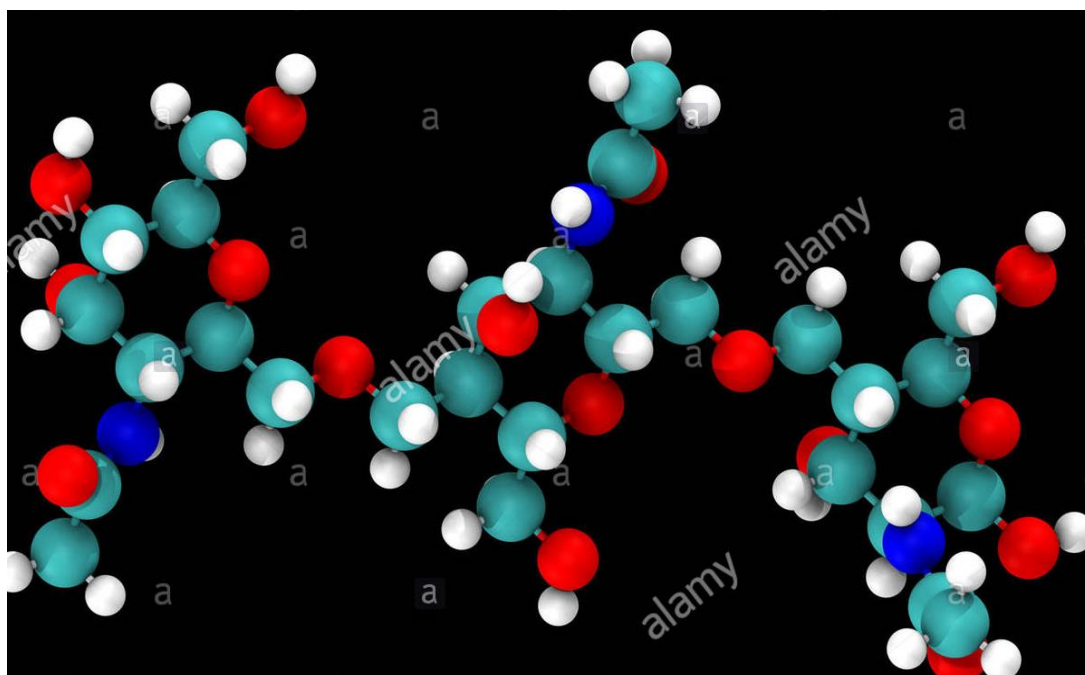


Figure 1 Structure of chitin

Chitin $C_8H_{13}O_5$ is a long-chain polymer of N-acetylglucosamine, a derivative of glucose and the scales of fish and skin of lissamphibians. The structure of chitin is comparable to another polysaccharide, cellulose, forming crystalline nanofibrils or whiskers.

It is functionally comparable to the protein keratin. Chitin has proved useful for several medicinal, industrial and biotechnological purposes.

1.4 Chemistry, Physical properties and biological function

Chemical configurations of the different monosaccharides (glucose and N-acetyl glucosamine) and polysaccharides (chitin and cellulose) presented in Haworth projection.

The structure of chitin was determined by Albert Hofmann in 1929. Hofmann hydrolyzed chitin using a crude preparation of the enzyme chitinase, which he obtained from the snail *Helix pomatia*.

Chitin is a modified polysaccharide that contains nitrogen; it is synthesized from units of *N*-acetyl-D-glucosamine (to be precise, 2-(acetylamino)-2-deoxy-D-glucose). These units form covalent β -(1 \rightarrow 4)-linkages (like the linkages between glucose units forming cellulose). Therefore, chitin may be described as cellulose with one hydroxyl group on each monomer replaced with an acetyl amine group. This allows for increased hydrogen bonding between adjacent polymers, giving the chitin-polymer matrix increased strength. Chitosan is produced commercially by deacetylation of chitin; chitosan is soluble in water, while chitin is not. A cicada emerges from its chitinous larval exoskeleton.

In its pure, unmodified form, chitin is translucent, pliable, resilient, and quite tough. In most arthropods, however, it is often modified, occurring largely as a component of composite materials, such as in sclerotin, a tanned proteinaceous matrix, which forms much of the exoskeleton of insects. Combined with calcium carbonate, as in the shells of crustaceans and molluscs, chitin produces a much stronger composite. This composite material is much harder and stiffer than pure chitin, and is tougher and less brittle than pure calcium carbonate. Another difference between pure and composite forms can be seen by comparing the flexible body wall of a caterpillar (mainly chitin) to the stiff, light elytron of a beetle (containing a large proportion of sclerotin).

Chitin is primarily a structural material in organisms. It is the main component of fungal cell walls. It forms the exoskeletons of insects and crustaceans. It forms the radulae (teeth) of mollusks and the beaks of cephalopods. Chitin also occurs in vertebrates. Fish scales and some amphibian scales contain chitin.

1.5 Health Effects in Plants

Plants have multiple immune receptors to chitin and its degradation products. When these receptors are activated in plants jasmonate hormones are released that initiate an immune response. This is one way plants defend themselves against insect pests. In agriculture, chitin may be used to boost plant defences against disease and as a fertilizer.

1.6 Health Effects in Humans

Humans and other mammals do not produce chitin. However, they have an enzyme called chitinase that degrades it. Chitinase is present in human gastric juice, so chitin is digestible. Chitin and its degradation products are sensed in the skin, lungs, and digestive tract, initiating an immune response and potentially conferring protection against parasites. Allergies to dust mites and shellfish are often due to a chitin allers.

1.7 Uses

Because they stimulate an immune response, chitin and chitosan may be used as vaccine adjuvants. Chitin may have applications in medicine as a component of bandages or for surgical thread. Chitin is used in paper manufacturing as a strengthener and sizing agent. Chitin is used as a food additive to improve flavour and as an emulsifier. It is sold as a supplement as an anti-inflammatory agent, to reduce cholesterol, support weight loss, and control blood pressure. Chitosan may be used to make biodegradable plastic.

1.8 Adsorption

Adsorption is the process in which matter is extracted from one phase and concentrated at the surface of a second phase. This is a surface phenomenon as opposed to adsorption where matter changes solution phase. Eg. gas transfer.

1.9 Adsorbate

Substance which is deposited on the surface of another substance. For example H_2 and O_2 gases.

1. 10 Adsorbent

Surface of a substance on which adsorbent adsorbs for example charcoal, silica gel, alumina etc.

1.11 Types of Adsorption

- Chemical Adsorption
- Physical Adsorption

1.12 Chemical Adsorption

Chemisorption in this kind of adsorption the gas molecules or atom are held to the solid by chemical bonds. For example hydrogen is chemisorbed on nickel.

Characteristics of chemical adsorption

- This type of adsorption is caused by chemical forces.
- It is a very strong process.
- This type of adsorption is almost a single-layered phenomenon.
- Chemisorption is highly specific and takes place at reaction centers on the adsorbent.
- Surface area, temperature, nature of adsorbate effects chemisorption.
- Energy of activation is very high 40-400 KJ/mol.

1.13 Physical Adsorption

Physisorption is a type of adsorption in which the adsorbate adheres to the surface only through Van der Waals interaction which are also responsible for the non-ideal behaviour of real gases.

Characteristics of physical adsorption

- This type of adsorption is caused by physical forces.
- Physisorption is a weak phenomenon.
- This adsorption is a multi-layered process.
- Physical adsorption is not specific and takes place all over the adsorbent.
- Surface area, temperature, pressure, nature of adsorbent effects physisorption.
- Energy for activation is low (20-40 KJ/mol).

1.14 Advantages of Adsorption

- Complete automation and simplicity of operation.
- No manned attendance required during operation.
- Enhanced failure safety and reliability.
- Quick start and stop.
- Moderate dimensions and light weight.
- Low noise level.
- Extended operational life.
- Low operating costs.
- No special workshop requirements.
- Easy installation and integration into an existing air system.

1.15 Disadvantages of Adsorption

- Desorption of enzymes from the carrier.
- Efficiency is less.
- This method is slowest.
- Relatively low surface area for binding.

1.16 Factors affecting Adsorption

i) pH

Affects surface charge of the adsorbent and the charge on the solute.

ii) Temperature

As adsorption is exothermic process, increasing temperature decreases adsorption.

iii) Presence of other solutes

Compete for the limited number of adsorption sites.

iv) Surface area

Adsorption being a surface phenomenon the extent of adsorption depends on the surface area. Increase in the surface area of the adsorbent, Increase the total amount of the gas adsorption.

v) Nature of gas

The amount of gas adsorbed by a solid depends on the gas. In general more easily liquefiable is more readily adsorbed.



CHAPTER – 2

REVIEW OF LITERATURE

REVIEW OF LITERATURE

- Zhang Juan, Fan Kaixuan, Wang Pingping, Zhong Yue, Zhong Yongke et al. has been reported as A commercial activated carbon that is based on coconut shell was modified to increase its mesopore size for the adsorption of albumin-bound bilirubin (AB bilirubin) and bilirubin. The characterization of activated carbon that was modified via liquid nitrogen adsorption indicated that its micropores were reduced in size and its mesopores enlarged. According to the adsorption kinetics results, its adsorption capacities for both AB bilirubin and bilirubin are substantially increased due to its enlarged mesopores. Along with the increased adsorption capacity, its adsorption rate to bilirubin is also substantially increased. The adsorption capacities for bilirubin and AB bilirubin depend linearly on the cumulative mesopore volume in the size ranges of 2.4–4.1 nm and 8.0–30.0 nm, respectively. Additionally, bilirubin presents a faster adsorption rate than AB bilirubin.

- Xin-Qiao He, Yuan-Yuan Cui, Yan Zhanga, Hai-Tao Li, Cheng-Xiong Yang et al. has been reported as Fabrication of novel magnetic porous materials for efficient magnetic adsorption and removal of environmental contaminants still remains great important and interesting in environmental science. Magnetic microporous organic networks (MONs) are a recent class of magnetic microporous materials highly potential in diverse areas. However, the strategies for the fabrication of magnetic MONs or MONs-derived magnetic adsorbents are still quite limited. To further develop novel method for the fabrication of MONs-derived magnetic adsorbents and to extend the application of MONs in environmental science, here we reported a convenient and new method by decorating Fe³⁺ on MON-2COOH to fabricate MON-derived magnetic porous carbon (MPC) for efficient adsorption and removal of cationic dyes from aqueous solution. The Fe³⁺ was firstly decorated on -COOH enriched MON-2COOH and then calcined to produce MPC under Ar atmosphere. The obtained MPC were well characterized and conducted to the adsorption of cationic dyes. The porous, negatively charged and unsaturated bond contained MPC gave extremely fast adsorption kinetics for cationic dyes via electrostatic, hydrogen bonding and π - π interactions. The adsorption of malachite green on MPC was fitted well with pseudo-second-order kinetic, Langmuir adsorption and monolayer adsorption models, and gave much faster adsorption kinetics and larger adsorption

capacities than anionic dyes. Furthermore, the good superparamagnetic behavior and reusability made MPC could be easily recycled and reused. This work not only provided a new strategy to synthesis MON-derived MPC, but also possessed the potential of magnetic MONs-based adsorbents for the adsorption and removal of cationic dyes or trace contaminants in environment.

- Istvan Bakos, Eric S. Muckley, Ilia N. Ivanov, Zsolt Keresztes et al. has been reported as A commercial activated carbon that is based on coconut shell was modified to increase its mesopore size for the adsorption of albumin-bound bilirubin (AB bilirubin) and bilirubin. The characterization of activated carbon that was modified via liquid nitrogen adsorption indicated that its micropores were reduced in size and its mesopores enlarged. According to the adsorption kinetics results, its adsorption capacities for both AB bilirubin and bilirubin are substantially increased due to its enlarged mesopores. Along with the increased adsorption capacity, its adsorption rate to bilirubin is also substantially increased. The adsorption capacities for bilirubin and AB bilirubin depend linearly on the cumulative mesopore volume in the size ranges of 2.4–4.1 nm and 8.0–30.0 nm, respectively. Additionally, bilirubin presents a faster adsorption rate than AB bilirubin.
- Boniface M. Muendo, Victor O. Shikuku, Zachary M. Getenga, Joseph O. Lalah, Shem O. Wandiga et al. has been reported as Michael Rothballer In this work, the adsorption-desorption dynamics of diuron in three typical Kenyan agricultural soils, Nzoia (NZ), Thika (TH) and Machakos (MK) was investigated. The equilibrium adsorption data, tested against three classical nonlinear adsorption isotherms, was best described by the Freundlich model. The Freundlich adsorption constant, (KF), increased in the order MK > TH > NZ soil. Additionally, the negative Gibb's free energy values indicate the adsorption processes were thermodynamically spontaneous and physical. Multiple linear regression analysis indicated that the adsorption-desorption behavior was controlled by the clay and phosphorus contents of the soil. Phosphorus negatively affected the adsorption of diuron and promoted desorption. The groundwater ubiquity score (GUS) indicated that diuron movement rating in MK soil was 'moderate' while the movement in TH and NZ soils was 'high'.
- Istvan Bakos, Eric S. Muckley Ilia N. Ivanov, Zsolt Keresztes et al. has been reported as We demonstrate the use of copper underpotential deposition (UPD) for measurement of

the electrochemically active surface area of a protein-modified gold electrode. The kinetics of adsorption and the subsequent structural rearrangement of β -casein, as a model protein, on the surface of a gold electrode have been followed over time. The protein-free surface area was determined by measuring the charge derived from UPD copper deposition on the non-blocked surface area at different stages of adsorption. The behaviour of β -casein adsorption as a function of surface roughness and the microstructure of the gold electrode, as well as the concentration of the protein solution.

- Rongbo XiaoIn et al. has been reported as this work, the adsorption-desorption dynamics of diuron in three typical Kenyan agricultural soils, Nzoia (NZ), Thika (TH) and Machakos (MK) was investigated. The equilibrium adsorption data, tested against three classical nonlinear adsorption isotherms, was best described by the Freundlich model. The Freundlich adsorption constant, (KF), increased in the order MK > TH > NZ soil. Additionally, the negative Gibb's free energy values indicate the adsorption processes were thermodynamically spontaneous and physical. Multiple linear regression analysis indicated that the adsorption-desorption behavior was controlled by the clay and phosphorus contents of the soil. Phosphorus negatively affected the adsorption of diuron and promoted desorption. The groundwater ubiquity score (GUS) indicated that diuron movement rating in MK soil was 'moderate' while the movement in TH and NZ soils was 'high'. 1. Introduction Contamination of water resources with pesticides and other organic pollutants, especially in regions largely dependent on groundwater for potable water is of great environmental concern . The use of agrochemicals is a leading source of pesticide-contaminated waters.
- Rajae Ghibate, Omar Senhaji, Rachid Taouil et al. has been reported as In the present study, the adsorption potential of pomegranate peel for the removal of Rhodamine B (RhB) was investigated in a batch system. Kinetic and thermodynamic studies of adsorption were conducted. The rate adsorption of RhB was rapid, attained equilibrium at about 120 min, at which the adsorption capacity is close to 30,47 mg/g, and this in the initial dye concentration of 100 mg/L. The kinetic modeling of RhB adsorption was investigated using four celebrated models: pseudo-first order, pseudo-second order, Elovich, and intraparticle diffusion. According to the values of R², RMSE, ARE, and χ^2 it was found that the pseudo-second order model provided a better fit to kinetic data. The

results also show that intraparticle diffusion is not the only rate-limiting step on RhB adsorption onto pomegranate peel.

- Manjit Haer, Kirsten Strahlendorf, Jessie Paynea, Ryan Jung, Emily Xiao, Clementine Mirabel Nausheen Rahmanb, Przemek Kowal, Gabriel Gemmiti, James T. Cronind, Tyler Gable, Kevin Park-Lee, Katherine Drolet-Vives, Matthew Balmer, Marina Kirkitadzea, et al. has been reported as The focus of this study was to examine the small-scale adsorption process of Tetanus Toxoid (TT) as a model protein antigen to aluminum phosphate (AlPO₄) and aluminum oxyhydroxide (AlOOH) adjuvants with real-time monitoring by in-line ReactIR™, ParticleTrack™ based on Focused Beam Reflectance Measurement (FBRM) and EasyViewer™ probes. The adsorption process of AlPO₄ and AlOOH with TT using was monitored in the small-scale reactors. Conformational changes in TT were monitored using in-line infrared probe ReactIR, whereas particle formation associated with protein adsorption were measured by particle size, count, and imaging tools, such as ParticleTrack with FBRM and EasyViewer probes. ParticleTrack distribution results and kinetic measurements were also supported by observations made using EasyViewer. In addition to EasyMax, BioBLU reactor was also used for the adsorption experiments. ReactIR with ATR-Fiber probe was effectively able to monitor adsorption progress of TT to AlOOH and to AlPO₄. ReactIR, EasyViewer, and ParticleTrack provided detailed mechanistic and kinetic information for reaction of TT with AlPO₄ and AlOOH. These in-situ measurements revealed a possible multi-step process for TT to AlPO₄ which may be an indication of antigen adsorption.
- Cheng Fu, Xiaping Zhu a, Xun Dong, Ping Zhao, Zepeng Wang et al. has been reported as Study of the adsorption property and mechanism about the environmental functional material can provide theoretical guidance for its actual application. The sulfhydryl attapulgit (SH-ATP) was prepared by solution blending method. The saturated adsorption capacity to Pb²⁺ and Ca²⁺ in the experiment were 65.57 and 22.71 mg/g, which increased by 57.74% and 31.96% comparing with the attapulgit (ATP), respectively. The adsorption kinetics experiments illustrated that the adsorption of Pb²⁺ and Ca²⁺ onto SH-ATP accorded with multiple kinetic models. Among them, the pseudo second-order model had the best correlation, the correlation coefficients were all above 0.998. The adsorption thermodynamics experiments testified that the adsorption of Pb²⁺

and Ca^{2+} onto SH-ATP conformed to the Langmuir, Tempkin and DubininRadushkevich models, those models indicated that the adsorption processes belonged to the monolayer adsorption, the adsorbent surface was homogeneous, and the micropore distribution of the adsorbent was also relatively uniform. Various thermodynamic parameters ($\Delta H > 0$, $\Delta S > 0$, $\Delta G < 0$) under 25-45°C indicated that the adsorption processes of Pb^{2+} and Cd^{2+} onto SHATP were endothermic and spontaneous. 2021 The Authors.

- Mandala . Chabalalaa, Mohammed Z. Al-Abri, Bhekie. Mambaa, Edward N. Nxumalo, et al. has be reported asThe present work describes a unique modification process for electrospun polyacrylonitrile (PAN) nanofiber membranes modified with -cyclodextrin (-CD) monomers and their application in the adsorption of bromophenol blue and atrazine from aqueous systems. PAN and -CD were successfully crosslinked using citric acid followed by electrospinning of PAN-CD nanofiber membranes. XRD and FTIR spectroscopy demonstrated successful crosslinking of PAN, -CD, and citric acid to form PAN-CD nanofiber membranes. The microstructure and surface morphology of nanofibers were investigated using SEM and AFM and our data show that the nanofibers are uniform, have an average diameter range of 497–557nm and possess rougher surfaces. UV-Vis spectroscopic technique was used to determine the nanofiber membranes' adsorption efficiency and to evaluate their adsorption capacity. Batch adsorption studies at optimized conditions revealed that the removal of 66% and 89% was achieved for bromophenol blue using PAN and PAN-CD nanofibers with adsorption capacity of 0.886 and 1.197mg/g, respectively. PAN and PAN-CD nanofibers removed 67% and 91% atrazine with adsorption capacity of 0.603 and 0.817mg/g, respectively. The adsorptive removal of these pollutants followed the pseudo-second order kinetics and best fitted the Freundlich isotherm model. The increased removal is therefore credited to the increased surface area per volume ratio obtained from reduced diameters, intermolecular interactions, and inclusion complexation after the incorporation of -CD monomers. Thus, it is shown that the addition of CDs improved the adsorption capacity of the hybrid materials via distinctive adsorption mechanisms. Thus, the uniqueness of this work lies on the mechanistic adsorption of bromophenol blue and atrazine through modified PAN-CD nanofiber matrix induced by the grafting of citric acid crosslinked CD.
- Roman Marsalek,Martin Svidrnoch et al. has been reported asThe adsorption of the tricyclic antidepressants amitriptyline and nortriptyline was studied. Activated carbon,

diosmectite and nano-sized titanium dioxide were selected as adsorbent materials. After monitoring the effect of contact time on the amount adsorbed, it was determined that the adsorption kinetics follow a pseudo-second kinetic equation. The system reached equilibrium more rapidly in the case of nortriptyline adsorption compared to amitriptyline. After evaluation of the adsorption isotherms, it was stated that the adsorption in the case of amitriptyline better corresponds to the Freundlich model, on the contrary, the adsorption of nortriptyline can be described by the Langmuir model. The adsorption of amitriptyline on all three adsorbents was approximately twice as high as that of nortriptyline. Activated carbon has the highest adsorption capacity for both drugs. The specific adsorption capacities are as follows. For amitriptyline: activated carbon 3.75 mmol g⁻¹, diosmectite 3.30 mmol g⁻¹, titanium dioxide 2.97 mmol g⁻¹; for nortriptyline: activated carbon 1.87 mmol g⁻¹, diosmectite 1.82 mmol g⁻¹, titanium dioxide 0.79 mmol g⁻¹. In addition, the zeta potential of the individual adsorbent materials was also monitored depending on the pH and the amount of antidepressants absorbed. pH and ionic strength significantly affect the critical micellar concentration of antidepressants. This is subsequently reflected in the different adsorption behavior of amitriptyline and nortriptyline. The adsorption of the tricyclic antidepressants amitriptyline and nortriptyline was studied. Activated carbon, diosmectite and nano-sized titanium dioxide were selected as adsorbent materials. After monitoring the effect of contact time on the amount adsorbed, it was determined that the adsorption kinetics follow a pseudo-second kinetic equation. The system reached equilibrium more rapidly in the case of nortriptyline adsorption compared to amitriptyline. .

- Kovtun E.S., Kartashynska D., Vollhar, et al. has been reported as The surface tension and dilational rheological properties (viscoelasticity modulus and phase angle) of chitosan lactate solutions at the liquid-gas interface are investigated by the oscillating drop shape method. The results were analyzed using the adsorption model proposed earlier for proteins in the framework of non-ideal two-dimensional solution theory. It was found that the experimental values of equilibrium surface tension of chitosan lactate solutions are in good agreement with this model. The results of the dynamic surface tension and adsorption kinetics analysis showed that chitosan lactate is characterized by a non-diffusion (barrier) adsorption mechanism. This fact determines the qualitative predictive value of the applied theoretical model to describe the extreme behaviour of the dependence of the viscoelasticity modulus on the surface pressure.

- Pham Kim Ngoc, Trung Kien, MacHuu Tuan NguyenDo, Thanh VietTran, Dang ThanhPham, Van VinhBach Thang, PhanAnh Tuan DuongRaja Das et.al has be report as α -Fe₂O₃ and Fe₃O₄ nanoplates and nanorices were synthesized by hydrothermal reaction and used for organic pollutant adsorption and removal studies. The effect of size and morphology of α -Fe₂O₃ and Fe₃O₄ nanoplates and nanorices on the dye adsorption efficiency were investigated systematically. The adsorption studies showed a good selectivity and high adsorption capacity (~93%) of the α -Fe₂O₃ nanoplates towards congo red (C.R.) dye, due to the formation of hydrogen bonding between amine group (e NH₂) of C.R. and surface carboxylate group (e COOH), and adsorbed e OH groups of α -Fe₂O₃ nanoplates. The α -Fe₂O₃ nanoplates also showed excellent recyclability with negligible loss of the adsorption capacity, owing to their stable morphology and crystal structure. The excellent C.R. adsorption capacity of the α -Fe₂O₃ nanoplates was further confirmed by conducting experiments with a solution containing a mixture of dyes. Our findings indicate that the synthesized α -Fe₂O₃ nanoplates have a great potential in removing industrial waste, such as C.R. from polluted water. © 2021 The Authors. Publishing services by Elsevier B.V. on behalf of Vietnam National University, Hanoi. This is an open access article under the CC BY-NC-ND license.

- Rasool PelalakZahra, HeidariSeyed Mola, KhatamiTonni Agustiono, KurniawanAzam, MarjaniSaeed Shirazia et al. has been reported as AbstractMagneticOak woodash/Graphene oxide (Ash/GO/Fe₃O₄) nanocomposites weredesigned as a high potent adsorbent in the removal of toxic heavy metals such as Lead (Pb(II))and Cadmium (Cd(II)) ions from aquatic medium. Characterization of Ash/GO/Fe₃O₄sampleswas carried out using FESEM, TEM, EDX mapping, BET/BJH, XRD, FTIR, and VSM methods.The obtained results confirmed the successful synthesis of Ash/GO/Fe₃O₄nanocomposites. In theadsorption process, almost complete adsorption efficiency of produced Ash/GO/Fe₃O₄nanocom-posite was attained under the optimized conditions (99.67% and 98.68% for Pb(II) and Cd(II)adsorption, respectively). The modeling results of kinetics indicated that the mechanism of Pb(II)and Cd(II) adsorption process well fitted by pseudo-second order equation with a high regressioncoefficient (99.67%).

- Makhosazana, MasukuLind, OumaAgnesPho et al. has been reportedas Benzene is a carcinogenic, mutagenic and highly toxic nonpolar organic compound, its presence in

water occurs as a result of leakage of underground pipes and improper effluent disposal. Adsorption techniques have proven to be efficient for benzene removal from water providing a low maintenance method with high removal efficiencies. Nanoparticles provide high surface areas for adsorption and magnetite particles are specifically advantageous owing to their magnetic characteristics. Magnetite surfaces require modification with hydrophobic compounds for the adsorption of nonpolar pollutants. Herein, magnetite nanoparticles (MNP) were modified with oleic acid to form a magnetite-oleic acid composite (MNP-OA) via microwave synthesis for the adsorption of benzene from simulated wastewater. Infrared analysis confirmed the interaction between magnetite and oleic acid and particle diameters were determined by XRD analysis as 19.7 nm and 17.1 nm for MNP and MNP-OA respectively. Magnetic measurements indicated that both materials were superparamagnetic with a decrease in saturation magnetization after modification due to the non-magnetic layer on the surface. Oleic acid modification improved the benzene uptake of magnetite nanoparticles by approximately 30 % while kinetic studies suggested that a concentration driving force controlled the adsorption process. The adsorbent was regenerated and was efficient for five adsorption-desorption cycles.

1. Introduction Water is the earth's most important liquid. Its abundance in nature has led to human civilization and economic development through agricultural use as well as power generation. Although water is an important commodity, it has not gone unnoticed that water scarcity has become a major global challenge. Industries are high water consumers generating high quantities of liquid effluent. One of the most common oil-based pollutants in natural resources is benzene. Benzene is a mono aromatic hydrocarbon mainly used in industry to produce synthetic rubber, polystyrene, and detergents (Parvizi et al., 2020). As a gasoline additive, benzene improves the octane rating and reduces knocking (Hussein and Ahmed, 2016; Russo et al., 2018). Although benzene compound is used in the industry it is highly toxic and ranked in sixth place on the priority list of dangerous substances. It enters water systems through leakage of petroleum from underground storage tanks, improper disposal of effluent containing benzene, the extraction process, and vehicle exhaust (Alves et al., 2017; Yang et al., 2016). Benzene has negative impacts on both human beings and the environment. Exposure to between 700 and 3,000 ppm leads to effects such as cancer, brain damage, respiratory and excretory system damage (Khodaei et al., 2017; Salvi et al., 2017). Other health effects include leukaemia, and kidney failure which can be chronic and fatal if not treated (Salvi et al., 2017). As an environmental problem, benzene

contributes to the formation of ground-level, global warming, and toxic peroxyacyl nitrates through atmospheric photochemical reactions (Niu et al., 2016). Despite all these health factors reported on the dangers of benzene compounds, many industries worldwide still use it due to the extent of their applications (Vidal et al., 2012). Different studies have been conducted for the removal of benzene from wastewater and government authorities have placed very stringent environmental standards for the maximum allowable levels of these organics in water for human consumption. The United States Environmental Protection Agency and the German guideline have established the benzene concentration to be 1 µg/L.

- Chunhua XiaXueying, ZhangLinghui et.al has be report more than 60% of oyster shells (OS) are discarded on the beach, which pollute the soil. At 800°C, OS completely cracks into calcium oxide (CaO), which has the physical adsorption characteristic of a mesoporousstructure. The permeable oyster shell bricks (POSB) used for purifying water were made by improving theprocess with OS as an aggregate. The adsorption effect on heavy metal ions in landscape water under different OS contents, adsorption times and pH values was investigated by using POSB via atomic absorptionspectrometry. The results show that the optimum OS content for the standard weight (2.5 kg) POSB is515–525 g, and the effect of the adsorption of nickel (Ni(II)), zinc (Zn(II)) and manganese (Mn(II)) wereNi(II) > Zn(II) >Mn(II) in the water environment with pH values of 7.5–7.9 for a long time period (>22 h).However, the adsorption effect of trace copper (Cu(II)) was not significant at the same time. The mesoporous structure of CaO has coordination centres and hydroxyl functional groups that have a strong adsorption effect on Ni(II), Zn(II) and Mn(II) to form complexes in the alkaline environment, and micro-scale Ca(II) can exchange ions with Ni(II), Zn(II) and Mn(II) to produce chemical precipitates. POSB wereused in the simulation of sidewalks, squares and the revetment of a park. The experimental results showthat the POSB of the revetment absorbs a larger amount of heavy metal ions than others due to a longersoak. The result shows that the POSB has a continuous adsorption effect and has great potential forwastewater treatment .
- GuangshengCao,Yujie Bai,XiaohanNan,HongxinAn,Lei Wang,Tong Du et al has been reported as The effect of CO₂ adsorption on oil displacement in tight reservoirs is analyzed. The composition of clay minerals in a reservoir is analyzed, and a molecular model of the formed rock structure is established to investigate the adsorption

characteristics of different clay minerals on the fluid. The effect of CO₂ adsorption on oil displacement is investigated through a CO₂ injection experiment. The results show that the adsorption capacity of reservoir minerals is greater for light hydrocarbons than for heavy hydrocarbons as well as for water and CO₂ than for hydrocarbons, indicating that the oil recovery rate of the reservoir composed primarily of silica is higher when supercritical CO₂ and water are alternately injected. The oil recovery can reach 23.78% by water and CO₂ alternate flooding. Intermittent stop injection enables CO₂ to enter rock samples more easily, and crude oil can subsequently be discharged more easily. As the mixing of CO₂ and crude oil cannot be realized under the experimental conditions, the intermittent stop injection time is short and the gravity migration in tight cores is slow. Hence, we infer that the adsorption of CO₂ significantly affects the displacement of tight reservoirs.

- Mohammed, Benjelloun Youssef, Miyah Gulsun, Akdemir, Evrendilek Farid, Zerrouq Sanae Lairini et al. has been reported as the increased environmental awareness and tighter regulatory standards have prompted various industries to seek appropriate wastewater treatment technologies, in particular, for colored wastewater. This review provides detailed information on dyes, their classification, the environmental impact of water pollution on the national (Morocco) and international scales. Recent studies about the adsorption treatment process for the removal of dyes from the aqueous solution with different adsorbents recognized as a sustainable solution in terms of minimization, recovery, and reuse were evaluated. It is also aimed to synthesize the current literature data concerning low-cost adsorbents by systematically highlighting both their characteristics and capacities. Moreover, the applicability of various kinetic adsorption and isothermal models to the removal of dyes by a wide range of adsorbents is reported in addition to information regarding continuous system adsorption.

CHAPTER – 3

SCOPE OF THE WORK

3. SCOPE OF THE WORK

Adsorption is a surface process that leads to transfer of a molecule from a fluid bulk to solid surface. This can occur because of physical forces or by chemical bonds. Usually it is reversible (the reverse process is called desorption); then it is responsible not only for a subtraction of substances but also for release. In most of the cases, this process is described at the equilibrium by means of some equations that quantify the amount of substance attached on the surface given the concentration in the fluid. These equations are called isotherms (the most famous are the Langmuir and the Freundlich equations) because of the dependence of their parameters on the temperature, which is one of the most important environmental factors affecting adsorption. Adsorption has a fundamental role in ecology: it regulates the exchanges between geosphere and hydrosphere and atmosphere, accounts for the transport of substances in the ecosystems, and triggers other important processes like ionic exchange and enzymatic processes.

The major source of water pollution is domestic waste from rural and industrial wastes which are discharged into natural water bodies. The most important of these technologies includes chemical precipitation, electro floatation, ion exchange, reverse osmosis and adsorption on activated carbon. There is a need for the development of low cost, easily available material, which can be easily used more economically on large scale.

The main objectives of this project are

- To study the adsorption efficiency of chitin present in crabs' shell as an adsorbent for the removal of toxic metal ion Cu(II)
- To determine the structural properties and particle size by FT-IR and UV-Vis spectroscopic techniques
- To study the adsorption isotherm model and adsorption kinetics
- To analyse the surface morphology of chitin using Scanning Electron Microscope (SEM)
- To study the effect of time, amount of adsorbent, temperature and concentration of CuSO₄
- To investigate the equilibrium data from Freundlich, Langmuir and Temkin adsorption isotherm expressions

- To determine the pseudo first order, pseudo second order kinetics and intra particle diffusion models of chitin
- To evaluate the thermodynamic parameter such as ΔG° , ΔS° and ΔH° for the adsorption process

CHAPTER - 4

EXPERIMENT

4. MATERIAL AND METHODS

4.1 Chemicals Used

1. Copper sulphate
2. Ammonium chloride
3. Con. Ammonia
4. Fast sulphon black-T
5. Adsorbent
6. Ethylene Diammine Tetra acetic acid (EDTA)

4.2 Preparation of stock solution

The synthetic wastewater solution of copper was prepared using analytical grade chemicals. 24.968 g of copper sulphate was weighed accurately and made up to 1000 mL in a SMF (0.1 N). 20mL of this solution was pipetted out in a 100 mL conical flask. 5 mL of buffer solution and 5 drops of fast sulphon black-T indicator were added. This solution was titrated against EDTA. End point is the colour change from blue to darkgreen. The titrations were repeated to get concordant value.

4.3 Refining of Adsorbent

Crab shell was thoroughly washed with water and cleaned boiled for few minutes and tried then crab shell is ground into fine powder.

4.4 Characterization Techniques

4.4.1 Fourier Transform - Infrared Spectroscopy (FT-IR)

Infrared spectroscopy is one of the most powerful techniques available for analytical chemists. Fourier transform infrared (FT-IR) spectroscopy is an interferometer-based IR technology offering a faster, more sensitive means of analysis than traditional dispersive IR

spectroscopy. FT-IR spectroscopy is a non-destructive technique for determination of chemical compounds in liquid, gases, powders and films that has been widely used in laboratory and industry for several years. FT-IR spectroscopy is used within a broad range of application including; biomedical research, foodstuff analysis, gas and solid surface analysis. The advantages of FT-IR method include multi-component analysis capability, good sensitivity, excellent specificity, speed and simplicity of calibration. Infrared spectroscopy is applicable to both qualitative and quantitative analyses. The FT-IR spectrum provides information about the molecules present in a given sample. Thus FT-IR spectroscopy can provide information about presence of chitin in crabs' shell and any interaction between them. FT-IR spectrum of chitin before and after the removal of Cu(II) from aqueous solution were taken by KBr disc method at room temperature performed on FT-Infra red spectrophotometer housed at Avinashilingam University, Coimbatore.

4.4.2 UV-Visible Spectroscopy

Ultraviolet and visible (UV-Vis) spectroscopy is reliable and accurate analytical laboratory assessment procedure that allow for both qualitative and quantitative analyses of a substances specifically, UV-Vis spectroscopy probes the electronic transition of molecules as they absorb light in the UV and Visible regions of the electromagnetic spectrum. Any species with an extended system of alternating double and single bond will absorb visible light, making UV-Visible spectroscopy applicable to a wide range of samples (molecules and inorganic ions or complexes in solution) in different field such as forensic science, pharmaceutical food, biochemistry and analytical chemistry.

When sample molecules are exposed to light having energy that matches a possible electronic transition within the molecule, some of the light energy will be adsorbed as an electron is promoted to a higher energy orbital. An optical spectrometer records the wavelength. Both the shape of the peaks and the wavelength of maximum absorbance in spectrum give information about the structure of the compound. The combination of electronic absorption spectroscopy and electrochemistry provides valuable information regarding electrochromic properties of materials. For chitin, UV-Vis spectroscopy can provide information about electrochromism properties, electrochromic stability and pH sensitivity etc.

In the present study, UV-Visible absorption measurements were recorded by using JASCO V-650 diffuse reflectance housed at V.O.Chidambaram College, Thoothukudi.

4.4.3 Morphology

Scanning Electron Microscopy (SEM)

The morphology and distribution of chitin were studied by using MIRA3 TESCAN equipment.

The condenser lens focus the light on the sample and the objective lens magnifies the beams, which contain the image to the projector lens so that image was viewed by the observer. The SEM is a type of electron microscope that image the sample surface by scanning it with a high-energy beam of electrons in a raster scan pattern. The electrons interact with the atoms that make up the sample producing signals that contain information about the sample's surface topography, composition and other properties such as electrical conductivity.

4.4.4 Energy Dispersive X-Ray (EDAX)

Energy is an analytical technique used for the elemental analysis or chemical characterisation of a sample. It relies on an interaction of some source of X-ray excitation and a sample. The intensity or area of a peak in an EDX spectrum is proportional to the concentration of the corresponding element in the specimen.

4.5 Adsorption Experiment

Removal of different heavy metal ions (ie) Cu(II) by using adsorption on chitosan nanoparticles and chitosan/TiO₂ nanocomposites have been studied.

4.5.1 Batch Experiments

Batch studies were conducted to evaluate the effect on the following parameters on adsorption kinetics.

- Contact Time
- Adsorbent Dosage
- Concentration

➤ Temperature

4.5.2 Experiment for Contact Time

From the stock solution of known concentration, 5mL of the solution was taken in seven 250ML NM bottles. To each bottle exactly 0.1g of the adsorbent was introduced and diluted to 50mL. The solution were shaken well for different time intervals such as 20, 30, 40, 50, 60, 70, and 80 minutes. The contents were filtered through the whatmann no.1 filter paper. From the filtrate the amount of metal ion present in the solution after adsorption was calculated by using titrimetric procedure /spectrophotometric method.

4.5.3 Experiment For Adsorbent Dosage

Form the stock solution of known concentration 35mL of the solution was taken in six 250ML NM bottle and diluted to 100mL. To each bottle 0.05, 0.10, 0.15, 0.20, 0.25, 0.30 of adsorbent were added. These solution were shaken well for 50 minutes and allowed to stand for 10 minutes. The sample were filter in a conical flask using whatmann no1 filter paper. The amount of metal ion present in the after adsorption was calculated by using trimetric procedure/spectrophotometric method

4.5.4 Experiment for Varying concentration of metal Ion

Form the solution different of solution (0.01, 0.02, 0.03, 0.04, 0.05, and 0.06M) were taken in six 250mL Narrow mouth (NM) bottles. Exactly 0.1g of the adsorbent was introduced into the bottle and diluted to 50mL. These solution were shaken well for 50 minutes in a mechanical shaker and allowed to stand for 10 minutes. The contents were filtered in a conical flask using Whatmann no1 filter paper. The amount of metal ion present in the solution after adsorption was calculated by using titrimetric procedure/spectrophotometric method.

4.5.5 Experiment for Temperature

From the stock solution of known concentration, 70 mL of the solution was taken in six 250mL NM bottles and diluted to 100mL. To study the effect of temperature the temperature of the metal solution was adjusted to different values ranging from 30-80K by using constant temperature. Exactly 2g of the adsorbent was introduced into the NM bottles. These solution were shaken well for 50 minutes and allowed to stand for minutes. The solution were filtered in a

conical flask using Whatmann no 1 filter paper. The amount of metal ion present in the solution after adsorption was calculated by using titrimetric procedure/spectrophotometric method.

4.5.4 Procedure for the Estimation of Copper ion

Estimation of Copper

Exactly 20mL of the standard solution containing copper ion was pipetted out into a clean conical flask. The mineral acid if any is carefully neutralised with buffer solution. The solution was titrated against EDTA solution using fast sulphon black-T as indicator. The end point is the colour from blue to dark green. From the titre value, the amount of copper present in the solution was calculated.

Calculation

The adsorption behaviour of the adsorption sample was studied by evaluating the percentage removal of the metal ions from the solution using the following equation.

$$\text{Removal of Efficiency}(\%) = \frac{C_i - C_e}{C_i} \times 100 \quad (1)$$

Where C_i is the initial concentration of the metal ion in the solution (M) which is calculated from the measured concentration of the stock solution, C_e is the concentration of the metal ion (M) left in the solution after adsorption equilibrium was reached.

Adsorption Isotherm

The relation between amount adsorbed and concentration is known as the adsorption isotherm. Adsorption equilibrium data are typically plotted in the form of an adsorption with the mass adsorbed on the y-axis and the mass in the x-axis at constant temperature.

Adsorption isotherms are mathematical models that describe the distribution of the adsorbate species among liquid and solid phase, based on a set of assumptions that are related to the heterogeneity \ homogeneous of the solids surface, the type of coverage and the possibility of interaction between the adsorbate species.

4.5.5 Freundlich Adsorption Isotherm

A brief empirical equation often used to represent adsorption data is called the Freundlich equation. The Freundlich isotherm describes physical adsorption from liquids.

The empirically derived Freundlich isotherm is defined as follows

$$q_e = K_f C_e^{1/n} \quad (2)$$

Where q_e -amount adsorbed per unit weight of adsorbent at equilibrium (mg/g),(mol/g)

C_e -Equilibrium concentration of adsorbate in solution after adsorption (mg/g),(mol/L)

K_f -Empirical Freundlich constant or capacity factors(mg/g),(mol/g)

$1/n$ -Freundlich exponent

The exponent $1/n$ is an index of the diversity of free energies associated with the adsorption of the solute by multiple components of a heterogeneous adsorbent. When $1/n = 1$, the isotherm is linear and system has a constant free energy at all adsorbate concentrations. When $1/n < 1$, the isotherm is concave and sorbates are bound with weaker free energies, finally, when $1/n > 1$, the isotherm is convex and more adsorbate presence in the adsorbent enhances the free energies of further adsorption.

The good fit of Freundlich isotherm to an adsorption system means there is almost no limit to the amount adsorbed and there is a multilayer adsorption. The applicability of the

$$\log q_e = \log K_f + 1/n \log C_e \quad (3)$$

Freundlich equation to a particular case is tested by plotting $\log q_e$ against $\log C_e$ from the logarithmic form of equation 3 such a plot should yield a straight line with intercept equal to $\log K$ and slope equal to $n/1$.

4.5.6 Langmuir Adsorption isotherm

An alternative equation was derived by Langmuir on the basis of a definite case of the nature of the process of adsorption from solution. The Langmuir adsorption isotherm was developed assuming that;

- A fixed number of accessible sites are available on the adsorbent surface, all of which have the same energy.
- Adsorption is reversible
- Monolayer adsorption occurs
- There are no lateral interactions among the adsorbates.

The Langmuir adsorption isotherm is defined as

Where q_e - amount adsorbed per unit weight of adsorbent at equilibrium (mg/g), (mol/g)

C_e - Equilibrium concentration of adsorbate in solution after adsorption (mg/g), (mol/L)

q_o - Empirical Langmuir constant which represents maximum adsorption capacity (mg/g), (mol/g).

K_L - Empirical Langmuir constant (L/mg), (L/mol)

The q represents the total number of surface sites per mass of adsorbent. In the ideal case q would be equal for all adsorbates. However q may vary somewhat between different compounds because of differences in adsorbate sizes. Therefore it usually represents the maximum achievable surface concentration of a given compound. The constant K which is commonly referred to as the Langmuir constant is defined as the equilibrium constant of the adsorption reaction. The K also implies a constant adsorbate affinity for all surface sites assuming the about Equation (4) and (5)

$$\frac{c_e}{q_e} = \frac{1}{q_o} K_L + \frac{c_e}{q_o} \quad (4)$$

And plotting of c_e/q_e Vs c_e given a straight line with slope and intercept.

The Langmuir isotherm is limited in its application to adsorption in monolayer. It applies well to chemical adsorption and to physical adsorption when saturation is approached Temkin Isotherm.

Temkin adsorption isotherm was developed assuming that;

- The heat of adsorption of all the molecules in the layer decreases linearly with coverage due to adsorbate-adsorbate interactions
- Adsorption is characterized by a uniform distribution of binding energies, up to some maximum binding energy.

The Temkin isotherm is represented by following equation

$$q_e = \frac{RT}{b} \log (K_T c_e) \quad (5)$$

Equation 7 can be expressed in its linear form as;

$$q_e = B_T \log K_T + B_T \log c_e \quad (6)$$

$B_T = \frac{RT}{b}$ (Temkin constant related to the heat of adsorption (KJ/mol))

R- Gas constant

T-Temperature (K)

K_T – Empirical Temkin constant related to the equilibrium binding constant related to the maximum binding energy (L/mg), (L/mol)

The adsorption data can be analysed according to the equation (7). A plot of the versus $\log C_e$ enables the determination of the isotherm constant K_T and B_T .

4.6 Adsorption Kinetics

The prediction of batch adsorption kinetics is necessary for the design of industrial adsorption columns. The nature of the adsorption process will depend on physical or chemical characteristics of the adsorbent system and also on the system conditions. Previously several researchers used different kinetic models, such as Lagergren's pseudo first order, pseudo second

order, Elovich kinetic equation, and parabolic diffusion model, in order to predict the mechanism involved in the adsorption process. From these models the adsorption kinetics was usually described by the Lagergren pseudo first order model. Currently the pseudo second order model has been widely used for adsorption systems due to its good representation of the experimental data for the most of the adsorbent-adsorbate system.

4.6.1 Lagergren's Pseudo First Order Kinetics

The pseudo first kinetic model has been widely used to predict the metal adsorption kinetics. The metal adsorption kinetics following the pseudo first order model is given by

$$\frac{dq}{dt} = K_1(q_e - q_t) \quad (8)$$

Where

q_t – Amount of metal adsorbed at any time (mg/g), (mol/g)

q_e – Amount of metal adsorbed at equilibrium time (mg/g), (mol/g)

K_1 – Pseudo first order rate constant (min)

Integrating Equation (8) with respect to boundary condition $q=0$ at $t=0$ and $q=q$ at $t=t$ then Equation (8) between

$$\log(q_e - q_t) = \log q_e - K \frac{1}{2.303} \times t$$

Thus the rate constant K (min) can be calculated from the plot of $\log(q_e - q_t)$ versus time.

4.6.2 Ho's Pseudo Second Order Kinetics

The adsorption kinetic data can be further analysed using Ho's pseudo second order kinetics, which is represented by

$$\text{Where } \frac{dq}{dt} = K_2 (q_e - q_t)^2$$

q_t – Amount of metal adsorbed at any time (mg/g), (mol/g)

q_e -Amount of metal adsorbed at equilibrium time(mg/g),(mol/g)

K_2 –Pseudo second order rate constant (min)

Separating the variables in Equation (10)

$$d_q(q_e - q_0)^2 = K_2 d_t$$

Integrating Equation (11) for the boundary condition $t=0$ to $t=t$ and $q=0$ and $q=q$ gives

$$\frac{t}{q_t} = \frac{1}{K_2 q_e} + \frac{1}{q_0} \times t \quad (12)$$

A plot between t/q versus time gives the value of the constant K (g/mg h),(g/mole h) and also q (mg/g),(mole/g) can be calculated. The constant K_2 is used to calculate the initial adsorption rate h , at $t=0$ as follows

$$h = K_2 q_e^2 \quad (13)$$

Thus the rate constant K initial adsorption rate h and predicted q can be calculated from the plot of t/q versus time using equation (12) and (13).

4.6.3 Intraparticle Diffusion Model

The most commonly used technique for identifying the mechanism involved in the adsorption process is by fitting experimental data in an intra-particle diffusion plot. Previous studies by various researchers showed that the plot of q versus t represents multi-linearity which characterizes the two or more steps involved in the adsorption process. According to; an intra-particle diffusion coefficient K is defined by the equation:

$$K_i = \frac{q_t}{t} + C$$

Where

q_t – Amount of metal adsorbed at any time (mg/g),(mol/g)

K_i -Intraparticle diffusion rate constant (mg/min)/g (mol/min)/g

C - Gives information about the boundary layer thickness

Upon fitting data to the above equation, if the linear correlation value is close to unity then intra-particle diffusion process is effective.

4.7 Thermodynamic Parameters of Adsorption

For designing adsorption column or batch adsorption systems, the designer should be able to understand the following; What changes can be expected to occur and how fast will they take place. The fast of the reaction can be calculated from the knowledge of kinetic studies. But the changes in reaction that can be expected during the process require the brief idea of thermodynamic parameters. The concept of thermodynamic assumes that in an isolated system Where energy cannot be gained or lost, the entropy change is the driving force. The thermodynamic parameters that must be considered to determine the process, are enthalpy of adsorption (ΔH^0) free energy change (ΔG^0) and entropy change (ΔS^0) Due to transfer of unit mole of solute from solution onto the solid-liquid interface. The important thermodynamic function ΔH^0 is very useful wherever there is a differential change occurs in the system. The exothermic process and positive value indicates the endothermic process. The other important thermodynamic parameter is the change in entropy ΔS^0 . The parameter ΔS^0 is used to identify the adsorption process. The value of ΔH^0 and computed using the equation as follows

$$\ln k_d = \frac{\Delta S^0}{R} - \frac{\Delta H}{RT} \quad (15)$$

Where

R- Universal gas constant(8.314J/mol.K)

T-Absolute solution temperature(K)

K_d -Distribution coefficient

$$K_d = q_e / C_e$$

Where

q-Amount of adsorbed per unit weight of solid (mg/g)

C – Equilibrium concentration of solute in solution(mg/g),(mg/g)

The value of $\ln K$ can be calculated from the slope and intercept of plot between $\ln K$ versus $1/T$.

Another most important thermodynamic parameter involved in the adsorption process is the free energy change and can be calculated using the relation;

Where

ΔG° - Gibbs free energy change

R-Universal gas constant (8.314J/mol.K)

T – Temperature (K)

CHAPTER – 5

RESULTS AND DISCUSSION

5. RESULT AND DISCUSSION

Adsorption Studies

Thorough studies were carried out in order to determine the effects of the operational parameters on metal ion adsorption. The operational parameters studies included the time required for equilibrium, the biomass dose, metal ion concentration, temperature and the pH of the solution.

Effect of Contact Time

The effect of contact time on the adsorption process was studied by varying the contact time and keeping other factors constant. The effect of contact time on the removal of metal ion are shown in table. The purpose of the experiment was to determine the contact time required to reach the equilibrium between the solid phase (biomass) and liquid phase (effluent). Figure show that the percentage uptake increases with time and after some time, it reaches a constant value where no more metal ion can be removed from the solution. At this point, the amount of metal ions being absorbed by adsorbent was in a state of dynamic equilibrium with the amount of metal ion desorbed from the adsorbent. The time required to attain this state of equilibrium is termed the equilibrium time. The amount of metal ion adsorbed at the equilibrium time reflects the maximum adsorption capacity of the adsorbent under these particular condition. The result showed that the heavy metal ion removal using chitin was increased with the contact time variation from 10 to 70 minutes. From 60 to 70 minutes, the percentage removal remains constant which showed that equilibrium was reached at 60 minutes itself.

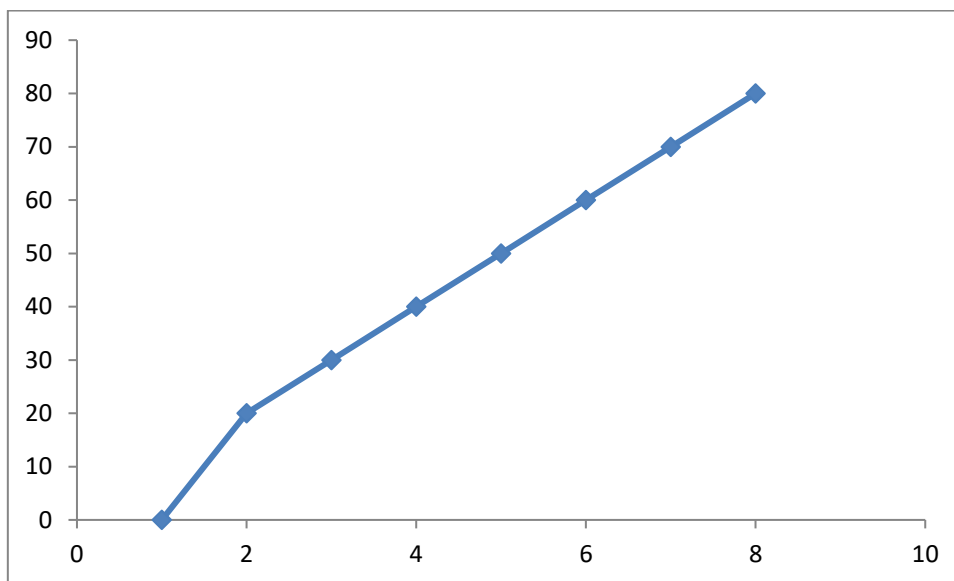
It can be concluded that the rate of metal binding with biomass is more predominant during initial stages, which gradually decreases and remains almost constant after 60 minutes for chitin.

Effect of Time

Parameters for the Adsorption of Cu(II) on Chitin

Time	Equilibrium concentration	Percentage
20	0.0787	7.872
30	0.0777	7.770
40	0.0762	7.620

50	0.0738	7.380
60	0.0698	6.980
70	0.0723	7.230
80	0.0649	6.490



Effect of Adsorbent Dose

The effect of the adsorbent dose was studied at room temperature by varying the sorbent amounts from 0.20 to 0.120 g. For all these runs, initial concentration of the metal ions was fixed. In the present study, the extent of adsorption increases with increase in the amount of adsorbent and the relevant data are given in table.

The effect of adsorbent dosage on metal adsorption is shown in Figure. Figure shows the adsorption of heavy metal ions increase rapidly with increase in the amount of adsorbent due to greater availability of the surface area at higher concentration of the adsorbent. The significant increase in uptake was observed when the adsorbent dose was increased from 0.05 to 0.30 g. Any further addition of the adsorbent beyond this did not cause any significant change in the adsorption. This might be due to overlapping of adsorption sites as a result of overcrowding of the adsorbent particles. These results indicate that removal efficiency is directly related to the number of available adsorption sites. Once equilibrium is attained, there is no effect on adsorption efficiency.

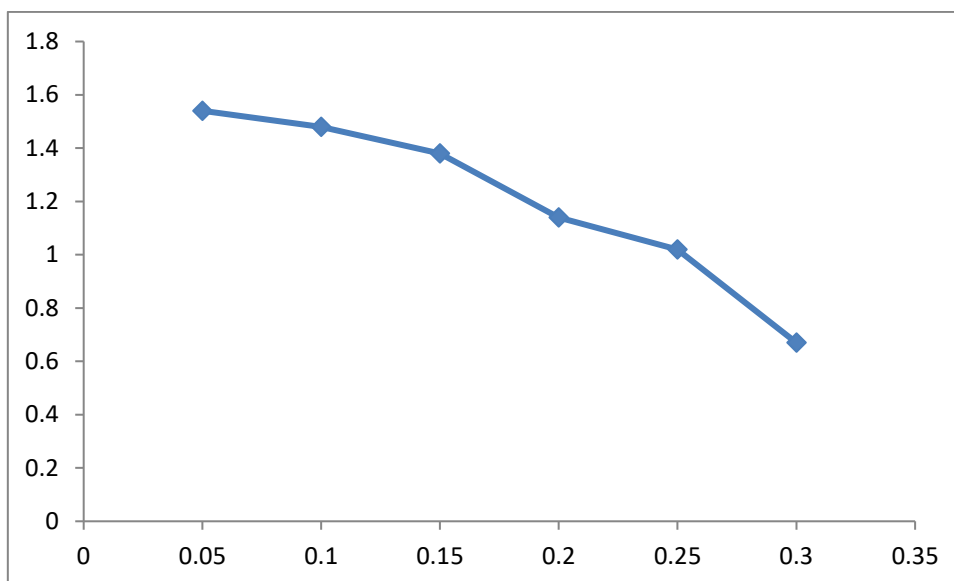
The amount of adsorbent employed was found to influence the efficiency of the adsorption process. This parameter was optimized in conjunction with the other optimized parameters by shaking different amount of Chitin.

The maximum percentage removal of heavy metal ion is observed at the dosage of 0.05 g of chitin. This is due to the increase in the active adsorption sites of the adsorbent.

Effect of Adsorbent

Parameters for the Adsorption of Copper Ion on Chitin

Amount of Adsorbent	Equilibrium concentration	Percentage
0.05	0.0154	1.54
0.10	0.0148	1.48
0.15	0.0137	1.38
0.20	0.0114	1.14
0.25	0.0102	1.02
0.30	0.0068	0.67



Effect of concentration of metal ions

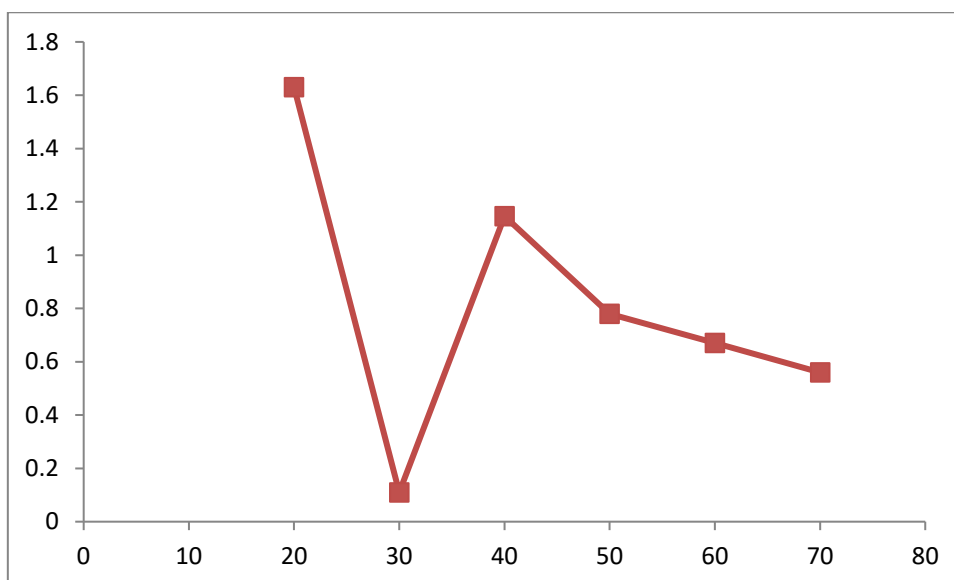
Effect of concentration variation on the percentage removal of heavy metal ions were studies by varying the amount of adsorption decreases with increase in the amount of metal ion concentration and the relevant data are given in table.

The rate of adsorption is a function of concentration of metal ions. Figure indicates that higher adsorption was found to take place at lower concentrations. This may be due to the interaction of all metal ions present in the solution with binding sites. At higher concentrations, more metal ions are left unabsorbed in solution due to saturation of adsorption sites.

Concentration of copper sulphate (M)	Equilibrium concentration (M)	Percentage (%) of metal Ion Removal
20	0.0163	1.630
30	0.0115	0.110
40	0.0114	1.146
50	0.0078	0.780
60	0.0076	0.670
70	0.0056	0.560

At lower metal ions concentration, the percentage uptake was higher due to larger surface area of adsorbent being available for adsorption. When the concentration of metal ions became higher, the percentage removal decreased since the available sites for adsorption became less due to saturation of adsorption sites. At a higher concentration of metal ions, the ratio of initial number of moles of metal ions to the adsorption sites available was higher, resulting in lower adsorption percentage.

However, different from the percentage uptake, with the increasing initial metal ions concentration from 0.01-0.06M, the amount of metal ions adsorbed at equilibrium increased. This occurred due to increase in driving force of the concentration gradient to overcome all mass transfer resistance of metal ions between aqueous and solid phases and accelerate the probable collision between metal ions and sorbents, thus resulting in higher uptake of metal.



Effect of Temperature

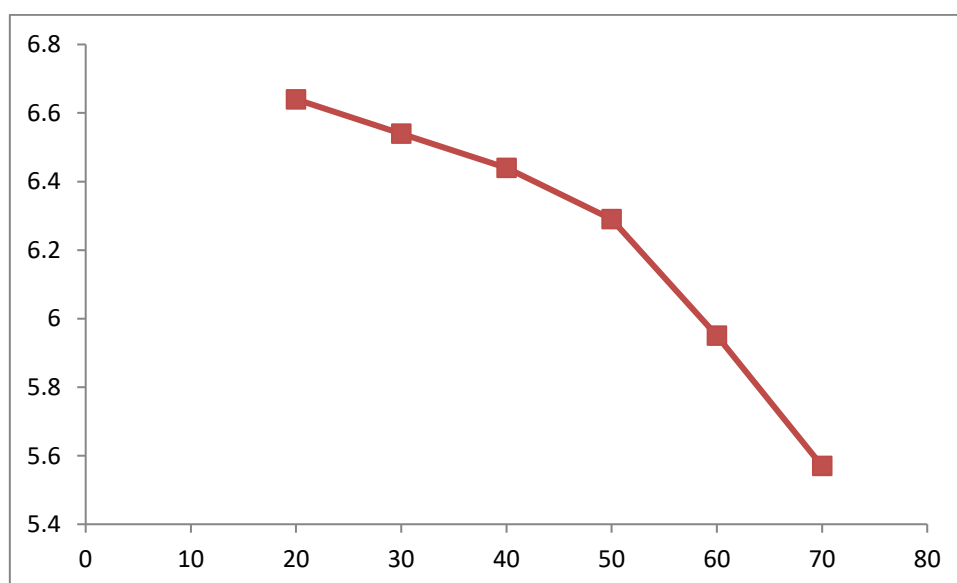
The effect of temperature on the adsorption process was studied by varying the temperature and keeping other factors constant. The temperature dependence of the adsorption process is related with several thermodynamic parameters. The temperature showed the negative effect on adsorption of heavy metal ions using chitin. In order to evaluate the effect of this parameter on the adsorption, the experiments are carried out at different temperature 293-343K. The effect of temperature on the removal of metal ions is shown in the table 5. It is evident that removal of metal ions is maximum only at lower temperature.

With increase in temperature from 313-343K the percentage removal of heavy metal ions was decreased. From the figure 8 & 9 it is clear that the low temperatures are in favour of heavy metal ion removal. This may be due to a tendency for the heavy metal ions to

escape from the solid phase to the bulk phase with an increase in temperature of the solution. The result shows that adsorption mechanism related with removal of heavy metal ions is physical in nature. The adsorption process takes place from the electrostatic interaction, which is in general related with low adsorption heat. This implies that the adsorption process was exothermic in nature.

From the figure, it is concluded that when the temperature decreases, the adsorption of heavy metal ions increases presumably due to the weakening of adsorptive forces between the active site of the adsorbent and adsorbate species.

Concentration of temperature	Equilibrium concentration of temperature	Percentage
20	0.0664	6.64
30	0.0654	6.54
40	0.0644	6.44
50	0.0629	6.29
60	0.0595	5.95
70	0.0575	5.75



ADSORPTION ISOTHERM MODELS

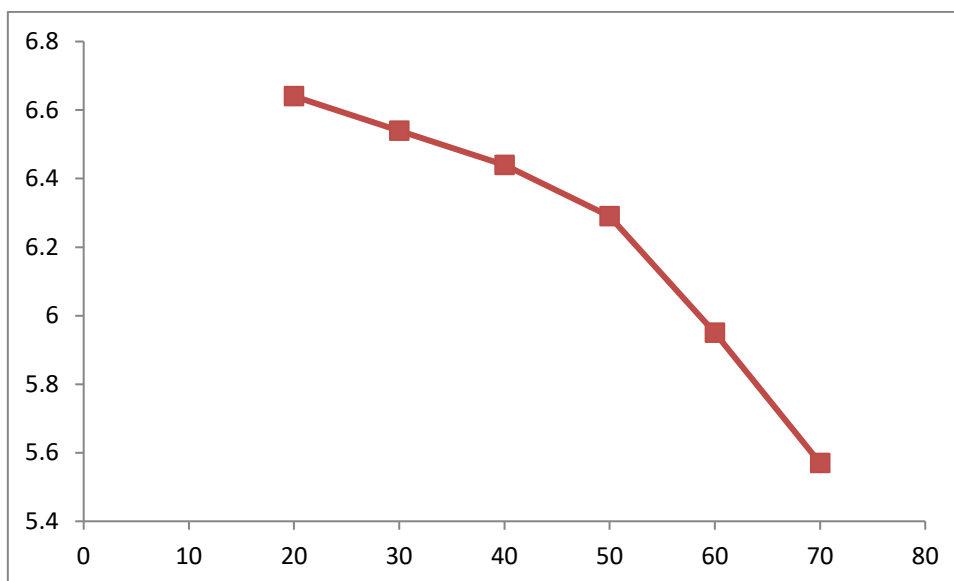
The analysis and design of the adsorption process requires the relevant adsorption equilibrium, which is the most important piece of information in understanding an adsorption process. Adsorption equilibria provide fundamental physicochemical data for evaluating the applicability of the adsorption process as a unit operation. In this study, investigation the equilibrium data was analyzed using the Freundlich, Langmuir and Temkin isotherm expression.

Freundlich isothermal was discussed in Chapter 3 and its linear form is given by the equation

$$\log q_e = \log K_f + \frac{1}{n} \log C_e$$

The Freundlich isothermal parameters obtained by the fitting of the adsorption data are describes by the elemental concentration in solid and liquid are in equilibrium at the end of the experiments. The magnitude of the Freundlich parameters K_f gives the quantitative information on the relative adsorption affinity towards the adsorbed cation and magnitude of constant $1/n$ provide the information about linearity of adsorption. Nonlinear behavior of adsorption indicates that adsorption energy barrier increase exponentially with increasing fraction of filled sites on Chitin.

C_e	$\log C_e$	q_e	$\log q_e$
0.0115	-1.9393	0.0002	-3.6989
0.0114	-1.9430	0.0002	-3.6989
0.0114	-1.9430	0.0002	-3.6989
0.0078	-2.1549	0.0001	-4.0000
0.0067	-2.1739	0.0001	-4.0000
0.0056	2.2518	0.0001	-4.0000

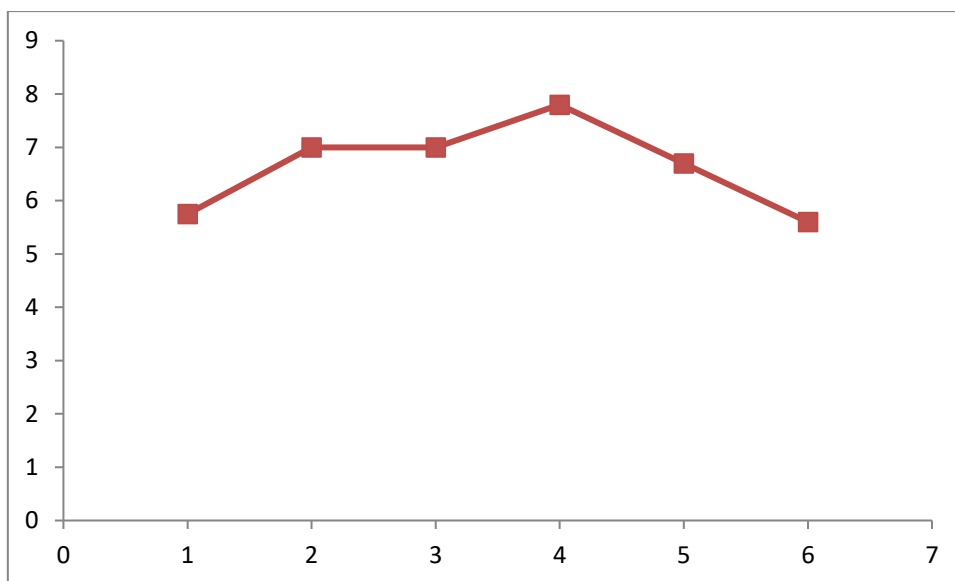


Langmuir isotherm was discussed in Chapter 4 and its linear form is given by the equation

$$\frac{C_e}{q_e} = \frac{1}{q_0 K_L} + \frac{C_e}{q_0}$$

The Langmuir isotherm parameters obtained by fitting the data of adsorption are describes by the elemental concentration in solid and liquid are equilibrium at the end of the experiments. The magnitude of the Langmuir parameters K_L is constant with the heat of adsorption. The q_0 represents the total number of surface sites per mass of adsorbent

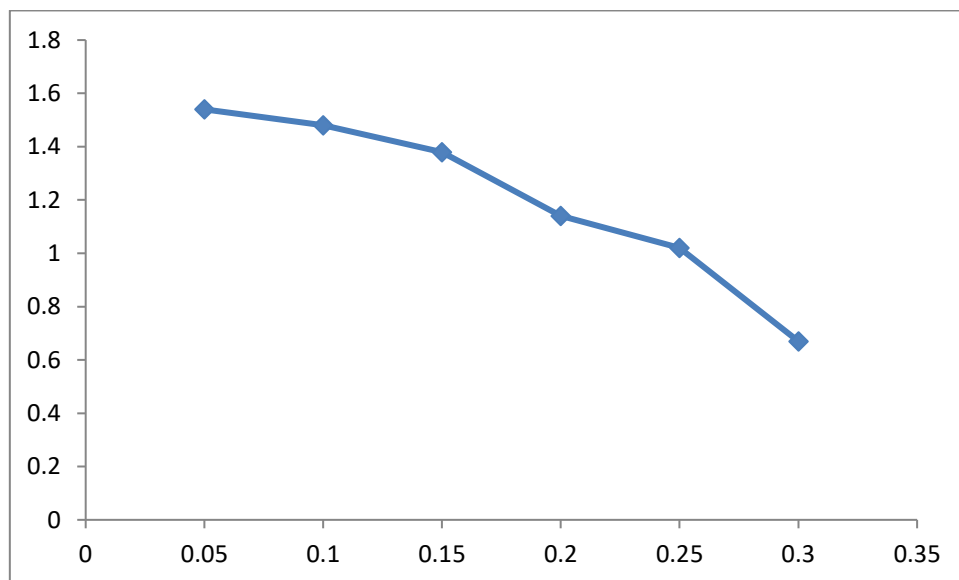
C_e	q_e	C_e/q_e
0.0115	0.0002	5.75
0.0014	0.0002	7.00
0.0114	0.0002	7.01
0.0078	0.0001	7.80
0.0067	0.0001	6.70
0.0056	0.0001	5.60



Temkin isothermal assumes that (i) the heat of adsorption of all the molecules in the layer decreases linearly with coverage due to adsorbate – adsorbate interactions and (ii) adsorption is characterized by a uniform distribution of binding energies, up to some maximum binding energy. The Temkin isothermal parameters obtained by fitting the data of adsorption are describes by assuming the elemental concentration in solid and liquid are equilibrium at the end of the experiments. The magnitude of the Temkin parameters B_T is the related to the heat of adsorption and K_T is equilibrium binding constant.

Figure shows the Freundlich, Langmuir and Temkin curves for metal ions adsorption on Chitin nanoparticles and Chitin/TiO₂ nanocomposites, along with the experimental data. Based on the isothermal parameters, Freundlich, Langmuir and Temkin adsorption constants evaluated from the isotherms with the correlation coefficients are also given in Table. As seen from the tables, regression correlation coefficients for all the adsorbate adsorbent systems are very high for Freundlich and Langmuir models. According to the $1/n$ values in Table 7, the deviation from linear adsorption is higher in Cu(II) metal ion for chitin. The magnitude of K_T values indicates that both chitin nanoparticles and chitin/TiO₂ nanocomposites favor the adsorption of Cu (II) and Pb (II) metal ions. Moreover, chitin/TiO₂ nanocomposites are seen to posses higher adsorption affinity towards heavy metal ions compared with chitin nanoparticles.

C_e	$\log C_e$	q_e
0.0115	-1.9393	0.0002
0.0014	-1.9430	0.0002
0.0114	-1.9430	0.0002
0.0078	-2.1549	0.0001
0.0067	-2.1739	0.0001
0.0056	-2.2518	0.0001



Characterisation of Chitin

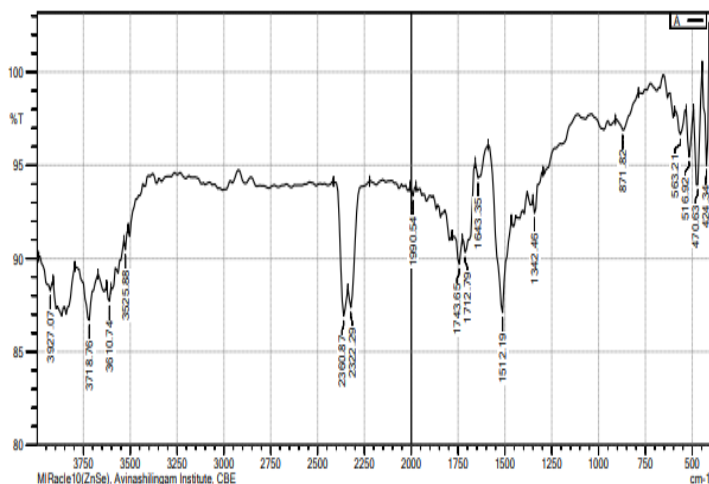
This Chapter carries the detailed discussion of the result which is shown by various characterization techniques. The new composite which has been developed will be verified by result if the various characterization techniques.

FT-IR Spectral Studies

Characterization of Chitin

The stretching frequencies of chitin are listed in table.

Assignments	Frequency, cm^{-1}
O-H Stretching vibration of hydroxyl groups	3610
C-H Stretching vibration	2360
Deformed vibration of NH_2	1642
C-H bending vibrations	1512
Asymmetric C-O-C Vibration	1342
C-O Stretching vibration	871



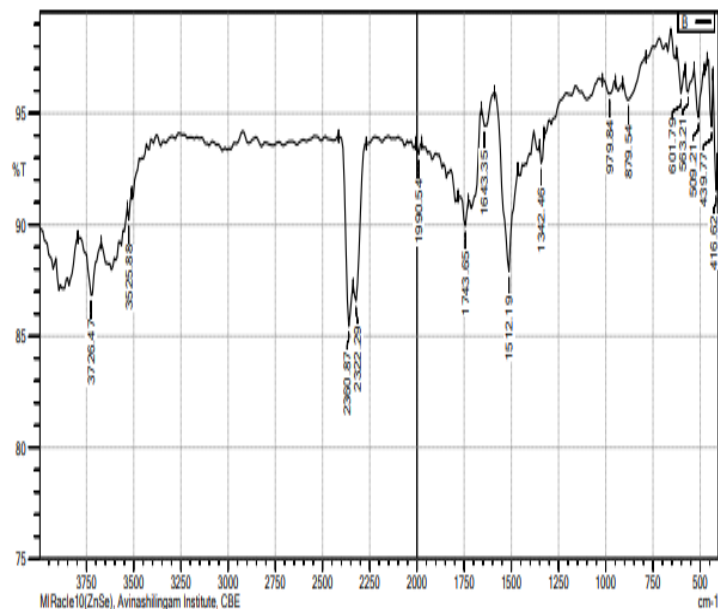


Figure FT-IR spectrum of chitin a) Before and b) After adsorption

In the FTIR spectrum of chitin (figure), the band at 3610 cm^{-1} was observed through the main band due to stretching vibration of OH groups. Intensive absorption band at 2360 cm^{-1} are observed due to the C–H stretching vibrations. The band at 1642 cm^{-1} corresponds to the deformation vibration of –NH_2 ; 1512 cm^{-1} for C–H bending vibration, 1342 cm^{-1} for asymmetric C–O–C stretching vibrations, and stretching vibrations and 871 cm^{-1} for C–O Stretching vibration of CH–OH were observed.

UV-Visible spectral studies

The UV absorption measurements were recorded by using JASCO model V-650 serious diffuse reflectance spectrometer installed at V.O.Chidambaram College, Thoothukudi. UV-visible spectra of the conducting chitin before and after adsorption were recorded at room temperature.

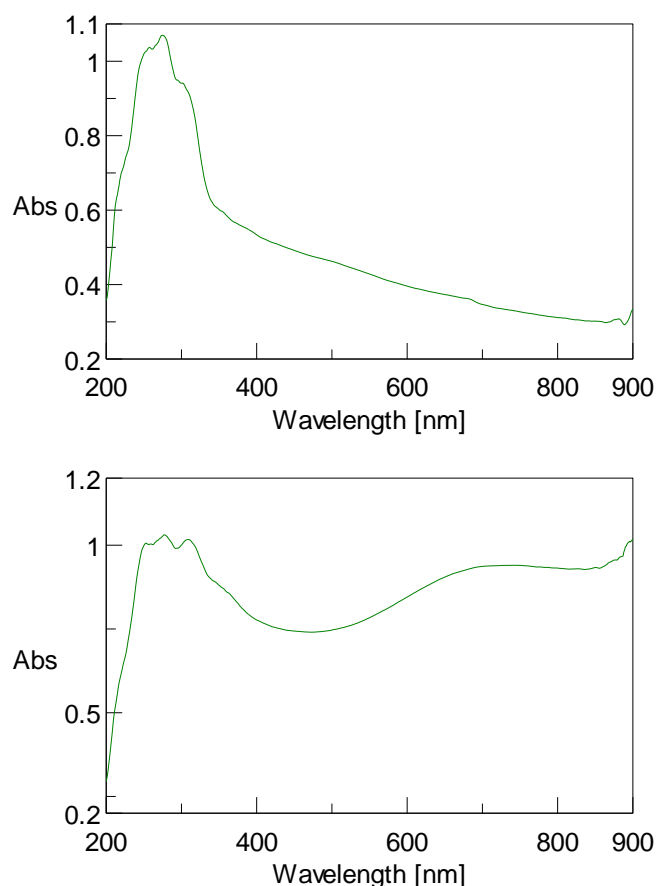


Figure UV-Visible Spectra of Chitin a) Before and b) After adsorption

The UV-Visible spectrum of the sample at room temperature with 1 nm resolution is shown in figure. An adsorption band was observed in the 300-400 nm. The wave length of chitin was found to be 297 nm and 375 nm respectively. The band at 300-400 nm gives the adsorption which is related to the direct electronic π - π^* transition and is called the Soret band.

SEM Studies

Scanning electronic microscopy (SEM) was used to investigate the surface morphology of chitin powder with references to without (figure) and with (figure) copper ions. The SEM images of chitin powder were recorded in Avinashilingam University, Coimbatore and are shown in the figure.

SEM images at magnification show that chitin is spherical with a slightly wrinkled surface and nonporous, uneven granular structure shown in figure. The SEM changes in crystal structure, morphology and agglomerated structure. The SEM image reveals the

surface structure of chitin with small-flake surface presented separately in the exterior morphology of powder. Chitin film, the net morphology changes to homogenous, regular form.

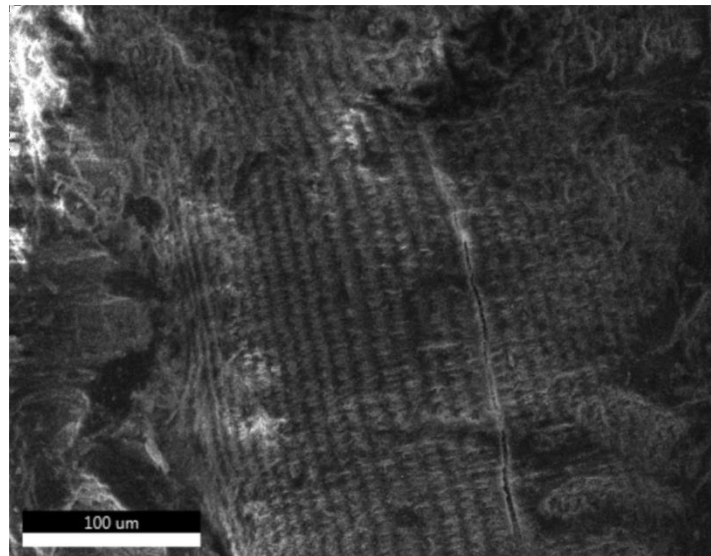
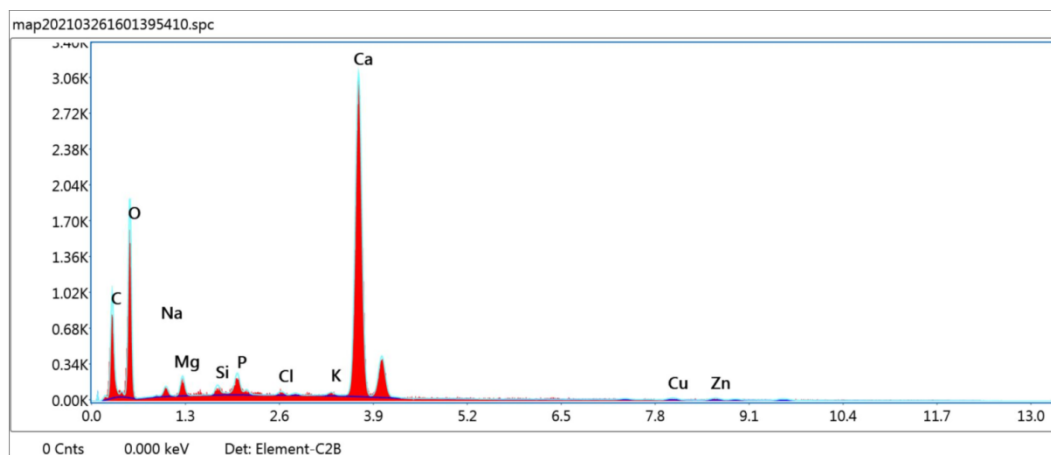
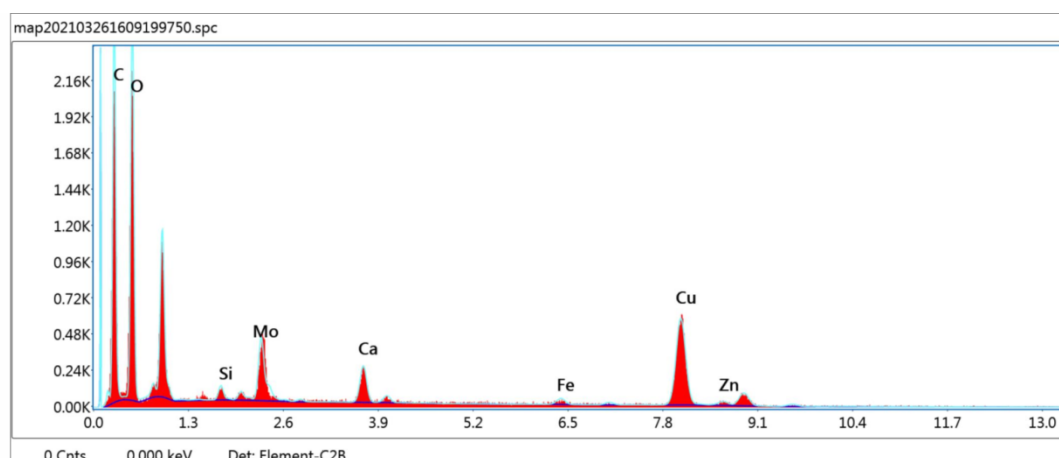
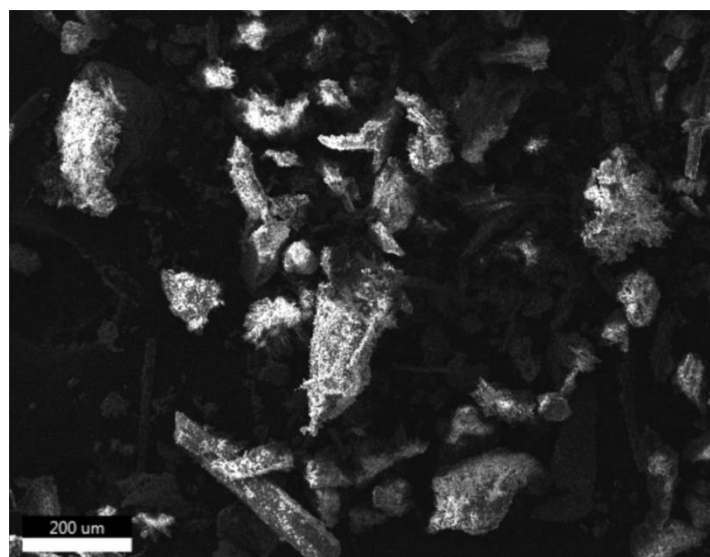
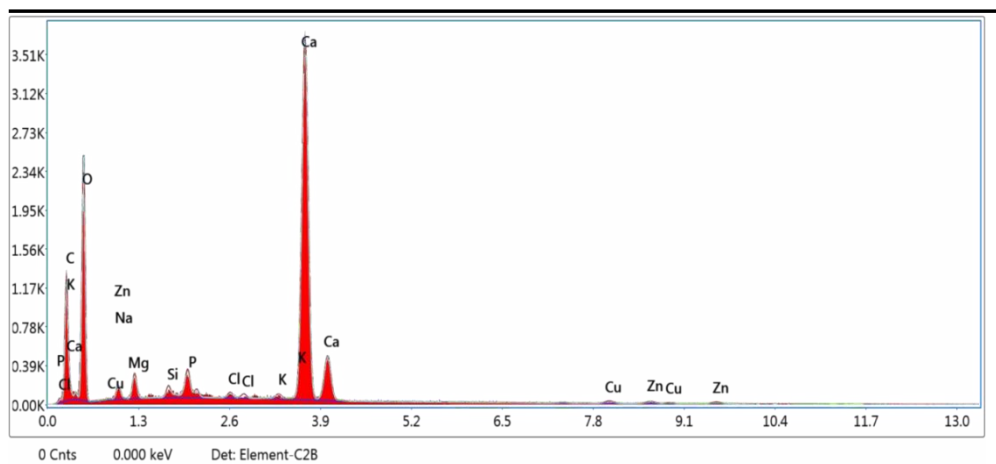
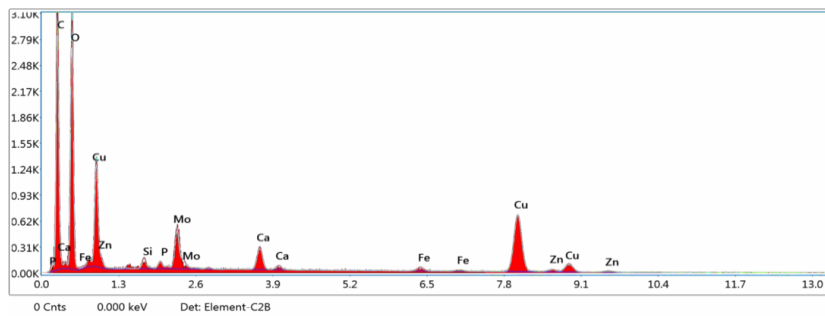
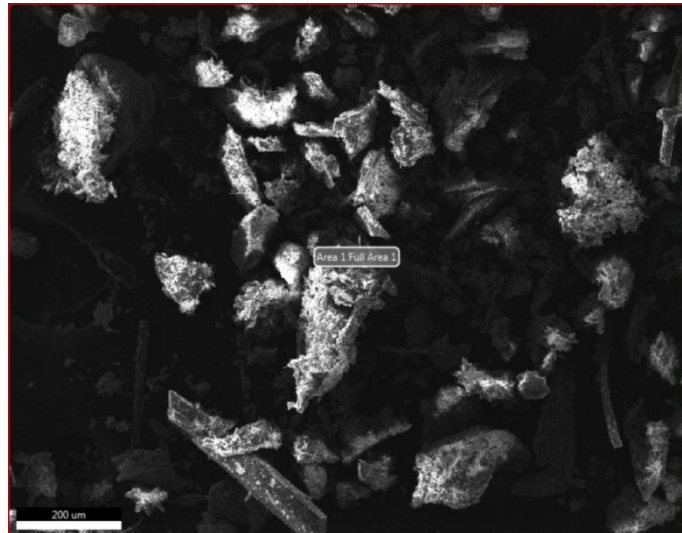


Figure SEM images of chitin a) Without and b) With copper ion







CHAPTER – 6

CONCLUSION

CONCLUSION

- The physico-chemical properties of the chitin were determined using FT-IR, UV-Visible, and SEM-EDX analysis.
- FT-IR spectral studies indicate the presence of various stretching frequencies in the chitin.
- EDX studies and SEM images show a mixed like morphology copper ions introduced chitin.
- Adsorption studies were performed to investigate the adsorption capacity of Chitin towards copper ions under different conditions such as contact time, adsorbent dosage, metal ion concentration and temperature. The adsorption kinetic studies were analyzed using the pseudo first order, pseudo second order kinetic and intra-particle diffusion models. The data on the effect of solution temperature were used in the determination of the thermodynamic parameters of adsorption of copper ions onto Chitin such as Enthalpy of adsorption (ΔS^0) and Gibbs Free energy of adsorption (ΔG^0). The Freundlich, Langmuir and Temkin isotherms were used for the mathematical description of the adsorption equilibrium of toxic metal ions on Chitin and its nanocomposites.

The results can be summarized as follows:

- The equilibrium time for adsorption of copper ions from waste water was achieved within 60 minutes for Chitin to attain the equilibrium.
- Increasing in mass of adsorbent sites, maximum uptake was obtained at adsorbent dose of 0.1g, which may be considered as optimum adsorbent dosage level at the specific conditions.
- Adsorption of metal ions decreases with increase in the concentration of the metal ions. The percentage removal of metal ion is maximum only at lower concentration.
- The percentage removal of metal ions is found to be maximum in lower temperature and it indicates a physisorption process of adsorption.

- Adsorption isotherm experiments showed that the Temkin model did not correlate well with the experimental data. On the contrary, Freundlich and Langmuir models are well fitted with the experimental data than Freundlich model.
- The adsorption data of Cu(II) ions on chitin shows that pseudo-second order model was more suitable than pseudo-first order model.
- Kinetic experiments showed that the intra-particle diffusion seems to play a role at later stages of the adsorption of Cu (II) onto Chitin.
- Negative Enthalpy(ΔH^0) values were obtained for copper ions adsorption on Chitin indicating that the uptake process is exothermic.
- Positive Entropy (ΔS^0) value shows increase randomness at the solid-liquid interface during the adsorption of metal ions on Chitin.
- The negative Gibbs-free energy (ΔG^0) values obtained indicate that the adsorption reaction of copper ions on Chitin favours the products. Then the adsorption process is spontaneous and the degree of spontaneity of the reaction increases with increasing temperature.
- Chitin has significantly higher adsorption capacity towards toxic metal ions from waste water.

REFERENCE

1. Weijie Dai, Meili Xu, Zilin, Zhao Jiatong, Zheng Fei, Huang Heng, Wang Chufan, Liu Rongbo Xiao. *Characteristics and quantification of mechanisms of Cd^{2+} adsorption by biochars derived from three different plant-based biomass*. *Arabian Journal of Chemistry* 15 (2021)
2. Boniface M. Muendo, Victor O. Shikuku, Zachary M. Getenga, Joseph O. Lalah, Shem O. Wandiga, Michael Rothballer. Adsorption-desorption and leaching behavior of diuron on selected Kenyan agricultural soils. *Journal of Magnesium and Alloys*. 23 (2019).
3. Zhang Juan, Fan Kaixuan, Wang Pingping, Zhong Yue, Zhong Yongke. Enhancement of the adsorption of bilirubin on activated carbon via modification. *Results in Materials*. 9 (2021).
4. Hongyan Wang, Haonan Yuan, Jinming Wang, Engui Zhang, Mingyun Bai, Yufeng Sun, Jianfeng Wang, Shijie Zhu, Yufeng Zhen, Shaokang Gao. *Influence of the second phase on protein adsorption on biodegradable Mg alloys' surfaces: comparative experimental and molecular dynamics simulation studies*. *Chemical Engineering Journal*. 30 (2021).
5. Manji Haer, Kirsten Strahlendorf, Jessie Paynea, Ryan Jung, Emily Xiao, Clementine Mirabel, Nausheen Rahman, Przemek Kowal, Gabriel Gemmiti, James T. Cronin, Tyler Gable, Kevin Park-Lee, Katherine Drolet-Vives, Matthe. PAT solutions to monitor adsorption of Tetanus Toxoid with aluminum adjuvants. *Journal of Pharmaceutical and Biomedical Analysis*. 198 (2021).
6. Rajae Ghibate, Rachid Taouil. Kinetic and thermodynamic approaches on Rhodamine B adsorption onto pomegranate peel. *Case Studies in Chemical and Environmental Engineering*. 3 (2020).
7. Cheng Fu, Xiaping Zhu, Xun Dong, Ping Zhao. Study of adsorption property and mechanism of lead(II) and cadmium(II) onto sulfhydryl modified. *Chemical Engineering Journal*. 27 (2020).
8. Mandla B. Chabalalaa, Mohammed Z. Al-Abri, B. Mambaa, Edward N. Nxumalo. modified Mechanistic aspects for the enhanced adsorption of bromophenol blue and atrazine over cyclodextrin polyacrylonitrile nanofiber membranes. *Chemical Engineering Research and Design*. 169 (2021).

9. Istvan Bakos , A am Vass, Eric S. Muck,Llia N. Ivanov,Zsofia, Keresztes.*Indirect electrochemical method for high accuracy quantification of protein adsorption on gold surfaces*9 (2020).
10. Claudio Natalio Lima, H.O. Frota, PuspitapallabChaudhuri, AngsulaGhosh. Density functional study of adsorption of atoms and molecules on single-walled BN nanotubes.*Applied surface Science Advances*.4 (2021).
11. Xin-Qiao He, Yuan-Yuan Cui, Yan Zhanga,Hai-Tao Lib.*Decoration of Fe³⁺ o of cationic dyesn carboxyl microporous organic network to fabricate magnetic porous carbon for efficient adsorption*.*Chemical Engineering JouralAdvances*.6(2021)
- 12.AnisAtikahAhmam, MohdAzmier Ahmad, Nasehir Khan E.M. Yahaya, JamilahKarim. Adsorption of malachite green by activated carbon derived from gasifiedHeveabrasiliensis root. *Arabian Journal of Chemistry*14 (2021).
13. H.M. Badran, Kh.M. Eid,H.Y. Ammar. DFT and TD-DFT studies of halogens adsorption on cobalt-doped porphyrin: Effect of the external electric field. *Result Of physical*. 23(2021).
14. RafikMalleke, FrédéricPlantier, Christophe .Experimental characterization of cyclopentane adsorption/desorption in microporousactivated .*Carbon Trends* 2(2020)
- 15.Wenyan Shi, Yuting Chu,MingzhuXia,The adsorption performance and micro-mechanism of MoS₂/ montmorillonite composite to atenolol and acebutolol: Adsorption experiments and a novel visual study of interaction. *Ecotoxicology and EnvirnomentalSafety*.213(2020).
16. Roman Marsalek, Martin svidrnoch. The adsorption of amitriptyline and nortriptyline on activated carbon, diosmectite and titanium dioxide.*Envinomental Challenges*.1 (2020).
- 17.A.I. Kovtun, E.S. Kartashynska,D. Vollhardt. Adsorption and viscoelastic properties of chitosan lactate at the liquid-gas interface.*JCIS Open*1 (2020).
18. Carina Sampl, Samuel Eyle, WimThielemansReal-time adsorption of optical brightening agents on cellulose thin films. *Carbohydrate Polymer*.261(2020).
19. Pham Kim Ngou, Trung Kien Mac, Huu Tuan Nguyen, Do Thanh Viet, Tran Dang Thanh Pham Van Vinh, Bach Thang Pha.*Excellent organic dye adsorption capacity and*

recyclability of hydrothermally synthesized α -Fe₂O₃ nanoplates and nanorices. *Journal Of Science Advanced Materials and Devices*. 2 (2018) .

20.Rasool Pelalak, Zahra Heidari, Seyed Mola Khatam, Tonni Agustiono Kurniawa, AzamMarjani,SaeedShirazian. Oak wood ash/GO/Fe₃O₄ adsorption efficiencies for cadmium and lead removal from aqueous solution: Kinetics, equilibrium and thermodynamic evaluation.*Arabian Journal of Chemistry* 14 (2021).

21.Makhosazana Masuku, Linda Ouma, Microwave assisted synthesis of oleic acid modified magnetite nanoparticles for benzene adsorptionness.*Environmental Nanotechnology Monitoring and Management*.15 (2021).

22. Daniel Tunega, Ali Zaoui. Adsorption of polycyclic aromatic hydrocarbons on FeOOH polymorphs: A theoretical study.*Surface Science*.706 (2019) .

23.Chunhua Xia,Xueying Zhan, Linghui Xia. Heavy metal ion adsorption by permeable oyster shell bricks.*Construction and Building Materials*.275(2019).

24. Mohammed Benjelloun, Youssef Miyah, GulsunAkdemirEvrendilek,FaridZerrouq,Sanae Lairini. Recent Advances in Adsorption Kinetic Models: Their Application to Dye Types.*Arabian Journal of Chemistry*.14(2020).

25. Aida Arabpour,Sasan Dan, Hassan Hashem, Preparation and optimization of novel grapheneoxide and adsorption isotherm study of methyleneblue.*Arabian Journal of Chemistry*.14 (2020).

26. Bi-lan Lin, Jun-jie Shao, Yu-ye Xu, Yi-ming La Adsorption and corrosion of inhibitor of Pomelo peel extract for mild steel in phosphoric acid solution. *Arabian Journal Of Chemistry*. 40 (2018).

27. RegassaBeksissaa,BeteleyTekolaa,Investigation performance of acid treated lignite coal for Cr (VI) removal from aqueous of the adsorption solution.*Environmental Challenges*.4(2021).

28. RegassaBeksissaa, BeteleyTekolaaInvestigation of the adsorption performance of acid treated lignite coal for Cr (VI) removal from aqueous solution.*Environmental Challenges*.4(2020).

29. Nam Q, Daniel Gunlycke, Le. Vibrational Signatures of Sarin Adsorption on Anatase Surface. *Surface Science*. 705 (2021).
30. Zhe Cao, Guanggang Zhou. Nanoscale liquid hydrocarbon adsorption on clay minerals a molecular dynamics simulation of shale oils. *Environmental Challenges*. 40(2021)

SYNTHESIS AND CHARACTERIZATION OF TELLURIDE NANOPRTICLES

A project submitted to

ST MARY'S COLLEGE (Autonomous), Thoothukudi

Affiliated to

Manonmaniam Sundaranar University,

Tirunelveli

In partial fulfilment of the award of the degree of

MASTER OF SCIENCE IN CHEMISTRY

Submitted by

J.RAJARATHNA

Reg. No: 19SPCH03

Under the Supervision and Guidance of

Mrs.K.SARAVANADEVI M.Sc. M.Phil., SET.,



PG DEPARTMENT OF CHEMISTRY (SSC)


St. Mary's College (Autonomous),


Thoothukudi

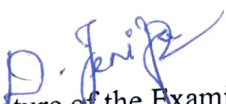
April – 2021


CERTIFICATE


This is to certify that this project work entitled "SYNTHESIS AND CHARACTERIZATION OF TELLURIDE NANOPARTICLES" is submitted to **St. Mary's College (Autonomous)**, Thoothukudi affiliated to **Manonmaniam Sundaranar University**, Tirunelveli in partial fulfilment for the award of the **Degree of Master of Science in Chemistry** and this work done during the year 2020 - 2021 by **J.RAJARATHNA (Reg. No: 19SPCH03)**


Signature of the Guide


Signature of the Coordinator


Signature of the Examiner


Signature of the Director
Director
Self Supporting Courses
St. Mary's College (Autonomous),
Thoothukudi - 628 001.


Signature of Principal
Principal
St. Mary's College (Autonomous)
Thoothukudi - 628 001.

DECLARATION

I do hereby declare that the project entitled "**SYNTHESIS AND CHARACTERIZATION OF TELLURIDE NANOPARTICLES**" submitted for the degree of Master of Science in Chemistry is my original work carried out under the guidance of **Mrs.K.SARAVANADEVI M.Sc.,M.Phil.,SET., Assistant Professor, PG Department of Chemistry (SSC), St. Mary's College (Autonomous), Thoothukudi** and that it has not previously formed the basis for award of any Degree.

Station: Thoothukudi

Date:

J.RAJARATHNA

ACKNOWLEDGEMENT

I express my first and humble thanks to **GOD ALMIGHTY** for giving an opportunity to devote this work

I would like to express my sincere thanks to our principal **Dr. Sr. A.S.J. LUCIA ROSE**, Secretary **Dr. Sr. FLORA MARY**, Deputy principal **Dr. S. C. SHIBANA** Director of SSC **Sr. F. MARY JOYCE BABY** and **Dr. J. ANTONY RAJAM M.Sc., M. Phil., SET, Ph.D**, (SSC Coordinator), St Mary's College (Autonomous), Thoothukudi for providing the permission to complete the project work

I find it difficult for me to write something in short to acknowledge my guide **Mrs K.SARAVANADEVI M.Sc., M.Phil., SET**. she taught me to think and solve the unconventional problems in a conventional way. Her constant inspiration, evaluable guidance tremendous patience and constructive criticism helped a lot to focus my views in the proper perspective I take this opportunity to express my deepest sense of gratitude and reference towards her for guiding me in the right direction throughout the course of this work My deep personal regards are due for her forever

I heartly express my sincere thanks to my parents and Friends.

CONTENT

S.NO	TITLE	PAGE NO.
1	INTRODUCTION	1
2	REVIEW OF LITERATURE	12
3	SCOPE OF WORK	18
4	MATERIALS AND METHODS	20
5	RESULTS AND DISCUSSION	32
6	CONCLUSION	45
7	REFERENCE	46

LIST OF ABBRIVIATION

UV- Vis	Ultra – Violet Visible Spectroscopy
FT- IR	Fourier Transform Infrared Spectroscopy
XRD	X-Ray Diffraction
SEM	Scanning Electron Microscope
EDAX	Energy Dispersive X- Ray Analysis

ABSTRACT

In this present work, synthesis and characterization of Zirconium and Cadmium Telluride nanoparticles was studied. The prepared nanoparticles were characterized using FT-IR, XRD, SEM, EDAX. From the XRD data confirmed that the samples were Body centred cubic (BCC) and cubic in nature and average crystalline size was 1 nm and 3 nm for ZrTe and CdTe nanoparticles respectively. The morphology and size of the prepared nanoparticles was studied using SEM. The surface morphology of the prepared nanoparticles look like nanoflower and nano brittle fracture. The composition of element in ZrTe and CdTe nanoparticle is confirmed by EDAX.

CHAPTER - 1

INTRODUCTION

1. INTRODUCTION

Tellurium is a chemical element with the symbol Te and atomic number 52. It is a brittle, mildly toxic, rare, silver-white metalloid. Tellurium is chemically related to selenium and sulphur, all three of which are chalcogens. It is occasionally found in native form as elemental crystals. Tellurium is far more common in the Universe as a whole than on Earth. Its extreme rarity in the Earth's crust, comparable to that of platinum, is due partly to its formation of a volatile hydride that caused tellurium to be lost to space as a gas during the hot nebular formation of Earth,^[1] and partly to tellurium's low affinity for oxygen, which causes it to bind preferentially to other chalcophiles in dense minerals that sink into the core.

Tellurium-bearing compounds were first discovered in 1782 in a gold mine in Kleinschlatten, Transylvania (now Zlatna, Romania) by Austrian mineralogist Franz-Joseph Müller von Reichenstein, although it was Martin Heinrich Klaproth who named the new element in 1798 after the Latin word for "earth", tellus. Gold telluride minerals are the most notable natural gold compounds. However, they are not a commercially significant source of tellurium itself, which is normally extracted as a by-product of copper and lead production.

Commercially, the primary use of tellurium is copper (tellurium copper) and steel alloys, where it improves machinability. Applications in CdTe solar panels and cadmium telluride semiconductors also consume a considerable portion of tellurium production. Tellurium is considered a technology-critical element. Tellurium has no biological function, although fungi can use it in place of sulphur and selenium in amino acids such as tellurocysteine and telluromethionine.^[2] In humans, tellurium is partly metabolized into dimethyl telluride, (CH₃)₂Te, a gas with a garlic-like odor exhaled in the breath of victims of tellurium exposure or poisoning.

Tellurium is usually found as calaverite, the telluride of gold, and also combined with other metals. It is found commercially in electrolytic refining of blister copper from anode muds during the process. It is occasionally found in its native state. Amorphous tellurium is made by precipitating it from a solution of telluric acid. Tellurium has no known biological function, although fungi can incorporate it in place of sulfur and selenium into amino acids such as telluro-cysteine and telluro-methionine. Organisms have shown a highly variable tolerance to tellurium compounds.

1.1.1. History

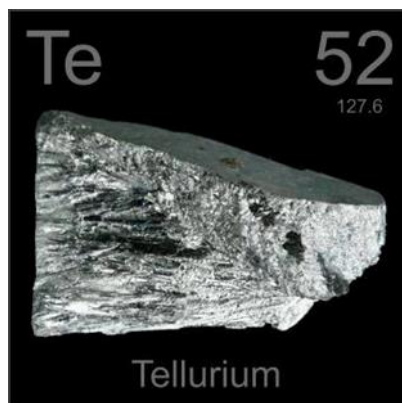


Figure 1.1 Tellurium

Tellurium (Latin tellus meaning "earth") was discovered in the 18th century in a gold ore from the mines in Kleinschlatten (today Zlatna), near today's city of Alba Iulia, Romania. This ore was known as "Faczebajer weißes blättriges Golderz" (white leafy gold ore from Faczebaja, German name of Facebánya, now Fața Băii in Alba County) or antimonite gold pyrite), and according to Anton von Rupprecht, was containing native antimony.^{[3][4]} In 1782 Franz-Joseph Müller von Reichenstein, who was then serving as the Austrian chief inspector of mines in Transylvania, concluded that the ore did not contain antimony but was bismuth sulphide.^[5] The following year, he reported that this was erroneous and that the ore contained mostly gold and an unknown metal very similar to antimony.

After a thorough investigation that lasted three years and included more than fifty tests, Müller determined the specific gravity of the mineral and noted that when heated, the new metal gives off a white smoke with a radish-like odor; that it imparts a red color to sulphuric acid; and that when this solution is diluted with water, it has a black precipitate. Nevertheless, he was not able to identify this metal and gave it the names aurum paradoxum (paradoxical gold) and metallum problematicum (problem metal), because it did not exhibit the properties predicted for antimony.^{[6][7][8]}

In 1789, a Hungarian scientist, Pál Kitaibel, discovered the element independently in an ore from Deutsch-Pilsen that had been regarded as argentiferous molybdenite, but later he gave the credit to Müller. In 1798, it was named by Martin Heinrich Klaproth, who had earlier isolated it from the mineral calaverite.^{[9][10][11][12]} The 1960s brought an increase in thermoelectric applications for tellurium (as bismuth telluride), and in free machining steel alloys, which became the dominant use.^[13]

1.1.2. Characteristics

1.1.2.1. Physical properties

Tellurium has two allotropes, crystalline and amorphous. When crystalline, tellurium is silvery-white with a metallic luster. It is a brittle and easily pulverized metalloid. Amorphous tellurium is a black-brown powder prepared by precipitating it from a solution of tellurous acid or telluric acid ($\text{Te}(\text{OH})_6$).^[14] Tellurium is a semiconductor that shows a greater electrical conductivity in certain directions depending on atomic alignment; the conductivity increases slightly when exposed to light (photoconductivity).^[15] When molten, tellurium is corrosive to copper, iron, and stainless steel. Of the chalcogens (oxygen-family elements), tellurium has the highest melting and boiling points, at 722.66 K (841.12 °F) and 1,261 K (1,810 °F), respectively.^[16]

1.1.2.2. Chemical properties

Tellurium adopts a polymeric structure consisting of zig-zag chains of Te atoms. This gray material resists oxidation by air and is not volatile.

1.1.2.3. Isotopes

Naturally occurring tellurium has eight isotopes. Six of those isotopes, ^{120}Te , ^{122}Te , ^{123}Te , ^{124}Te , ^{125}Te , and ^{126}Te , are stable. The other two, ^{128}Te and ^{130}Te , have been found to be slightly radioactive,^{[17][18][19]} with extremely long half-lives, including 2.2×10^{24} years for ^{128}Te . This is the longest known half-life among all radionuclides^[20] and is about 160 trillion (10^{12}) times the age of the known universe. Stable isotopes comprise only 33.2% of naturally occurring tellurium.

A further 31 artificial radioisotopes of tellurium are known, with atomic masses ranging from 104 to 142 and with half-lives of 19 days or less. Also, 17 nuclear isomers are known, with half-lives up to 154 days. With the exception of beryllium-8 and beta-delayed alpha emission branches in some lighter nuclides, tellurium (^{104}Te to ^{109}Te) is the lightest element with isotopes known to undergo alpha decay.^[21] The atomic mass of tellurium ($127.60 \text{ g}\cdot\text{mol}^{-1}$) exceeds that of iodine ($126.90 \text{ g}\cdot\text{mol}^{-1}$), the next element in the periodic table.^[22] Tellurium is believed to have been depleted from the crust during the formation of the planet due to its volatile reaction with hydrogen.

It is sometimes found in its natural form, but is more often found with gold or other metals in mineral forms. It is typically produced from the sludge by product of copper refining.

1.1.2.4. Occurrence

1.1.2.4.1. Telluride mineral



Figure 1.2. Silver Telluride Ore

With abundance in the Earth's crust comparable to that of platinum (about $1 \mu\text{g/kg}$), tellurium is one of the rarest stable solid elements.^[23] In comparison, even the rarest of the stable lanthanides have crustal abundances of $500 \mu\text{g/kg}$ (see Abundance of the chemical elements).^[24] This rarity of tellurium in the Earth's crust is not a reflection of its cosmic abundance. Tellurium is more abundant than rubidium in the cosmos, though rubidium is 10,000 times more abundant in the Earth's crust. The rarity of tellurium on Earth is thought to be caused by conditions during preaccretional sorting in the solar nebula, when the stable form of certain elements, in the absence of oxygen and water, was controlled by the reductive power of free hydrogen.

Under this scenario, certain elements that form volatile hydrides, such as tellurium, were severely depleted through evaporation of these hydrides. Tellurium and selenium are the heavy elements most depleted by this process.^[25] Tellurium is sometimes found in its native (i.e., elemental) form, but is more often found as the tellurides of gold such as calaverite and krennerite (two different polymorphs of AuTe_2), petzite, Ag_3AuTe_2 , and sylvanite, AgAuTe_4 . The city of Telluride, Colorado, was named in hope of a strike of gold telluride (which never materialized, though gold metal ore was found). Gold itself is usually found uncombined, but when found as a chemical compound, it is most often combined with tellurium.

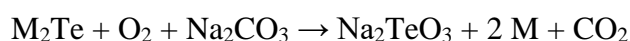
Although tellurium is found with gold more often than in uncombined form, it is found even more often combined as tellurides of more common metals (e.g. melonite, NiTe_2). Natural tellurite and tellurate minerals also occur, formed by oxidation of tellurides near the Earth's surface. In contrast to selenium, tellurium does not usually replace sulfur in minerals

because of the great difference in ion radii. Thus, many common sulphide minerals contain substantial quantities of selenium and only traces of tellurium.^[26]

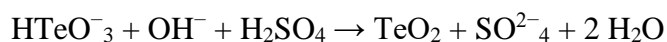
In the gold rush of 1893, miners in Kalgoorlie discarded a pyritic material as they searched for pure gold, and it was used to fill in potholes and build sidewalks. In 1896, that tailing was discovered to be calaverite, a telluride of gold, and it sparked a second gold rush that included mining the streets.^[27]

1.1.3. Production

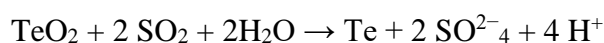
The principal source of tellurium is from anode sludges from the electrolytic refining of blister copper. It is a component of dusts from blast furnace refining of lead. Treatment of 1000 tons of copper ore typically yields one kilogram (2.2 pounds) of tellurium. The anode sludges contain the selenides and tellurides of the noble metals in compounds with the formula M_2Se or M_2Te ($M = Cu, Ag, Au$). At temperatures of 500 °C the anode sludges are roasted with sodium carbonate under air. The metal ions are reduced to the metals, while the telluride is converted to sodium tellurite.^[28]



Tellurites can be leached from the mixture with water and are normally present as hydrotellurites $HTeO_3^-$ in solution. Selenites are also formed during this process, but they can be separated by adding sulphuric acid. The hydrotellurites are converted into the insoluble tellurium dioxide while the selenites stay in solution.^[29]



The metal is produced from the oxide (reduced) either by electrolysis or by reacting the tellurium dioxide with sulphur dioxide in sulphuric acid.^[30]



Commercial-grade tellurium is usually marketed as 200-mesh powder but is also available as slabs, ingots, sticks, or lumps. The year-end price for tellurium in 2000 was US\$14 per pound. In recent years, the tellurium price was driven up by increased demand and limited supply, reaching as high as US\$100 per pound in 2006.^{[31][32]} Despite the expectation that improved production methods will double production, the United States Department of Energy (DoE) anticipates a supply shortfall of tellurium by 2025.^[33] Tellurium is produced mainly in the United States, Peru, Japan and Canada.^[34] The British Geological Survey gives the following production numbers for 2009: United States 50 t, Peru 7 t, Japan 40 t and Canada 16 t.^[35]

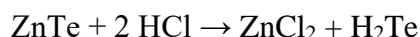
1.1.4. Compounds

1.1.4.1. Tellurium compounds and Telluride minerals

Tellurium belongs to the chalcogen (group 16) family of elements on the periodic table, which also includes oxygen, sulfur, selenium and polonium: Tellurium and selenium compounds are similar. Tellurium exhibits the oxidation states -2 , $+2$, $+4$ and $+6$, with $+4$ being most common.^[9]

1.1.4.2. Tellurides

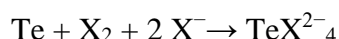
Reduction of Te metal produces the tellurides and polytellurides, Te_n^{2-} . The -2 oxidation state is exhibited in binary compounds with many metals, such as zinc telluride, ZnTe , produced by heating tellurium with zinc.^[36] Decomposition of ZnTe with hydrochloric acid yields hydrogen telluride (H_2Te), a highly unstable analogue of the other chalcogen hydrides, H_2O , H_2S and H_2Se :



H_2Te is unstable, whereas salts of its conjugate base $[\text{TeH}]^-$ are stable.

1.1.4.3. Halides

The $+2$ oxidation state is exhibited by the dihalides, TeCl_2 , TeBr_2 and TeI_2 . The dihalides have not been obtained in pure form,^{[37]:274} although they are known decomposition products of the tetrahalides in organic solvents, and the derived tetrahalotellurates are well-characterized:



where X is Cl, Br, or I. These anions are square planar in geometry.^{[37]:281} Polynuclear anionic species also exist, such as the dark brown $\text{Te}_2\text{I}_6^{2-}$,^{[37]:283} and the black $\text{Te}_4\text{I}_{14}^{2-}$.^{[37]:285} Fluorine forms two halides with tellurium: the mixed-valence Te_2F_4 and TeF_6 . In the $+6$ oxidation state^[38] the square antiprismatic anion TeF_6^{2-} is also attested.^[30] The other halogens do not form halides with tellurium in the $+6$ oxidation state, but only tetrahalides (TeCl_4 , TeBr_4 and TeI_4) in the $+4$ state, and other lower halides (Te_3Cl_2 , Te_2Cl_2 , Te_2Br_2 , Te_2I and two forms of TeI). In the $+4$ oxidation state, halotellurate anions are known, such as TeCl_6^{2-} and $\text{Te}_2\text{Cl}_{10}^{2-}$. Halotellurium cations are also attested, including TeI^+ , found in TeI_3AsF_6 .^[39]

1.1.4.4. Oxo compounds

Tellurium monoxide was first reported in 1883 as a black amorphous solid formed by the heat decomposition of TeSO_3 in vacuum, disproportionating into tellurium

dioxide, TeO_2 and elemental tellurium upon heating.^{[40][41]} Since then, however, existence in the solid phase is doubted and in dispute, although it is known as a vapor fragment; the black solid may be merely an equimolar mixture of elemental tellurium and tellurium dioxide.^[42]



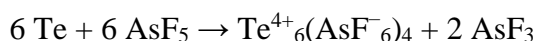
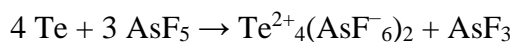
Figure 1.3 A sample of tellurium dioxide powder

Tellurium dioxide is formed by heating tellurium in air, where it burns with a blue flame.^[36] Tellurium trioxide, $\beta\text{-TeO}_3$, is obtained by thermal decomposition of $\text{Te}(\text{OH})_6$. The other two forms of trioxide reported in the literature, the α - and γ - forms, were found not to be true oxides of tellurium in the +6 oxidation state, but a mixture of Te^{4+} , OH^- and O^{2-} .^[43]

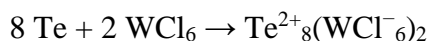
Tellurium also exhibits mixed-valence oxides, Te_2O_5 and Te_4O_9 .^[43] The tellurium oxides and hydrated oxides form a series of acids, including tellurous acid (H_2TeO_3), orthotelluric acid ($\text{Te}(\text{OH})_6$) and metatelluric acid ($((\text{H}_2\text{TeO}_4)_n)$).^[42] The two forms of telluric acid form tellurate salts containing the TeO_4^{2-} and TeO_6^{4-} anions, respectively. Tellurous acid forms tellurite salts containing the anion TeO_3^{2-} .

1.1.4.5. Zintl cations

When tellurium is treated with concentrated sulphuric acid, the result is a red solution of the Zintl ion, Te^{2+}_4 .^[44] The oxidation of tellurium by AsF_5 in liquid SO_2 produces the same square planar cation, in addition to the trigonal prismatic, yellow-orange Te^{4+}_6 .^[30]



Other tellurium Zintl cations include the polymeric Te^{2+}_7 and the blue-black Te^{2+}_8 , consisting of two fused 5-membered tellurium rings. The latter cation is formed by the reaction of tellurium with tungsten hexachloride.^[30]



Inter chalcogen cations also exist, such as $\text{Te}_2\text{Se}^{2+}_6$ (distorted cubic geometry) and $\text{Te}_2\text{Se}^{2+}_8$. These are formed by oxidizing mixtures of tellurium and selenium with AsF_5 or SbF_5 .^[30]

1.1.4.6. Organotellurium compounds

Tellurium does not readily form analogues of alcohols and thiols, with the functional group -TeH , that are called tellurols. The -TeH functional group is also attributed using the prefix tellanyl-.^[45] Like H_2Te , these species are unstable with respect to loss of hydrogen. Telluraethers (R-Te-R) are more stable, as are telluroxides.

1.1.4.7. Tellurite ion

The tellurite ion is TeO_3^{2-} . A tellurite (compound), for example sodium tellurite, is a compound that contains this ion. They are typically colorless or white salts, which in some ways are comparable to sulphite.^[46] A mineral with the formula TeO_2 is called tellurite.

1.1.4.7.1. Structure and reaction

Tellurite dianion is pyramidal, like selenite and sulphite. The anion has C_{3v} symmetry. Tellurites can be reduced to elemental tellurium by electrolysis or a strong reducing agent. When fused with nitrate salts, tellurite salts oxidize to tellurates (TeO_4^{2-}). Upon acidification of aqueous solutions of tellurite salts, solid hydrated tellurium dioxide (TeO_2) precipitates. This reaction allows the separation of tellurium from selenium since selenous acid remains soluble at low pH. The intermediate in the protonation occurs at oxygen to give $[\text{TeO}_2(\text{OH})]^-$.

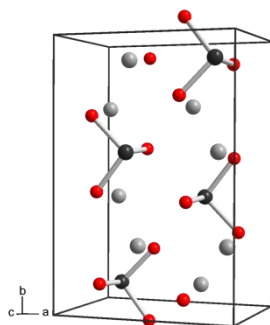


Figure 1.4 Crystal structure of sodium tellurite, highlighting the pyramidal structure of the anion.

1.1.5. Application

1.1.5.1. Metallurgy

The largest consumer of tellurium is metallurgy in iron, stainless steel, copper, and lead alloys. The addition to steel and copper produces an alloy more machinable than otherwise. It is alloyed into cast iron for promoting chill for spectroscopy, where the presence of electrically conductive free graphite tends to interfere with spark emission testing results. In lead, tellurium improves strength and durability, and decreases the corrosive action of sulfuric acid.^{[29][46]}

1.1.5.2. Semiconductor and electronic industry uses



Figure 1.5 A CdTe photovoltaic array

Tellurium is used in cadmium telluride (CdTe) solar panels. National Renewable Energy Laboratory lab tests of tellurium demonstrated some of the greatest efficiencies for solar cell electric power generators. Massive commercial production of CdTe solar panels by First Solar in recent years has significantly increased tellurium demand.^{[47][48][49]} Replacing some of the cadmium in CdTe with zinc, producing (Cd,Zn)Te, produces a solid-state X-ray detector, providing an alternative to single-use film badges.^[50]

Infrared sensitive semiconductor material is formed by alloying tellurium with cadmium and mercury to form mercury cadmium telluride.^[51]

Organotellurium compounds such as dimethyl telluride, diethyl telluride, diisopropyl telluride, diallyl telluride and methyl allyl telluride are precursors for synthesizing metalorganic vapor phase epitaxy growth of II-VI compound semiconductors.^[52] Diisopropyl telluride (DIPTe) is the preferred precursor for low-temperature growth of CdHgTe by MOVPE.^[53] The greatest purity metalorganics of both selenium and tellurium are used in these processes. The compounds for semiconductor industry and are prepared by adduct purification.^{[54][55]}

Tellurium, as tellurium suboxide, is used in the media layer of rewritable optical discs, including ReWritable Compact Discs (CD-RW), ReWritable Digital Video Discs (DVD-RW), and ReWritable Blu-ray Discs.^{[56][57]} Tellurium dioxide is used to create acousto-optic modulators (AOTFs and AOBs) for confocal microscopy. Tellurium is used in the new phase change memory chips^[58] developed by Intel.^[59] Bismuth telluride (Bi_2Te_3) and lead telluride are working elements of thermoelectric devices. Lead telluride is used in far-infrared detectors.

1.1.5.3. Photocathodes

Tellurium shows up in a number of popular photocathodes used in solar blind photomultiplier tubes^[60] and for high brightness photo injectors driving modern particle accelerators. The photocathode Cs-Te, which is predominantly Cs_2Te , has a photoemission threshold of 3.5 eV and exhibits the uncommon combination of high quantum efficiency

(>10%) and high durability in poor vacuum environments (lasting for months under use in RF electron guns).^[61] This has made it the go to choice for photoemission electron guns used in driving free electron lasers.^[62] In this application, it is usually driven at the wavelength 267 nm which is the third harmonic of commonly used Ti-sapphire lasers. More Te containing photocathodes have been grown using other alkali metals such as rubidium, Potassium, and Sodium, but they have not found the same popularity that Cs-Te has enjoyed.^{[63][64]}

1.1.5.4. Other uses

- ❖ Tellurium compounds are used as pigments for ceramics.^[65]
- ❖ Selenides and tellurides greatly increase the optical refraction of glass widely used in glass optical fibers for telecommunications.^{[66][67]}
- ❖ Mixtures of selenium and tellurium are used with barium peroxide as an oxidizer in the delay powder of electric blasting caps.^[68]
- ❖ Organic tellurides have been employed as initiators for living radical polymerization and electron-rich mono- and di-tellurides possess antioxidant activity.
- ❖ The tellurium compounds are used widely in synthetic organic chemistry for reduction- and oxidation-, cyclofunctionalization-, dehalogenation-, carbanion generation reactions and removal of protecting groups.^[69]
- ❖ The organometallic compounds are intermediates in the synthesis of amines, diols, and natural products.^[70]
- ❖ Rubber can be vulcanized with tellurium instead of sulphur or selenium. The rubber produced in this way shows improved heat resistance.^[71]
- ❖ Tellurite agar is used to identify members of the corynebacterium genus, most typically *Corynebacterium diphtheriae*, the pathogen responsible for diphtheria.^[72]
- ❖ Tellurium is a key constituent of high performing mixed oxide catalysts for the heterogeneous catalytic selective oxidation of propane to acrylic acid.^{[73][74]} The surface elemental composition changes dynamically and reversibly with the reaction conditions. In the presence of steam the surface of the catalyst is enriched in tellurium and vanadium which enhances the acrylic acid production.^{[75][76]}
- ❖ Neutron bombardment of tellurium is the most common way to produce iodine-131.^[77] This in turn is used to treat some thyroid conditions, and as a tracer compound in hydraulic fracturing, among other applications.
- ❖ Biological Role

- ❖ Tellurium has no known biological function, although fungi can incorporate it in place of sulfur and selenium into amino acids such as telluro-cysteine and telluro-methionine.^{[81][78]} Organisms have shown a highly variable tolerance to tellurium compounds.
- ❖ Many bacteria, such as *Pseudomonas aeruginosa*, take up tellurite and reduce it to elemental tellurium, which accumulates and causes a characteristic and often dramatic darkening of cells.^[79] In yeast, this reduction is mediated by the sulphate assimilation pathway.^[80]
- ❖ Tellurium accumulation seems to account for a major part of the toxicity effects. Many organisms also metabolize tellurium partly to form dimethyl telluride, although dimethyl ditelluride is also formed by some species. Dimethyl telluride has been observed in hot springs at very low concentrations.^{[81][82]}

1.1.6. Precautions

Tellurium and tellurium compounds are considered to be mildly toxic and need to be handled with care, although acute poisoning is rare.^[85] Tellurium poisoning is particularly difficult to treat as many chelation agents used in the treatment of metal poisoning will increase the toxicity of tellurium. Tellurium is not reported to be carcinogenic.^[85] Humans exposed to as little as 0.01 mg/m³ or less in air exude a foul garlic-like odor known as "tellurium breath".^{[65][86]} This is caused by the body converting tellurium from any oxidation state to dimethyl telluride, (CH₃)₂Te. This is a volatile compound with a pungent garlic-like smell. Even though the metabolic pathways of tellurium are not known, it is generally assumed that they resemble those of the more extensively studied selenium because the final methylated metabolic products of the two elements are similar.^{[87][88][89]}

People can be exposed to tellurium in the workplace by inhalation, ingestion, skin contact, and eye contact. The Occupational Safety and Health Administration (OSHA) limits (permissible exposure limit) tellurium exposure in the workplace to 0.1 mg/m³ over an eight-hour workday. The National Institute for Occupational Safety and Health (NIOSH) has set the recommended exposure limit (REL) at 0.1 mg/m³ over an eight-hour workday. In concentrations of 25 mg/m³, tellurium is immediately dangerous to life and health.^[90]



CHAPTER – 2

REVIEW OF LITERATURE

2. REVIEW OF LITERATURE

- *Raja Azadar Hussaina and Iqtadar Hussain et. al* has reported that Metal tellurides have been explored extensively just like their sulfide and selenide cousins due to their surface chemistry, quantum confinement and physical properties. Nanotubular metal tellurides are more promising in terms of their unique physics and chemistry. This review article presents synthesis of metal telluride nanotubes via hydro/solvothermal methods, electrochemical methods, chemical methods, microwave methods and combination processes. Thermoelectric applications, electrocatalytic activities for water oxidation and supercapacitive behavior of metal telluride nanotubes have also been discussed and compared with other materials.

- *Y. Hayashibe*, in Encyclopedia of Analytical Science has reported that minute amounts of Pd can be co-precipitated with elemental tellurium obtained by reduction of a tellurite with tin(II) chloride or similar strong reducing agents. The slight solubility of Pd(II) dimethylglyoximate and other dioximates in dilute HCl solution enables fairly small amounts of Pd to be separated from most other metals except Au (Pt tends to contaminate Pd dimethylglyoximate). Such precipitation fails at the low Pd concentrations frequently encountered, but $<1 \text{ mg l}^{-1}$ of Pd can be co-precipitated with Ni dimethylglyoximate from a solution (pH 6.5) containing tartrate, $(\text{NH}_3\text{OH})\text{Cl}$, and acetate. Pd can be separated from large amounts of Fe, Ni, and Cu on a strongly basic anion-exchange resin at pH ~ 1.5 ; the chloro complexes of Pd, Pt, Rh, and Ir pass through the column. Chloroform extraction of Pd(II) dimethylglyoximate provides the most selective separation of Pd from other elements. This extraction has not been systematically studied, but it is known that Pd can be quantitatively extracted from $0.2\text{--}0.3 \text{ mol l}^{-1}$ HCl or $\sim 0.5 \text{ mol l}^{-1}$ H_2SO_4 solutions. Fe(III) is reported to hinder the extraction of Pd. Extraction with IBMK from $\sim 7.5 \text{ mol l}^{-1}$ HCl removes Fe(III), Mo(VI), etc.

- *Mostafa M., Abo Elsouda Ola E.A., Al-Hagarb Eman S., Abdelkhalek N. and M.Sidkey et.al* has reported that Tellurium has attracted the attention of many researchers and manufacturers due to its unique properties. Through the current work,

six fungal isolates were screened for their ability to reduce potassium tellurite (K_2TeO_3) into elemental tellurium nanoparticles (TeNPs). The most promising fungal isolate was identified as *Aspergillus welwitschiae* and given the accession number (KY766958) based on molecular basis and has been used for biogenic (enzymatic) production of TeNPs. The produced TeNPs were characterized using DLS, TEM and FTIR. Data showed that, the particle size is 60.80 nm with oval to spherical shape. The produced TeNPs have been evaluated for antimicrobial activity at 25 mg/ml. Data revealed antibacterial activity against *E. coli* and *Staphylococcus aureus* (MRSA). Evaluation of the effect of γ -irradiation on TeNPs production showed that, the productivity was improved at 1 kGy and suppressed gradually at higher doses.

- *Tamires Martinhão, Machado, Maurício Antoni, Pereira da Silva et al.* was reported that In this work, the synthesis and structural and spectroscopy properties of glasses of the $\text{NaPO}_3\text{--Sb}_2\text{O}_3\text{--TeO}_2$ system were investigated. Tellurium particles were obtained through the reduction action of antimony oxide when heated, via the $\text{Sb}_2\text{O}_3 \rightarrow \text{Sb}_2\text{O}_4$ phase transition during the production of glasses. Heat treatment of the glasses also leads to tellurium particles formation. The reduction of Te^{4+} to Te^0 process could be observed through Raman Spectroscopy, Scanning Electronic Microscopy images and Differential Scanning Calorimetry curves. The higher Sb_2O_3 concentration, the larger Te amount produced, while permanent changes of refraction index occur owing to metal – glass interface effect by the optical response of Te particles. The proposal approached in this work reveals a research field, which deserves attention according to the possibility of obtainment of new vitreous compounds containing a great variety of particles (metal-glass composites).
- *Kevin M. Kubachka, Joseph A. Caruso et al (2008)* Tellurium is similar to selenium in terms of its toxicity, as Te^{IV} is 10 times more toxic than Te^{VI} . [141] Tellurium is commonly used in electronics, metallurgy, and pharmaceuticals [141]. Little research has been presented using HPLC-ICP-MS to separate both species simultaneously. Two such methods have been used to detect only Te^{IV} using HPLC-IC. One method by Viñas *et al.* involves complexing the tellurium species with 50 mM citric acid. Speciation is then carried out using a PRP-X100 column with 8 mM EDTA and 2 mM potassium hydrogen phthalate as a mobile phase. The separation is less than 8 min, with atomic fluorescence spectrometry used as the detection method; it is feasible that

ICP-MS could easily be substituted. Detection limits were $0.69 \mu\text{gTe L}^{-1}$ and $0.76 \mu\text{gTe L}^{-1}$ for Te^{VI} and Te^{IV} , respectively.

- *Koji Maeda, et al (2019)* Tellurium is a precursor of iodine. TeO_2 cannot be formed because the oxygen potential of the Te/TeO_2 system is much higher than that in the fuel. Formation energy of stable Cs_2Te appears to be approximately 376 kJ mol^{-1} , which is just enough for Cs_2Te to be stable at the conditions in the fuel. Cs_2Te showed an appreciable volatility at the conditions in a fuel.⁹² The vapor pressure of Cs_2Te is about 10^{-4} atm at 727°C , which means that an appreciable amount of tellurium is already present as Cs_2Te in the gap at normal operating conditions of the fuel pins. If gas-phase transport is the main path for FPs to reach the fuel surface, as has been stated,⁹³ it is important to know the vapor pressure of Cs_2Te . Pure tellurium showed marked penetration in stainless steel up to depths comparable with those observed in irradiated fuel pins at temperatures below 800°C . Furthermore, out-of-pile experiments showed that the reaction of tellurium does not depend on the oxygen potential unlike in the case of cesium.⁹⁴ The reactions with tellurium are clearly functions of irradiation period and temperature. Götzmann and Hofmann⁹⁵ determined the maximum penetration depths of tellurium in stainless steels as a function of the temperature and annealing period. At 500 and 700°C , attack occurred along the grain boundaries of the cladding. Below 500°C a uniform attack was observed, and tellurium migrated into the cladding by interfacial reactions. Above 700°C , the penetration depths of tellurium were dependent on the grain size of the cladding material. The maximum penetration depth of tellurium was greater in coarse grains than in fine grains. When the oxygen potential $\Delta G_{\text{O}_2}^-$ is approximately 376 kJ mol^{-1} , Cs_2Te is stable in the fuel. When the oxygen potential reaches a sufficiently high level ($>418 \text{ kJ mol}^{-1}$), Cs_2Te becomes less stable than cesium molybdate or urinate.⁹⁶ Cs_2Te can attack the cladding by reaction with the cladding constituents, forming cesium chromate, iron telluride, and nickel telluride. Because of the dissolution of the cladding materials into Te, the cladding constituents diffuse into the fuel even at temperatures as low as 400°C . In contrast, tellurium diffuses into the cladding material and is found at the reaction front together with Cr.⁹⁶ However, the highly localized concentration of tellurium required for cladding attack in FR fuel pins appears to be inconsistent with the postirradiation investigations of numerous cladding attack regions in which tellurium has not been detected.^{37,39,40,46} The role of

tellurium in cladding attack is largely based on results from out-of-pile tests^{38,40,61,94,97–103} in which the average tellurium content per unit area of cladding inner surface was much greater than that encountered in irradiation tests.

- *H. Palme, H.St.C. O'Neill et al* ,(2007) Tellurium is chalcophile (Hattori *et al.*, 2002), but is not correlated with other chalcophile elements, or anything else. Empirically, tellurium appears to be quite compatible. Morgan (1986) found 12.4 ± 3 ppb for fertile spinel-lherzolite xenoliths (previously published in BVSP), mainly from Kilbourne Hole, with somewhat lower values for more depleted samples. Yi *et al.* (2000) found 1–7 ppb for MORB, most OIB and submarine IAB, but with samples from Loihi extending to 29 ppb. These MORB data confirm the earlier data of Hertogen *et al.* (1980), who analyzed five MORBs with tellurium from 1 to 5 ppb, and two outliers with 17 ppb, which also had elevated selenium. The important point is that tellurium in peridotites is often higher than in basalts, plausibly explained by retention in a residual sulfide phase. Thus, future work on tellurium needs to address the composition of mantle sulfides. If Te/S were chondritic, the PM with 200 ppm S would have 8 ppb Te. We have adopted this as the default value, as to use anything else would have interesting but unwarranted cosmochemical implications.
- *Zygmunt Marczenko, Maria Balcerzak, et al* ,(2000) Tellurium(IV) has been separated from large amounts of Se(IV) by sorption of the Te(IV) complex in 6 M HCl on a strongly basic anion exchanger .Tellurium can be separated from many metals on a strongly basic anion- exchanger by using a cone, aqueous LiCl medium .Strongly acid cation-exchangers retain Te from a 0.3 M HCl medium, whereas Se is not sorbed. Mixtures of Te and Se were separated on Dowex 50W-X8 cation-exchanger from a mixed medium containing formic acid, methyl ethyl ketone, and 50% methanol.Tellurium(IV) can be separated from Te(VI), Se(IV) and Se(VI) on a diethylaminocellulose column, using 1 M hydrochloric acid - glacial acetic acid (1+9) mixture as eluent .Tellurium (and Se) has also sorbed on a polyurethane foam .Tellurium has been separated as bromide by distillation from cone, phosphoric acid at about 300°C .

- *S.C. Gad, T. Pham, et al,(2014)*, Exposure and Exposure Monitoring Tellurium is ingested with foods such as nuts, fish, and certain dairy products. Many fatty foods contain tellurium, and some plants, like garlic, accumulate tellurium from the soil. Neither drinking water nor ambient air contains significant amounts of tellurium. Skin contact is not a significant exposure pathway. In industrial settings, inhalation may be a significant exposure pathway. Airborne concentrations of tellurium are higher than the vicinity of metallurgical industries. Like selenium, tellurium is obtained as a by-product of copper, lead, and zinc refining. It is produced mainly from the tailings of bismuth.
- *Hiroyuki Tetsuka , Yue Jin Shan, Keitaro Tezuka, Hideo Imoto et al,(2005)* Polycrystalline $\text{Cd}_{3xy}\text{Cu}_x\text{AyTeO}_6$ ($A = \text{Li, Na}$) samples were prepared by solid-state reaction, and their crystal structure and electrical properties were investigated. In $\text{Cd}_{3x}\text{Cu}_x\text{TeO}_6$ and $\text{Cd}_{3y}\text{AyTeO}_6$ ($A = \text{Li, Na}$), the maximum solubility of x and y was 0.15 and 0.15 for $A = \text{Li}$, 0.05 for $A = \text{Na}$, respectively. For co-substituted samples $\text{Cd}_{2.9y}\text{Cu}_{0.1}\text{Li}_y\text{TeO}_6$ and $\text{Cd}_{2.9y}\text{Cu}_{0.1}\text{Na}_y\text{TeO}_6$, the maximum solubility of x was the same as single substitution above-mentioned. The alkali-metal substituted samples $\text{Cd}_{3y}\text{AyTeO}_6$ ($A = \text{Li, Na}$) showed a negative Seebeck coefficient, which indicates that the major conduction carriers are electron. On the other hand, the co-substituted samples $\text{Cd}_{2.9y}\text{Cu}_{0.1}\text{AyTeO}_6$ ($A = \text{Li, Na}$) represented a positive Seebeck coefficient, and major conduction carriers were hole through substitution by copper ion.
- *Sujan Dhungana , Bhoj Raj Poudel, & Surendra K. Gautam et al*, In this work, we report the ZnTe semiconductor nanoparticles (NPs) prepared by aqueous chemical precipitation method using the tellurium precursor solution with different zinc compounds. Three batches of ZnTe NPs were synthesized to study the effect of dilution on the size and phase purity of ZnTe. The influence of source compounds and concentrations of the size and structure of NPs were studied. ZnTe NPs have great applications as field-effect transistors and photodetectors. The existing controversy regarding the crystalline structure of ZnTe NPs, whether it is cubic or hexagonal, has been resolved using X-ray Diffraction (XRD) data. The ZnTe NPs possess cubic structure, which is also confirmed by Electron Diffraction (ED) pattern. The average particle size determined from XRD data with the help of Debye-Scherrer equation is about 6 nm. The particle size can be further verified by Transmission Electron Microscopy (TEM) studies.

- *Eman Abdul Rahman Assirey et al*, The perovskite structure is shown to be the single most versatile ceramic host. Inorganic perovskite type oxides are attractive compounds for varied applications due to its large number of compounds, they exhibit both physical and biochemical characteristics and their Nano-formulation have been utilized as catalysts in many reaction due to their sensitivity, unique long-term stability and anti-interference ability. Some perovskites materials are very hopeful applicants for the improvement of effective anodic catalysts performance. Depending Perovskite-phase metal oxides distinct variety of properties they became useful for various applications they are newly used in electrochemical sensing of alcohols, glucose, hydrogen peroxide, gases, and neurotransmitters. Perovskite organometallic halide showed efficient essential properties for photovoltaic solar cells. This review presents a full coverage of the structure, progress of perovskites and their related applications. Stress is focused particularly to different methods of perovskites properties and there related application.

CHAPTER – 3

SCOPE OF THE WORK

3.1 SCOPE OF THE WORK

With abundance in the Earth's crust comparable to that of platinum (about 1 $\mu\text{g/kg}$), tellurium is one of the rarest stable solid elements.^[23] In comparison, even the rarest of the stable lanthanides have crustal abundances of 500 $\mu\text{g/kg}$ (see Abundance of the chemical elements).^[24] This rarity of tellurium in the Earth's crust is not a reflection of its cosmic abundance. Tellurium is more abundant than rubidium in the cosmos, though rubidium is 10,000 times more abundant in the Earth's crust. The rarity of tellurium on Earth is thought to be caused by conditions during preaccretionary sorting in the solar nebula, when the stable form of certain elements, in the absence of oxygen and water, was controlled by the reductive power of free hydrogen.

Tellurium is used in cadmium telluride (CdTe) solar panels. National Renewable Energy Laboratory lab tests of tellurium demonstrated some of the greatest efficiencies for solar cell electric power generators. Massive commercial production of CdTe solar panels by First Solar in recent years has significantly increased tellurium demand.^{[47][48][49]} Replacing some of the cadmium in CdTe with zinc, producing (Cd,Zn)Te, produces a solid-state X-ray detector, providing an alternative to single-use film badges.^[50] Infrared sensitive semiconductor material is formed by alloying tellurium with cadmium and mercury to form mercury cadmium telluride.

Tellurium has no known biological function, although fungi can incorporate it in place of sulfur and selenium into amino acids such as telluro-cysteine and telluro-methionine.^{[8][78]} Organisms have shown a highly variable tolerance to tellurium compounds. Many bacteria, such as *Pseudomonas aeruginosa*, take up tellurite and reduce it to elemental tellurium, which accumulates and causes a characteristic and often dramatic darkening of cells.^[79] In yeast, this reduction is mediated by the sulphate assimilation pathway.^[80]

Tellurium accumulation seems to account for a major part of the toxicity effects. Many organisms also metabolize tellurium partly to form dimethyl telluride, although dimethyl ditelluride is also formed by some species. Dimethyl telluride has been observed in hot springs at very low concentrations.^{[81][82]}

3.2 OBJECTIVES

Zirconium Telluride and Cadmium Telluride nanoparticles are prepared by chemical synthesis.

- To study the optical properties by using UV – Visible Spectrometer.
- To identify the various stretching frequencies and bonding within the nanocomposites using Fourier Transform - Infra Red Spectroscopy.
- To determine the surface morphology and size of the particles using Scanning Electron Microscope.
- To find out particle size and shape of the crystal using X-Ray Diffraction studies.
- To confirm the elements present in the synthesized nanoparticles using Energy Dispersive X- Ray Spectroscopy.

CHAPTER – 4

MATERIALS AND METHODS

MATERIALS AND METHODS

4.1 MATERIALS

<p>POTASSIUM TELLURITE</p>	
<p>HYDRAZINE HYDRO CHLORIDE</p>	
<p>ZIRCONIUM OXYCHLORIDE</p>	
<p>CADMIUM CHLORIDE</p>	

4.2 METHODS

4.2.1 PREPARATION OF ZIRCONIUM TELLURIDE

4.2.1.1 CHEMICALS REQUIRED

Potassium Tellurite	– 2g
Hydrazine Hydrochloride	– 2g
Zirconium Oxychloride	– 2g

4.2.1.2 PROCEDURE

2g of potassium tellurite and 2g of hydrazine hydrochloride was weighed and dissolved in 200 ml of double distilled water and stirred in a magnetic stirrer for about 20 minutes. After stirring process 2g of zirconium oxychloride was weighed and added to the mixture and then it was stirred in a magnetic stirrer for half an hour at room temperature. Then it was kept in oven and the temperature was maintained at 90°C for about 3 hours. It was cooled at room temperature and then it was filtered, dried and purified with ethanol.

4.2.2 PREPARATION OF CADMIUM TELLURIDE

4.2.2.1 CHEMICALS REQUIRED

Potassium Tellurite	– 2g
Hydrazine Hydrochloride	– 2g
Cadmium chloride	– 2g

4.2.2.2 PROCEDURE

2g of potassium tellurite and 2g of hydrazine hydrochloride was weighed and dissolved in 200 ml of double distilled water and stirred in a magnetic stirrer for about 20 minutes. After stirring process 2g of cadmium chloride was weighed and added to the mixture and then it was stirred in a magnetic stirrer for half an hour at room temperature. Then it was kept in oven and the temperature was maintained at 90°C for about 3 hours. It was cooled at room temperature and then it was filtered, dried and purified with ethanol.

4.3 INSTRUMENTATION

4.3.1. Ultraviolet–visible spectroscopy or ultraviolet–visible spectrophotometry

It refers to absorption spectroscopy or reflectance spectroscopy in part of the ultraviolet and the full, adjacent visible spectral regions. This means it uses light in the visible and adjacent ranges. The absorption or reflectance in the visible range directly affects the perceived color of the chemicals involved. In this region of the electromagnetic

spectrum, atoms and molecules undergo electronic transitions. Absorption spectroscopy is complementary to fluorescence spectroscopy, in that fluorescence deals with transitions from the excited state to the ground state, while absorption measures transitions from the ground state to the excited state.^[91]



Fig : 4.3.1.1 schematic representation of UV – Visible spectrometer

4.3.1.1. Principle

Molecules containing bonding and non-bonding electrons (n-electrons) can absorb energy in the form of ultraviolet or visible light to excite these electrons to higher anti-bonding molecular orbitals.^[92] The more easily excited the electrons (i.e. lower energy gap between the HOMO and the LUMO), the longer the wavelength of light it can absorb. There are four possible types of transitions ($\pi\text{--}\pi^*$, $n\text{--}\pi^*$, $\sigma\text{--}\sigma^*$, and $n\text{--}\sigma^*$), and they can be ordered as follows : $\sigma\text{--}\sigma^* > n\text{--}\sigma^* > \pi\text{--}\pi^* > n\text{--}\pi^*$.

4.3.1.2. Application

UV/Vis spectroscopy is routinely used in analytical chemistry for the quantitative determination of different analytes, such as transition metal ions, highly conjugated organic compounds, and biological macromolecules. Spectroscopic analysis is commonly carried out in solutions but solids and gases may also be studied.

- Solutions of transition metal ions can be colored (i.e., absorb visible light) because d electrons within the metal atoms can be excited from one electronic state to another. The colour of metal ion solutions is strongly affected by the presence of other species, such as certain anions or ligands. For instance, the colour of a dilute solution of copper sulfate is a very light blue; adding ammonia intensifies the colour and changes the wavelength of maximum absorption (λ_{max}).

- Organic compounds, especially those with a high degree of conjugation, also absorb light in the UV or visible regions of the electromagnetic spectrum. The solvents for these determinations are often water for water-soluble compounds, or ethanol for organic-soluble compounds. (Organic solvents may have significant UV absorption; not all solvents are suitable for use in UV spectroscopy. Ethanol absorbs very weakly at most wavelengths.) Solvent polarity and pH can affect the absorption spectrum of an organic compound. Tyrosine, for example, increases in absorption maxima and molar extinction coefficient when pH increases from 6 to 13 or when solvent polarity decreases.
- While charge transfer complexes also give rise to colours, the colours are often too intense to be used for quantitative measurement. The Beer–Lambert law states that the absorbance of a solution is directly proportional to the concentration of the absorbing species in the solution and the path length.^[93] Thus, for a fixed path length, UV/Vis spectroscopy can be used to determine the concentration of the absorber in a solution. It is necessary to know how quickly the absorbance changes with concentration. This can be taken from references (tables of molar extinction coefficients), or more accurately, determined from a calibration curve.

A UV/Vis spectrophotometer may be used as a detector for HPLC. The presence of an analyte gives a response assumed to be proportional to the concentration. For accurate results, the instrument's response to the analyte in the unknown should be compared with the response to a standard; this is very similar to the use of calibration curves. The response (e.g., peak height) for a particular concentration is known as the response factor.

The wavelengths of absorption peaks can be correlated with the types of bonds in a given molecule and are valuable in determining the functional groups within a molecule. The Woodward–Fieser rules, for instance, are a set of empirical observations used to predict λ_{max} , the wavelength of the most intense UV/Vis absorption, for conjugated organic compounds such as dienes and ketones. The spectrum alone is not, however, a specific test for any given sample. The nature of the solvent, the pH of the solution, temperature, high electrolyte concentrations, and the presence of interfering substances can influence the absorption spectrum. Experimental variations such as the slit width (effective bandwidth) of the spectrophotometer will also alter the spectrum. To apply UV/Vis spectroscopy to analysis, these variables must be controlled or accounted for in order to identify the substances present.^[94]

The Beer–Lambert Law is useful for characterizing many compounds but does not hold as a universal relationship for the concentration and absorption of all substances. A 2nd order polynomial relationship between absorption and concentration is sometimes encountered for very large, complex molecules such as organic dyes (Xylenol Orange or Neutral Red, for example).[citation needed]UV–Vis spectroscopy is also used in the semiconductor industry to measure the thickness and optical properties of thin films on a wafer. UV–Vis spectrometers are used to measure the reflectance of light, and can be analyzed via the Forouhi–Bloomer dispersion equations to determine the Index of Refraction (n) and the Extinction Coefficient (k) of a given film across the measured spectral range.

4.3.2. Scanning Electron Microscope (SEM)

A scanning electron microscope (SEM) is a type of electron microscope that produces images of a sample by scanning the surface with a focused beam of electrons. The electrons interact with atoms in the sample, producing various signals that contain information about the surface topography and composition of the sample. The electron beam is scanned in a raster scan pattern, and the position of the beam is combined with the intensity of the detected signal to produce an image. In the most common SEM mode, secondary electrons emitted by atoms excited by the electron beam are detected using a secondary electron detector (Everhart-Thornley detector). The number of secondary electrons that can be detected, and thus the signal intensity, depends, among other things, on specimen topography. Some SEMs can achieve resolutions better than nanometer.

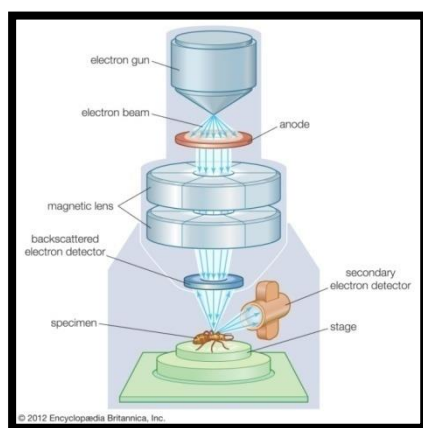


Fig : 4.3.2.1 schematic representation of Scanning Electron Microscope

4.3.2.1. Principles

The signals used by an SEM to produce an image result from interactions of the electron beam with atoms at various depths within the sample. Various types of signals are produced including secondary electrons (SE), reflected or back-scattered electrons (BSE), characteristic X-rays and light (cathodoluminescence) (CL), absorbed current (specimen current) and transmitted electrons. Secondary electron detectors are standard equipment in all SEMs, but it is rare for a single machine to have detectors for all other possible signals.

Secondary electrons have very low energies on the order of 50 eV, which limits their mean free path in solid matter. Consequently, SEs can only escape from the top few nanometers of the surface of a sample. The signal from secondary electrons tends to be highly localized at the point of impact of the primary electron beam, making it possible to collect images of the sample surface with a resolution of below 1 nm. Back-scattered electrons (BSE) are beam electrons that are reflected from the sample by elastic scattering. Since they have much higher energy than SEs, they emerge from deeper locations within the specimen and, consequently, the resolution of BSE images is less than SE images.

However, BSE are often used in analytical SEM, along with the spectra made from the characteristic X-rays, because the intensity of the BSE signal is strongly related to the atomic number (Z) of the specimen. BSE images can provide information about the distribution, but not the identity, of different elements in the sample. In samples predominantly composed of light elements, such as biological specimens, BSE imaging can image colloidal gold immuno-labels of 5 or 10 nm diameter, which would otherwise be difficult or impossible to detect in secondary electron images.^[95] Characteristic X-rays are emitted when the electron beam removes an inner shell electron from the sample, causing a higher-energy electron to fill the shell and release energy. The energy or wavelength of these characteristic X-rays can be measured by Energy-dispersive X-ray spectroscopy or Wavelength-dispersive X-ray spectroscopy and used to identify and measure the abundance of elements in the sample and map their distribution.

Due to the very narrow electron beam, SEM micrographs have a large depth of field yielding a characteristic three-dimensional appearance useful for understanding the surface structure of a sample.^[96] This is exemplified by the micrograph of pollen shown above. A wide range of magnifications is possible, from about 10 times (about equivalent

to that of a powerful hand-lens) to more than 500,000 times, about 250 times the magnification limit of the best light microscopes.

4.3.2.2 Applications

- One possible application is measuring the roughness of ice crystals.
- This method can combine variable-pressure environmental SEM and the 3D capabilities of the SEM to measure roughness on individual ice crystal facets, convert it into a computer model and run further statistical analysis on the model.^[97]
- Other measurements include fractal dimension, examining fracture surface of metals, characterization of materials, corrosion measurement, and dimensional measurements at the nano scale (step height, volume, angle, flatness, bearing ratio, coplanarity, etc.)

4.3.3 X-ray powder diffraction (XRD)

X-ray powder diffraction (XRD) is a rapid analytical technique primarily used for phase identification of a crystalline material and can provide information on unit cell dimensions. The analyzed material is finely ground, homogenized, and average bulk composition is determined.^[98]



Fig : 4.3.3.1 schematic representation of X-ray powder diffraction

4.3.3.1. Principles of X-ray Powder Diffraction (XRD)

Max von Laue, in 1912, discovered that crystalline substances act as three-dimensional diffraction gratings for X-ray wavelengths similar to the spacing of planes in a crystal lattice. X-ray diffraction is now a common technique for the study of crystal structures and atomic spacing.

X-ray diffraction is based on constructive interference of monochromatic X-rays and a crystalline sample. These X-rays are generated by a cathode ray tube, filtered to produce monochromatic radiation, collimated to concentrate, and directed toward the sample. The interaction of the incident rays with the sample produces constructive interference (and a diffracted ray) when conditions satisfy Bragg's Law ($n\lambda = 2d \sin \theta$). This law relates the wavelength of electromagnetic radiation to the diffraction angle and the lattice spacing in a crystalline sample. These diffracted X-rays are then detected, processed and counted. By scanning the sample through a range of 2θ angles, all possible diffraction directions of the lattice should be attained due to the random orientation of the powdered material. Conversion of the diffraction peaks to d-spacings allows identification of the mineral because each mineral has a set of unique d-spacings.^[99] Typically, this is achieved by comparison of d-spacings with standard reference patterns.

All diffraction methods are based on generation of X-rays in an X-ray tube. These X-rays are directed at the sample, and the diffracted rays are collected. A key component of all diffraction is the angle between the incident and diffracted rays. Powder and single crystal diffraction vary in instrumentation beyond this.

4.3.3.2. Applications

X-ray powder diffraction is most widely used for the identification of unknown crystalline materials (e.g. minerals, inorganic compounds). Determination of unknown solids is critical to studies in geology, environmental science, material science, engineering and biology.^[100]

Other applications include:

- ❖ characterization of crystalline materials
- ❖ identification of fine-grained minerals such as clays and mixed layer clays that are difficult to determine optically
- ❖ determination of unit cell dimensions
- ❖ measurement of sample purity
- ❖ With specialized techniques, XRD can be used to:
- ❖ determine crystal structures using Rietveld refinement
- ❖ determine of modal amounts of minerals (quantitative analysis)
- ❖ characterize thin films samples by:
- ❖ determining lattice mismatch between film and substrate and to inferring stress and strain

- ❖ determining dislocation density and quality of the film by rocking curve measurements
- ❖ measuring superlattices in multilayered epitaxial structures
- ❖ determining the thickness, roughness and density of the film using glancing incidence X-ray reflectivity measurements
- ❖ make textural measurements, such as the orientation of grains, in a polycrystalline sample

4.3.4 Fourier-transform infrared spectroscopy

FTIR may also refer to Frustrated total internal reflection. Fourier-transform infrared spectroscopy (FTIR)^[101] is a technique used to obtain an infrared spectrum of absorption or emission of a solid, liquid or gas. An FTIR spectrometer simultaneously collects high-resolution spectral data over a wide spectral range. This confers a significant advantage over a dispersive spectrometer, which measures intensity over a narrow range of wavelengths at a time. The term Fourier-transform infrared spectroscopy originates from the fact that a Fourier transform (a mathematical process) is required to convert the raw data into the actual spectrum.



4.3.4.1 schematic representation of FTIR Spectroscopy

4.3.4.1. Principles of FTIR Spectroscopy

In FTIR analyses, Infrared light from the light source passes through a Michelson interferometer along the optical path. The Michelson interferometer comprises a beam splitter, moving mirror, and fixed mirror. The light beam split into two by the beam splitter is reflected from the moving mirror and fixed mirror, before being recombined by the beam splitter. As the moving mirror makes reciprocating movements, the optical path

difference to the fixed mirror changes, such that the phase difference changes with time. The light beams are recombined in the Michelson interferometer to produce interference light. The intensity of the interference light is recorded in an interferogram, with the optical path difference recorded along the horizontal axis.

4.3.4.2. Applications

FTIR can be used in all applications where a dispersive spectrometer was used in the past (see external links). In addition, the improved sensitivity and speed have opened up new areas of application. Spectra can be measured in situations where very little energy reaches the detector and scan rates can exceed 50 spectra a second. Fourier transform infrared spectroscopy is used in geology, chemistry, materials and biology research fields.

- **Biological materials**

FTIR is used to investigate proteins in hydrophobic membrane environments. Studies show the ability of FTIR to directly determine the polarity at a given site along the backbone of a transmembrane protein.^{[102][103]}

- **Microscopy and imaging**

An infrared microscope allows samples to be observed and spectra measured from regions as small as 5 microns across. Images can be generated by combining a microscope with linear or 2-D array detectors. The spatial resolution can approach 5 microns with tens of thousands of pixels. The images contain a spectrum for each pixel and can be viewed as maps showing the intensity at any wavelength or combination of wavelengths. This allows the distribution of different chemical species within the sample to be seen. Typical studies include analysing tissue sections as an alternative to conventional histopathology and examining the homogeneity of pharmaceutical tablets.

- **Nanoscale and spectroscopy below the diffraction limit**

The spatial resolution of FTIR can be further improved below the micrometer scale by integrating it into scanning near-field optical microscopy platform. The corresponding technique is called nano-FTIR and allows for performing broadband spectroscopy on materials in ultra-small quantities (single viruses and protein complexes) and with 10 to 20 nm spatial resolution.^[104]

- **FTIR as detector in chromatography**

The speed of FTIR allows spectra to be obtained from compounds as they are separated by a gas chromatograph. However this technique is little used compared to GC-MS (gas chromatography-mass spectrometry) which is more sensitive. The GC-IR method is particularly useful for identifying isomers, which by their nature have identical masses. Liquid chromatography fractions are more difficult because of the solvent present. One notable exception is to measure chain branching as a function of molecular size in polyethylene using gel permeation chromatography, which is possible using chlorinated solvents that have no absorption in the area in question.

- **TG-IR (thermogravimetric analysis-infrared spectrometry)**

Measuring the gas evolved as a material is heated allows qualitative identification of the species to complement the purely quantitative information provided by measuring the weight loss.

- **Water content determination in plastics and composites**

FTIR analysis is used to determine water content in fairly thin plastic and composite parts, more commonly in the laboratory setting. Such FTIR methods have long been used for plastics, and became extended for composite materials in 2018, when the method was introduced by Krauklis, Gagani and Echtermeyer.^[105] FTIR method uses the maxima of the absorbance band at about 5,200 cm^{-1} which correlates with the true water content in the material.

4.3.5 Energy Dispersive X-ray spectroscopy (EDAX)

EDAX is an analytical technique used for the elemental analysis or chemical characterization of a sample. It relies on an interaction of some source of X-ray excitation and a sample. Its characterization capabilities are due in large part to the fundamental principle that each element has a unique atomic structure allowing a unique set of peaks on its electromagnetic emission spectrum (which is the main principle of spectroscopy).

Four primary components of the EDS setup are

- the excitation source (electron beam or x-ray beam)

- the X-ray detector
- the pulse processor
- the analyzer



Electron beam excitation is used in electron microscope, scanning electron microscope (SEM) and scanning transmission electron microscope (STEM) X-ray beam excitation is used in X-ray Fluorescence (XRF) spectrometers. A detector is used to convert X-ray energy into voltage signals, this information is sent to a pulse processor, which measures the signals and passes them onto an analyzer for data display and analysis. The most common detector used to be (Li) detector cooled to cryogenic temperature with liquid nitrogen. Now, newer systems are often equipped with silicon Drift Detector (SDD) with Peltier cooling systems. ^[106]

CHAPTER – 5

RESULTS AND DISCUSSION

5. RESULTS AND DISCUSSION

5.1 FT-IR Analysis:

5.1.1 FT-IR Analysis of ZrTe

FT-IR spectrum of ZrTe were recorded and it was shown in the figure 5.1.1. The peaks observed for the ZrTe shown in the presence of Zr=Te stretching 1635.64 cm^{-1} , 447.49 cm^{-1} , 408.91 cm^{-1} Te=Te stretching 771.53 cm^{-1} , 663.51 cm^{-1} , 594.08 cm^{-1} .

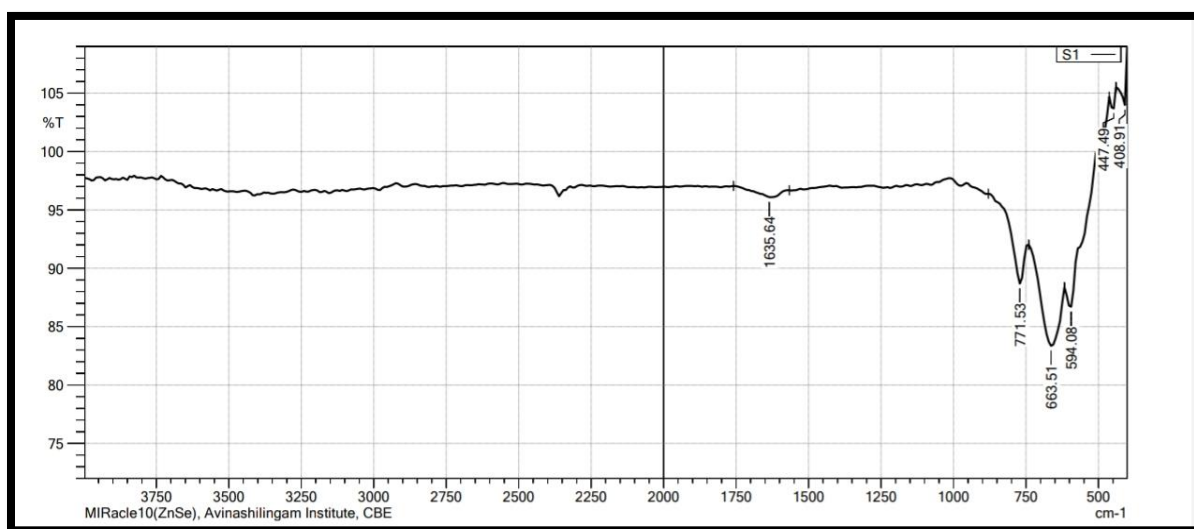


Fig 5.1.1.1 FT- IR Spectra of ZrTe

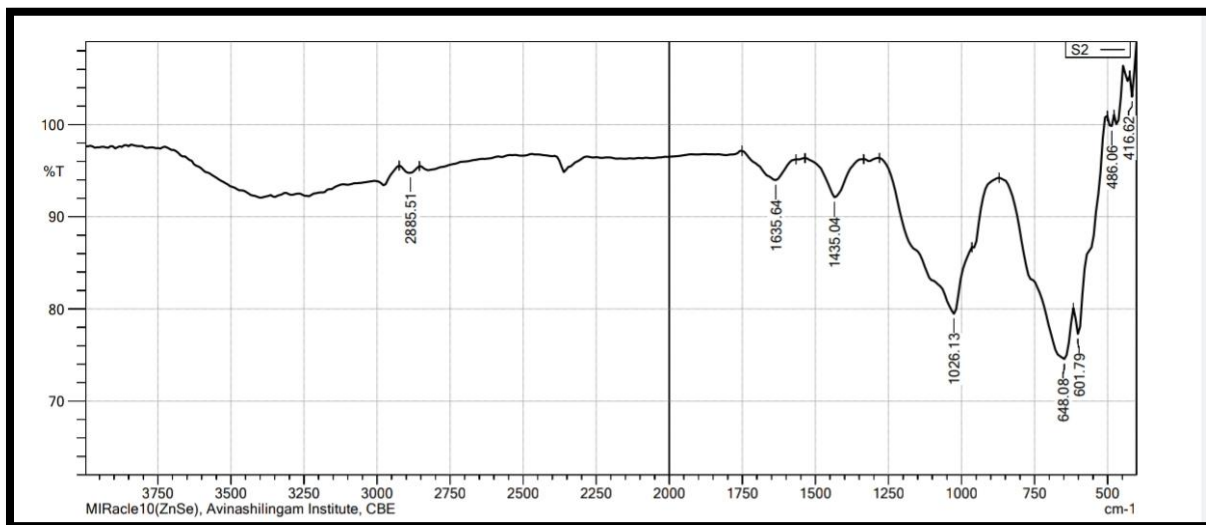
5.1.1.1 FT- IR Spectra of ZrTe

VIBRATION	WAVENUMBER cm^{-1}
Te=Te stretching	1635.64 cm^{-1} , 447.49 cm^{-1} , 408.91 cm^{-1}
Zr= Te stretching	771.53 cm^{-1} , 663.51 cm^{-1} , 594.08 cm^{-1} .

5.1.2 FTIR spectrum of CdTe

Ftir spectrum of CdTe were recorded and it was shown in the figure 5.1.1. The peaks observed for the CdTe shown in the presence of Cd=Te stretching at 1026.13 cm^{-1} , 648.08 cm^{-1} ,

601.79 cm⁻¹.Te= Te stretching 2885.51 cm⁻¹, 1635.54 cm⁻¹,1435.04 cm⁻¹, 486.06 cm⁻¹, 416.62 cm⁻¹.



5.1.2 FTIR spectrum of CdTe

5.1.2.2 FT- IR Spectra of CdTe

VIBRATION	WAVENUMBER cm ⁻¹
Cd=Te stretching	1026.13 cm ⁻¹ , 648.08 cm ⁻¹ , 601.79 cm ⁻¹
Te= Te stretching	2885.51cm ⁻¹ , 1635.54cm ⁻¹ , 1435.04 cm ⁻¹ , 486.06 cm ⁻¹ , 416.62 cm ⁻¹ .

5. 2. XRD Analysis

The structural properties of ZrTe nanoparticles was studied using XRD analysis. the crystalline peaks corresponding to the planes (200), (211), (310) ,(222) indexed as body centered cubic (BCC) ZrTe . The average crystalline size of ZrTe nanoparticle is 1nm which was calculated by Debye - Scherrer formula

$$D = \frac{k\lambda}{\beta \cos \theta}$$

Where D is the average crystalline diameter in nanometer.

K is dimensionless shape factor,

λ is the X-ray wavelength,

β is the line broadening at half the maximum intensity (FWHM)

$$\beta = \frac{\pi}{180^\circ} \times 2\theta$$

θ is the Bragg angle

5.2.1 XRD Calculation for ZrTe

5.2.1.1 Calculate average crystalline size (D)

2θ	θ	B	Cos θ	D
26.4840	0.1338	0.4608	1	3.1428
29.0241	0.1338	0.5050	1	2.8677
30.1511	0.0753	0.5246	1	2.7606
37.6145	0.1338	0.6545	1	2.2127
48.0397	0.1004	0.8359	1	1.7325
48.8261	0.1506	0.8496	1	1.7046
54.4750	0.1004	0.9427	1	1.5362
55.4750	0.1673	0.9653	1	1.5003
61.1914	0.2008	1.0647	1	1.3602
62.4181	0.1338	1.0861	1	1.3336
75.7733	0.2008	1.3185	1	1.0984
78.0061	0.1338	1.3573	1	1.0069
Average				1.7127

5.2.1.2. Identify the lowest common quotient be k

2θ	θ	$\sin^2\theta$	$\frac{\sin^2}{2}\theta$	$\frac{\sin^2}{3}\theta$	$\frac{\sin^2}{4}\theta$	$\frac{\sin^2}{5}\theta$	$\frac{\sin^2}{6}\theta$	$\frac{\sin^2}{7}\theta$	$\frac{\sin^2}{8}\theta$
26.4840	13.2420	0.0525	0.0263	0.0175	0.0131	0.0105	0.0088	0.0075	0.0065
29.0241	14.5121	0.0628	0.0314	0.0209	0.0157	0.0126	0.0105	0.0087	0.0079
30.1511	15.0756	0.0676	0.0338	0.0225	0.0169	0.0135	0.0113	0.0096	0.0085
37.6145	18.8073	0.1039	0.0519	0.0346	0.0259	0.0208	0.0173	0.0148	0.0129
48.0397	24.0199	0.1657	0.0829	0.0552	0.0414	0.0331	0.0271	0.0237	0.0207
48.8261	24.4131	0.1708	0.0854	0.0569	0.0427	0.0342	0.0285	0.0244	0.0214
54.4750	27.0904	0.2074	0.1037	0.0691	0.0519	0.0415	0.0346	0.0296	0.0259
55.4750	27.7375	0.2166	0.1083	0.0722	0.0542	0.0433	0.0361	0.0309	0.0271
61.1914	30.5957	0.2591	0.1296	0.0864	0.0648	0.0518	0.0432	0.0370	0.0324
62.4181	31.2091	0.2685	0.1343	0.0864	0.0671	0.0537	0.0448	0.0384	0.0336
75.7733	37.8867	0.3771	0.1886	0.0895	0.0943	0.0754	0.0629	0.0539	0.0471
78.0061	39.0031	0.3961	0.1981	0.1320	0.0990	0.0792	0.0660	0.0566	0.0495

k = 0.0271

5.2.1.3 Calculate the lattice value

$$a = \frac{K\lambda}{2 \times \sqrt{k}}$$

$$a = \frac{0.94 \times 1.5406}{2 \times \sqrt{0.0271}}$$

$$a = \frac{1.4482}{2 \times 0.16}$$

$$a = 4.5256 \text{ \AA}$$

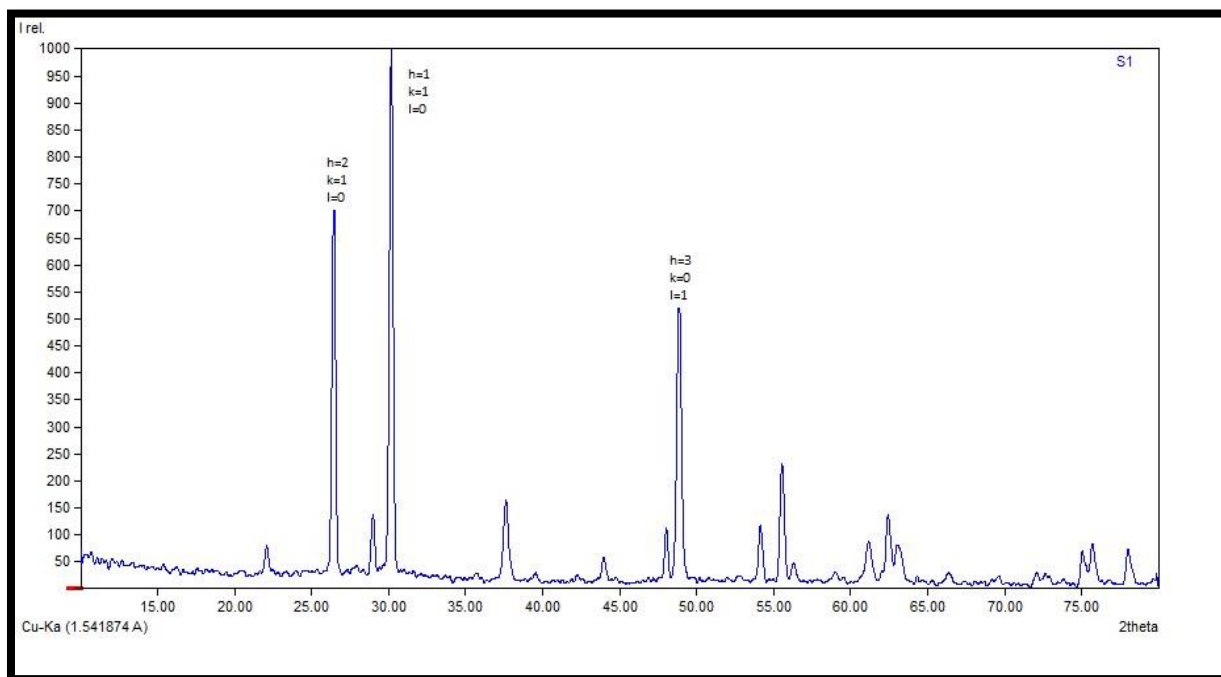


Fig 5.2.1 XRD spectrum of ZrTe

5.2.2 XRD Calculation for CdTe

The structural properties of CdTe nanoparticles was studied using XRD analysis. the crystalline peaks corresponding to the planes (111), (220) and (311). CdTe were cubic in structure. The average crystalline size of CdTe nanoparticle is 3nm which was calculated by Debye - Scherrer formula.

5.2.2.1 Calculate average crystalline size (D)

2θ	θ	B	Cos θ	D
30.0753	0.2448	0.5246	1	2.7606
Average				2.7606

5.2.2.2 Identify the lowest common quotient be k

2θ	θ	$\text{Sin}^2\theta$	$\frac{\sin^2}{2}\theta$	$\frac{\sin^2}{3}\theta$	$\frac{\sin^2}{4}\theta$	$\frac{\sin^2}{5}\theta$	$\frac{\sin^2}{6}\theta$	$\frac{\sin^2}{7}\theta$	$\frac{\sin^2}{8}\theta$
30.0753	15.0377	0.0673	0.0337	0.0224	0.0168	0.0135	0.0112	0.0096	0.0084

$$k = 0.0135$$

5.2.2.3 Calculate the lattice value

$$a = \frac{K\lambda}{2 \times \sqrt{k}}$$

$$a = \frac{0.94 \times 1.5406}{2 \times \sqrt{0.0135}}$$

$$a = \frac{1.4482}{2 \times 0.12}$$

$$a = 6.0341 \text{ \AA}$$

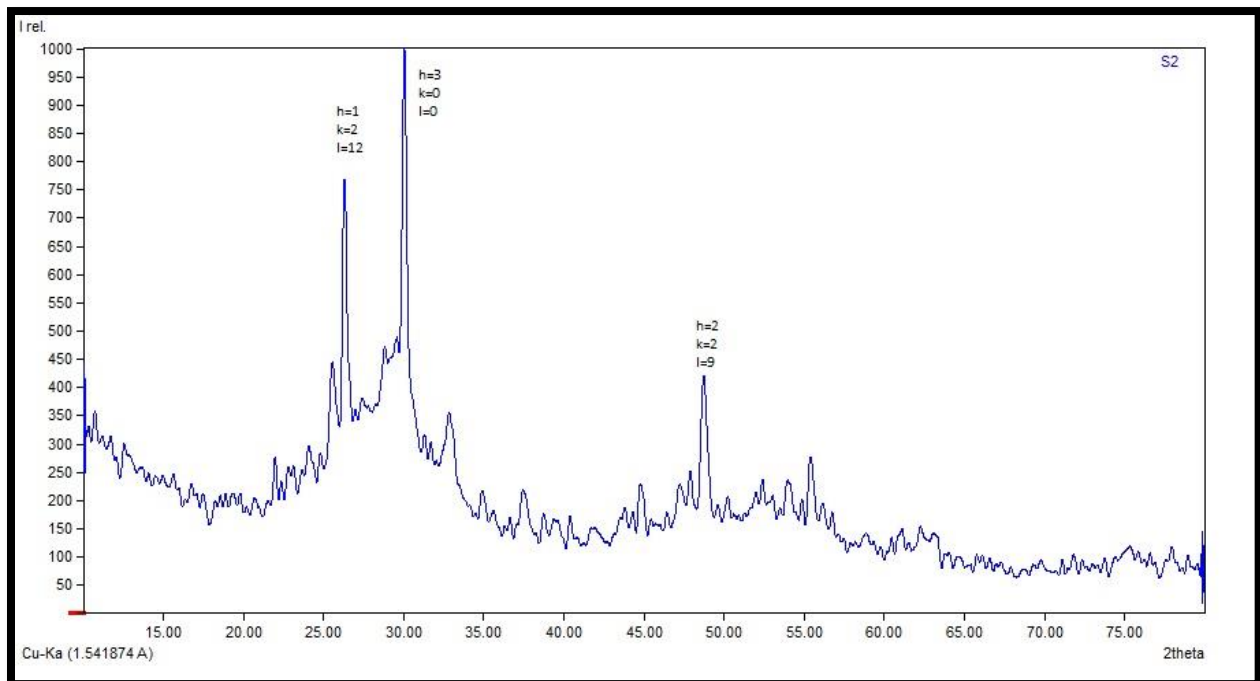


Fig 5.2.2 XRD spectrum of CdTe

5.3. SEM Analysis

5.3.1 SEM characterization of ZrTe

SEM characterization of ZrTe nanoparticles prepared by reverse micelles. ZrTe nanoparticles are magnified in the ranges from 50 μ m-200nm which was shown in figure 5.4.1. SEM images shows that the particles are heavily aggregated due to surface activity. From SEM results, it is concluded that the surface morphology of ZrTe nanoparticles are nano flowers in lower magnification and nanorods in higher frequency range.

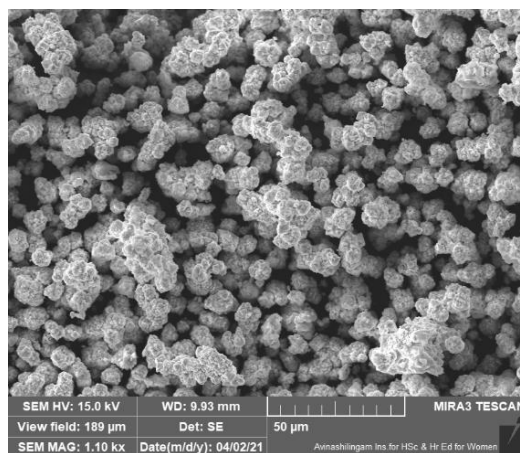


Fig 5.3.1.1.

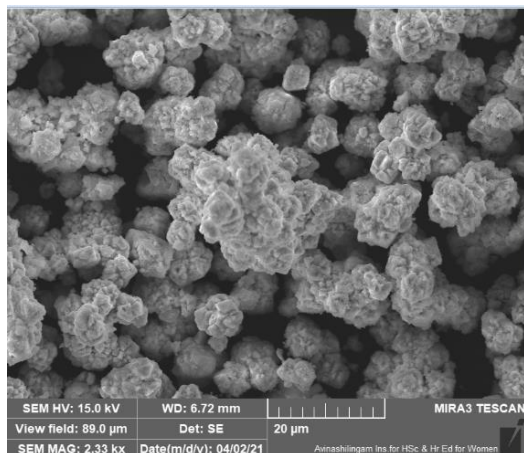


Fig 5.3.1.2.

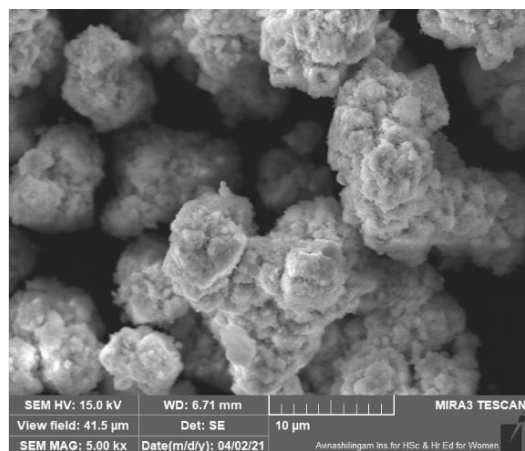


Fig 5.3.1.3.

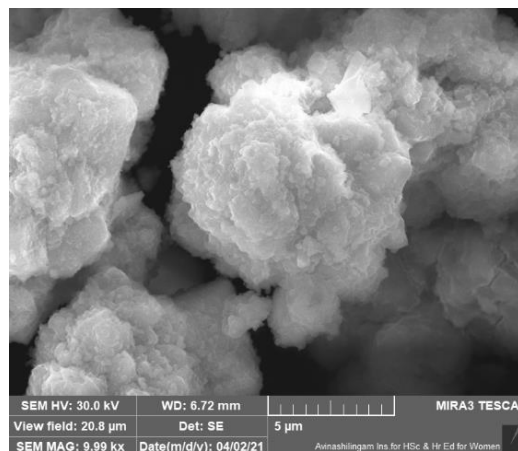


Fig 5.3.1.4

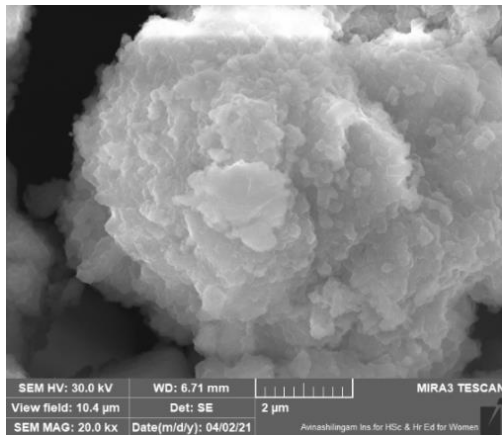


Fig 5.3.1.5.

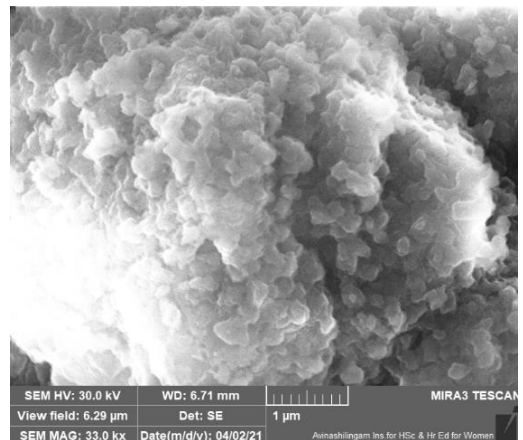


Fig 5.3.1.6.

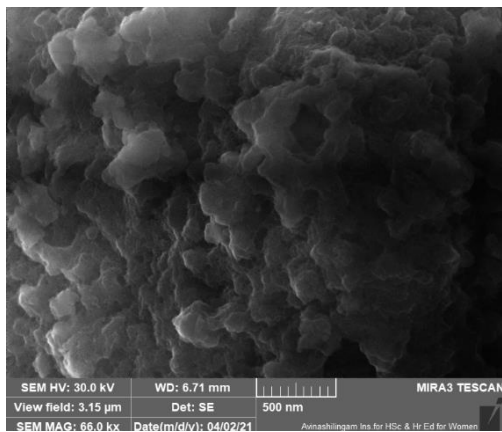


Fig 5.3.1.7.

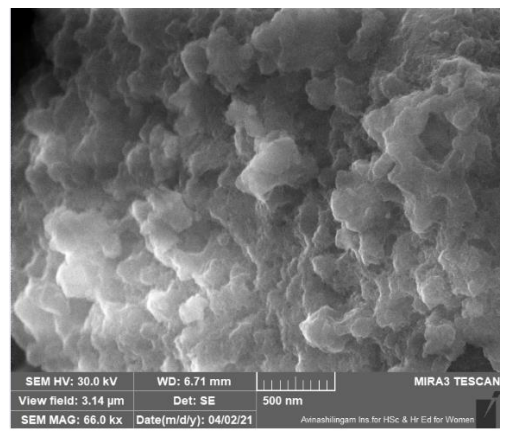


Fig 5.3.1.8.

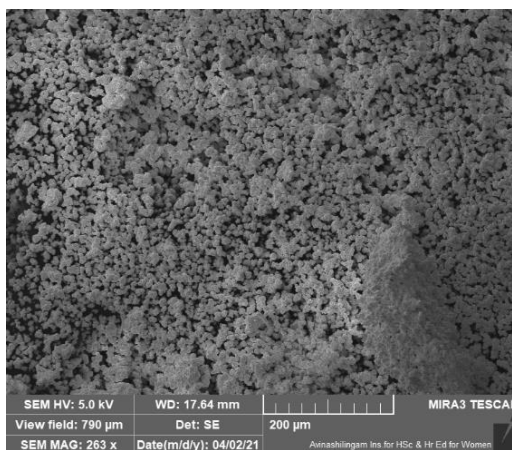


Fig 5.3.1.9.

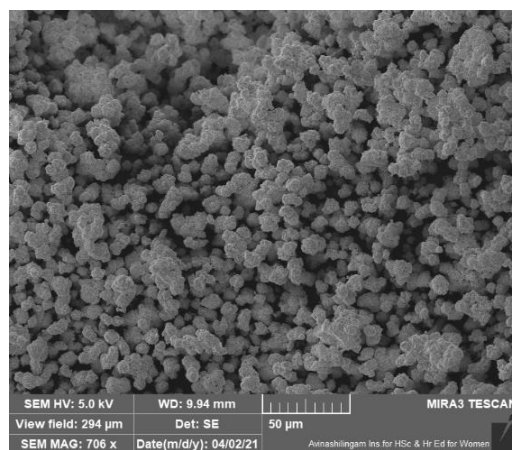


Fig 5.3.1.10.

5.3.2 SEM characterization of CdTe

SEM characterization of CdTe nanoparticles prepared by reverse micelles. CdTe nanoparticles are magnified in the ranges from 50 μ m-200nm which was shown in figure 5.4.2.1-5.4.2.8 SEM images shows that the particles are heavily aggregated due to surface activity. From SEM results, it is concluded that the surface morphology of CdTe nanoparticles are nano brittle fracture in lower magnification and nanorods in higher frequency range.

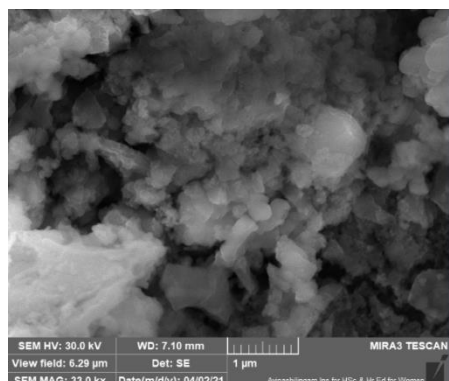


Fig5.3.2.1

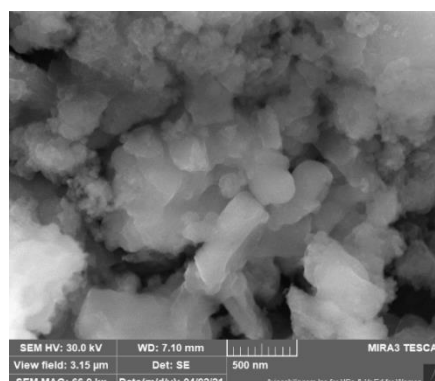


Fig 5.3.2.2

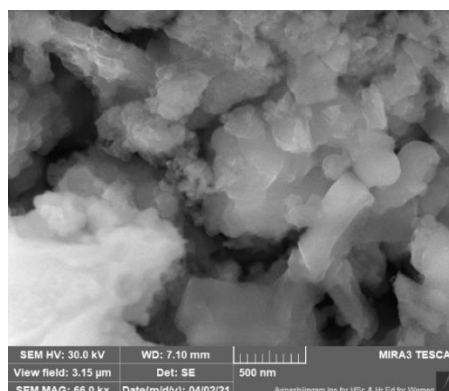


Fig 5.3.1.2.

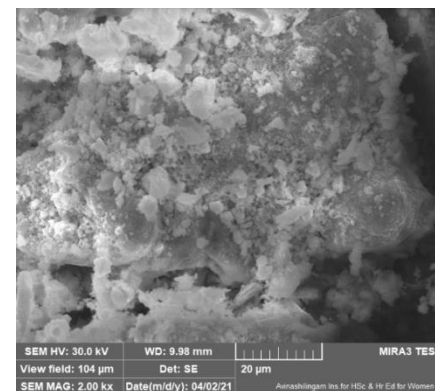


Fig 5.3.1.2

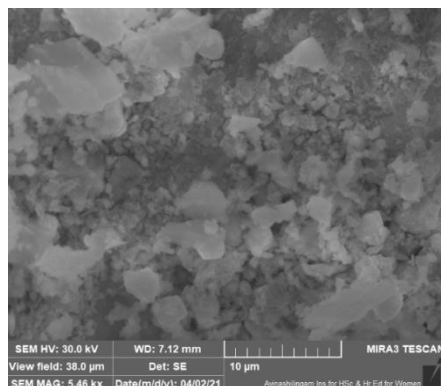


Fig 5.3.1.2.

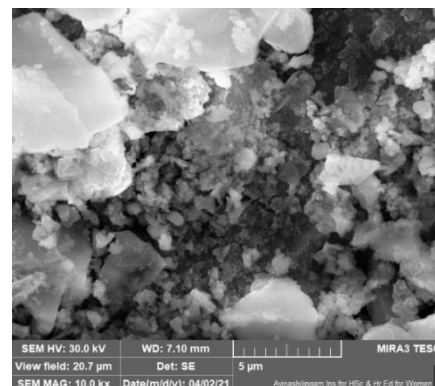


Fig 5.3.1.2.

5.4 EDAX Analysis

5.4.1. EDAX Analysis of ZrTe

Energy dispersive x-ray analysis was used to confirm the elemental composition of ZrTe nanoparticles. The figure 5.5.1.a - 5.5.1.g. shown below indicates the presence of zirconium and telluride in synthesized ZrTe nanoparticles.



Fig 5.4.1.a

Fig 5.4.1.b

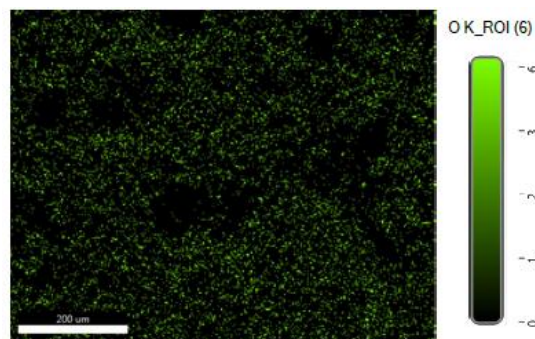


Fig 5.4.1.c

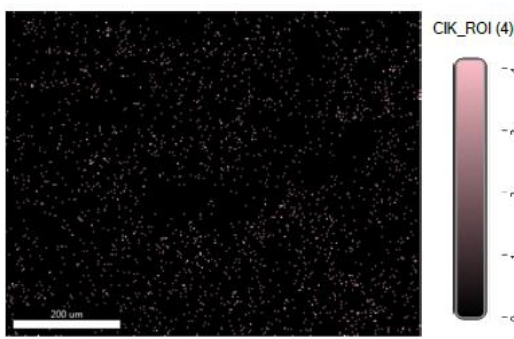


Fig 5.4.1.d

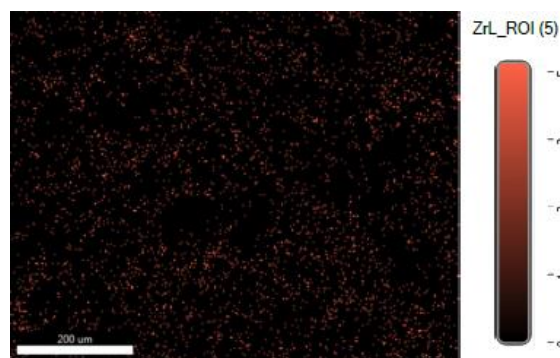


Fig 5.4.1.e

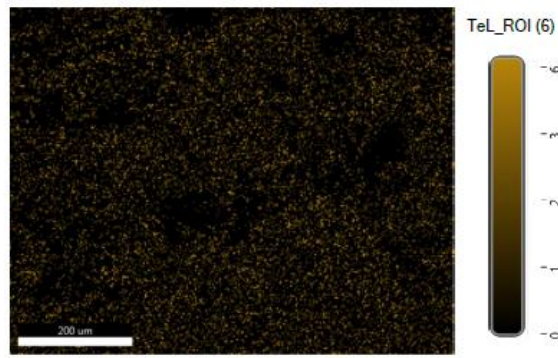


Fig 5.4.1.f

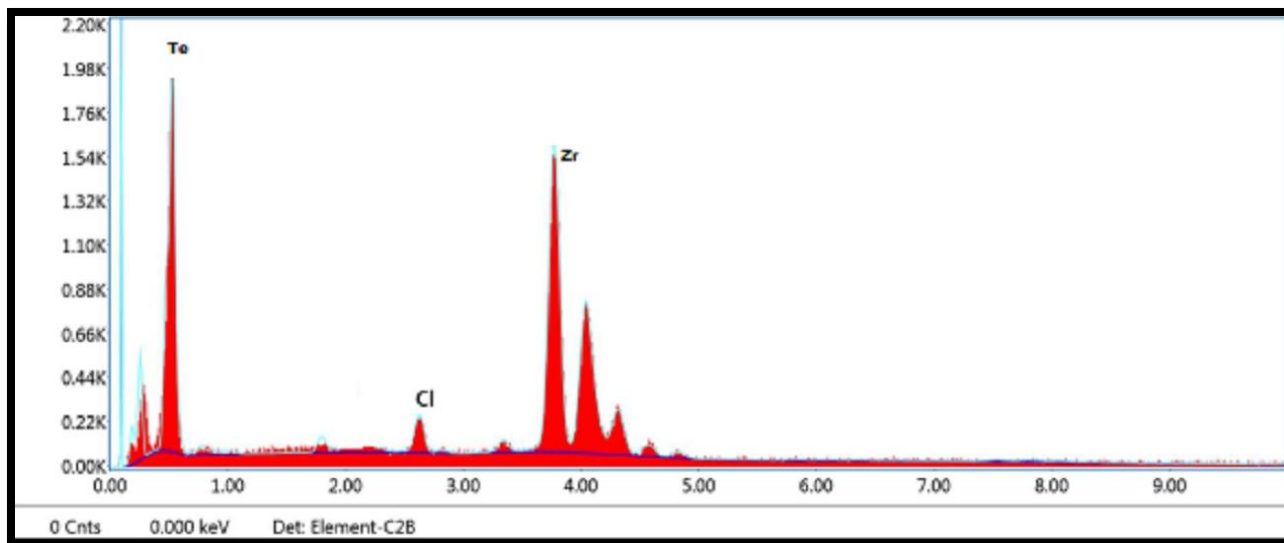


Fig .5.4.1.g. EDAX spectrum of ZrTe

5.4.2. EDAX Analysis of CdTe

Energy dispersive x-ray analysis was used to confirm the elemental composition of CdTe nanoparticles. The figure 5.5.2.a - 5.5.2.i. shown below indicates the presence of cadmium and telluride in synthesized CdTe nanoparticles.

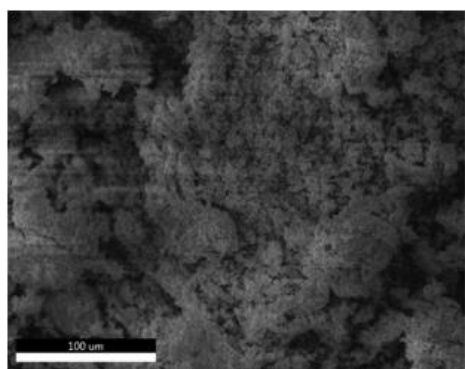


Fig 5.4.2.a

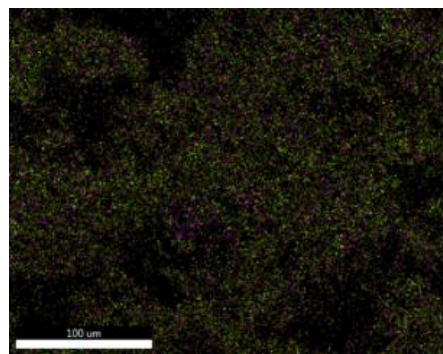
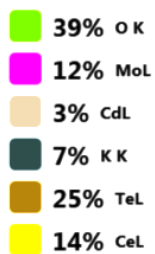


Fig 5.4.2.b

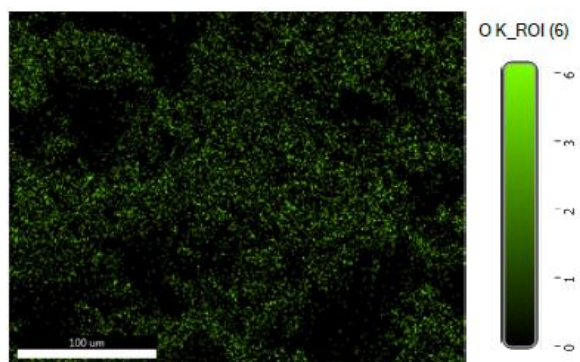


Fig 5.4.2.c

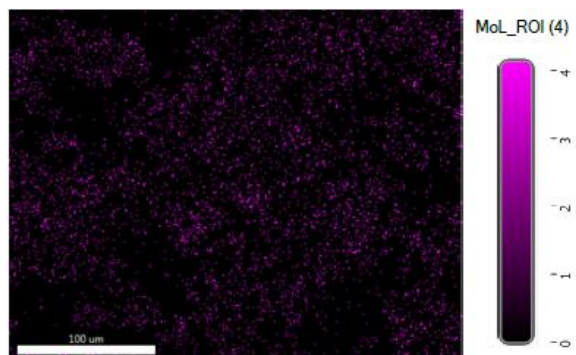


Fig 5.4.2.d



Fig 5.4.2.e

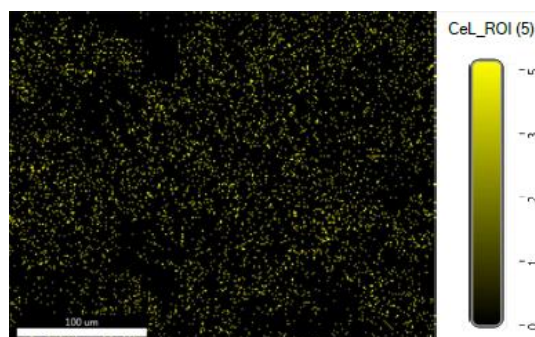


Fig 5.4.2.f

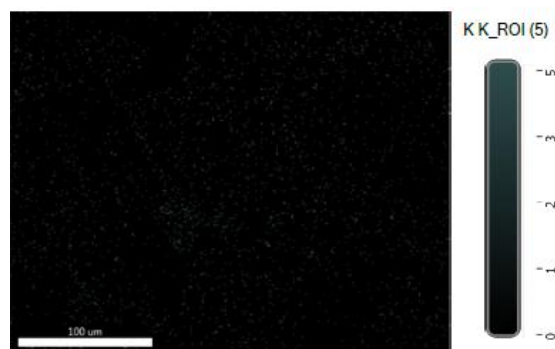


Fig 5.4.2.g

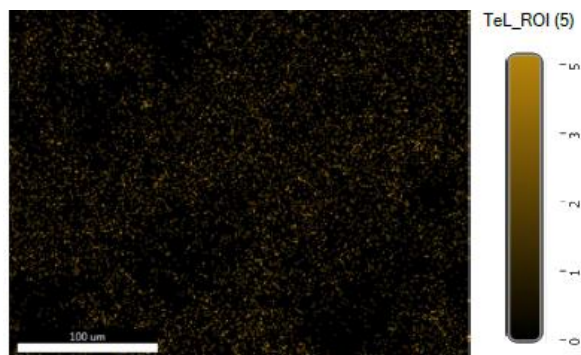


Fig 5.4.2.h

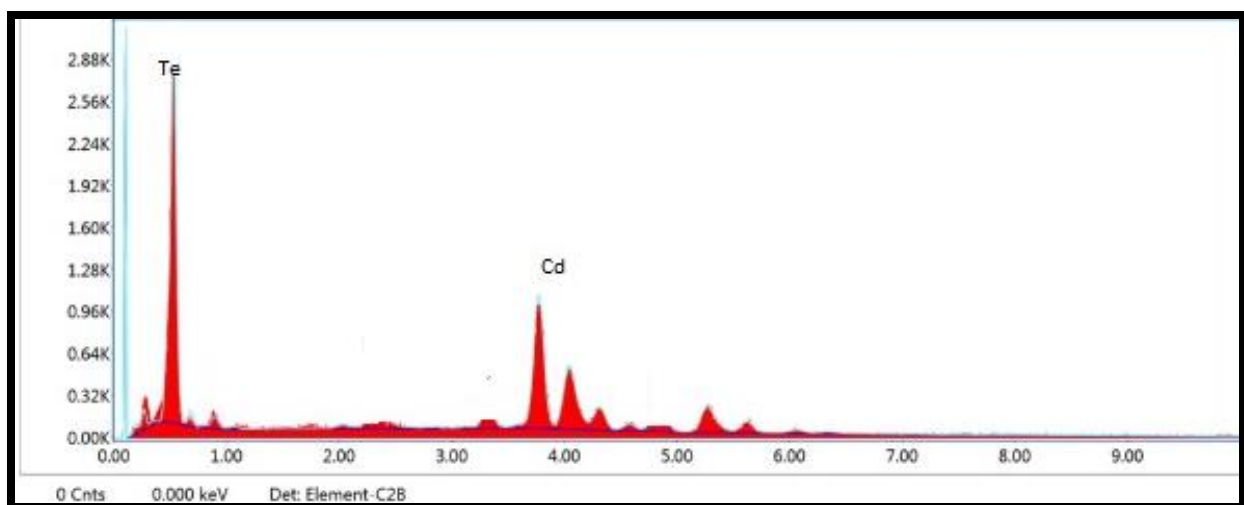


Fig 5.4.2.i. EDAX spectrum of CdTe

CHAPTER – 6

CONCLUSION

CONCLUSION

- ❖ A The shape and size are more important factors in determining the structural, physical and chemical properties of nanoparticles Shape controlled synthesis of nanoparticles has become a focus point as different morphologic nanoparticles would have different electronic, optic and magnetic properties
- ❖ ZrTe and CdTe nanoparticles are synthesized by organic synthesis using reverse micelles
- ❖ The prepared ZrTe and CdTe nanoparticles are characterized using several techniques such as FT-IR. XRD, SEM, EDAX.
- ❖ From FT-IR the Metal-Oxygen stretching vibrations are confirmed the Formation of ZrTe and CdTe nanoparticles
- ❖ The morphology and size of the prepared nanoparticles are nano flower and nano brittle fracture which was detected by SEM analysis.
- ❖ The composition of element in ZrTe and CdTe nanoparticles are founded by EDAX.

CHAPTER – 7

REFERENCE

REFERENCE

1. Meija, Juris; et al. (2016). *"Atomic weights of the elements 2013 (IUPAC Technical Report)". Pure and Applied Chemistry*. 88 (3): 265–91. doi:10.1515/pac-2015-0305.
2. Adenis, C.; Langer, V.; Lindqvist, O. (15 June 1989). *"Reinvestigation of the structure of tellurium"*. *Acta Crystallographica Section C Crystal Structure Communications*. 45 (6): 941–942. doi:10.1107/S0108270188014453.
3. Cverna, Fran (2002). *"Ch. 2 Thermal Expansion"*. ASM Ready Reference: Thermal properties of metals (PDF). ASM International. ISBN 978-0-87170-768-0.
4. Lide, D. R., ed. (2005). *"Magnetic susceptibility of the elements and inorganic compounds"*. *CRC Handbook of Chemistry and Physics (PDF) (86th ed.)*. Boca Raton (FL): CRC Press. ISBN 0-8493-0486-5.
5. Weast, Robert (1984). *CRC, Handbook of Chemistry and Physics*. Boca Raton, Florida: Chemical Rubber Company Publishing. pp. E110. ISBN 0-8493-0464-4.
6. Alessandrello, A.; Arnaboldi, C.; Brofferio, C.; Capelli, S.; Cremonesi, O.; Fiorini, E.; Nucciotti, A.; Pavan, M.; Pessina, G.; Pirro, S.; Previtali, E.; Sisti, M.; Vanzini, M.; Zanotti, L.; Giuliani, A.; Pedretti, M.; Bucci, C.; Pobes, C. (2003). "New limits on naturally occurring electron capture of ^{123}Te ". *Physical Review C*. 67: 014323. arXiv:hep-ex/0211015. Bibcode:2003PhRvC..67a4323A. doi:10.1103/PhysRevC.67.014323.
7. Jump up to:^{a b} Anderson, Don L.; *"Chemical Composition of the Mantle"* in *Theory of the Earth*, pp. 147-175 ISBN 0865421234
8. Jump up to:^{a b} Ramadan, Shadia E.; Razak, A. A.; Ragab, A. M.; El-Meleigy, M. (1989). "Incorporation of tellurium into amino acids and proteins in a tellurium-tolerant fungi". *Biological Trace Element Research*. 20 (3): 225–32. doi:10.1007/BF02917437. PMID 2484755. S2CID 9439946.
9. Jump up to:^{a b} Leddicotte, G. W. (1961). *"The radiochemistry of tellurium"* (PDF). Nuclear science series (3038). Subcommittee on Radiochemistry, National Academy of Sciences-National Research Council: 5.
10. Berger, Lev Isaakovich (1997). *"Tellurium"*. *Semiconductor materials*. CRC Press. pp. 89–91. ISBN 978-0-8493-8912-2.
11. Periodic Table. ptable.com

12. Jump up to:^{a b} Audi, G.; Bersillon, O.; Blachot, J.; Wapstra, A. H. (2003). *"The NUBASE Evaluation of Nuclear and Decay Properties"*. Nuclear Physics 3–128. Bibcode:2003NuPhA.729....3A. doi:10.1016/j.nuclphysa.2003.11.001.
13. "WWW Table of Radioactive Isotopes: Tellurium". *Nuclear Science Division, Lawrence Berkeley National Laboratory*. 2008. Archived from the original on 2010-02-05. Retrieved 2010-01-16.
14. Alessandrello, A.; Arnaboldi, C.; Brofferio, C.; Capelli, S.; Cremonesi, O.; Fiorini, E.; Nucciotti, A.; Pavan, M.; Pessina, G.; Pirro, S.; Previtali, E.; Sisti, M.; Vanzini, M.; Zanotti, L.; Giuliani, A.; Pedretti, M.; Bucci, C.; Pobes, C. (2003). *"New limits on naturally occurring electron capture of ¹²³Te"*. *Physical Review C*. 67 (1): 014323. arXiv:hep-ex/0211015. Bibcode:2003PhRvC..67a4323A. doi:10.1103/PhysRevC.67.014323. S2CID 119523039.
15. "Noble Gas Research". Laboratory for Space Sciences, *Washington University in St. Louis*. 2008. Archived from the original on September 28, 2011. Retrieved 2013-01-10.
16. Emsley, John (2003). "Tellurium". *Nature's building blocks: an A-Z guide to the elements*. Oxford University Press. pp. 426–429. ISBN 978-0-19-850340-8.
17. Ayres, Robert U.; Ayres, Leslie (2002). *A handbook of industrial ecology*. Edward Elgar Publishing. p. 396. ISBN 1-84064-506-7.
18. Suess, Hans; Urey, Harold (1956). "Abundances of the Elements". *Reviews of Modern Physics*. 28 (1): 53–74. Bibcode:1956RvMP...28...53S. doi:10.1103/RevModPhys.28.53.
19. Nekrasov, I. Y. (1996). *"Phase Relations in the Selenide Telluride Systems"*. *Geochemistry, mineralogy and genesis of gold deposits*. Taylor & Francis. pp. 217–256. ISBN 978-90-5410-723-1.
20. Fortey, Richard (2004). *The Earth: An Intimate History*. Harper Perennial. p. 230. ISBN 978-0-00-257011-4.
21. v. Born, Abh. Privatges. v. Böhmen 5 (1782): 383.
22. Rupprecht, von, A. (1783). "Über den vermeintlichensiebenbürgischennatürlichenSpiessglaskönig" [On the supposedly native antimony of Transylvania]. *PhysikalischeArbeiten der EinträchtigenFreunde in Wien*. 1 (1): 70–74.
23. Müller,F.J.(1783). *"ÜberdenvermeintlichennatürlichenSpiessglaskönig"*. *PhysikalischeArbeiten der EinträchtigenFreunde in Wien*. 1 (1): 57–59.

24. vonReichenstein, F. J. M. (1783). "*Versuchemitdem in der GrubeMariahilf in demGebirgeFazebaybeyZalathnavorkommendenvermeintengediegenenSpiesglaskönig*"[Experiments with supposedly native antimony occurring in the Mariahilf mine in the Fazebymountains near Zalathna]. *PhysikalischeArbeiten der EinträchtigenFreunde in Wien*. 1783(1.Quartal): 63–69.
25. Jump up to:^{a b} Diemann, Ekkehard; Müller, Achim; Barbu, Horia (2002). "Die spannendeEntdeckungsgeschichte des Tellurs (1782–1798) Bedeutung und Komplexität von Elemententdeckungen". *Chemie in UnsererZeit*. 36 (5): 334–337. doi:10.1002/1521-3781(200210)36:5<334::AID-CIUZ334>3.0.CO;2-1.
26. Jump up to:^{a b} Weeks, Mary Elvira (1932). "The discovery of the elements. VI. Tellurium and selenium". *Journal of Chemical Education*. 9 (3): 474–485. Bibcode:1932JChEd...9..474W. doi:10.1021/ed009p474.
27. Klaproth (1798) "Ueber die siebenbürgischenGolderze, und das in selbigenenthaltene neueMetall" (On the Transylvanian gold ore, and the new metal contained in it), *ChemischeAnnalenfür die Freunde der Naturlehre, Arzneigelahrtheit, Haushaltungskunst und Manufacturen* (Chemical Annals for the Friends of Science, Medicine, Economics, and Manufacturing), 1 : 91–104. From page 100: "*und welchemichhiermit den, von der altenMuttererdeentlehnten, Namen Tellurium beylege.*" and to which I hereby bestow the name tellurium, derived from the old Mother of the Earth.)
28. Weeks, Mary Elvira (1935). "The discovery of tellurium". *Journal of Chemical Education*. 12 (9): 403–408. Bibcode:1935JChEd..12..403W. doi:10.1021/ed012p403.
29. Jump up to:^{a b} George, Micheal W. (2007). "Mineral Yearbook 2007: Selenium and Tellurium"(PDF). United States geological Survey.
30. Jump up to:^{a b c d e f g} Wiberg, Egon; Holleman, Arnold Frederick (2001). Nils Wiberg (ed.). *Inorganic chemistry*. translated by Mary Eagleson. Academic Press. p. 588. ISBN 0-12-352651-5.
31. "An Arizona tellurium rush?". *arizonageology.blogspot.com*. May 21, 2007. Retrieved 2009-08-08.
32. "Byproducts Part I: Is There a Tellurium Rush in the Making?". *resourceinvestor.com*. April 19, 2007. Retrieved 2009-08-08.
33. Crow, James Mitchell (2011). "13 elements you can't live without". *New Scientist*. 210(2817):39. Bibcode:2011NewSc.210...36C. doi:10.1016/S0262-4079(11)61452-8.

34. Addicks, Lawrence (2008). "By-Products". Copper Refining. Read books. pp. 111–114. ISBN 978-1-4437-3230-7.
35. Brown, T. J. (2011). World mineral statistics British Geological Survey. Keyworth, Nottingham. p. 95. ISBN 978-0-85272-677-8.
36. Jump up to:^{a b} Roscoe, Henry Enfield; Schorlemmer, Carl (1878). A treatise on chemistry. 1. Appleton. pp. 367–368.
37. Jump up to:^{a b c d} Emeleus, H. J. (1990). A. G. Sykes (ed.). Advances in Inorganic Chemistry. 35. Academic Press. ISBN 0-12-023635-4.
38. Holloway, John H.; Laycock, David (1983). "Preparations and Reactions of Inorganic Main-Group Oxide-Fluorides". In Harry Julius Emeléus; A. G. Sharpe (eds.). Advances in inorganic chemistry and radiochemistry. Serial Publication Series. 27. Academic Press. p. 174. ISBN 0-12-023627-3.
39. Xu, Zhengtao (2007). "Recent developments in binary halogen-chalcogen compounds, polyanions and polycations". In Francesco A. Devillanova (ed.). Handbook of chalcogen chemistry: new perspectives in sulfur, selenium and tellurium. Royal Society of Chemistry. pp. 457–466. ISBN 978-0-85404-366-8.
40. Schwartz, Mel M. (2002). "Tellurium". Encyclopedia of materials, parts, and finishes(2nd ed.). CRC Press. ISBN 1-56676-661-3.
41. Divers, Edward; Shimosé, M. (1883). "On a new oxide of tellurium". Journal of the Chemical Society. 43: 319–323. doi:10.1039/CT8834300319.
42. Jump up to:^{a b} Dutton, W. A.; Cooper, W. Charles (1966). "The Oxides and Oxyacids of Tellurium". Chemical Reviews. 66 (6): 657–675. doi:10.1021/cr60244a003.
43. Jump up to:^{a b} Wickleder, Mathias S. (2007). "Chalcogen-Oxygen Chemistry". In Francesco A. Devillanova (ed.). Handbook of chalcogen chemistry: new perspectives in sulfur, selenium and tellurium. Royal Society of Chemistry. pp. 348–350. ISBN 978-0-85404-366-8.
44. Molnar, Arpad; Olah, George Andrew; Surya Prakash, G. K.; Sommer, Jean (2009). Superacid Chemistry (2nd ed.). Wiley-Interscience. pp. 444–445. ISBN 978-0-471-59668-4.
45. Sadekov, I. D.; Zakharov, A. V. (1999). "Stable tellurols and their metal derivatives". Russian Chemical Reviews. 68 (11): 909–923. Bibcode:1999RuCRv..68..909S. doi:10.1070/RC1999v068n11ABEH000544.
46. Guo, W. X.; Shu, D.; Chen, H. Y.; Li, A. J.; Wang, H.; Xiao, G. M.; Dou, C. L.; Peng, S. G.; Wei, W. W.; Zhang, W.; Zhou, H. W.; Chen, S. (2009). "Study on the structure and

- property of lead tellurium alloy as the positive grid of lead-acid batteries". *Journal of Alloys and Compounds*. 475 (1–2): 102–109. doi:10.1016/j.jallcom.2008.08.011.
47. Fthenakis, Vasilis M.; Kim, HyungChul; Alsema, Erik (2008). "Emissions from Photovoltaic Life Cycles". *Environmental Science & Technology*. 42 (6): 2168–2174. Bibcode:2008EnST...42.2168F. doi:10.1021/es071763q. hdl:1874/32964. PMID 18409654.
 48. Sinha, Parikhit; Kriegner, Christopher J.; Schew, William A.; Kaczmar, Swiatoslav W.; Traister, Matthew; Wilson, David J. (2008). "*Regulatory policy governing cadmium-telluride photovoltaics: A case study contrasting life cycle management with the precautionary principle*". *Energy Policy*. 36: 381–387. doi:10.1016/j.enpol.2007.09.017.
 49. Zweibel, K. (2010). "*The Impact of Tellurium Supply on Cadmium Telluride Photovoltaics*". *Science*. 328 (5979): 699–701. Bibcode:2010Sci...328..699Z. doi:10.1126/science.1189690. PMID 20448173. S2CID 29231392.
 50. Saha, Gopal B. (2001). "*Cadmium zinc telluride detector*". *Physics and radiobiology of nuclear medicine*. New York: Springer. pp. 87–88. ISBN 978-0-387-95021-1.
 51. Willardson, R.K.; Beer, Albert C, eds. (1981). *Mercury cadmium telluride*. New York: Academic Press. ISBN 978-0-12-752118-3.
 52. Capper, Peter; Elliott, C. T., eds. (2001). "*Metalorganic vapour phase epitaxy*". *Infrared detectors and emitters: materials and devices*. Boston, Mass.: Kluwer Academic. pp. 265–267. ISBN 978-0-7923-7206-6.
 53. Shenai-Khatkhate, Deodatta V.; Webb, Paul; Cole-Hamilton, David J.; Blackmore, Graham W.; Brian Mullin, J. (1988). "*Ultra-pure organotellurium precursors for the low-temperature MOVPE growth of II/VI compound semiconductors*". *Journal of Crystal Growth*. 93 (1–4): 744–749. Bibcode:1988JCrGr..93..744S. doi:10.1016/0022-0248(88)90613-6.
 54. Shenai-Khatkhate, Deodatta V.; Parker, M. B.; McQueen, A. E. D.; Mullin, J. B.; Cole-Hamilton, D. J.; Day, P. (1990). "Organometallic Molecules for Semiconductor Fabrication [and Discussion]". *Phil. Trans. R. Soc. Lond. A*. 330 (1610): 173–182. Bibcode:1990RSPTA.330..173S. doi:10.1098/rsta.1990.0011. S2CID.
 55. Mullin, J.B.; Cole-Hamilton, D.J.; Shenai-Khatkhate, D.V.; Webb P. (May 26, 1992) U.S. Patent 5,117,021 "Method for purification of tellurium and selenium alkyls"
 56. Farivar, Cyrus (2006-10-19). "Panasonic says that its 100GB Blu-ray discs will last a century". Retrieved 2008-11-13.

57. Nishiuchi, Kenichi; Kitaura, Hideki; Yamada, Noboru; Akahira, Nobuo (1998). "Dual-Layer Optical Disk with Te–O–Pd Phase-Change Film". *Japanese Journal of Applied Physics*. 37(4B):2163–2167.
58. Hudgens, S.; Johnson, B. (2004). "*Overview of Phase-Change Chalcogenide Nonvolatile Memory Technology*". *MRS Bulletin*. 29 (11): 829–832. doi:10.1557/mrs2004.236.
59. Geppert, Linda (2003). "The New Indelible Memories". *IEEE Spectrum*. 40 (3): 48–54. doi:10.1109/MSPEC.2003.1184436.
60. Taft, E.; Apker, L. (1953-02-01). "Photoemission from Cesium and Rubidium Tellurides". *JOSA*. 43 (2):81–83.
61. Rao, T., & Dowell, D. H. (2013). *An engineering guide to photoinjectors*. CreateSpace Independent Publishing.
62. LCLS-II Project Team. (2015). *LCLS-II Final Design Report (LCLSII-1.1-DR-0251-R0)*. SLAC.
63. "*Bi-alkali telluride photocathode*", issued 1978-07-20
64. Trautner, H. (2000). *Spectral Response of Cesium Telluride and Rubidium Telluride Photocathodes for the Production of Highly Charged Electron Bunches*. CERN.
65. Jump up to:^{a b} Lide, D. R., ed. (2005). *CRC Handbook of Chemistry and Physics* (86th ed.). Boca Raton (FL): CRC Press. ISBN 0-8493-0486-5.
66. Nishii, J.; Morimoto, S.; Inagawa, I.; Iizuka, R.; Yamashita, T.; Yamagishi, T. (1992). "Recent advances and trends in chalcogenide glass fiber technology: a review". *Journal of Non-Crystalline Solids*. 140: 199–208.
67. El-Mallawany, Raouf A. H. (2002). *Tellurite glasses handbook: physical properties and data*. CRC Press. pp. 1–11. ISBN 978-0-8493-0368-5.
68. Johnson, L. B. (1960). "*Correspondence. Representing Delay Powder Data*". *Industrial & Engineering Chemistry*. 52 (10): 868. doi:10.1021/ie50610a035.
69. Petraghani, Nicola; Wai-Ling, Lo (September 1998). "Organometallic Reagents for Synthetic Purposes: Tellurium". *Journal of the Brazilian Chemical Society*. 9 (5): 415–425. doi:10.1590/S0103-50531998000500002. ISSN 0103-5053.
70. Comasseto, João V.; Toledo, Fabiano T.; Vargas, Fabricio (2010). "N-Functionalized organolithium compounds via tellurium/lithium exchange reaction". *Journal of the Brazilian Chemical Society*. 21 (11): 2072–2078. doi:10.1590/S0103-50532010001100007. ISSN 0103-5053.
71. Morton, Maurice (1987). "Sulfur and Related Elements". *Rubber Technology*. Springer. p. 42. ISBN 978-0-412-53950-3.

72. Kwantes, W. (1984). *"Diphtheria in Europe"*. The Journal of Hygiene. 93 (3): 433–437. doi:10.1017/S0022172400065025. JSTOR 3862778. PMC 2129475. PMID 6512248.
73. Amakawa, Kazuhiko; Kolen'Ko, Yury V.; Villa, Alberto; Schuster, Manfred E.; Csepei, Lénárd-István; Weinberg, Gisela; Wrabetz, Sabine; Naumann d'Alnoncourt, Raoul; Girgsdies, Frank; Prati, Laura; Schlögl, Robert; Trunschke, Annette (2013). *"Multifunctionality of Crystalline MoV(TeNb) M1 Oxide Catalysts in Selective Oxidation of Propane and Benzyl Alcohol"*. ACS Catalysis. 3 (6): 1103–1113. doi:10.1021/cs400010q.
74. Csepei, L.-I. (2011). "Kinetic studies of propane oxidation on Mo and V based mixed oxide catalysts". PhD Thesis, Technische Universität, Berlin.
75. Hävecker, Michael; Wrabetz, Sabine; Kröhnert, Jutta; Csepei, Lenard-Istvan; Naumann d'Alnoncourt, Raoul; Kolen'Ko, Yury V.; Girgsdies, Frank; Schlögl, Robert; Trunschke, Annette (2012). "Surface chemistry of phase-pure M1 MoVTeNb oxide during operation in selective oxidation of propane to acrylic acid". Journal of Catalysis. 285: 48–60. doi:10.1016/j.jcat.2011.09.012. hdl:11858/00-001M-0000-0012-1BEB-F.
76. Naumann d'Alnoncourt, Raoul; Csepei, Lénárd-István; Hävecker, Michael; Girgsdies, Frank; Schuster, Manfred E.; Schlögl, Robert; Trunschke, Annette (2014). *"The reaction network in propane oxidation over phase-pure MoVTeNb M1 oxide catalysts"*. Journal of Catalysis. 311: 369–385. doi:10.1016/j.jcat.2013.12.008. hdl:11858/00-001M-0000-0014-F434-5.
77. [http://www.nordion.com/wp-content/uploads/2014/10/MI_Iodine_131_Solution_Canada.pdf]
78. Atta-ur- Rahman (2008). Studies in Natural Products Chemistry. Elsevier. pp. 905–. ISBN 978-0-444-53181-0.
79. Chua SL, Sivakumar K, Rybtke M, Yuan M, Andersen JB, Nielsen TE, Givskov M, Tolker-Nielsen T, Cao B, Kjelleberg S, Yang L (2015). *"C-di-GMP regulates Pseudomonas aeruginosa stress response to tellurite during both planktonic and biofilm modes of growth"*. Scientific Reports.
80. Ottosson, L. G.; Logg, K.; Ibstedt, S.; Sunnerhagen, P.; Käll, M.; Blomberg, A.; Warringer, J. (2010). "Sulfate assimilation mediates tellurite reduction and toxicity in *Saccharomyces cerevisiae*". Eukaryotic Cell. 9 (10): 1635–47. doi:10.1128/EC.00078-10. PMC 2950436. PMID 20675578.

81. Chasteen, Thomas G.; Bentley, Ronald (2003). "Biomethylation of Selenium and Tellurium: Microorganisms and Plants". *Chemical Reviews*. 103 (1): 1–26. doi:10.1021/cr010210+. PMID 12517179.
82. Taylor, Andrew (1996). "Biochemistry of tellurium". *Biological Trace Element Research*. 55(3):2319. doi:10.1007/BF02785282. PMID 9096851. S2CID 10691234.
83. PubchemLCSS <https://pubchem.ncbi.nlm.nih.gov/compound/6327182#datasheet=LCSS§ion=GHS-Classification>
84. "Tellurium 452378". Sigma-Aldrich.
85. Jump up to:^{a b} Harrison, W.; Bradberry, S.; Vale, J. (1998-01-28). "Tellurium". International Programme on Chemical Safety. Retrieved 2007-01-12.
86. Kean, Sam (2017). "The Scent of a Molecule". *Distillations*. 3 (3): 5. Retrieved May 16,2018.
87. Wright, PL; B (1966). "Comparative metabolism of selenium and tellurium in sheep and swine". *American Journal of Physiology. Legacy Content*. 211 (1): 6–10. doi:10.1152/ajplegacy.1966.211.1.6. PMID 5911055.
88. Müller, R.; Zschesche, W.; Steffen, H. M.; Schaller, K. H. (1989). "Tellurium-intoxication". *KlinischeWochenschrift*. 67 (22): 1152–5. doi:10.1007/BF01726117. PMID 2586020.
89. Taylor, Andrew (1996). "Biochemistry of tellurium". *Biological Trace Element Research*. 55(3): 231–239. doi:10.1007/BF02785282. PMID 9096851. S2CID 10691234.
90. " CDC – NIOSH Pocket Guide to Chemical Hazards – Tellurium". www.cdc.gov. Retrieved 2015-11-24.
91. Skoog, Douglas A.; Holler, F. James; Crouch, Stanley R. (2007). *Principles of Instrumental Analysis* (6th ed.). Belmont, CA: Thomson Brooks/Cole. pp. 169–173. ISBN 978-0-495-01201-6.
92. Jump up to:a b Metha, Akul (13 December 2011). "Principle". PharmaXChange.info.
93. Metha, Akul (22 April 2012). "Derivation of Beer–Lambert Law". PharmaXChange.info.
94. Misra, Prabhakar; Dubinskii, Mark, eds. (2002). *Ultraviolet Spectroscopy and UV Lasers*. New York: Marcel Dekker. ISBN 978-0-8247-0668-5.
95. Stokes, Debbie J. (2008). *Principles and Practice of Variable Pressure Environmental Scanning Electron Microscopy (VP-ESEM)*.
96. Chichester: John Wiley & Sons. ISBN 978-0470758748.McMullan, D. (2006). "Scanning electron microscopy 1928–1965".
97. *Scanning*. **17** (3): 175–185. doi:10.1002/sca.4950170309. PMC 2496789.

98. McMullan, D. (1988). "Von Ardenne and the scanning electron microscope". *Proc Roy Microsc Soc.* **23**: 283–288.
99. Knoll, Max (1935). "Aufladepotential und Sekundäremissionselektronenbestrahlter Körper". *Zeitschrift für Technische Physik.* 16: 467–475
100. Tille, P. (2017). *Bailey & Scott's Diagnostic Microbiology* (14 edition). Mosby.
101. Madigan Michael T, Bender, Kelly S, Buckley, Daniel H, Sattley, W. Matthew, & Stahl, David A. (2018).
102. *Brock Biology of Microorganisms* (15th Edition). Pearson.
103. Bish, DL and Post, JE, editors. 1989. *Modern Powder Diffraction*. Reviews in Mineralogy, v. 20. Mineralogical Society of America.
104. Cullity, B. D. 1978. *Elements of X-ray diffraction*. 2nd ed. Addison-Wesley, Reading, Mass.
105. Klug, H. P., and L. E. Alexander. 1974. *X-ray diffraction procedures for polycrystalline and amorphous materials*. 2nd ed. Wiley, New York.
106. Moore, D. M. and R. C. Reynolds, Jr. 1997. *X-Ray diffraction and the identification and analysis of clay minerals*. 2nd Ed. Oxford University Press, New York.
107. "The Infracord double-beam spectrophotometer". *Clinical Science.* 16 (2). 1957.
108. "Agilent Technologies to Acquire Varian, Inc. for \$1.5 Billion". *Agilent.* July 27, 2009. Brault, James W. (1996).
109. "New Approach to high-precision Fourier transform spectrometer design". *Applied Optics.* 35 (16): 2891–2896. Bibcode:1996ApOpt..35.2891B. doi:10.1364/AO.35.002891. PMID 21085438 Connes, J.; Connes, P. (1966).
110. "Near-Infrared Planetary Spectra by Fourier Spectroscopy. I. Instruments and Results". *Journal of the Optical Society of America.* 56 (7): 896–910. doi:10.1364/JOSA.56.000896. Smith, D.R.; Morgan, R.L.; Loewenstein, E.V. (1968).

AN INHIBITION STUDY OF DIABETES

A project submitted to

ST MARY'S COLLEGE (Autonomous), Thoothukudi

Affiliated to

Manonmaniam Sundaranar University,

Tirunelveli

In partial fulfilment of the award of the degree of

MASTER OF SCIENCE IN CHEMISTRY

Submitted by

L.LINGA PRABHA

Reg. No: 19SPCH01

Under the Supervision and Guidance of

Dr.C.Zozimus Divya Lobo



PG DEPARTMENT OF CHEMISTRY (SSC)

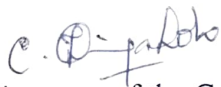
St. Mary's College (Autonomous),

Thoothukudi

April – 2021

CERTIFICATE

This is to certify that this project work entitled " ANA INHIBITION STUDY OF DIABETES" is submitted to **St. Mary's College (Autonomous)**, Thoothukudi affiliated to **Manonmaniam Sundaranar University**, Tirunelveli in partial fulfilment for the award of the **Degree of Master of Science in Chemistry** and this work done during the year 2020 - 2021 by **L.LINGA PRABHA** (Reg. No: 19SPCH01)



Signature of the Guide



Signature of the Coordinator



Signature of the Examiner



Signature of the Director

Director

Self Supporting Courses

St. Mary's College (Autonomous)

Thoothukudi - 628 001.



Signature of Principal

Principal

St. Mary's College (Autonomous)

Thoothukudi - 628 001.

DECLARATION

I do hereby declare that the project entitled "**IN-SILICO DESIGN OF NOVEL INHIBITORS OR DIABETES FROM ALKALOIDS AND FLAVONIDS** " submitted for the degree of Master of Science in Chemistry is my original work carried out under the guidance of **Mrs.C.ZOZIMUS DIVYA LOBO M.Sc.,M.Phil.,Ph.D; Assistant Professor, PG Department of Chemistry (SSC), St. Mary's College (Autonomous), Thoothukudi** and that it has not previously formed the basis for award of any Degree.

Station: Thoothukudi

Date:

L.LINGA PRABHA

ACKNOWLEDGEMENT

I express my first and humble thanks to **GOD ALMIGHTY** for giving an opportunity to devote this work

I would like to express my sincere thanks to our principal **Dr. Sr. A.S.J. LUCIA ROSE**, Secretary **Sr. FLORA MARY**, Deputy principal **Dr. S. C. SHIBANA** Director of SSC **Sr. F. MARY JOYCE BABY** and Dean of Physical Science, **Dr ANTONY RAJAM M.Sc., M. Phil., SET, Ph.D**, (SSC Coordinator), St Mary's College (Autonomous), Thoothukudi for providing the permission to complete the project work

I find it difficult for me to write something in short to acknowledge my guide **Mrs C.ZOZIMUS DIVYA LOBO M.Sc., M.Phil., Ph.D**; she taught me to think and solve the unconventional problems in a conventional way. Her constant inspiration, evaluable guidance tremendous patience and constructive criticism helped a lot to focus my views in the proper perspective I take this opportunity to express my deepest sense of gratitude and reference towards her for guiding me in the right direction throughout the course of this work My deep personal regards are due for her forever

I heartly express my sincere thanks to my parents and Friends.

CONTENT

S.NO	TITTLE	PAGE NO
1	INTRODUCTION	11
2	REVIEW OF LITERATURE	21
3	SCOPE OF INVESTIGATION	29
4	MATERIALS AND METHODS	32
5	RESULT AND DISCUSSION	38
6	CONCLUSION	63
7	REFERENCE	65

LIST OF ABBRIVATION

IGT	--	Impaired Glucose Tolerance
IFG	---	Impaired Fasting Glycaemia
GDM	---	Gestational Diabetes Mellitus
WHO	---	World Health Organization
MHC	---	Major Histocompatibility complex
IL-1	---	Inter Leukin -1
TNF	---	Tumor necrosis factor
MODY	---	Maturity Onset Diabetes of Young
DM	---	Diabetes mellitus
IAPP	---	Islet Amyloid Polypeptide
GA	---	Genetic algorithm
SA	---	Simulated annealing
MMFF	---	Merck Molecular force field
IDDM	---	Insulin Dependent diabetes mellitus
NIDDM	---	Non-alcoholic diabetes mellitus

LIST OF TABLES

TABLE NO	DESCRIPTION	PAGE NO
1	Selected phytochemical compounds and their plant source	40
2	Binding energies of phytochemical compounds by using PyRX	56

LIST OF FIGURES

S.NO	DESCRIPTION	PAGE NO
1	Autoimmune attack in type 1 diabetes	17
2	Protein 3G5E	39
3	The structure of streptocin	41
4	The structure of antidysentric	42
5	The structure of eupalitin	43
6	The structure of insulinotropin	44
7	The structure of alloxan monohydrate	45
8	The structure of punicalin	46
9	The structure of terflavin	47
10	The structure of geranin	48
11	The structure of corilagin	49
12	The structure of granatin	50
13	The structure of hexokinase	51
14	The structure of glipenclamide	52

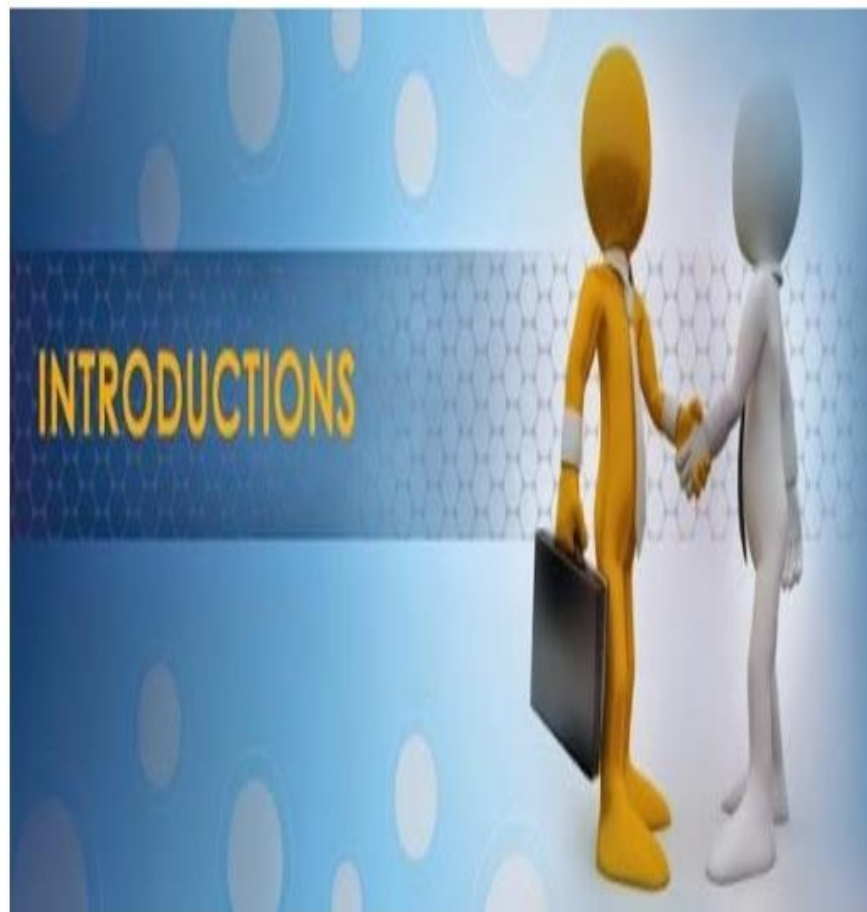
15	The structure of lupeol	53
16	The structure of campesterol	54
17	Docking complex and interactions of lupeol	58
18	Docking complex and interactions of corilagin	59
19	Docking complex and interactions of dumetroum	60
20	Docking complex and interactions of geranin	61
21	Docking complex and interactions of hexokinase	62

ABSTRACT

The metabolic disorder of diabetes mellitus is a fast global problem. It is a social health and economic consequences. These are two types of diabetes mellitus. The 3G5E protein is a control to the sugar serves as a drug target for diabetes mellitus. In the presence of molecular modelling study it is denominated that alkaloids and flavonoids. It is an interaction with 3G5E protein study alkaloids and flavonoids possess the properties of diabetes regulations. The binding pocket of insulin receptor and binding interaction of antagonist. It is inhibition activity and alternative therapeutic agent to replace the synthetic drugs of side effect. The blood sugar level is reduced slowly and continuous uses of ayurvedic drug are very safe because drug do not lead to hypoglycemia. The disease requires to medical diagnosis treatment and change in life style. The natural phytochemicals compound which contain hexokinase have high therapeutic efficiency.

CHAPTER I

INTRODUCTON



INTRODUCTION



Universal blue circle symbol for diabetes^[1]. Diabetes mellitus (DM), commonly known as diabetes, is a group of metabolic disorders characterized by a high blood sugar level over a prolonged period of time. Symptoms often include frequent urination, increased thirst and increased appetite.^[2] If left untreated, diabetes can cause many complications.^[2] Acute complications can include diabetic ketoacidosis, hyperosmolar hyperglycemic state, or death.^[3] Serious long-term complications include cardiovascular disease, stroke, chronic kidney disease, foot ulcers, damage to the nerves, damage to the eyes and cognitive impairment.^[2] Diabetes is due to either the pancreas not producing enough insulin, or the cells of the body not responding properly to the insulin produced.^[12] There are three main types of diabetes mellitus:^[2]

Type 1 diabetes results from failure of the pancreas to produce enough insulin due to loss of beta cells.^[2] This form was previously referred to as "insulin-dependent diabetes mellitus" (IDDM) or "juvenile diabetes".^[2] The loss of beta cells is caused by an autoimmune response.^[13] The cause of this autoimmune response is unknown.^[2]

Type 2 diabetes begins with insulin resistance, a condition in which cells fail to respond to insulin properly.^[2] As the disease progresses, a lack of insulin may also develop.^[14] This form was previously referred to as "non insulin-dependent diabetes mellitus" (NIDDM) or "adult-onset diabetes".^[2] The most common cause is a combination of excessive body weight and insufficient exercise.^[2]

Type 1 diabetes must be managed with insulin injections.^[2] Prevention and treatment of type 2 diabetes involves maintaining a healthy diet, regular physical exercise, a normal body weight, and avoiding use of tobacco.^[2] Type 2 diabetes may be treated with medications such as insulin sensitizers with or without insulin.^[15] Control of blood pressure and maintaining proper foot and eye care are important for people with the disease.^[2] Insulin and some oral medications can cause low blood sugar.^[16] Weight loss surgery in those with obesity is sometimes an effective measure in those with type 2 diabetes.^[17] Gestational diabetes usually resolves after the birth of the baby.^[18]

As of 2019, an estimated 463 million people had diabetes worldwide (8.8% of the adult population), with type 2 diabetes making up about 90% of the cases.^[10] Rates are similar in women and men.^[19] Trends suggest that rates will continue to rise.^[10] Diabetes at least doubles a person's risk of early death.^[2] In 2019, diabetes resulted in approximately 4.2 million deaths.^[10] It is the 7th leading cause of death globally.^{[20][21]} The global economic cost diabetes related health expenditure in 2017 was estimated at US\$727 billion.^[10] In the United States, diabetes cost nearly US\$327 billion in 2017.^[22] Average medical expenditures among people with diabetes are about 2.3 times higher.^[23]

Signs and symptoms

The classic symptoms of untreated diabetes are unintended weight loss, polyuria (increased urination), polydipsia (increased thirst), and polyphagia (increased hunger).^[24] Symptoms may develop rapidly (weeks or months) in type 1 diabetes, while they usually develop much more slowly and may be subtle or absent in type 2 diabetes.^[25]

Several other signs and symptoms can mark the onset of diabetes although they are not specific to the disease. In addition to the known ones above, they include blurred vision, headache, fatigue, slow healing of cuts, and itchy skin. Prolonged high blood glucose can cause glucose absorption in the lens of the eye, which leads to changes in its shape, resulting in vision changes. Long-term vision loss can also be caused by diabetic retinopathy. A number of skin rashes that can occur in diabetes are collectively known as diabetic dermadromes.^[26]

People with diabetes (usually but not exclusively in type 1 diabetes) may also experience diabetic ketoacidosis (DKA), a metabolic disturbance characterized by nausea,

vomiting and abdominal pain, the smell of acetone on the breath, deep breathing known as Kussmaul breathing, and in severe cases a decreased level of consciousness. DKA requires emergency treatment in hospital.^[27] A rarer but more dangerous condition is hyperosmolar hyperglycemic state (HHS), which is more common in type 2 diabetes and is mainly the result of dehydration caused by high blood sugars.^[27]

Treatment-related low blood sugar (hypoglycemia) is common in people with type 1 and also type 2 diabetes depending on the medication being used. Most cases are mild and are not considered medical emergencies. Effects can range from feelings of unease, sweating, trembling, and increased appetite in mild cases to more serious effects such as confusion, changes in behavior such as aggressiveness, seizures, unconsciousness, and rarely permanent brain damage or death in severe cases.^{[28][29]} Rapid breathing, sweating, and cold, pale skin are characteristic of low blood sugar but not definitive.^[30] Mild to moderate cases are self-treated by eating or drinking something high in rapidly absorbed carbohydrates. Severe cases can lead to unconsciousness and must be treated with intravenous glucose or injections with glucagon.^[31]

Complications

The major long-term complications relate to damage to blood vessels. Diabetes doubles the risk of cardiovascular disease^[32] and about 75% of deaths in people with diabetes are due to coronary artery disease.^[33] Other macrovascular diseases include stroke, and peripheral artery disease.

The primary complications of diabetes due to damage in small blood vessels include damage to the eyes, kidneys, and nerves.^[34] Damage to the eyes, known as diabetic retinopathy, is caused by damage to the blood vessels in the retina of the eye, and can result in gradual vision loss and eventual blindness.^[34] Diabetes also increases the risk of having glaucoma, cataracts, and other eye problems. It is recommended that people with diabetes visit an eye doctor once a year.^[35] Damage to the kidneys, known as diabetic nephropathy, can lead to tissue scarring, urine protein loss, and eventually chronic kidney disease, sometimes requiring dialysis or kidney transplantation.^[34] Damage to the nerves of the body, known as diabetic neuropathy, is the most common complication of diabetes.^[34] The symptoms can include numbness, tingling, pain, and altered pain sensation, which can lead to damage to the

skin. Diabetes-related foot problems (such as diabetic foot ulcers) may occur, and can be difficult to treat, occasionally requiring amputation. Additionally, proximal diabetic neuropathy causes painful muscle atrophy and weakness.

There is a link between cognitive deficit and diabetes. Compared to those without diabetes, those with the disease have a 1.2 to 1.5-fold greater rate of decline in cognitive function.^[36] Having diabetes, especially when on insulin, increases the risk of falls in older people.^[37]

Causes

Diabetes mellitus is classified into six categories: type 1 diabetes, type 2 diabetes, hybrid forms of diabetes, hyperglycemia first detected during pregnancy, "unclassified diabetes", and "other specific types".^[40] The "hybrid forms of diabetes" contains slowly evolving, immune-mediated diabetes of adults and ketosis-prone type 2 diabetes. The "hyperglycemia first detected during pregnancy" contains gestational diabetes mellitus and diabetes mellitus in pregnancy (type 1 or type 2 diabetes first diagnosed during pregnancy). The "other specific types" are a collection of a few dozen individual causes. Diabetes is a more variable disease than once thought and people may have combinations of forms.^[41] The term "diabetes", without qualification, refers to diabetes mellitus.^[42]

Type 1

Type 1 diabetes is characterized by loss of the insulin-producing beta cells of the pancreatic islets, leading to insulin deficiency. This type can be further classified as immune-mediated or idiopathic. The majority of type 1 diabetes is of the immune-mediated nature, in which a T cell-mediated autoimmune attack leads to the loss of beta cells and thus insulin.^[43] It causes approximately 10% of diabetes mellitus cases in North America and Europe. Most affected people are otherwise healthy and of a healthy weight when onset occurs. Sensitivity and responsiveness to insulin are usually normal, especially in the early stages. Although it has been called "juvenile diabetes" due to the frequent onset in children, the majority of individuals living with type 1 diabetes are now adults.^[6] "Brittle" diabetes, also known as unstable diabetes or labile diabetes, is a term that was traditionally used to describe the dramatic and recurrent swings in glucose levels, often occurring for no apparent reason in

insulin-dependent diabetes. This term, however, has no biologic basis and should not be used.^[44] Still, type 1 diabetes can be accompanied by irregular and unpredictable high blood sugar levels, and the potential for diabetic ketoacidosis or serious low blood sugar levels. Other complications include an impaired counterregulatory response to low blood sugar, infection, gastroparesis (which leads to erratic absorption of dietary carbohydrates), and endocrinopathies (e.g., Addison's disease).^[44] These phenomena are believed to occur no more frequently than in 1% to 2% of persons with type 1 diabetes.^[45] Type 1 diabetes is partly inherited, with multiple genes, including certain HLA genotypes, known to influence the risk of diabetes. In genetically susceptible people, the onset of diabetes can be triggered by one or more environmental factors,^[46] such as a viral infection or diet. Several viruses have been implicated, but to date there is no stringent evidence to support this hypothesis in humans.^{[46][47]} Among dietary factors, data suggest that gliadin (a protein present in gluten) may play a role in the development of type 1 diabetes, but the mechanism is not fully understood.^{[48][49]}

Type 1 diabetes can occur at any age, and a significant proportion is diagnosed during adulthood. Latent autoimmune diabetes of adults (LADA) is the diagnostic term applied when type 1 diabetes develops in adults; it has a slower onset than the same condition in children. Given this difference, some use the unofficial term "type 1.5 diabetes" for this condition. Adults with LADA are frequently initially misdiagnosed as having type 2 diabetes, based on age rather than cause.^[50]

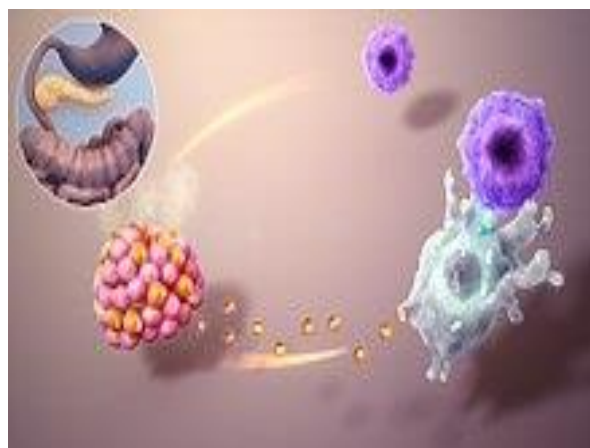


Fig.1 Autoimmune attack in type 1 diabetes.

Type 2

Type 2 diabetes is characterized by insulin resistance, which may be combined with relatively reduced insulin secretion.^[12] The defective responsiveness of body tissues to insulin is believed to involve the insulin receptor. However, the specific defects are not known. Diabetes mellitus cases due to a known defect are classified separately. Type 2 diabetes is the most common type of diabetes mellitus.^[2] Many people with type 2 diabetes have evidence of prediabetes (impaired fasting glucose and/or impaired glucose tolerance) before meeting the criteria for type 2 diabetes.^[51] The progression of prediabetes to overt type 2 diabetes can be slowed or reversed by lifestyle changes or medications that improve insulin sensitivity or reduce the liver's glucose production.^[52]

Type 2 diabetes is primarily due to lifestyle factors and genetics.^[53] A number of lifestyle factors are known to be important to the development of type 2 diabetes, including obesity (defined by a body mass index of greater than 30), lack of physical activity, poor diet, stress, and urbanization.^[38] Excess body fat is associated with 30% of cases in people of Chinese and Japanese descent, 60–80% of cases in those of European and African descent, and 100% of Pima Indians and Pacific Islanders.^[12] Even those who are not obese may have a high waist–hip ratio.^[12]

Dietary factors such as sugar-sweetened drinks are associated with an increased risk.^{[54][55]} The type of fats in the diet is also important, with saturated fat and trans fats increasing the risk and polyunsaturated and monounsaturated fat decreasing the risk.^[53] Eating white rice excessively may increase the risk of diabetes, especially in Chinese and Japanese people.^[56] Lack of physical activity may increase the risk of diabetes in some people.^[57]

Adverse childhood experiences (ACEs), including abuse, neglect, and household difficulties, increase the likelihood of type 2 diabetes later in life by 32%, with neglect having the strongest effect.^[58]

Gestational diabetes

Gestational diabetes resembles type 2 diabetes in several respects, involving a combination of relatively inadequate insulin secretion and responsiveness. It occurs in about 2–10% of

all pregnancies and may improve or disappear after delivery.^[59] It is recommended that all pregnant women get tested starting around 24–28 weeks gestation.^[60] It is most often diagnosed in the second or third trimester because of the increase in insulin-antagonist hormone levels that occurs at this time.^[60] However, after pregnancy approximately 5–10% of women with gestational diabetes are found to have another form of diabetes, most commonly type 2.^[59] Gestational diabetes is fully treatable, but requires careful medical supervision throughout the pregnancy. Management may include dietary changes, blood glucose monitoring, and in some cases, insulin may be required.^[61]

Though it may be transient, untreated gestational diabetes can damage the health of the fetus or mother. Risks to the baby include macrosomia (high birth weight), congenital heart and central nervous system abnormalities, and skeletal muscle malformations. Increased levels of insulin in a fetus's blood may inhibit fetal surfactant production and cause infant respiratory distress syndrome. A high blood bilirubin level may result from red blood cell destruction. In severe cases, perinatal death may occur, most commonly as a result of poor placental perfusion due to vascular impairment. Labor induction may be indicated with decreased placental function. A caesarean section may be performed if there is marked fetal distress or an increased risk of injury associated with macrosomia, such as shoulder dystocia.^[62]

Other type

Maturity onset diabetes of the young (MODY) is a rare autosomal dominant inherited form of diabetes, due to one of several single-gene mutations causing defects in insulin production.^[63] It is significantly less common than the three main types, constituting 1–2% of all cases. The name of this disease refers to early hypotheses as to its nature. Being due to a defective gene, this disease varies in age at presentation and in severity according to the specific gene defect; thus there are at least 13 subtypes of MODY. People with MODY often can control it without using insulin.^[64]

Some cases of diabetes are caused by the body's tissue receptors not responding to insulin (even when insulin levels are normal, which is what separates it from type 2 diabetes); this form is very uncommon. Genetic mutations (autosomal or mitochondrial) can lead to defects in beta cell function. Abnormal insulin action may also have been genetically determined in some cases.

Any disease that causes extensive damage to the pancreas may lead to diabetes (for example, chronic pancreatitis and cystic fibrosis). Diseases associated with excessive secretion of insulin-antagonistic hormones can cause diabetes (which is typically resolved once the hormone excess is removed). Many drugs impair insulin secretion and some toxins damage pancreatic beta cells, whereas others increase insulin resistance (especially glucocorticoids which can provoke "steroid diabetes"). The ICD-10 (1992) diagnostic entity, malnutrition-related diabetes mellitus (MRDM or MMDM, ICD-10 code E12), was deprecated by the World Health Organization (WHO) when the current taxonomy was introduced in 1999.^[65] Yet another form of diabetes that people may develop is double diabetes. This is when a type 1 diabetic becomes insulin resistant, the hallmark for type 2 diabetes or has a family history for type 2 diabetes.^[66] It was first discovered in 1990 or 1991. The following is a list of disorders that may increase the risk of diabetes:^[67]

1. Genetic defects of β -cell function
 - a. Maturity onset diabetes of the young
 - b. Mitochondrial DNA mutations
2. Genetic defects in insulin processing or insulin action
 - a. Defects in proinsulin conversion
 - b. Insulin gene mutations
 - c. Insulin receptor mutations
3. Exocrine pancreatic defects
 - a. Chronic pancreatitis
 - b. Pancreatectomy
 - c. Pancreatic neoplasia
 - d. Cystic fibrosis
 - e. Hemochromatosis
 - f. Fibrocalculous pancreatopathy

pathophysiology

Insulin is the principal hormone that regulates the uptake of glucose from the blood into most cells of the body, especially liver, adipose tissue and muscle, except smooth muscle, in which

insulin acts via the IGF-1. Therefore, deficiency of insulin or the insensitivity of its receptors play a central role in all forms of diabetes mellitus.^[69]

The body obtains glucose from three main sources: the intestinal absorption of food; the breakdown of glycogen (glycogenolysis), the storage form of glucose found in the liver; and gluconeogenesis, the generation of glucose from non-carbohydrate substrates in the body.^[70] Insulin plays a critical role in regulating glucose levels in the body. Insulin can inhibit the breakdown of glycogen or the process of gluconeogenesis, it can stimulate the transport of glucose into fat and muscle cells, and it can stimulate the storage of glucose in the form of glycogen.^[70]

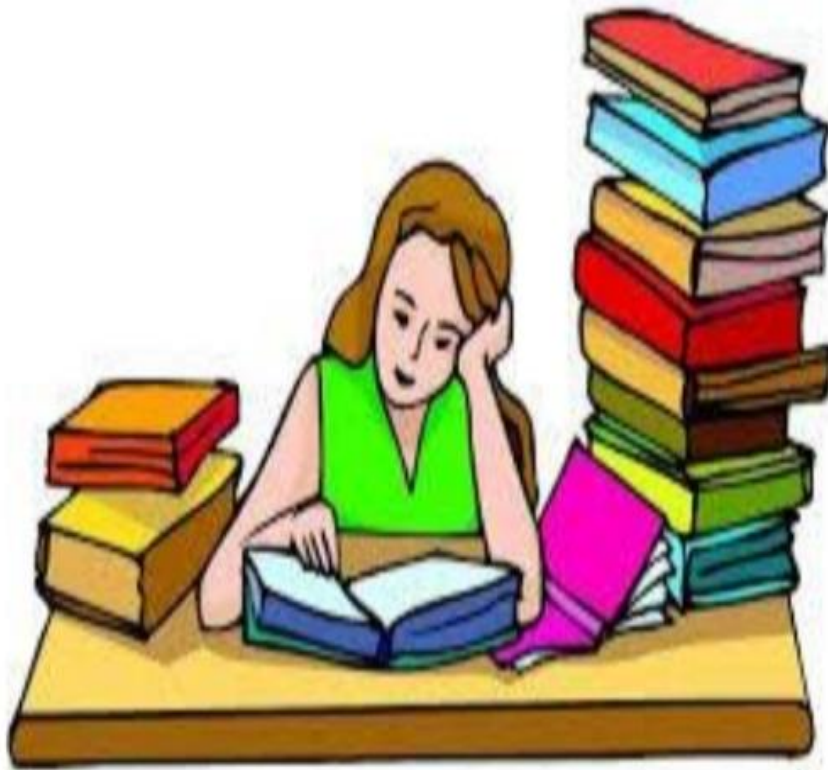
Insulin is released into the blood by beta cells (β -cells), found in the islets of Langerhans in the pancreas, in response to rising levels of blood glucose, typically after eating. Insulin is used by about two-thirds of the body's cells to absorb glucose from the blood for use as fuel, for conversion to other needed molecules, or for storage. Lower glucose levels result in decreased insulin release from the beta cells and in the breakdown of glycogen to glucose. This process is mainly controlled by the hormone glucagon, which acts in the opposite manner to insulin.^[71]

If the amount of insulin available is insufficient, or if cells respond poorly to the effects of insulin (insulin resistance), or if the insulin itself is defective, then glucose is not absorbed properly by the body cells that require it, and is not stored appropriately in the liver and muscles. The net effect is persistently high levels of blood glucose, poor protein synthesis, and other metabolic derangements, such as metabolic acidosis in cases of complete insulin deficiency.^[70]

When glucose concentration in the blood remains high over time, the kidneys reach a threshold of reabsorption, and the body excretes glucose in the urine (glycosuria).^[72] This increases the osmotic pressure of the urine and inhibits reabsorption of water by the kidney, resulting in increased urine production (polyuria) and increased fluid loss. Lost blood volume is replaced osmotically from water in body cells and other body compartments, causing dehydration and increased thirst (polydipsia).^[70] In addition, intracellular glucose deficiency stimulates appetite leading to excessive food intake (polyphagia).^[73]

CHAPTER II

REVIEW OF LITERATURE



CHAPTER II

REVIEW OF LITERATURE

Ashrita c .Haldipur ,N.Srividya et.al 2020 suggest that The study reports the in vitro antihyperglycemic potential of Bamboo seed rice/BSR, a brown rice from *Bambusa arundinacea* species in comparison to a traditional Indian brown rice - Garudan samba/GS from *Oryza sativa* species using an integrated approach. Untargeted phenolic profiling using Q-TOF-LC-MS/MS confirmed sixty-three phenolic metabolites in BSR and thirty-nine in GS. The most abundant phenolics in BSR and GS were gallic acid, 4-hydroxybenzaldehyde, caffeic acid 4-O-glucoside and *p*-coumaric acid. Additionally, eriocitrin was abundant in BSR and cirsimaritin in GS. Predicted glycemic index determined using an in vitro starch digestibility technique indicated BSR to be a low GI variety and GS a moderate GI variety. In terms of antihyperglycemic enzyme inhibitory potential, BSR exhibited better α -amylase inhibition, whereas GS exhibited greater inhibition of dipeptidyl peptidase IV. This was further confirmed using molecular docking techniques which revealed that eriocitrin and cirsimaritin were strong inhibitors of α -amylase and DPP IV enzymes. The study thus revealed brown rice varieties from both *Bambusa sp.* and *Oryza sp.* as healthier options to white rice in the dietary management of diabetes and as good sources of several bioactive phenolic compounds.

S. Prabhu, S.Vijaya kumar, P.Manogar, Gaanty pragas maniyam,Natanamurugaraj Govindam et.al 2017 suggested that Peroxisome proliferator-activated receptor gamma (PPAR γ), a type II nuclear receptor present in adipose tissue, colon and macrophages. It reduces the hyperglycemia associated metabolic syndromes. Particularly, type II diabetes-related cardiovascular system risk in human beings. The fatty acid storage and glucose metabolism are regulated by PPAR γ activation in human body. According to recent reports commercially available PPAR γ activating drugs have been causing severe side effects.

At the same time, natural products have been proved to be a promising area of drug discovery. Recently, many studies have been attempted to screen and identify a potential drug candidate to activate PPAR γ . Hence, in this study we have selected some of the bio-active molecules from traditional medicinal plants. Molecular docking studies have been carried out against the target, PPAR γ . We Results suggested that Punigluconin has a efficient docking score and it is found to have good binding affinities than other ligands. Hence, we concluded that Punigluconin is a better drug candidate for activation of PPAR γ gene expression. Further studies are necessary to confirm their efficacy and possibly it can develop as a potential drug in future

Rangachari Balamurugan, Antony stalin, Savarimuthu gnacimuthu et.al suggest that γ -sitosterol isolated from *Lippia nodiflora* was taken as ligand for molecular docking. The molecular targets, glucokinase, Fructose 1, 6- bisphosphatase 1, Human multidrug resistance protein 1 and Cytochromes P450 whose crystallographic structures are available on the PDB database as 1V4S, 2JJK, 3LC4, 2CBZ respectively, were used for the docking analysis using the Autodock tool v 4.2 and ADT v1.5.4 programs. The docking studies of the ligand γ - sitosterol with four different target proteins showed that this is a good molecule which docks well with various targets related to diabetes mellitus. Hence γ -sitosterol can be considered for developing into a potent antidiabetic drug.

Rishita Dey, Sisir Nandi, Asmita Samadder et.al 2020 suggest that Food-additive toxicity has become a major health hazard issue globally. Alloxan (ALX), a food-additive, intaken daily through flour causes diabetes and genotoxicity by inducing chromosomal-aberration and DNA-damage. The use of phytochemicals as a protective measure of health hazards has become quite evident because of their least side effects. Pelargonidin (PG), one such phyto-product, have an anti-genotoxic and anti-diabetic effect. In this study, the possibility of PG to inhibit alloxan-induced chromosomal-aberration and DNA-damage was assessed in mice model in vivo and the experimental outcome was validated theoretically through in silico structure-based molecular docking study. Results of the mitotic-index observed from the PG-pre-treated-alloxan-administered (PG+ALX) mice group revealed a significant reduction in chromosomal-anomaly, DNA-damage, and an upregulation of the p53 and PARP protein expression when compared to the ALX-treated mice group. Additionally, the in silico molecular docking study predicted the biochemical mechanism of actions of pelargonidin by identifying the two important amino acid residues p53 and PARP as the active bio-targets of

pelargonidin. Therefore, results of our present *in vivo* and *silico* studies implicate that pelargonidin could effectively restrict DNA-damage and chromosomal-aberration by modulating PARP and p53 repair proteins showing its ability for possible protein-drug interaction, an effective therapeutic tool in future drug discovery.

Moshtak Ahmed Jaseem Al Jaseem , K.M.Abdullah ,Faizan Abul Qais,Anas Shami,Imrana Naseem et.al 2021 suggest that iabetAdvanced glycation end products (AGEs) formation produces free radicals that play a role in diabetes mellitus; hence inhibition of glycation plays a part in minimizing diabetes-related complications. This study was intended to examine the AGEs formation of HSA upon prolonged incubation of 28 days at 37 °C and further investigate the antiglycation potential of folic acid (FA). FA shows a significant binding affinity to the HSA with a binding constant (K) of 10^4 M^{-1} . The evaluation of enthalpy change (ΔH^0) and entropy change (ΔS^0) implied that the HSA-FA complex is stabilized primarily by hydrophobic interaction and hydrogen bonding. Molecular docking analysis depicted that FA binds with HSA in subdomain IIA (Sudlow's site I) with a binding energy of $-7.0 \text{ kcal mol}^{-1}$. AGEs were characterized by free lysine and thiol groups, carbonyl content, and AGEs specific fluorescence. The presence of FA significantly decreased glycation from free lysine and carbonyl content estimation and AGEs specific fluorescence. Multispectroscopic observations and molecular docking and examination of various biomarkers demonstrate the antiglycation activity of FA and its capacity to prevent disease progression in diabetes.

S.Pangajavalli ,R.ranjith kumar,S. Ramaswamy et.al 2020 suggest that In the present study, a novel 6b', 7', 8', 9'-Tetrahydro-2*H*,6'*H*-Spiro [acenaphthylene-1,11'-chromeno [3,4-*a*] pyrrolizine]-2,6' (6a'*H*,11a'*H*)- dione (ACPD) single crystal was grown by the slow evaporation method. The single crystal X-ray diffraction analysis and density functional theory (DFT) calculations were carried out for the ACPD molecule. The ACPD crystallizes in the orthorhombic space group *Pbca* with $a = 18.3519 (14) \text{ \AA}$, $b = 11.3883 (9) \text{ \AA}$, $c = 18.3545 (14) \text{ \AA}$. Hirshfeld surface analysis and finger print plots were analysed using Crystal Explorer to confirm the existence of intermolecular, intramolecular and other weak interactions. The molecular geometry (X-ray coordinates) was optimized using Density Functional Theory (DFT/B3LYP) method with the 6-31G+ (d, p) basis set using Gaussian 09 W software. The

optimized geometrical parameters, structures and vibrational wavenumbers were compared with the experimental results. Natural Bond Orbital analysis (NBO) was carried out to evaluate the intramolecular stabilization interactions of the molecule. The highest occupied molecular orbital (HOMO) energy, the lowest unoccupied molecular orbital (LUMO) energy and their energy gap (ΔE) of the ACPD molecule were calculated. In addition, the molecular docking analysis was carried out to explore the inhibitory nature of the molecule against Cdc7 kinase, CK2 and PPAR γ . Docking results suggest that the ACPD molecule could be a novel inhibitor candidate of PPAR γ receptor which causes type 2 diabetes mellitus.

Min zhang , Xiaohui Zhu et.al 2020 suggest that Glucagon-like peptide 1 receptor agonists (GLP-1RA) have excellent performance in the treatment of diabetes, but the drugs used in the clinic are all macromolecular peptide injections. Therefore, non-peptide small molecule drugs that can be taken orally have become the research and development trend of GLP-1RA. Some flavonols have been proved to be small molecule GLP-1RA. We have conducted DFT and molecular docking studies on reported flavonol-based non-peptide GLP-1RA. Flavone, flavonol, 4'-hydroxyflavonol, 3',4'-dihydroxyflavonol and quercetin were investigated at B3LYP [6-311G (d, p)/6-311+G (d, p)/6-311++G (d, p)] levels in gas and water phase. The calculation was performed on their equilibrium structures and harmonic frequencies in gas and water phase, respectively. Vibration frequency and infrared spectrum of O—H and C=O can be used to identify structural analogs of this type of compounds. The topological properties of the IMHB for flavonols have been investigated using the atoms-in-molecules (AIM) approach. Electrostatic potential (ESP), conceptual density functional theory (CDFT) and condensed dual descriptor (CDD) were used for molecular reactivity studies. The preliminary investigations of binding details between flavonols and GLP-1R are explored by molecular docking technology. The results of this study are expected to aid the design and analyze of new flavonol-based small molecule GLP-1RA with improved properties.

Fang Liangzi, Zheng Qinfang, Han Jun et.al 2020 suggest that To explore the pharmacological mechanism of active saponin compounds of Tuchao Baibiandouren (Lablab Semen Album fried

with earth, TCBBDR) in treating type 2 diabetes (T2DM) using UHPLC-Q-Exactive Orbitrap MS and network pharmacology

CHAPTER III

SCOPE OF INVESTIGATION



CHAPTER III

SCOPE OF INVESTIGATION

- Diabetes is a world wide disease .molecular docking studies to known inhibitors and selected alkaloids and flavonoids.
- To find the blood glucose monitoring
- To identify target protein
- To select the diabetes disease inhibitors of phytochemical compounds
- To find out the natural phytochemical compounds .
- To find out which protein – ligands complex have high binding affinity
- To recognize the good pharmacological activities of phytochemical compounds in future.

CHAPTER IV

MATERIALS AND METHODS



CHAPTER IV

MATERIALS AND METHODS

1. TARGET SELECTION:

The X-ray crystal structure of 3G5E was retrieved from Protein Data Bank . The protein energy was minimized through 20 steps of steepest descent and conjugate by using SMILES of Swiss PDB Viewer and final energy minimized model was used for further docking studies

2. . PROTEIN PREPARATION

Load the protein and apply the force field. For docking studies, the protein 3G5E loads from RCSB protein data bank (www.rcsb.org/pdb) and apply the force field. Field refers to the functional form parameter sets which are used to find out potential energy of a system. It includes parameter which is obtained through experimental works and quantum mechanics calculations. All molecules in a molecule system are made up of a number of components. Covalently bonded atoms take into consideration several parameters such as bond length, bond angle, dihedral angles etc., similarly there exist non bonded interactions such as Vanderwaals interactions, electrostatic interactions. Thus, the total potential energy of the system is calculated as follows.

$$E1 = [E_{\text{bond}} + E_{\text{angle}} + E_{\text{vanderwaals}} + E_{\text{electronic}}]$$

This summation when gives is an explicit form, represents force field, evaluating the potential of a system .

3.LIGAND SELECTION

The SMILES notation of fifty phytochemical compounds including alkaloids and flavonoids from various medicinal plants were obtained by drawing their 2D structures in ACD [74,75]

4.LIGAND PREPARATION

The chemically synthesized individual ligand compounds were sketched using ACD/ChemSketch (12.01) software and saved in (.mol) file format. The saved ligand compounds were later imported in DS and go to Minimization studies using Gliding minimizer. After minimized ligands go to ligand preparation, then go for docking studies with ligand fit.

5.BINDING SITE AND SITE PARTITION

The active site of a receptor can be represented in many ways, for example a sphere or a list of residues. The Binding Site definition is one such representation. A binding site is a set of points on a grid that in a cavity. This definition is allowing the size and shape of the active site to be quantified. Docking algorithms such as Ligand Fit can use this to both screen out incompatible ligands and quickly create shape-based alignments of candidate poses. The location, volume and shape of the binding site or all used in docking.

To define a binding site, the receptor is first mapped to a grid. Grid points within a given distance of the receptor atoms are marked as occupied by receptors and as undesirable as locations for ligand atoms. Two methods exist to identify a Binding Site. The first uses an “eraser” algorithm to identify sites based on the shape of the receptor. The second uses the volume occupies by the known ligand force already in an active site

6 .VIRTUAL SCREENING

The 3D structures of all the selected fifty phytochemical compounds were virtually screened to reveal their binding efficiencies through docking in the predicted binding site of BChE using PyRx-Python Prescription (version 0.8). The docking was performed with the default parameters such as triangle matching base placements, zero, full score and no score contributions and threshold for full score and no score contributions of 30 and 70 respectively. Clash handling values of 2.9 Å and 0.6 for protein ligand clashes with maximum allowed overlap volume and in a ligand clash factors while considering the hydrogen in internal clash tests and 200 as the default docking values for maximum number of solutions per iteration and also per fragmentations [78]

7.DOCKING INTERACTION

The docking interactions revealing H-bond and Vanderwaals forces among the phytochemical compounds and the amino acid residues of were analyzed by [79] PyRx-Python Prescription (PyRx).

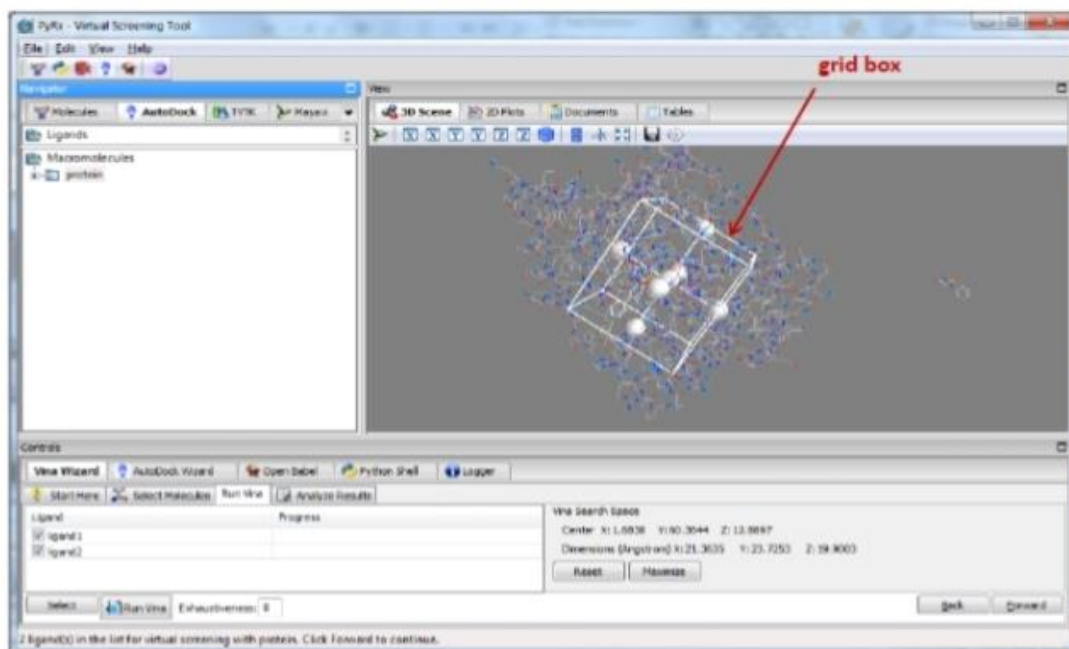
8.PYRX DOCKING

PyRx is a Virtual Screening software for Computational Drug Discovery that can be used to screen libraries of compounds against potential drug targets. PyRx enables Medicinal Chemists to run Virtual Screening from any platform and helps users in every step of this process. From data preparation to job submission and analysis of the results. While it is true that there is no magic button in the drug discovery process, PyRx includes docking wizard with an easy-to-use user interface which makes it a valuable tool for Computer-Aided Drug Design. PyRx also includes chemical spreadsheet-like functionality and powerful visualization engine that are essential for structure-based drug design.

9. DOCKING ALGORITHM:

Select upper left button Load molecule to load your protein and ligand into PyRx workspace. Right click on ligands and click AutoDock to Make ligand. Right click on protein and click AutoDock to Make Macromolecule. Now the protein and ligands files are ready for docking. Click on Start Here button under Vina Wizard. Select Local button under Vina execution Mode. Click Start button. Select protein and ligands by simply clicking on them. Click forward to Run Vina. The grid box (white box with spherical handles) in the 3D scene as shown below. This grid box allows to select search space (Part of the protein, where the docking performs and it is typically known binding site) in the protein. To help locating the binding site (or active site) use binding site amino acids. Click molecules button under Navigator panel, then click on + button located in front of protein tab. After selecting the amino acids (use shift button to select multiple amino acids) click on the Toggle selection Spheres button to see the selected amino acids. Make sure you select the grid box size big enough to allow the ligand to move freely in the search space. Use the search space (Vina search space) values close the ones mentioned in the picture below,

to get better results. Click the forward button to start Vina calculations. Once the calculations are done, results will be populated as seen in the below table with the Binding Affinity (kcal/mol) values.



More negative the binding affinity better the orientation of the ligand in the binding site. Results can be exported to other software programs like UCSF Chimera or Pymol for analysis. Click on Edit, go to Preferences. A pop-up window is opened. All your results will be saved in location specified as workspace. The protein folder contains three files (protein .pdbqt, ligand1_out.pdbqt and conf.txt), if you use only one ligand for docking. The ligand1_out.pdbqt contains 8 or 9 best poses (or orientations) of the ligand1 and conf.txt file contains search space (or grid box) parameters. Save this protein folder at your convenient location for further analysis with Pymol. You are done with PyRx, now let's analyse the results by using Pymol. Open protein .pdbqt file followed by ligand1_out.pdbqt to analyse the results. Select the ligand by using upper sequence bar and click on seleA(action:)>find >Polar contacts >to any atoms. Now the result of PyRx docking is screened[80]

CHAPTER V

RESULT AND DISCUSSION



CHAPTER V

RESULT AND DISCUSSION

TARGET SELECTION

The x- ray crystal structure of 3G5E was retrieved from protein Data Bank .The protein energy was minimized through 20 steps of steepest descent and conjugate by using SMILES of Swiss PDB viewer final energy minimized model was used for further docking studies [81]

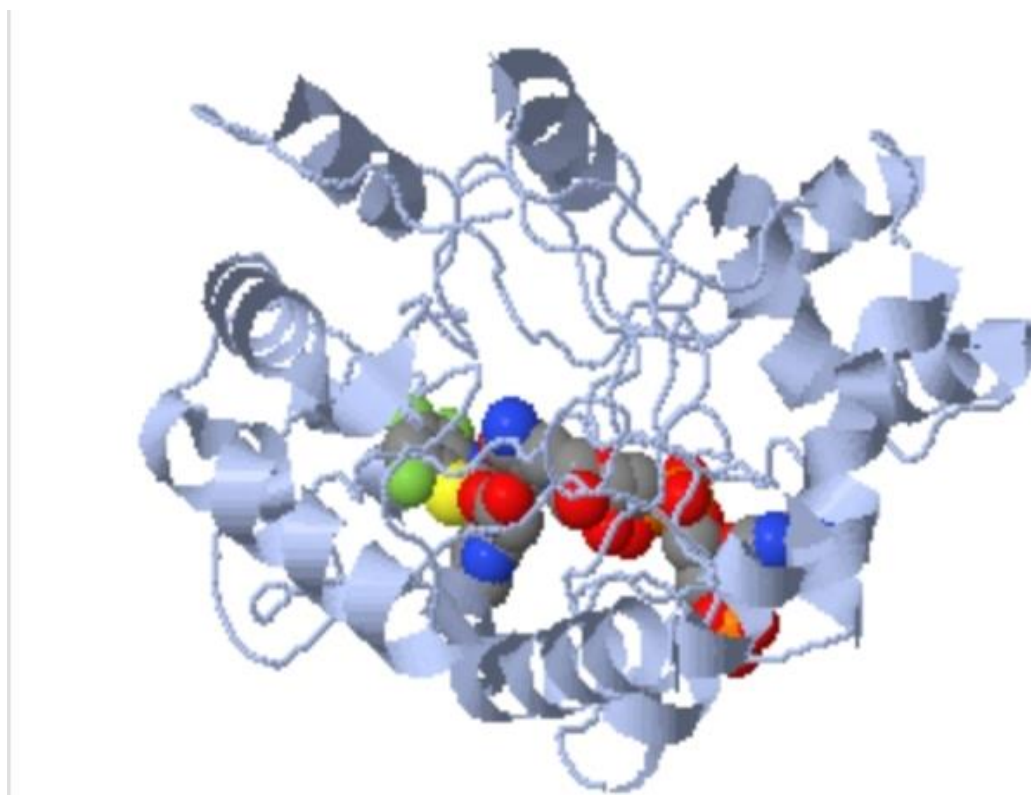


Fig.2 PROTEIN 3G5E

LIGAND SELECTION

The SMILES notation of phytochemical compounds including alkaloids and flavonoids from various medicinal plants were obtained by drawing their 2D structures in ACD-Chemsketch (version 12.01). The 3D structures of these compounds were generated and

converted into SDF format by using ‘Online SMILES convertor and structure file generator’ server[82].

Selected phytochemical compounds and plant source

S.NO	CID.NO	Ligand	Plant source
1	29327	Streptozocin	Anacardium occidentale linn
2	111109	Antidysentric	Annana sequamosa linn
3	5748611	Eupalitin	Boerhaavia diffusa linn
4	16137215	Insulinotropin	Coccinia indica
5	16723	Alloxan Monohydrate	Murra koenji
6	5464368	Punicalin	Terminallia catappa
7	14886031	Terflavin	Terminallia catappa
8	12850045	Geranin	Terminallia catappa
9	73568	Corilagin	Terminallia catappa
10	442674	Chebulagic	Terminallia catappa
11	441183	Granatin	Terminallia catappa
12	39562	Hexokinase	Cescinium fenestratum
13	5288620	Glipenclamide	Dioscorea dumetorum fedruts
14	259846	Lupeol	Camellia japonica
15	173183	campesterol	brassia

Fig 3 The structure of phytochemical compounds

The structure of streptozotocin

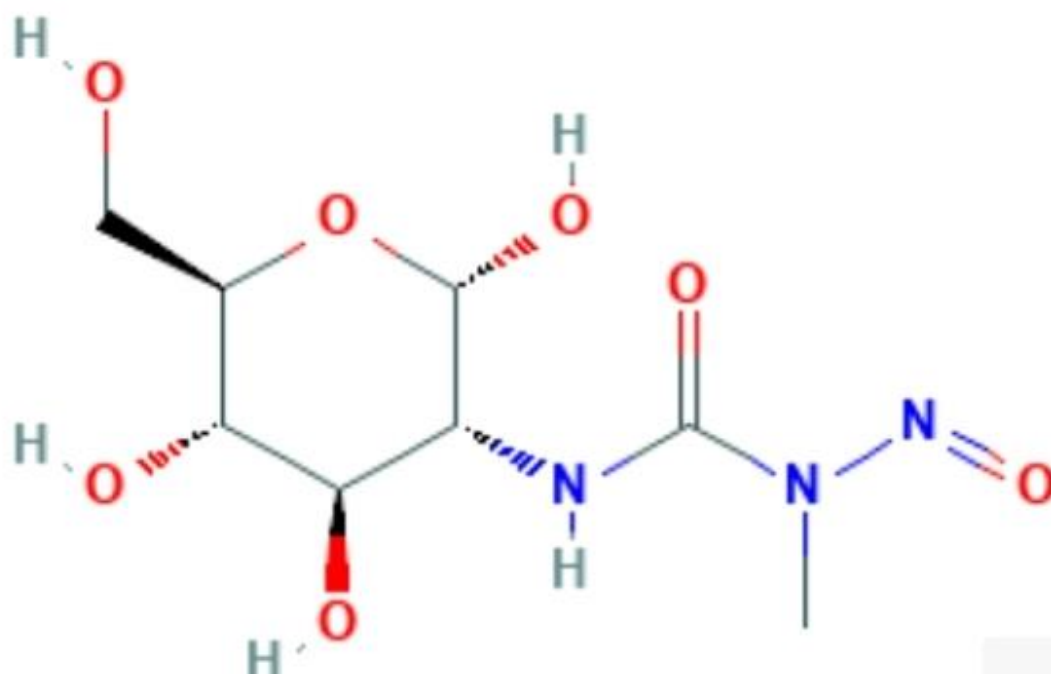


Fig 4The structure of antidysentric

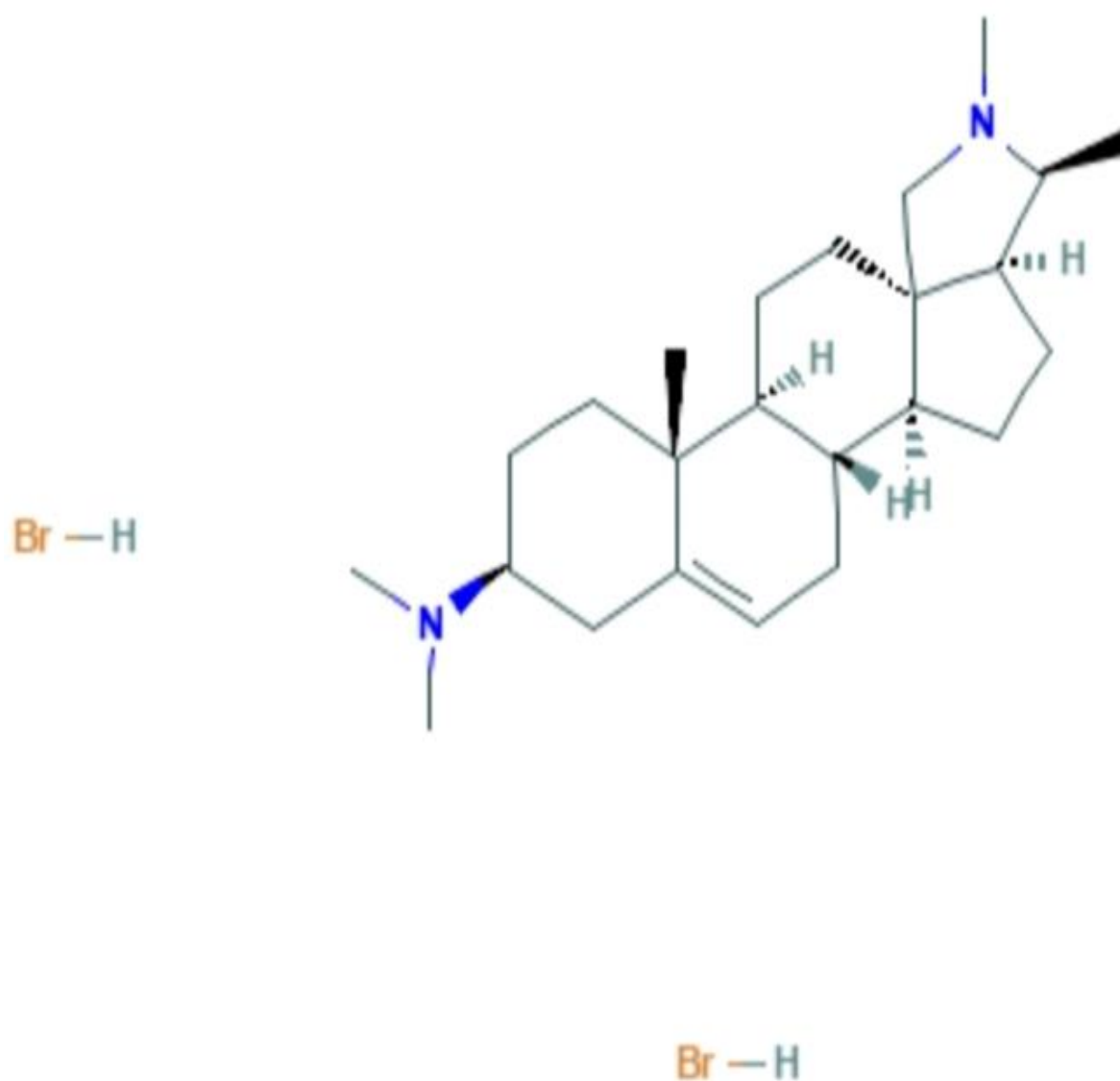


Fig 5 The structure of eupalitin

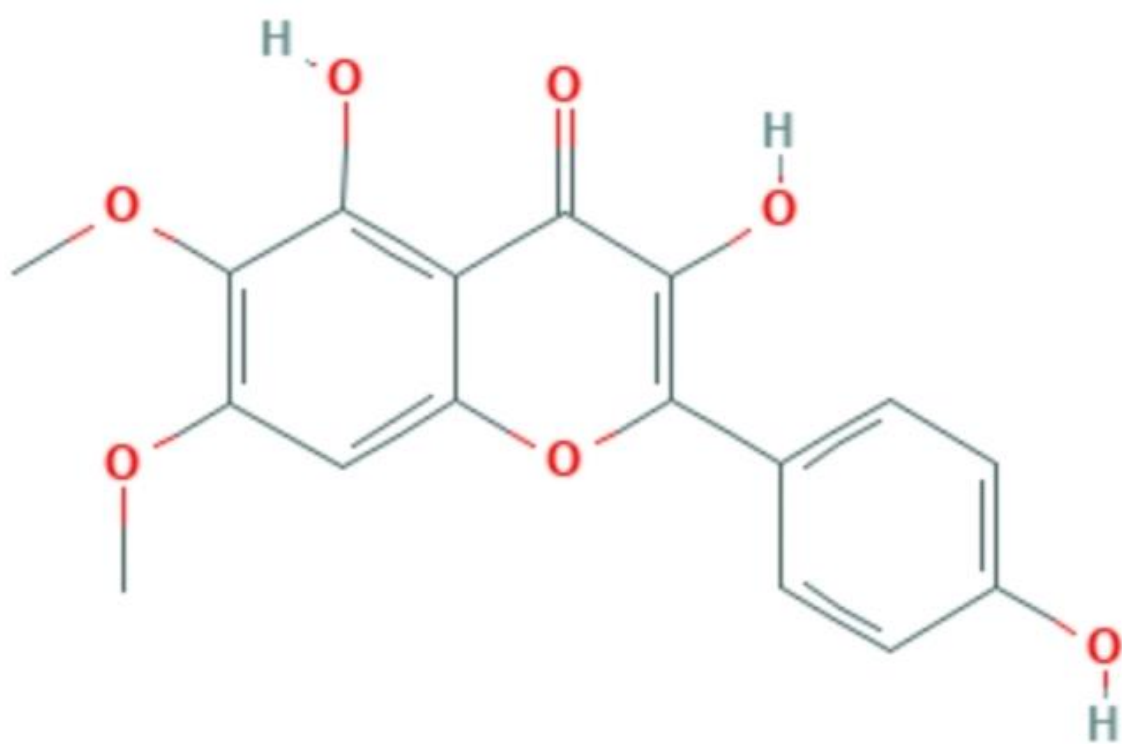


Fig 6 The structure of insulinotropin

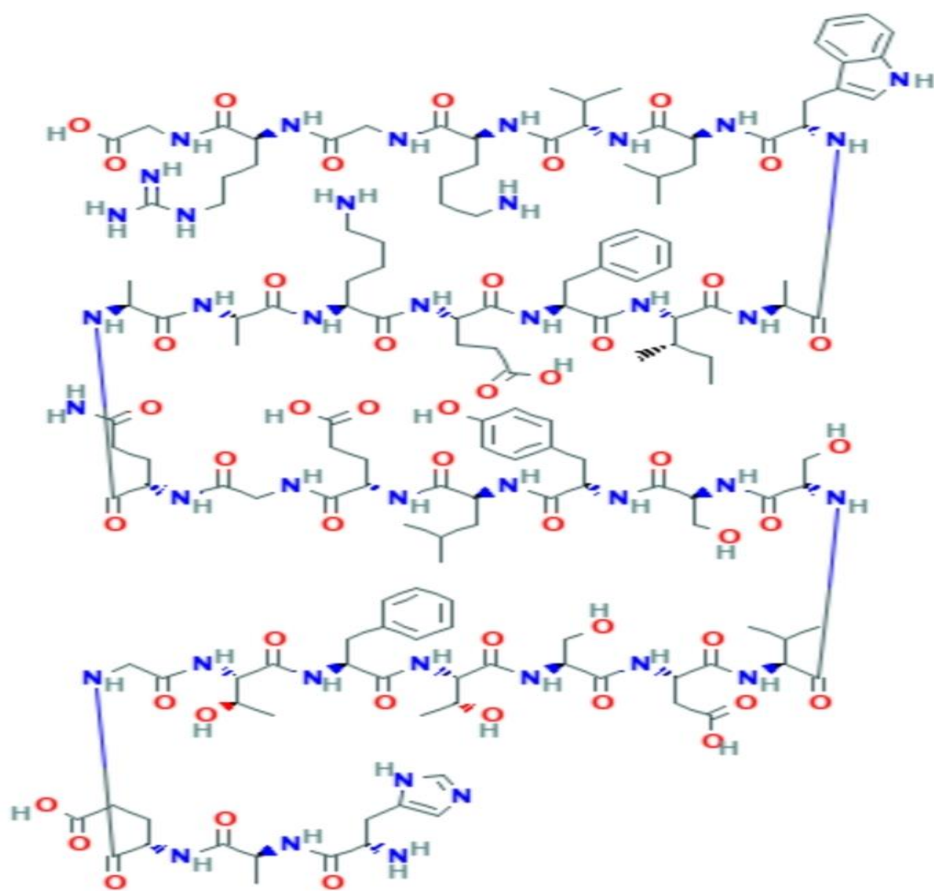


Fig 7The structure of alloxan monohydrate



Fig 8The structure of punicalin

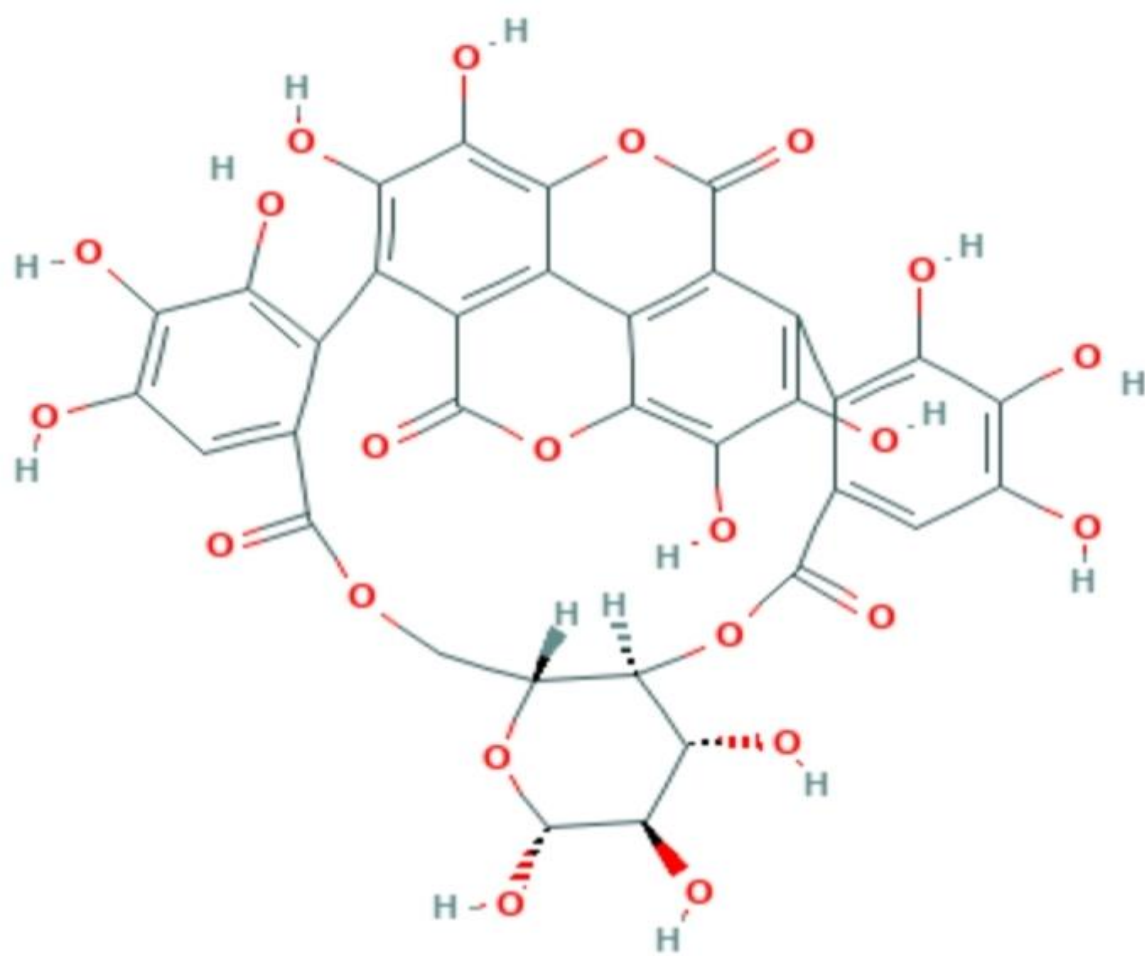


Fig 9 The structure of terflavin

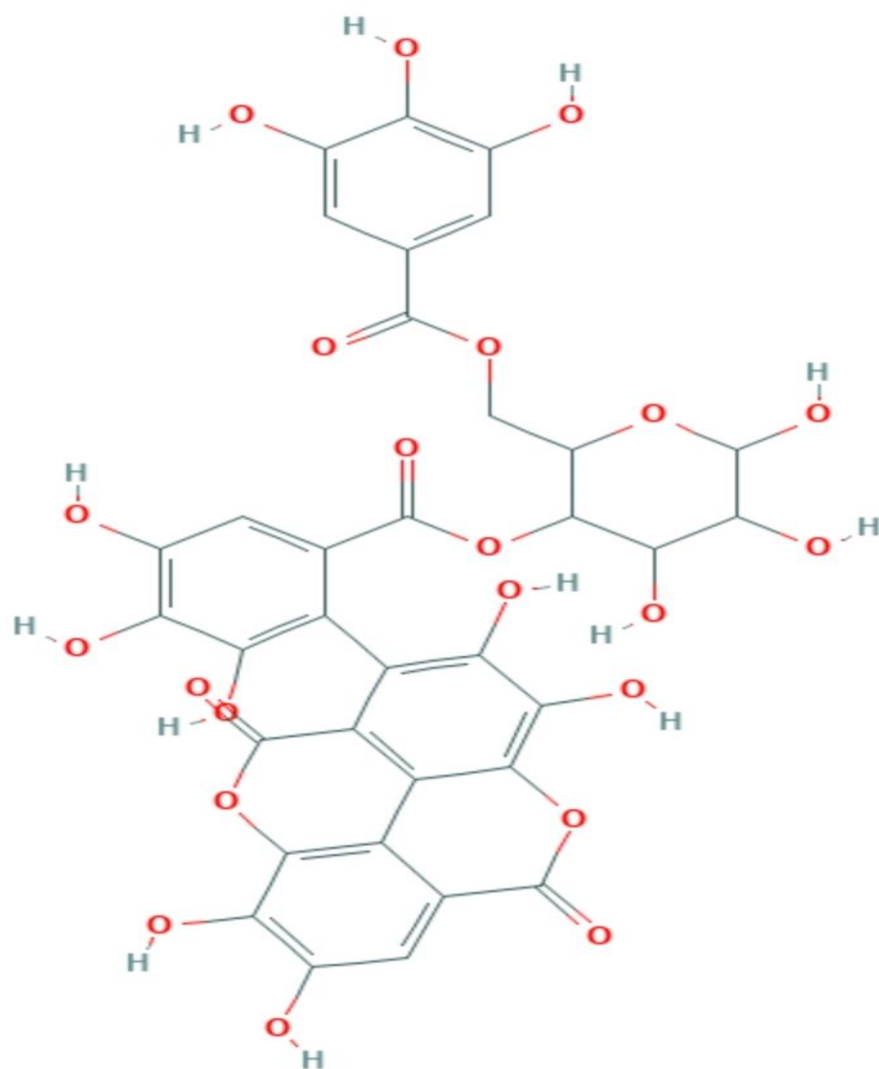


Fig 10 The structure of geranin

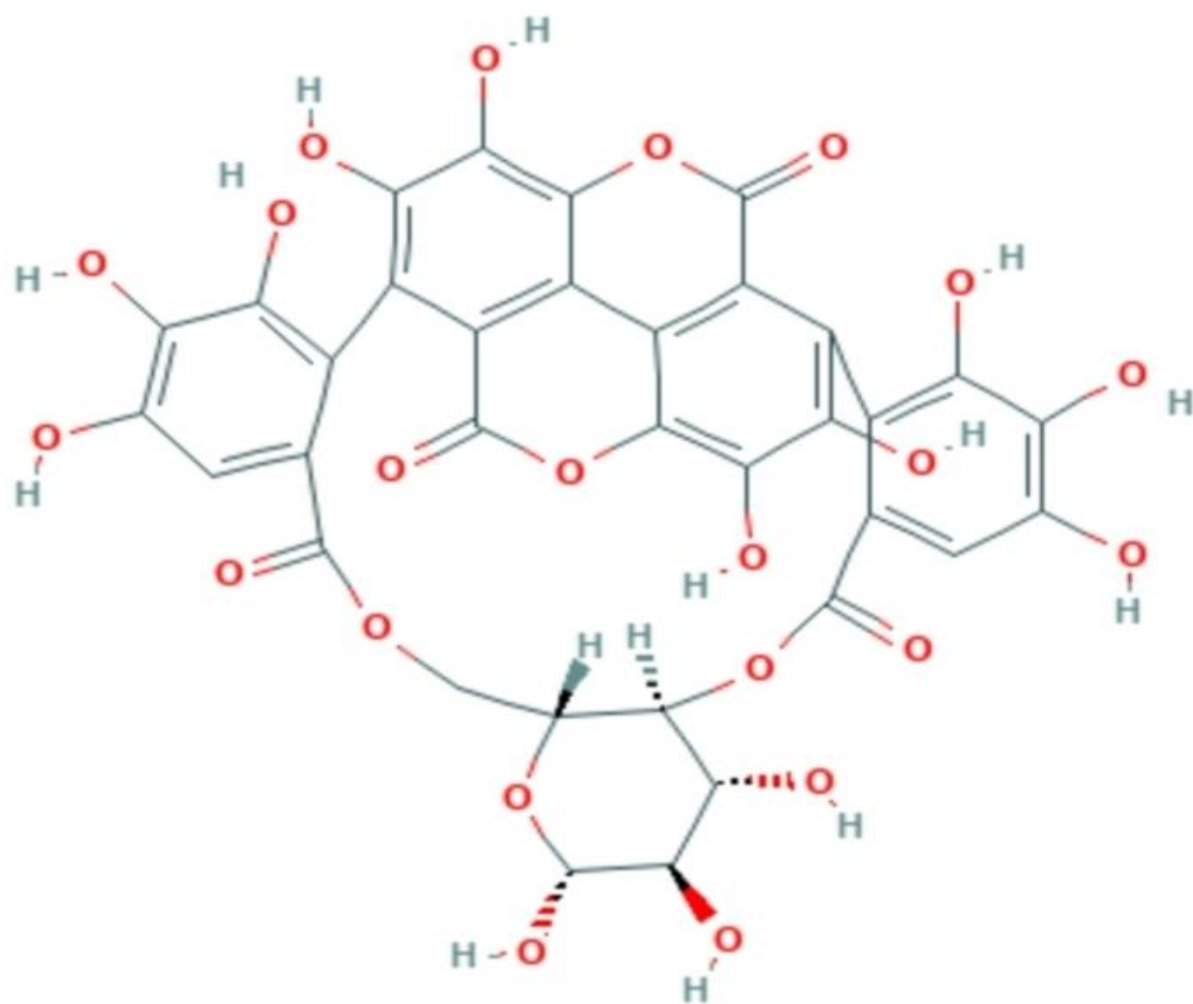


Fig 11 The structure of corilagin

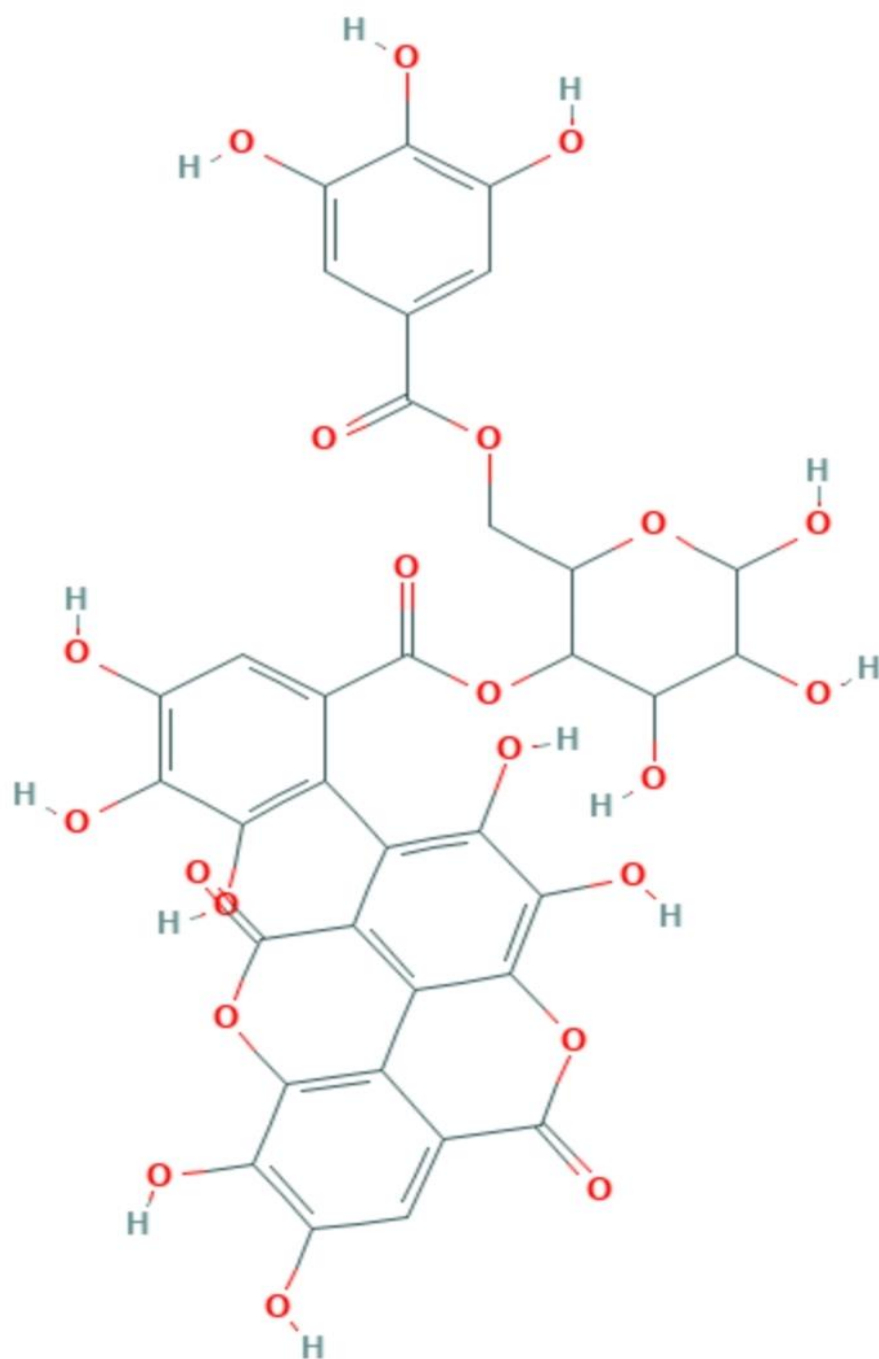


Fig 12 The structure of chebulagic

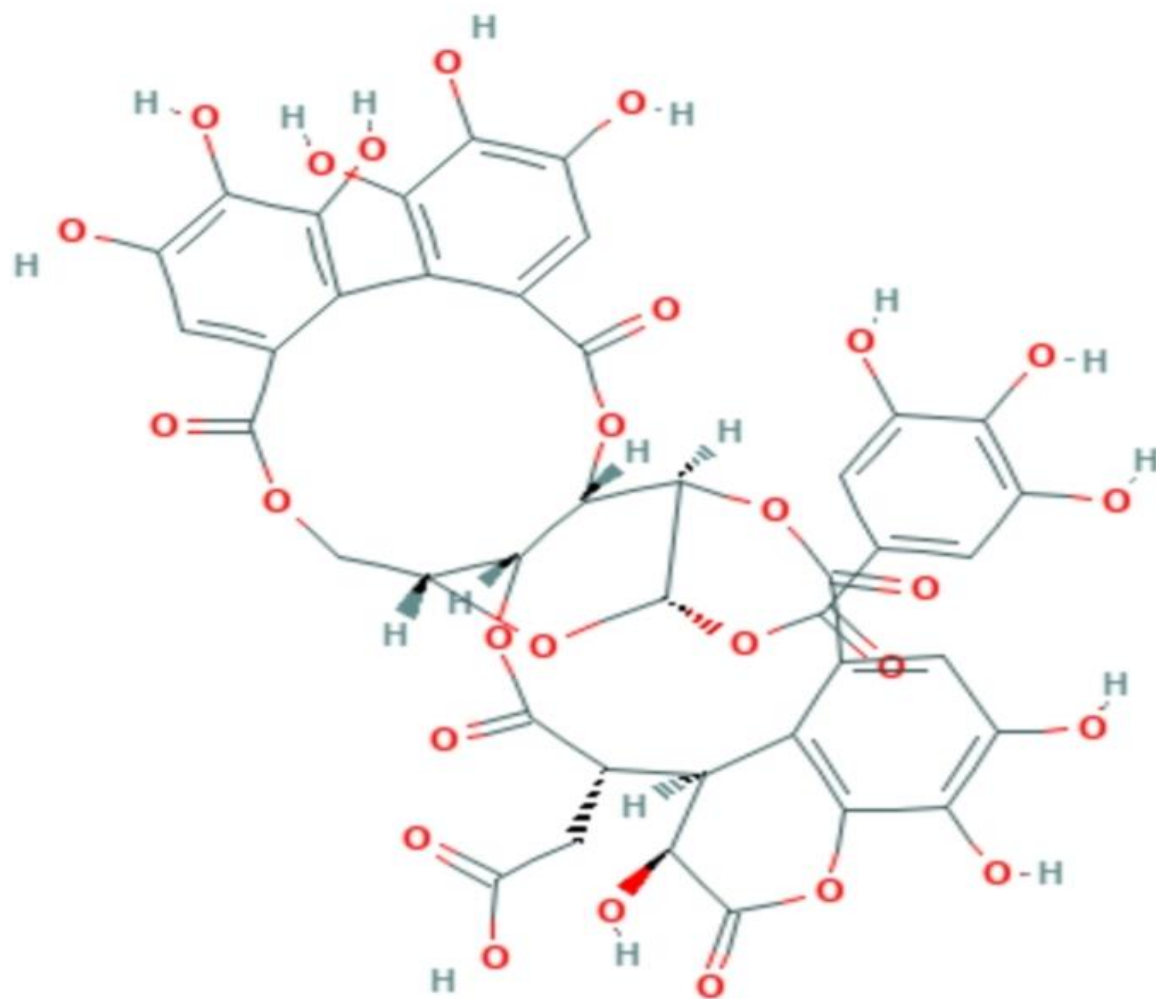


Fig 13 The structure of granatin

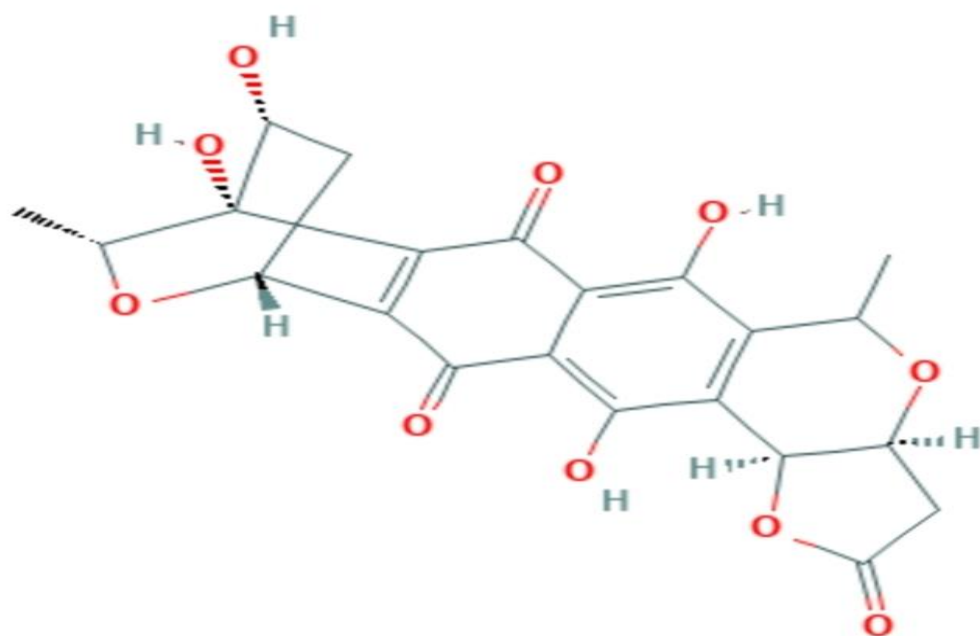


Fig14Thestructureofhexokinase

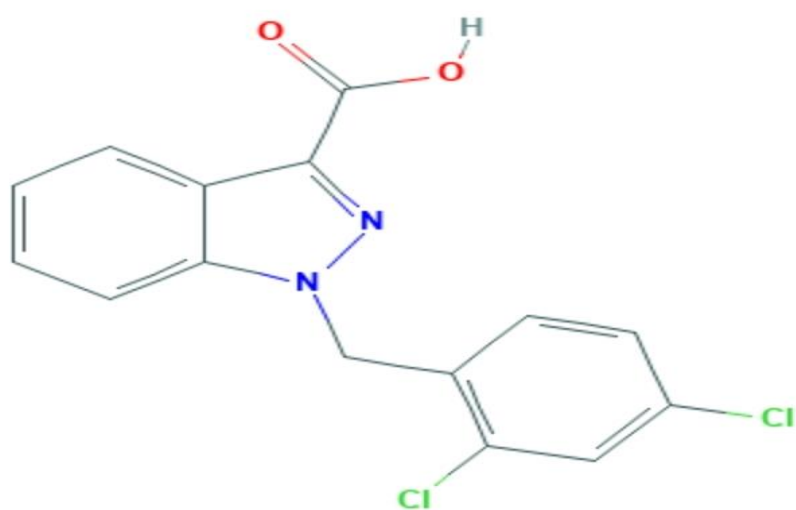


Fig 15 The structure of glipenclamide

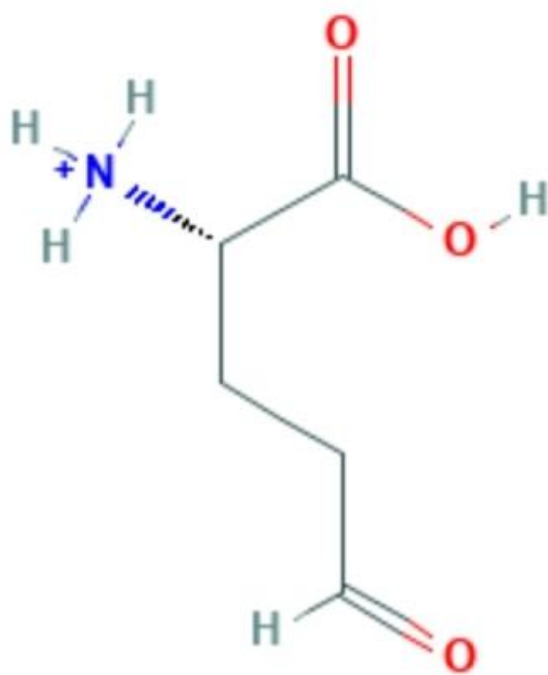


Fig 16 The structure of lupeol

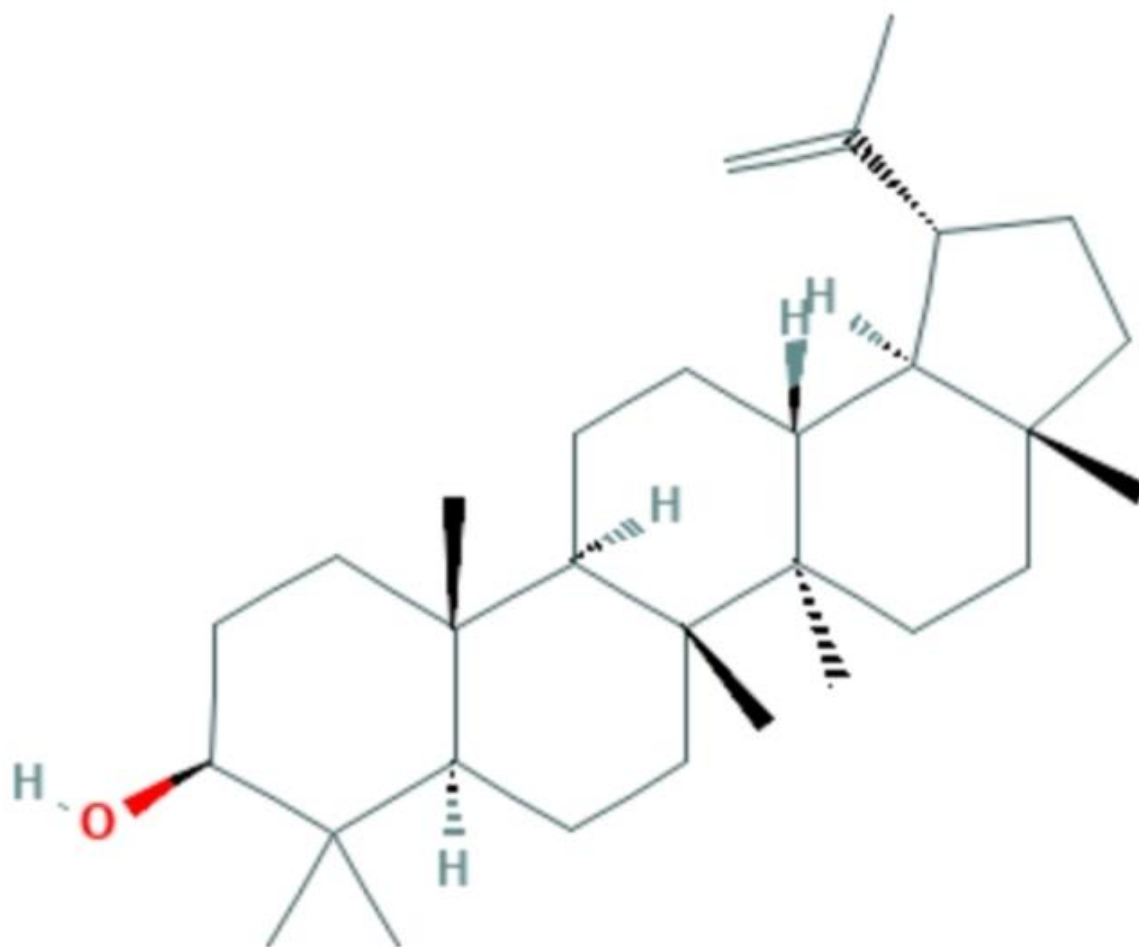
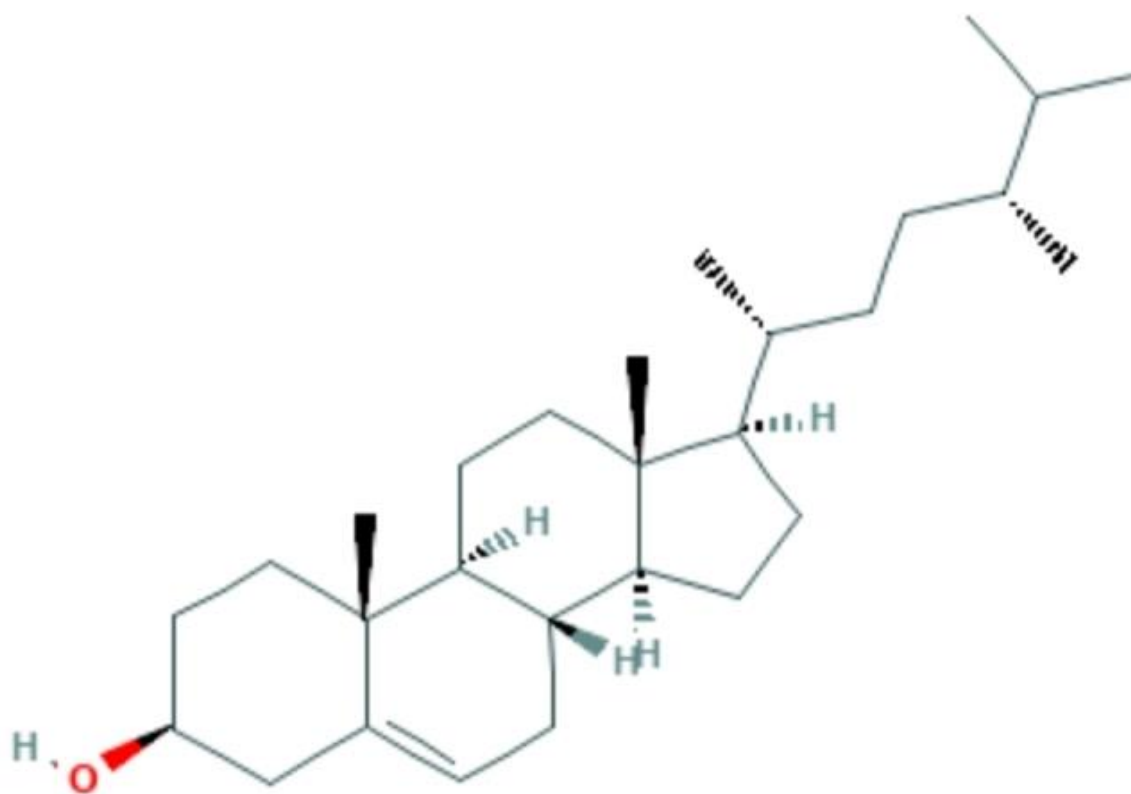


Fig 17 The structure of campesterol



BINDING SITE PREDICTION

The amino acid residues in binding site of 3G5E protein is defined by using the reference ligand complexed in the retrieved PDB file. The amino acid residues within 6 Å radius of reference ligand was included in the predicted binding site by using PyRx-Python Prescription (version 0.8)[83]

VIRTUAL SCREENING

The 3D structures of all the selected phytochemical compounds were virtually screened to reveal their binding efficiencies through docking in the predicted binding site using PyRx-Python Prescription. Docking values for maximum number of solutions per interaction and also per fragmentations[83] The best binding affinity with their docking scores are given in table[84]

BINDING AFFINITY OF PHYTOCHEMICAL BY USING PyRX

S.NO	Ligand	Binding Affinity	Rmsd/Ub	Rmsd/Ib
1	3G5E-RESULT-Alloxan Monohydrate	-5.7	5.149	3.547
2	3G5E- RESULT-Campesterol	-5.6	11.564	6.987
3	3G5E-RESULT-Corilagin	8.7	0	0
4	3G5E- RESULT-Dumetroum	-6.5	5.979	3.965
5	3G5E-RESULT-Glipenclamide	-5.1	6.596	6.047
6	3G5E-RESULT-Geranatin	4.3	5.039	2.834
7	3G5E-RESULT-Geranin	-8.1	7.477	2.844
8	3G5E-RESULT-Hexokinase	-7.6	8.008	6.096
9	3G5E-RESULT-Histamine	-4.8	5.158	3.257

10	3G5E-RESULT -Lupeol	12.2	7.749	2.509
11	3G5E-RESULT - Punicalin	-2.6	0	0
12	3G5E- RESULT-Terflavin	-2.6	3.537	1.018

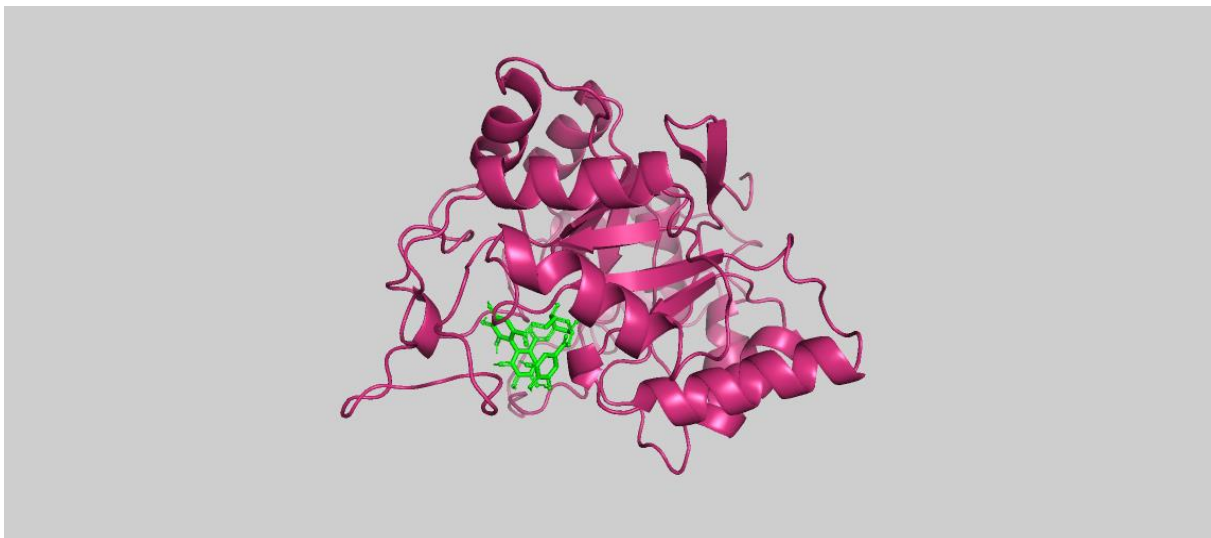
DOCKING INTERACTIONS

The docking interactions revealing H-bond and Vanderwaals forces among the phytochemical compounds and the amino acid residues of protein 3G5E were analyzed by PyRx-Python Prescription (version 0.8). PyRx is a Virtual Screening Software for Computational Drug Discovery that can be used to screen libraries of compounds against potential drug targets. PyRx enables Medicinal Chemists to run Virtual Screening from any platform and helps users in every step of this process – from data preparation to job submission and analysis of the results. PyRx also includes chemical spreadsheet – like functionality and powerful visualization engine that are essential for structure-based drug design. It excels at three-dimensional visualization of protein, ligand binding sites and surrounding amino acids of ligands were also visualized. Identified active sites were visualized in PyMOL molecular visualization tool. The higher binding affinity of best ten phytochemical compounds are shown below[84].

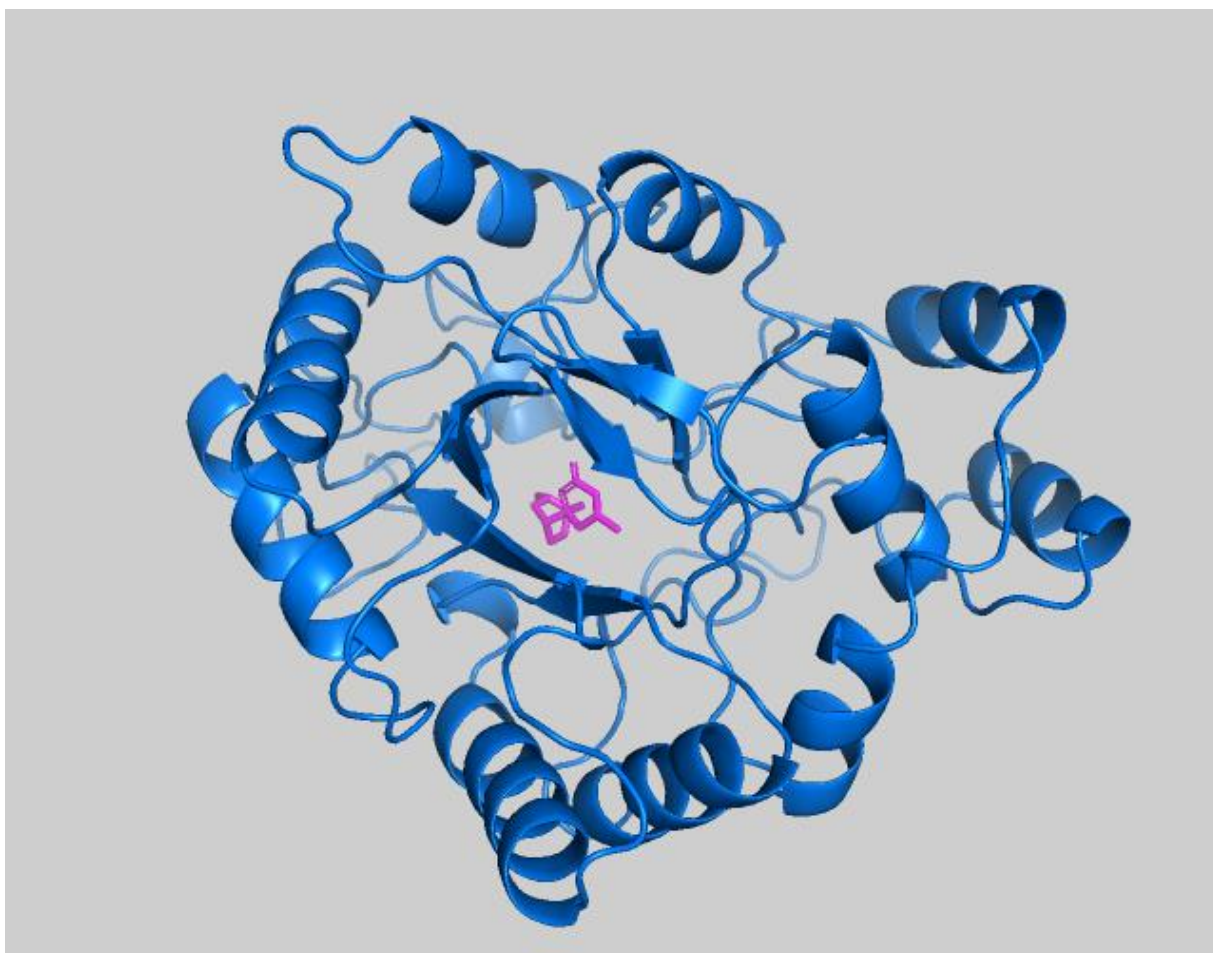
Docking complex and interaction of Lupeol(CID 259846)



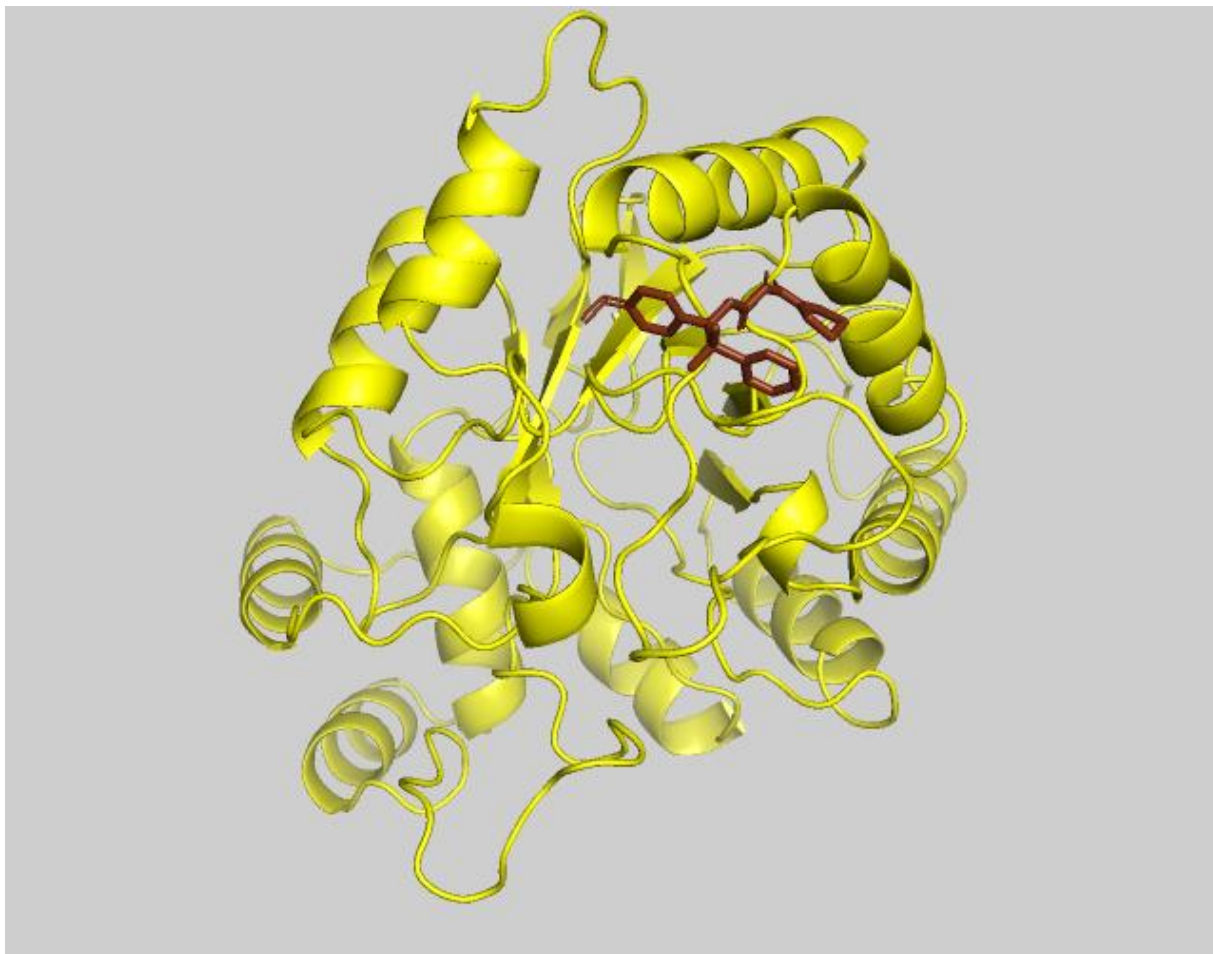
Docking complex and interaction of corilagin(CID 73568)



Docking complex and interaction of dumentroum(CID 65063)



Docking complex and interaction of geranin (CID 12850045)



Docking complex and interactions of hexokinase(CID39562)



CHAPTER VI

CONCLUSION



CHAPTER VI

CONCLUSION

The 3G5E a part of insulin that significantly controls sugars serves as a drug target for diabetes mellitus. Insulin receptor kinase complexed with an inhibitor 3G5E was used to explore the diabetes mellitus activity of phytochemical compounds including alkaloids and flavonoids. In the present molecular modeling study, results clearly demonstrated that alkaloids and flavonoids have similar binding sites and interaction with 3G5E taken for the study and prove that dietary alkaloids and flavonoids may possess properties of diabetes regulation.

CHAPTER VII

REFERENCE



CHAPTER VII

REFERENCE

1. "Diabetes Blue Circle Symbol". International Diabetes Federation. 17 March 2006. Archived from the original on 5 August 2007.
2. "Diabetes Fact sheet N°312". WHO. October 2013. Archived from the original on 26 August 2013. Retrieved 25 March 2014.
3. Kitabchi AE, Umpierrez GE, Miles JM, Fisher JN (July 2009). "Hyperglycemic crises in adult patients with diabetes". *Diabetes Care*. 32 (7): 1335–43. doi:10.2337/dc09-9032. PMC 2699725. PMID 19564476.
4. Krishnasamy S, Abell TL (July 2018). "Diabetic Gastroparesis: Principles and Current Trends in Management". *Diabetes Therapy*. 9 (Suppl 1): 1–42. doi:10.1007/s13300-018-0454-9. PMC 6028327. PMID 29934758.
5. Saedi, E; Gheini, MR; Faiz, F; Arami, MA (15 September 2016). "Diabetes mellitus and cognitive impairments". *World Journal of Diabetes*. 7 (17): 412–22. doi:10.4239/wjd.v7.i17.412. PMC 5027005. PMID 27660698.
6. Chiang JL, Kirkman MS, Laffel LM, Peters AL (July 2014). "Type 1 diabetes through the life span: a position statement of the American Diabetes Association". *Diabetes Care*. 37 (7): 2034–54. doi:10.2337/dc14-1140. PMC 5865481. PMID 24935775.
7. "Causes of Diabetes". National Institute of Diabetes and Digestive and Kidney Diseases. June 2014. Archived from the original on 2 February 2016. Retrieved 10 February 2016.
8. Ripsin, CM; Kang, H; Urban, RJ (January 2009). "Management of blood glucose in type 2 diabetes mellitus" (PDF). *American Family Physician*. 79 (1): 29–36. PMID 19145963. Archived (PDF) from the original on 2013-05-05.

9. Brutsaert, Erika F. (February 2017). "Drug Treatment of Diabetes Mellitus". MSDManuals.com. Retrieved 12 October 2018.
10. (PDF). www.diabetesatlas.org. Retrieved 18 May 2020.
11. "About diabetes". World Health Organization. Archived from the original on 31 March 2014. Retrieved 4 April 2014.
12. Shoback DG, Gardner D, eds. (2011). "Chapter 17". Greenspan's basic & clinical endocrinology (9th ed.). New York: McGraw-Hill Medical. ISBN 978-0-07-162243-1.
13. Norman A, Henry H (2015). Hormones. Elsevier. pp. 136–137. ISBN 9780123694447.
14. RSSDI textbook of diabetes mellitus (Revised 2nd ed.). Jaypee Brothers Medical Publishers. 2012. p. 235. ISBN 978-93-5025-489-9. Archived from the original on 14 October 2015.
15. The top 10 causes of death Fact sheet N°310". World Health Organization. October 2013. Archived from the original on 30 May 2017.
16. Rippe RS, Irwin JM, eds. (2010). Manual of intensive care medicine (5th ed.). Wolters Kluwer Health/Lippincott Williams & Wilkins. p. 549. ISBN 978-0-7817-9992-8.
17. Picot J, Jones J, Colquitt JL, Gospodarevskaya E, Loveman E, Baxter L, Clegg AJ (September 2009). "The clinical effectiveness and cost-effectiveness of bariatric (weight loss) surgery for obesity: a systematic review and economic evaluation". ..
18. Cash, Jill (2014). Family Practice Guidelines (3rd ed.). Springer. p. 396. ISBN 978-0-8261-6875-7. Archived from the original on 31 October 2015.
19. Vos T, Flaxman AD, Naghavi M, Lozano R, Michaud C, Ezzati M, et al. (December 2012). "Years lived with disability (YLDs) for 1160 sequelae of 289 diseases and injuries 1990–2010: a systematic analysis for the Global Burden of Disease Study 2010". *Lancet*. 380 (9859): 2163–96. doi:10.1016/S0140-6736(12)61729-2. PMC 6350784. PMID 23245607.
20. "What is Diabetes?". Centers for Disease Control and Prevention. 11 March 2020. Retrieved 18 May 2020.
21. "The top 10 causes of death". www.who.int. Retrieved 18 May 2020.

22. American Diabetes Association (2018-03-22). "Economic Costs of Diabetes in the U.S. in 2017". *Diabetes Care*. 41 (5): 917–928. doi:10.2337/dci18-0007. ISSN 0149-5992. PMC 5911784. PMID 29567642.
23. "Deaths and Cost | Data & Statistics | Diabetes | CDC". *cdc.gov*. 20 February 2019. Retrieved 2 July 2019.
24. Cooke DW, Plotnick L (November 2008). "Type 1 diabetes mellitus in pediatrics". *Pediatrics in Review*. 29 (11): 374–84, quiz 385. doi:10.1542/pir.29-11-374. PMID 18977856. S2CID 20528207.
25. . WHO. Retrieved 2019-03-23.
26. Rockefeller, J.D. (2015). *Diabetes: Symptoms, Causes, Treatment and Prevention*. ISBN 978-1-5146-0305-5.
27. , Umpierrez GE, Miles JM, Fisher JN (July 2009). "Hyperglycemic crises in adult patients with diabetes". .
28. Kenny C (April 2014). "When hypoglycemia is not obvious: diagnosing and treating under-recognized and undisclosed hypoglycemia". .
29. Verrotti A, Scaparrotta A, Olivieri C, Chiarelli F (December 2012). "Seizures and type 1 diabetes mellitus: current state of knowledge". *European Journal of Endocrinology*. 167(6): 749–58. doi:10.1530/EJE-12-0699. PMID 22956556.
30. "Symptoms of Low Blood Sugar". *WebMD*. Archived from the original on 18 June 2016. Retrieved 29 June 2016.
31. "Glucagon–Injection side effects, medical uses, and drug interactions". *MedicineNet*. Retrieved 2018-02-05.
32. Sarwar N, Gao P, Seshasai SR, Gobin R, Kaptoge S, Di Angelantonio E, Ingelsson E, Lawlor DA, Selvin E, Stampfer M, Stehouwer CD, Lewington S, Pennells L, Thompson A, Sattar N, White IR, Ray KK, Danesh J (June 2010). "Diabetes mellitus, fasting blood glucose concentration, and risk of vascular disease: a collaborative meta-analysis of 102 prospective studies". *Lancet*. 375 (9733): 2215–22. doi:10.1016/S0140-6736(10)60484-9. PMC
33. O'Gara PT, Kushner FG, Ascheim DD, Casey DE, Chung MK, de Lemos JA, Ettinger SM, Fang JC, Fesmire FM, Franklin BA, Granger CB, Krumholz HM, Linderbaum JA, Morrow DA, Newby LK, Ornato JP, Ou N, Radford MJ, Tamis-

- Holland JE, Tommaso CL, Tracy CM, Woo YJ, Zhao DX, Anderson JL, Jacobs AK, Halperin JL, Albert NM, Brindis RG, Creager MA, DeMets D, Guyton RA, Hochman JS, Kovacs RJ, Kushner FG, Ohman EM, Stevenson WG, Yancy CW (January 2013). "2013 ACCF/AHA guideline for the management of ST-elevation myocardial infarction: a report of the American College of Cardiology Foundation/American Heart Association Task Force on Practice Guidelines". .
34. "Diabetes Programme". World Health Organization. Archived from the original on 26 April 2014. Retrieved 22 April 2014.
 35. "Diabetes – eye care: MedlinePlus Medical Encyclopedia". medlineplus.gov. Retrieved 2018-03-27.
 36. Cukierman, *T* (8 Nov 2005). "Cognitive decline and dementia in diabetes – systematic overview of prospective observational studies". *Diabetologia*. *48* (12): 2460–69. doi:10.1007/s00125-005-0023-4. PMID 16283246.
 37. Yang Y, Hu X, Zhang Q, Zou R (November 2016). "Diabetes mellitus and risk of falls in older adults: a systematic review and meta-analysis". *Age and Ageing*. *45* (6): 761–67. doi:10.1093/ageing/afw140. PMID 27515679.
 38. Williams textbook of endocrinology (12th ed.). Elsevier/Saunders. 2011. pp. 1371–1435. ISBN 978-1-4377-0324-5.
 39. Lambert P, Bingley PJ (2002). "What is Type 1 Diabetes?". *Medicine*. 30: 1–5. doi:10.1383/medc.30.1.1.28264.
 40. "Classification of Diabetes mellitus 2019". *WHO*. Retrieved 2020-11-09.
 41. Tuomi T, Santoro N, Caprio S, Cai M, Weng J, Groop L (March 2014). "The many faces of diabetes: a disease with increasing heterogeneity". *Lancet*. 383 (9922): 1084–94. doi:10.1016/S0140-6736(13)62219-9. PMID 24315621. S2CID 12679248.
 42. "Definition of Diabetes mellitus". MedicineNet. Retrieved 2019-11-04.
 43. Rother KI (April 2007). "Diabetes treatment—bridging the divide". *The New England Journal of Medicine*. 356 (15): 1499–501. doi:10.1056/NEJMp078030. PMC 4152979. PMID 17429082.
 44. "Diabetes Mellitus (DM): Diabetes Mellitus and Disorders of Carbohydrate Metabolism: Merck Manual Professional". Merck Publishing. April 2010. Archived from the original on 2010-07-28. Retrieved 2010-07-30.

45. Dorner M, Pinget M, Brogard JM (May 1977). "[Essential labile diabetes (author's transl)]". *MMW, Munchener Medizinische Wochenschrift* (in German). 119 (19): 671–74. PMID 406527.
46. Petzold A, Solimena M, Knoch KP (October 2015). "Mechanisms of Beta Cell Dysfunction Associated With Viral Infection". *Current Diabetes Reports* (Review). 15(10): 73. doi:10.1007/s11892-015-0654-x. PMC 4539350. PMID 26280364. So far, none of the hypotheses accounting for virus-induced beta cell autoimmunity has been supported by stringent evidence in humans, and the involvement of several mechanisms rather than just one is also plausible.
47. Butalia S, Kaplan GG, Khokhar B, Rabi DM (December 2016). "Environmental Risk Factors and Type 1 Diabetes: Past, Present, and Future". *Canadian Journal of Diabetes*(Review). 40 (6): 586–93. doi:10.1016/j.jcjd.2016.05.
48. Serena G, Camhi S, Sturgeon C, Yan S, Fasano A (August 2015). "The Role of Gluten in Celiac Disease and Type 1 Diabetes". *Nutrients*. 7 (9): 7143–. doi:10.3390/nu7095329. PMC 4586524. PMID 26343710.
49. Visser J, Rozing J, Sapone A, Lammers K, Fasano A (May 2009). "Tight junctions, intestinal permeability, and autoimmunity: celiac disease and type 1 diabetes paradigms". *Annals of the New York Academy of Sciences*. 1165 (1): 195–205. Bibcode:2009NYASA1165..195V. doi:10.1111/j.1749-6632.2009.04037.x. PMC 2886850. PMID 19538307.
50. Laugesen E, Østergaard JA, Leslie RD (July 2015). "Latent autoimmune diabetes of the adult: current knowledge and uncertainty". *Diabetic Medicine*. 32 (7): 843–52. doi:10.1111/dme.12700. PMC 4676295. PMID 25601320.
51. American Diabetes Association (January 2017). "2. Classification and Diagnosis of Diabetes". *Diabetes Care*. 40 (Suppl 1): S11–S24. doi:10.2337/dc17-S005. PMID 27979889.
52. Carris NW, Magness RR, Labovitz AJ (February 2019). "Prevention of Diabetes Mellitus in Patients With Prediabetes". *The American Journal of Cardiology*. 123 (3): 512. doi:10.1016/j.amjcard.2018.10.032. PMC 6350898. PMID 30528418.

53. Risérus U, Willett WC, Hu FB (January 2009). "Dietary fats and prevention of type 2 diabetes". *Progress in Lipid Research*. 48 (1): 44–51.
54. Malik VS, Popkin BM, Bray GA, Després JP, Hu FB (March 2010). "Sugar-sweetened beverages, obesity, type 2 diabetes mellitus, and cardiovascular disease risk". *Circulation*. 121 (11): 1356– doi:10.1161/CIRCULATIONAHA.109.876185. PMC 2862465. PMID 20308626.
55. Malik VS, Popkin BM, Bray GA, Després JP, Willett WC, Hu FB (November 2010). "Sugar-sweetened beverages and risk of metabolic syndrome and type 2 diabetes: a meta-analysis". *Diabetes Care*. 33 (11): 2477–83. doi:10.2337/dc10-1079. PMC 2963518. PMID 20693348.
56. Hu EA, Pan A, Malik V, Sun Q (March 2012). "White rice consumption and risk of type 2 diabetes: meta-analysis and systematic review". *BMJ*. 344: *e1454*. doi:10.1136/bmj.e1454. PMC 3307808. PMID 22422870.
57. Lee IM, Shiroma EJ, Lobelo F, Puska P, Blair SN, Katzmarzyk PT (July 2012). "Effect of physical inactivity on major non-communicable diseases worldwide: an analysis of burden of disease and life expectancy". *Lancet*. 380 (9838): 219–29. doi:10.1016/S0140-6736(12)61031-9. PMC 3645500. PMID 22818936.
58. Huang, Hao; Yan, Peipei; Shan, Zhilei; Chen, Sijing; Li, Moying; Luo, Cheng; Gao, Hui; Hao, Liping; Liu, Liegang (2015-11-01). "Adverse childhood experiences and risk of type 2 diabetes: A systematic review and meta-analysis". *Metabolism – Clinical and Experimental*. 64 (11): 1408–1418. doi:10.1016/j.metabol.2015.08.019. ISSN 0026-0495. PMID 26404480.
59. "National Diabetes Clearinghouse (NDIC): National Diabetes Statistics 2011". U.S. Department of Health and Human Services. Archived from the original on 17 April 2014. Retrieved 22 April 2014.
60. Soldavini, Jessica (November 2019). "Krause's Food & The Nutrition Care Process". *Journal of Nutrition Education and Behavior*. 51 (10): 1225. doi:10.1016/j.jneb.2019.06.022. ISSN 1499-4046.
61. "Managing & Treating Gestational Diabetes | NIDDK". National Institute of Diabetes and Digestive and Kidney Diseases. Retrieved 2019-05-06.

62. National Collaborating Centre for Women's and Children's Health (February 2015). "Intrapartum care". Diabetes in Pregnancy: Management of diabetes and its complications from preconception to the postnatal period. National Institute for Health and Care Excellence (UK).
63. "Monogenic Forms of Diabetes". National institute of diabetes and digestive and kidney diseases. US NIH. Archived from the original on 12 March 2017. Retrieved 12 March 2017.
64. Thanabalasingham G, Owen KR (October 2011). "Diagnosis and management of maturity onset diabetes of the young (MODY)". *BMJ*. 343 (oct19 3): d6044. doi:10.1136/bmj.d6044. PMID 22012810. S2CID 44891167.
65. "Definition, Diagnosis and Classification of Diabetes Mellitus and its Complications" (PDF). World Health Organization. 1999. Archived (PDF) from the original on 2003-03-08.
66. Cleland, S. J.; Fisher, B. M.; Colhoun, H. M.; Sattar, N.; Petrie, J. R. (2013). "Insulin Resistance in Type 1 Diabetes". *Diabetologia*. National Library of Medicine. 56 (7): 1462–1470. doi:10.1007/s00125-013-2904-2. PMC 3671104. PMID 23613085.
67. Unless otherwise specified, reference is: Table 20-5 in Mitchell, Richard Sheppard; Kumar, Vinay; Abbas, Abul K.; Fausto, Nelson (2007). *Robbins Basic Pathology* (8th ed.). Philadelphia: Saunders. ISBN 978-1-4160-2973-1.
68. Sattar N, Preiss D, Murray HM, Welsh P, Buckley BM, de Craen AJ, Seshasai SR, McMurray JJ, Freeman DJ, Jukema JW, Macfarlane PW, Packard CJ, Stott DJ, Westendorp RG, Shepherd J, Davis BR, Pressel SL, Marchioli R, Marfisi RM, Maggioni AP, Tavazzi L, Tognoni G, Kjekshus J, Pedersen TR, Cook TJ, Gotto AM, Clearfield MB, Downs JR, Nakamura H, Ohashi Y, Mizuno K, Ray KK, Ford I (February 2010). "Statins and risk of incident diabetes: a collaborative meta-analysis of randomised statin trials". *Lancet*. 375 (9716): 735–42. doi:10.1016/S0140-6736(09)61965-6. PMID 20167359. S2CID 11544414.
69. "Insulin Basics". American Diabetes Association. Archived from the original on 14 February 2014. Retrieved 24 April 2014.
70. Shoback DG, Gardner D, eds. (2011). *Greenspan's basic & clinical endocrinology* (9th ed.). McGraw-Hill Medical. ISBN 978-0-07-162243-1.

71. Barrett KE, et al. (2012). Ganong's review of medical physiology (24th ed.). McGraw-Hill Medical. ISBN 978-0-07-178003-2.
72. Murray RK, et al. (2012). Harper's illustrated biochemistry (29th ed.). McGraw-Hill Medical. ISBN 978-0-07-176576-3.
73. Mogotlane, Sophie (2013). Juta's Complete Textbook of Medical Surgical Nursing. Cape Town: Juta. p. 83952.
74. ACD/ChemSketch Freeware, version 11, Advanced Chemistry Development, Inc., Toronto, ON, Canada, 2006, www.acdlabs.com.
75. Weininger D, 1988 'SMILES, a chemical language and information system introduction to methodology and encoding rules', J Chem Inf Comput Sci. vol 28, pp 31-36
76. www.ncbi.nlm.nih.gov/pubmed
77. Wolf LK, 2009, Digital briefs: New software and websites for the chemical enterprise. C&EN., vol.87, pp.32
78. Gnanendra Shanmugam, Anusuya Shanmugam, Natarajan Jeyakumar, 2012, 'Molecular modelling and active site analysis of SdiA homolog, a putative quorum for Salmonella typhimurium pathogenicity reveals specific binding patterns of AHL transcriptional regulators', J Mol Model, vol. 18, no. 10, pp. 4709 – 4719..
79. Liu, L.F., Desai, S. D., Li, T. K.; Mao, Y.; Sun, M.; Sim, S.P. Ann. N.Y. Acad. Sci. 2000, 922, 1-10.
80. Sargis Dallakyan, PyRx-Python Prescription 0.8, 2008-2010, The Scripps Research Institute [2008 – 2010].
81. Natesh R, Scjwager S.L.U., Evans H.R., Sturrock E.D., Acharya K.R., 2004, Structural Details on the Binding of Alzheimer's disease Drugs Captopril and Enalaprilat to Human BChE conversion.
82. Kim S, Thiessen PA, Bolton EE, Chen J, Fu G, Gindulyte A, Han L, He J, He S, Shoemaker BA, Wang J, Yu B, Zhang J, Bryant SH (2016) PubChem Substance and Compound databases. Nucl Acids Res, 44(DI):D1202-13.
83. Rarey M, Kramer B, Lengauer T, Klebe G (1996) A fast flexible docking method using an incremental construction algorithm, J Mol Biol, 261:470-89
84. Refer no: 79

85. Stierand K, Maab P, Rarey M (2006) Molecular complexes at a glance: automated generation of two-dimensional complex diagrams, *Bioinformatics*, 22:1710-1716.